Thermophysics 2009

29th and 30th October 2009

Valtice, Czech Republic

Brno University of Technology

Acknowledgment

Publication of this book was financially supported by the Czech Ministry of Education, Youth and Sports, under project No MSM 6840770031.

Committees

SCIENTIFIC COMMITTEE

prof. Ing. Robert Černý, DrSc.
prof. Ing. Oldřich Zmeškal, CSc.
Ing. Ľudovít Kubičár, DrSc.

ORGANIZING COMMITTEE

Ing. Zbyšek Pavlík, Ph.D.
Ing. Milena Pavlíková, Ph.D.
Ing. Pavla Štefková
Bc. Lenka Hřebenová
Tomáš Bžatek

Thermophysics 2009 - Proceedings

Brno University of Technology, Faculty of Chemistry, 2009

ISBN 978-80-214-3986-3

Included papers were not corrected.

Content

Measurement of the thermo-physical parameters of materials with the use of the generalized non-stationary regime

Ivan. Baník, Jozefa. Lukovičová

Physics Department of Faculty of Civil Engineering of Slovak University of Technology
in Bratislava, 813 68 Bratislava, Radlinského 11,

e-mail: ivan.banik@stuba.sk

Abstract: *In this paper the specific measurement method for the determination of thermo-physical parameters of materials is described. All kinds of non-stationary thermal processes in a specimen can be used in this method. In practice, some advantageous thermal processes (concerning the dimension, etc.) are chosen. The repeated measurement does not require the application of the self-same non-stationary thermal process. In the measurement of the thermal conductivity coefficient of thermal insulating materials, it is very advantageous to use an accumulated core. The time-dependence of the temperature in chosen points of the specimen is recorded continuously. The analysis of these records yields thermal parameters. In some cases, the variable thermal power of the laboratory oven is also continuously recorded. The method can be applied to the measurement of the temperature dependences of the thermo-physical parameters in a wide temperature interval.*

Keywords: *thermal measurement, thermo-physical parameters, thermal conductivity, accumulative core*

1 Introduction

Considering the measurement of thermo-physical parameters, there is a large number of measuring methods and set-ups. Many of them are described in papers [1 – 8]. The methods used for measuring of thermo-physical parameters of materials can be divided into steady state and dynamic ones. J. Krempaský [2] estimated that there are approximately 500 measuring methods.

1.1 Measurement of thermal conductivity coefficient by the Accumulation Core Method (ACM)

This paper is a follow up to an earlier one [5]: "Method of Accumulation Core and its use by measuring thermal parameters of porous materials". This paper includes a proposal and theoretical analysis of a measuring method for thermo-physical parameters of materials using so called accumulation core. The accumulation core AC is a body of very good thermal conductivity (Fig. 1). Heat penetrates into the accumulation core from an outer metal block MB through the measured specimen (sample) S. Thermal differences in the volume of the metal block are to be ignored. The work deduces some general relations applicable for the accumulation core method in case of permanent temperature increase. The accumulation core method is an integral method. It is suitable for measuring parameters of heat insulants within a wide temperature range from low up to high temperatures. Essentials of the accumulation core AC method are fully displayed in Fig. 1.

1.2 Steady temperature increase conditions

Under these conditions the temperature of the outer block is changed linearly in time - it increases linearly. Such increase of the border temperature all over the surface surrounding the specimen and the accumulation core steadily creates regular temperature conditions of the system characterized by linear temperature increase of all the specimen volume (at each point of the system) including the accumulation core.

After having reached the steady state the created profile of the temperature field is "evenly" shifted towards higher temperatures while the speed of the temperature shift at each point of the system equals the speed of the temperature increase at the outer isotherm. Next, it will be shown that under the condition of steady temperature increase the coefficient of the thermal conductivity λ of the specimen can be stated as

$$\lambda = \frac{A c_j m_j \frac{dT}{dt}}{\Delta \mathrm{T} - \frac{B}{a}\frac{dT}{dt}} \tag{1}$$

where the parameter c_j represents a specific thermal capacity of the accumulation core and m_j represents its mass. The product $m_j.c_j$ represents the thermal capacity of the accumulation core. The parameter a is the coefficient of the diffusivity of the specimen. The differential dT means an elementary temperature increase at any point of the system and thus of the outer block temperature. The derivation dT/dt indicates the speed of the outer block temperature increase. The constants A and B represent characteristic constants of a specific measuring arrangement independent from the speed of temperature increase, the thermal capacity of the core and the thermal parameters of the specimen. In case of analytical, or computer based numerical, determination of the value of the constants A, B for a given system the upper mentioned relation enables determination of the coefficient of thermal conductivity λ for any speed of the temperature increase and for a specimen of different temperature parameters. It is sufficient to measure a difference $\Delta T = T_2 - T_1$ between the temperature of the outer metal block (outer isotherm) and the temperature of the accumulation core (the inner isotherm) and determine the speed of the temperature increase.

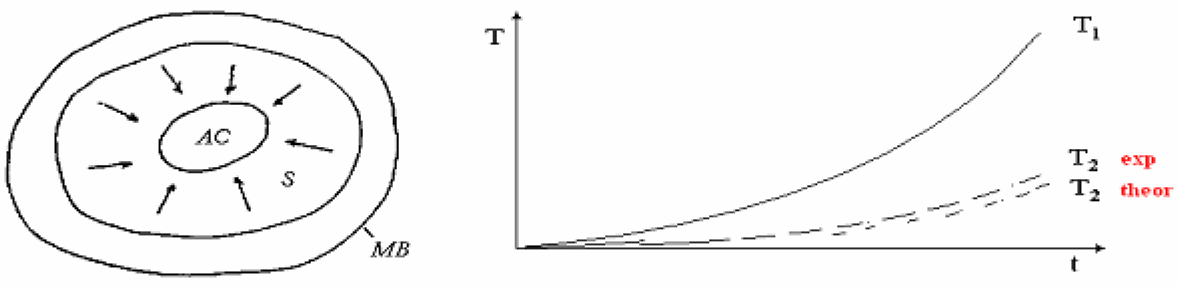

Fig. 1 Layout of the Accumulation Core Method, AC-accumulation core, MB-outer metal block, S – sample (specimen), T_1 – temperature of the MB, T_2– exp. – experimental temperature of AC, T_2- theor – theoretical temperature of AC

As the right side of the previous relation includes the coefficient *a* of the thermal conductivity of the specimen it seems impossible to determine the coefficient λ, unless the first coefficient is known. However, the real situation in case of thermal-insulating porous materials is more favorable. In the article we will also mention the way of measuring of coefficient *a*.

2 Accumulating core method of thermal conductivity measurement at general temperature regime.

By general thermal regime we can describe the change of the outer block temperature by:

$$\frac{dT}{dt} \neq const \tag{2}$$

The relation (1) is not valid. With small deviations from the regime with permanent increase of temperature is the relation (1) only usable for approximate estimation of the thermal conductivity coefficient and in order to achieve the precise values, we must use another procedure – described in following.

2.1 Measurement of the coefficient λ using ACM.

Using arrangement in Fig. 1 at general temperature regime, the outer metal block temperature T_1(t) is changed randomly (but not very fast). Subsequently, the accumulated core temperature T_2(t) changes. During measurement are these two temperature dependences recorded almost continuously.

We must underline that in this case the recorded dependence of accumulated core temperature T_2(t)-exp will be compared to another - to theoretical dependence T_2(t)-theor. This can be determined by theoretical calculation from the time dependence of the outer metal block temperature $T_1(t)$. It could only be done by knowing the specimen parameters λ and *a*, but we does not know them, on the contrary we want to measure them. In spite of that, this procedure can be used. The sample thermal conductivity coefficient λ will be assumed to be a changing parameter, which value is firstly only estimated. Using this estimated value we calculate the theoretical course of the function $T_2(t, \lambda, a) = T_2(t, \lambda, a)$-teor. This function will probably be not very similar to the real temperature course $T_2(t)$-exp in this phase. Next we will change the parameter λ in order to achieve a better agreement of these two functions. The least squares method is used for coincidence estimation of these two T_2-exp and T_2-theor functions. The sequence is parametric. The substantial step at its estimation describes the symbolic relation

$$\hat{P}\left[T_1, \lambda, a\right] = T_2 \; theor$$

which can be written more precisely in forms

$$\hat{P}\left[T_1\left(t\right), \lambda, a\right] = T_2\left(t\right) - theor$$

$$\hat{P}\left[T_1\left(x_1,t\right), \lambda, a\right] = T_2\left(x_3,t\right) - theor$$

Both these relations represent the fact, that by a computer program it is possible to determine the course of the accumulation core temperature T_2-theor, using the experimental temperature course $T_2(t)$-exp at selected parameters a and λ. The operator $\hat{P}$ is actually a computer program, which computes the function $T_2(t)$-theor. The parameter λ is changed in order to achieve a better agreement of the $T_2(t)$-theor with $T_2(t)$-exp curses. We assume that we already know the parameter a, eventually also its temperature dependence $a(T)$. Next we show how to find a better temperature dependence of $\lambda(T)$.

2.2 The procedure illustration

We assume that the sample temperature coefficient $\lambda(T)$ can be expressed as follows

$$\lambda = k_1\lambda_o + k_2 T + k_3 T^2 \tag{3}$$

where λ_o is an estimated input value of the temperature conductivity. Next we will look for the k_1, k_2, k_3 constants in Eq. (3), considering them components of a $\vec{k} = (k_1, k_2, k_3)$ vector, in a simplified version of two parameters $\vec{k} = (k_1, k_2)$. A specific function $\lambda(T)$ corresponds to each $\vec{k}$ vector according to Eq. (3). If we want to specify the $\lambda(T)$ dependence it is sufficient to change the $\vec{k}$ vector in small steps and in the "right" direction. Symbolically, we will realize changes:

$$\vec{k} \quad \rightarrow \quad \vec{k} + d\vec{k}$$

and so better the $\lambda(T) \rightarrow \lambda'(T)$. Fig. 2 explains this procedure for two dimensional $\vec{k} = (k_1, k_2)$.

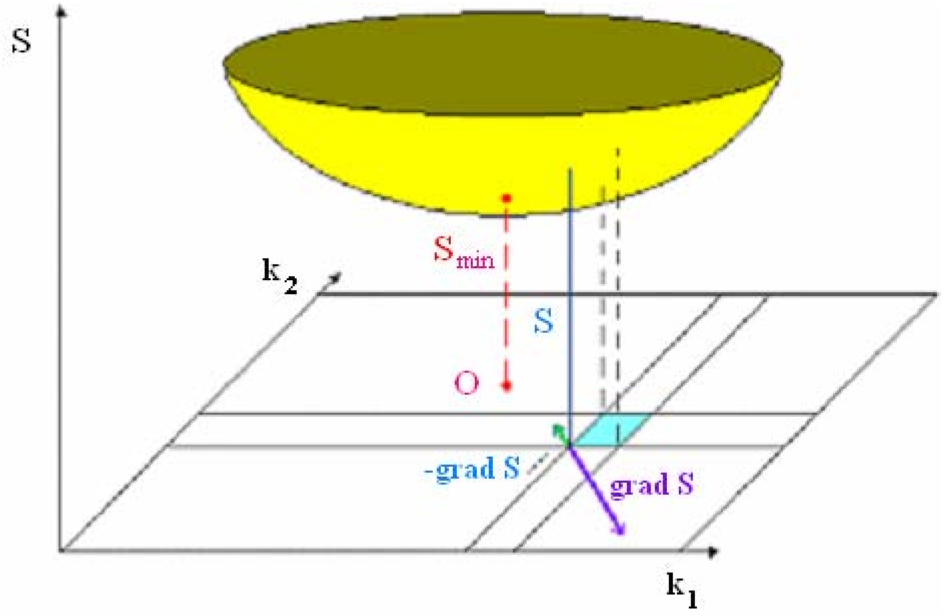

Fig. 1 Procedure for optimization of parameters k_1, k_2, k_3 I in Eq. (3)

The initial vector $\vec{k}$ in the k_1, k_2 plane is represented by its end point, to which a particular function $\Lambda(T)$ is assigned. The computer program generates the theoretical temperature course T_2 *theor* for this $\Lambda(T)$. Next, the computer evaluates the differences between this function and the real T_2-exp course, using the least squares method.

Let us mark the difference reached at this point as S (Fig. 2). Next, the program computes differences S′, S″ for two points close to $\vec{k}$ vector. A new vector grad S will be computed by a differential method from this three *S*, *S*′, S″ values. This grad S vector describes the direction of the fastest increase of *S* in the k_1, k_2 plane. The opposite directions (-grad S) shows, how to change the $\vec{k}$ vector in order to transpose to smaller S values. Next, the $\vec{k}$ vector will be replaced by $\vec{k} + d\vec{k}$, so

$$\vec{k} \quad \rightarrow \quad \vec{k} + d\vec{k}$$

where

$$d\vec{k} = -\, df \;\; grad \;\; S = -\, df \left(\frac{\partial S}{dk_1} \vec{i}\,' + \frac{\partial S}{dk_2} \vec{j}\,' + \frac{\partial S}{dk_3} \vec{k}\,' \right) \tag{4}$$

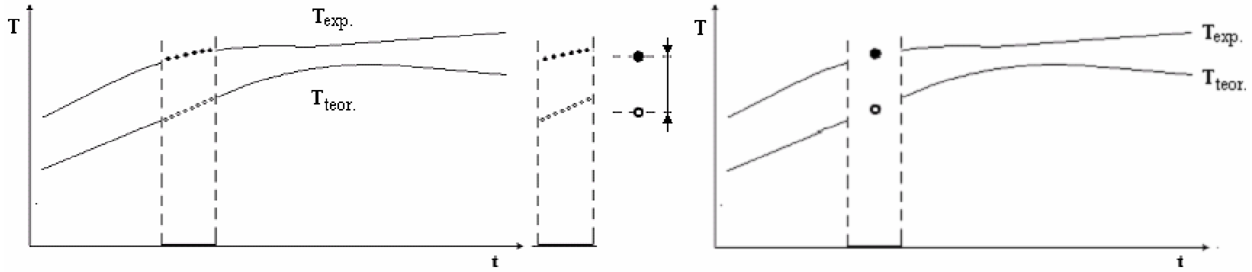

Fig. 3 Grouping of points on "point" curves creating of representative pairs

where df is a small chosen parameter. This phase enables a shift to a smaller S value, thus the new Λ(T) function defined by Eq. 2 gives a result better corresponding to the experimental course. This procedure will be repeated until a S-value minimum will be reached with sufficient accuracy.

Using a more dimensional $\vec{k}$ vector, the gradient will be more dimensional, too. The grad S vector will be then set by computing of the S value in more points of the more dimensional space. This procedure of searching for the Λ(T) function with k_1, k_2, k_3,.. parameters presents a non-standard use of the least squares method. The $\Lambda(T)$ curve is not superimposed over the measured $\Lambda_1(T_1)$, $\Lambda_2(T_2)$,.... points. The suitability of the k_1, k_2 parameters is set by the differential method computing (after considering the differences of the two temperature dependences - the computed and the measured one).

Evaluating the „agreement" or variance of the *T*(*t*)-theor and *T*(*t*)-exp functions it must be taken into account, that the functions are not continuous. The both compared functions consist of set of discrete points only, the density of which is different. That demands a non-standard procedure, core of which is shown in the Fig. 3. A point on one curve does not have his pair on the other curve, because each of them corresponds with high probability to other time data. Way out of this situation is the point grouping shown in the Fig. 3. It grounds in that, that for a group of points detected at a time interval we assign one representative point on one curve and another point on the other curve. In that way we reach an acceptable number of paired points in chosen time intervals. Based on them we can determine the differences of both functions and the corresponding S value. A similar sequence can be applied for measurements, at which a varying thermal power $P(t)$ of the heating body is recorded.

2.3 Accumulation core reduced to a point. Measurement of the a *coefficient.*

The measurement technique shown in Fig. 4 is a limited case of the accumulation core method. It corresponds to an endless small accumulation core, which was transformed into a point. The temperature sensor is placed in this point. Let us consider this question: How is it with the theoretical Eq. (1) in this specific case? The numerator in Eq. (1) is equal to zero in this case. The denominator must therefore have the zero value, too (because $\lambda \neq 0$) and thus

$$a = \frac{B}{\Delta \mathrm{T}} \frac{dT}{dt}$$

However this relation is only valid at the constant temperature increase regime. By sample simple geometries - e.g. block, cylinder or sphere - the B constant can be set analytically, too.

By these measurements at the general regime we must compare the real temperature course in the studying point of sample to the theoretically computed one. This can be achieved from the outer metal block temperature change data using the differential method, as well as by setting the a parameter. The a parameter is then changed in order to achieve the best coincidence of that two curves. In this way we achieve a value corresponding to the real thermal conductivity coefficient of the specimen.

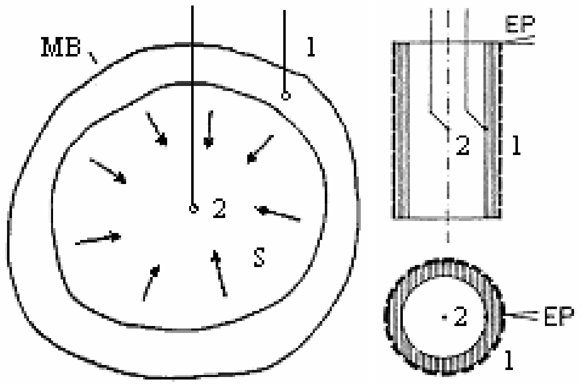

Fig. 4 Arrangement suitable for the thermal conductivity coefficient measurement

2.4 The computer programs testing

The computer programs used for theoretical curves determination and comparison to experimental ones can be tested as far as it concerns their quality and reliability by means of e.g. using the constant growth regime on a geometrically simple measuring sets. In this case we can find the precise analytical solution, which can be used for confrontation to numerical computing results. A good agreement between the computed and analytical results confirms the reliability of both, the methodology and the program. Analytical solutions by the constant growth regime are at disposal for the block, cylinder and sphere geometries.

3 Conclusion

The accumulation core method is an integral one. It uses the thermal capacity of a core inserted into the sample for the detection of heat transported through the sample. It does not require the source power measurement. The accumulation core has a big thermal conductivity, so it can be considered as an isothermal body. The accumulation core method is an integral one. It uses the thermal capacity of a core inserted into the sample for the detection of heat transported through the sample. It does not require the source power measurement. The accumulation core has a big thermal conductivity, so it can be considered as an isothermal body. The sample with the accumulation core is inserted into an outer metal block, which create another isothermal body. Measurement records the time-dependence of both these temperatures - the core and the outer block temperature. At a general temperature regime the temperature of the outer metal block is changed freely - it increases or decreases. Thereby an eventual error relating to the temperature regime repeatability at standard measurements is eliminated. The real outer block temperature course is "input" into the calculation, this regime need not to be repeated at another measurement. Errors at accumulation core temperature measurements are eliminating, however, speed temperature changes are inevitable from the point of view of measurement accuracy. The thermal conductivity is calculated parametrically by comparing the recorded accumulation core temperature to that one determined theoretically. The method can be applied to the measurement of the temperature-dependences of the thermo-physical parameters in a wide temperature interval.

4 **Acknowledgement**

At the end, we would like to thank Ing. Gabriela Pavlendová, PhD. and Prof. František Čulík from the FCE, Slovak University of Technology in Bratislava for valuable discussions on this topic.

This work was supported by the VEGA 1/4204/07 grant of Slovak Grant Agency.

5 References

[1] CARSLAW, H. S.; JAEGER, J. C.: Conduction of Heat in Solids, 2nd ed, Oxford University Press, London 2003, pp. 510. ISBN 0-19-853368-3.

[2] KREMPASKÝ, J.: The measurements of the thermo-physical Properties, SAV, Bratislava, 1969, pp. 288. ISBN 71-044-69.

[3] ČULÍK, F.; BANÍK, I.: Determination of temperature field created by planar heat source in a solid body consisting of three parts in mutual thermal contact, International journal of thermal sciences 48 (2009), p. 204-208.

[4] KONDRATIEV, G..M.: Teplovyje izmerenija, Mašgiz., Moskva-Leningrad 1957.

[5] BANÍK, I.: Method of Accumulation Core and its use by measuring thermal parameters of porous materials, Proc. Thermophysics 2006, p. 103-109. ISBN 80-227-2536-6.

[6] BANÍK, I.; LUKOVIČOVÁ, J.: Problem of elimination of undesirable thermal flows at thermo-physical measurements, Proc. Thermophysics 2007, p. 107-119, ISBN 978-80-227-2746-4.

[7] BANÍK, I.; MAĽA,P.; VESELSKÝ, J.; ZÁMEČNÍK, J.: Soil freezing technology, In: New Requirements for structures and their reliability, Prague 1994, Czech. Tech. Univ., Prague, 1994, p. 75-80.

[8] BANÍK, I.; BANÍK, R; VESELSKÝ, J.; ZÁMEČNÍK, J.: Meranie tepelných strát teplovodov, Pozemní stavby 1 - 1984, p. 29-32.

Investigation of moisture influence on thermophysical parameters of PORFIX aerated concrete

Vlastimil Boháč[1], Ľudovít Kubičár[1], Peter Dieška[2], Ladislav Némethy[3]

[1] Intitute of physics, SAS, Dúbravská cesta 9, 84511 Bratislava, Slovak Republic

[2] Department of Physics, FEI - STU, Ilkovičova 3, Bratislava, Slovak Republic

[3] PORFIX – pórobetón, a. s. Zemianske Kostoľany, Slovak Republic

Abstract: *Thermophysical properties of porous materials like aerated concrete are strongly dependent on moisture content in pores. This fact influences the use of such material in a practice. The knowledge of this behaviour and its influence on overall performance of the masonry material is one of the criteria for competitive success of the industrial product.*

Thermophysical parameters, e.g. the thermal conductivity, thermal diffusivity and specific heat of two PORFIX materials were measured by pulse transient method.

Two sets of PORFIX specimens of two different volume densities (400 and 520 Kg.m-3) were prepared. Specimen sets were conditioned under air protected conditions and were saturated with moisture content for a period of about one month. Final moisture content for each set was determined by weighting method. Thermophysical parameters were measured for six different moisture contents - 0, 3, 6, 10, 15 and 20 wt%.

The results show strong dependency on moisture content for all thermophysical parameters within an investigated range of conditioned moistures. We found, that the value of thermal conductivity of dry specimens and the conditioned one to the 20wt% of moisture content increases two times.

Keywords: *pulse transient method, moisture content and thermophysical properties, physical models.*

Introduction

Thermal properties of materials are basic criteria for quality of building construction and thermal insulation materials. New building materials PORFIX and PORFIX Plus have excellent thermal-insulation properties. Aerated concrete PORFIX Plus save expenses at the house construction as well as heating overheads. The energy prices are increasing so the needs of energy savings are highly demanded. Low thermal losses and energy saving are important economical and ecological aspects at the house keeping as the higher surface temperature of inner wall surface protect against dew of moisture and creation of fungus also. The only problem is that the moisture content influences the insulation performance that is decreasing with the increased moisture content in a wall. Thus the testing procedures and methods are required for measuring of these properties also. Nowadays, the class of transient techniques are used in practice that should satisfy all the testing requirements for new materials [1-5].

In this paper we used pulse transient technique for investigation of the moisture influence on insulation properties of PORFIX aerated concrete. For the parameter estimation the modified model considering real pulse width instead of Dirac's pulse was used. This model was previously analysed and tested including analysis of parameter estimation by difference analysis, analysis of sensitivity coefficients [1, 2].

The effects that are influencing measurements on building materials were described in some previous papers [1, 2], so just a short review of a problem is given here.

The problem is, that ideal model with infinite specimen geometry is simple and is keeping low number of unknown parameters for parameters estimation, but in real experiment it is valid under limited conditions. A detailed study was published for the cases when experimental circumstances and disturbing effects are influencing accuracy of calculations according to chosen model. The most important effect is the heat loss effect from the sample surface caused by real finite geometry of the specimen as well as the stabilized temperature of the specimen holder that fixes the temperature at the specimen end surfaces. In an ideal case in infinite media the heat flow forms a planar isotherm. In the real specimen the heat flux penetrates into the material and flow out through the surface. So the flux density near the surface area is lower. Final planar isotherm is deformed at the edges in time and thus the ideal model is valid just in limited time window of the total transient recording. This time corresponds to a certain penetration depth that means to the corresponding thickness of measured material. Then the evaluation procedure is based on manual selection of the time window for evaluation by fitting procedure. This is complicated and not objective. In previous works we avoided various disturbance effects by setting the optimal geometry that was in principal found for two classes of materials. As the result it was found optimized specimen geometry when no disturbance effects harm the measurement accuracy [1 / 3]. In this paper we used optimized specimen geometry, e.g. the thickness for PORFIX material that was 20 mm.

Pulse transient method

The principle of the pulse transient technique is based on generation of the heat pulse by the planar heat source and on registration of transient temperature response by thermocouple placed in distance h apart of the heat source. The thermophysical parameters, e.g. thermal diffusivity, thermal conductivity and specific heat are calculated from the characteristic parameters of the temperature response to the heat pulse [1]. The experimental arrangement is drawn in figure 1.

Experiment was evaluated using model that accounting the heat pulse duration. Temperature function that describe the temperature response to the heat pulse is given in a form

$$T(h,t) = \frac{2 \cdot Q}{c\rho\sqrt{a}} \left[\sqrt{t} \cdot i\Phi^* \left(\frac{h}{2\sqrt{at}} \right) - \sqrt{t - t_0} \cdot i\Phi^* \left(\frac{h}{2\sqrt{a(t - t_0)}} \right) \right] \tag{1}$$

where

$$i\Phi^* = \frac{e^{-x^2}}{\sqrt{\pi}} - x \cdot erfc(x) \tag{2}$$

For the simplicity of calculations of thermophysical parameters there were derived formulas that are valid for the maximum of the temperature response. This way of parameters estimation was signed as one-point evaluation procedure. The thermal diffusivity is given as

$$a = h^2 / 2t_m \cdot f_a \text{ ,} \tag{3}$$

where $f_a = \left(t_m/t_0 - 1\right) \cdot \ln\left(\frac{t_m/t_0}{t_m/t_0 - 1}\right)$

the specific heat,

$$c = \frac{Q}{\sqrt{2\pi e}\rho h T_m} f_c \ , \tag{4}$$

$$f_c = 2 \cdot \exp(1/2)\sqrt{\pi \ f_a} \cdot t_m/t_0 \left\{1/\sqrt{\pi}\left[\exp(-f_a/2) - \sqrt{(t_m/t_0 - 1)/t_m}\ \exp\left(t_m/t_0\, f_a/2(t_m/t_0 - 1)\right)\right] - \right.$$
$$\left. - \sqrt{f_a/2}\left[\Phi^*\left(\sqrt{f_a/2}\right) - ercf\left(\sqrt{t_m/t_0\, f_a/2(t_m/t_0 - 1)}\right)\right]\right\} \tag{5}$$

and the thermal conductivity

$$\lambda = ac\rho = h^2/2t_m \cdot f_a \frac{Q}{\sqrt{2\pi e}\rho h T_m} f_c \rho \ , \tag{6}$$

where $Q = RI^2 t_o$, R is the electrical resistance of the heat source, ρ is density, Tm is maximum temperature of the temperature response, tm is time when temperature rich the maximum and other parameters are given in the Figure 1.

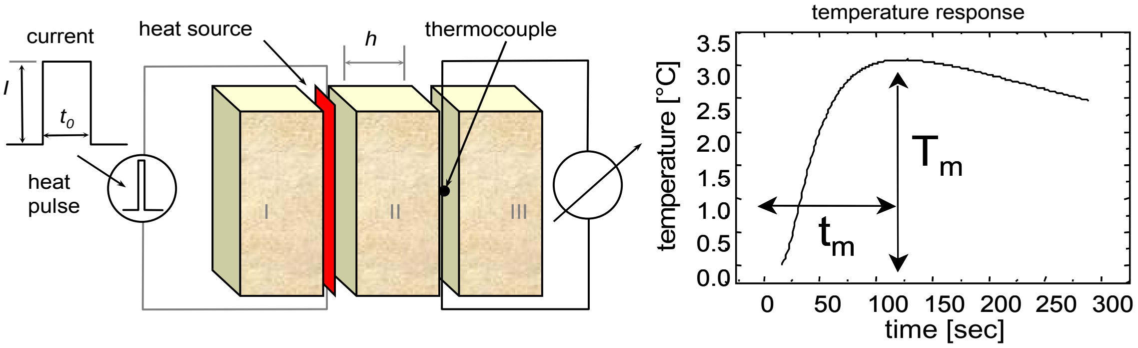

Figure 1. Principle of the Pulse transient technique. The specimen set with an electronic circuit on the left and temperature response on the right side.

Sample preparation

Four batches of two kinds of samples P2 and P5 were prepared. Their densities in dried states were 522, 527 and 398, 407 kg.m^{-3}. Each specimen set of four batches was conditioned on moisture content of 0, 3, 6, 10, 15, 30 Wt%. Totally 24 specimen sets were prepared and kept in plastic bags sealed with plastic zip to avoid moisture evaporation. Some evaporation was still possible during the storage time as the measurements were done in duration of two months for each material (P1&2 and P5&6). At the measurement the sample set in figure 3 was packed in a plastic foil to minimize the evaporation during the measurements. Sample dimensions were 100x100mm of square cross section and the thicknesses of environmental parts I and III were

35mm and 20mm for middle part II in average (Figure.1, 3). Over all dimensional fluctuations were about 1-2%.

Figure 3. Sample set (parts I, II and III) with inserted heat source and thermocouple. The silicon paste with Al_2O_3 powder filler (Midland Silicon Ltd.) was used to improve thermal contact between all parts.

The weight of each part of specimen set was measured before the measurement. After than the average volume densities of samples were recalculated and are plotted in figure 4 in dependency on moisture content. This plot gives the view on sate of conditioning. While the sample batches P1 and P2 show nearly linear dependency, the sample batches P5 and P6 show larger data scattering. The first reason of larger data scattering for lower density material is that the fluctuations of pore distribution should be larger than in a case of material having higher densities. This is the reason why the sample of 0 Wt% of moisture have the volume density greater than those one with moisture content 3 and 6 Wt%. Similar behaviour was observed for P6 specimens with 10 and 15 Wt% of moisture. The next reason of data scattering is caused most probably by the fact that moisture conditioning was broken. The measurements were performed in hot days from August till September 2008. The samples were kept just at room temperatures in plastic bags sealed with plastic zip and were probably dried in not defined way. Unfortunately, the moisture content was not able to recalculate before the measurement due to lost of weight data measured before the conditioning of materials in dry state. So in this case another view on data plot based on dependency on densities instead of moisture content give more reliable information on this problem. This fact is illustrated on figure 4, 5 and 6.

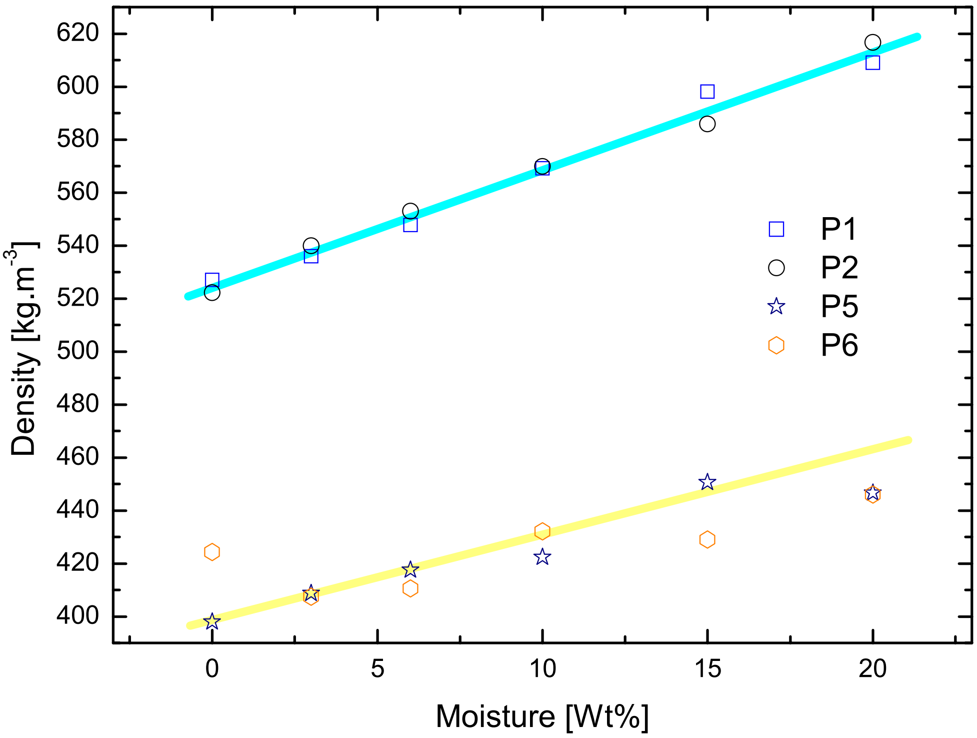

Figure 4. The values of sample densities plotted versus moisture content. Sample batches P5 and P5 show larger scattering.

Experimental results

The measured thermophysical parameters plotted versus moisture content are in figure 5. Lower values of transport parameters for material with lower density are caused by larger number of pores in structure. The measured values of thermophysical parameters are strongly dependent on moisture content. The larger data scattering in a case of material of lower density is caused by broken conditioning as it is clear from figure 4. Corresponding thermophysical data for all samples are in a figure 5 and 6. The data for P6 material are line connected to keep on mind increasing of moisture content. The sample P6 conditioned at 20Wt% of moisture content was dried in situ under the vacuum at 25°C for about 4 days to get stabile values. In this way we checked the values of thermophysical parameters for dry state of material. Values for originally dry sample are the same as the values obtained after vacuum drying process during in situ measurements. This was confirmation of thermophysical values for dry state of a sample.

Conclusions

The measured thermophysical parameters are clearly dependent on moisture content. The value of thermal conductivity can increase 2 times at 20%wt. of water content. The lower values of transport parameters for material with lower density are caused most probably by broken conditioning as it is clear from figure 4. Thermal resistivity of POROFEN P1 and P2 bricks having 375 mm thickness recalculated form measured value of thermal conductivity in dry state is R=2.93 $m^2.K.W^{-1}$ and 3.62 $m^2.K.W^{-1}$ for POROFEN P5 and P6 specimens that have lower volume densities. In a case of 20 Wt% of moisture content this values are decreased to R=1.46 and 2.34 $m^2.K.W^{-1}$ respectively. To satisfy the conditions imposed in STN 730540-2, the R-value

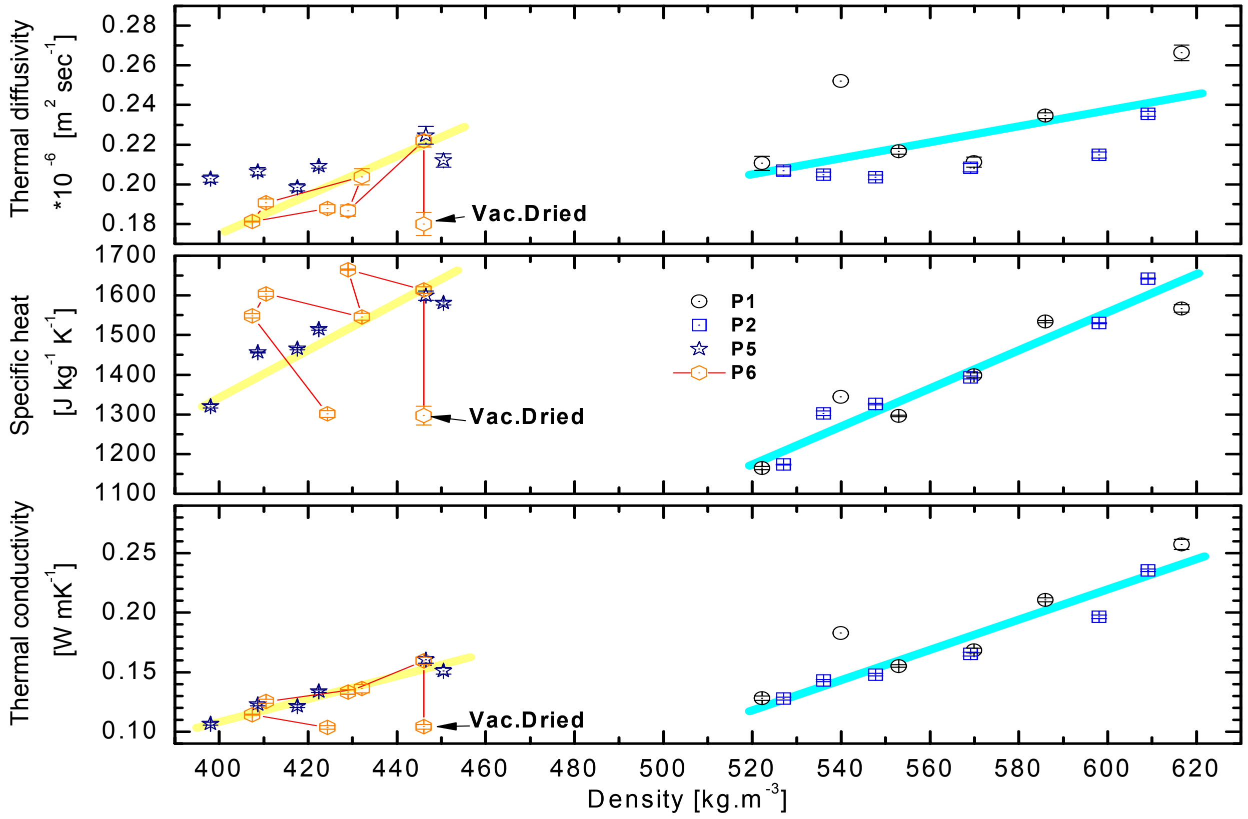

Figure 5. Thermophysical parameters plotted in dependency of moisture content.

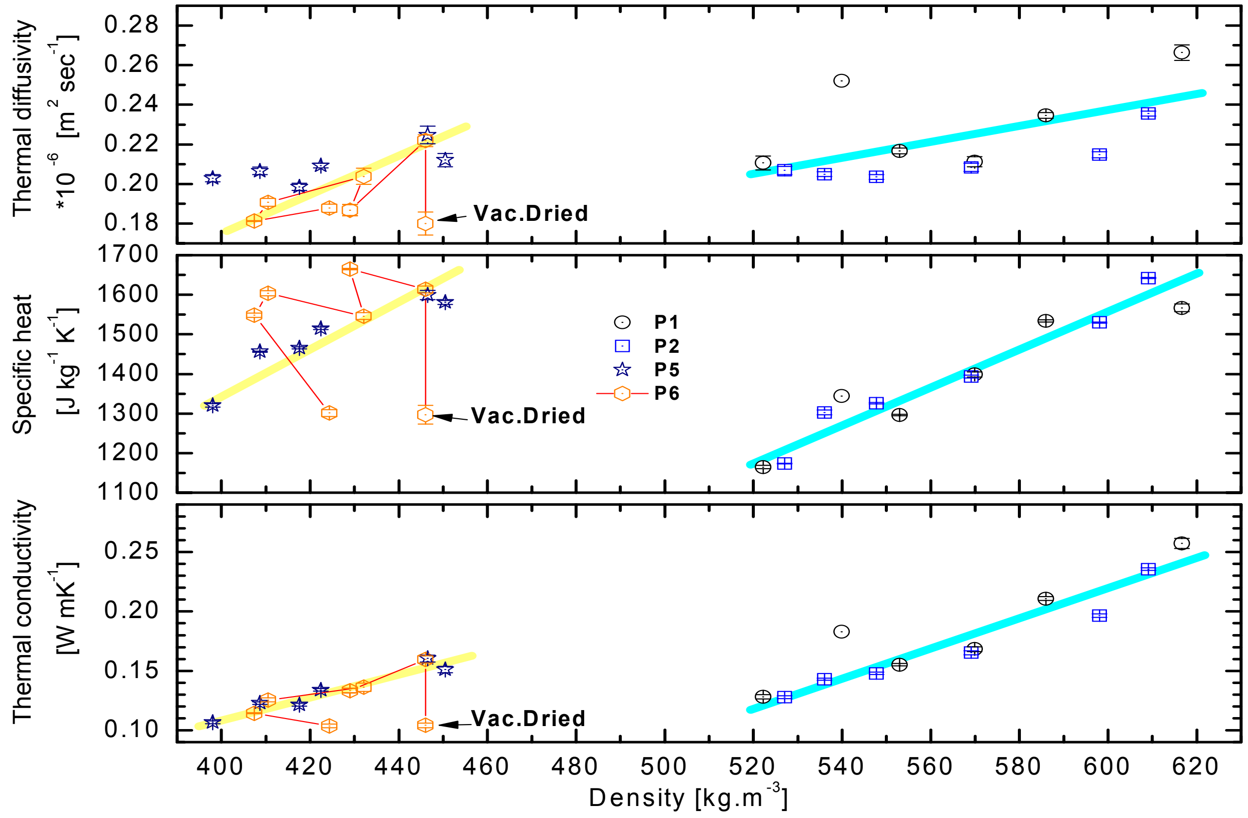

Figure 6. Thermophysical parameters plotted in dependency of density. The data for P6 material are line connected to keep on mind increased moisture content.

for a new building have to be greater than 3 $m^2.K.W^{-1}$. In each case of measured PORFIX materials in dry state the R values are high enough that extra insulation material becomes superfluous and the overall insulation level for our climate is easily achieved. This means that there it is no need of extra insulation for masonry walls build up from this kind of bricks.

References

[1] KUBIČÁR, Ľ. (1990): Pulse method of measuring basic thermophysical parameters. Comprehensive Analytical Chemistry, ed. G. Svehla, Elsevier, Amsterdam, Tokyo, Oxford, New York

[2] KUBIČÁR Ľ., BOHÁČ V., (1999): Review of several dynamic methods of measuring thermophysical parameters. in "*Proc. of 24th Int. Conf. on Thermal Conductivity / 12th Int. Thermal Expansion Symposium*", ed. P.S. Gaal, D.E. Apostolescu, Lancaster: Technomic Publishing Company, pp. 135–149.

[3] GUSTAFSSON S.E. 1991. *Rev. Sci. Instrum*. 62:797-804

[4] SABUGA W., HAMMERSCHMIDT U. *International Journal of Thermophysics*, 1995, 16 (2): 557-565

[5] KREMPASKÝ J. *Meranie termofyzikálnych veličín*. Vyd. SAV, Bratislava, 1969, 1-288.

[6] BOHÁČ V., KUBIČÁR Ľ., VRETENÁR V., *HIGH TEMP-HIGH PRESS*. 2003/2004, Vol. 35/36, pp. 67-74

[7] BOHÁČ V. et all. Methodology of parameter estimation of pulse transient method and the use of PMMA as standard reference material. *Proc. of TEMPMEKO 2004*, 22 - 25 June 2004 Dubrovník, Croatia

[8] BOHÁČ V., VRETENÁR V., KUBIČÁR Ľ. Optimization methodology for the pulse transient method and its application at the measurement of thermophysical properties of materials, *Proc. of the Thermophysics 2007.* Kočovce, October 12 – 13, 2005, Editors: Peter Matiašovský, Oľga Koronthályová, Issued by Institute of Construction and Architecture, Slovak Academy of Sciences in Bratislava, First Edition Released in 2005, ISBN 80-969434-2-1 EAN 9788096943425

[9] BOHÁČ V., DIEŠKA P., AND KUBIČÁR Ľ. The progress in Development of new models for pulse transient method. *Proc. of Thermophysics 2007*. Editor: Jozef Leja, Vydavateľstvo STU, Bratislava 2007, ISBN 978-80-227-2746-4

[10] BOHÁČ V., KUBIČÁR Ľ., VRETENÁR V. Methodology of the testing of model for contact pulse transient method and influence of the disturbance effects on evaluating thermophysical parameters of the PMMA, *Measurement Science Review*, Volume 5, Section 3, 2005, pp.98-103

[11] DIEŠKOVÁ M., DIEŠKA P., BOHÁČ V., KUBIČÁR Ľ. Determination of temperature field and an analysis of influence of certain factors on a temperature fields. *In collection of manuscripts* of the 17th ECTP, 2005, Bratislava, Slovakia. Vozár L., Medveď I. and Kubičár Ľ. editors. (CD-ROM).

[12] BOHÁČ V., DIEŠKA P., AND KUBIČÁR Ľ. The heat loss effect at the measurements by transient pulse method, *Measurement Science Review*, Vol. 7, Sect. 3, No.1, 2007, pp.24-28

Study of the curing process of an epoxy resin by monitoring of the thermal conductivity using the Hot Ball method

Carlos Calvo Aníbarro[1], Ľudovít Kubičár[1], Ivan Chodak[2], Igor Novak[2]

[1]Institute of Physics SAV, Dúbravská cesta 9, SK-845 11 Bratislava, Slovakia email: ccalvoanibarro@gmail.com

[2] Polymer Institute SAV, Dúbravská cesta 9, SK-845 11 Bratislava, Slovakia

Abstract: *Epoxy resins are materials capable of polymerizing under determined conditions, i.e. a temperature increase or the presence of a hardener, yielding a three-dimensional net formed by the cross-linking of the chains. This polymerization is also called curing process. During the curing process different physical changes can be detected. First, blocks of polymers are formed and then, the blocks are cross-linked obtaining the cured epoxy resin with high molecular weight and viscosity. As a consequence of the aforementioned changes, the heat capacity, the main free path of phonons and the velocity of phonons are affected, altering the thermal conductivity of the system as well. This paper deals with the study of the curing process of an epoxy resin by monitoring of the thermal conductivity using the Hot Ball method.*

Keywords: *Hot Ball method, epoxy resin, curing process, thermal conductivity*

1. **Introduction**

The polymerization is the technological process during which small molecules (monomers) reach to macromolecules (polymers). Depending on the kind and the conditions of the reaction we can change the macromolecules structure and, consequently, the final product properties.

Among the polymers, the epoxy resins have a huge commercial application. Epoxy resins can crosslink yielding a three-dimensional net. The properties of these cross-linked resins depend on the curing system and on the kind of resin, but in general they have excellent chemist resistance, a high adhesion to a huge number of substrates, very good mechanical properties and very good electrical isolation properties. [1]

With the Hot Ball method, we are able to follow the curing process measuring the thermal conductivity changes, related with the physical changes of the system. Several technological processes have been studied with the Hot Ball method, i.e. concrete stiffening, moisture diffusion through porous materials or vulcanization of a rubber. [2]

The Hot Ball method

The Hot Ball method belongs to transient measuring techniques. This method is based on the generation of a constant heat flux by a spherical heat source inside the material to be tested, measuring the temperature response with a thermometer placed in the centre of the heat source.

The constant heat flux is generated by the passage of an electrical current through a resistance assembled to the spherical heat source (r_b). The heat flux penetrates inside the hot ball sensor surrounding (R).

Fig.1. Photo of the hot ball sensor

A thermometer placed in the centre of the heat source measures the temperature response. While the heat transfer to the surrounding medium is being produced, the temperature of the sample is increased up to a maximal value (T_m), where the temperature is stabilized.

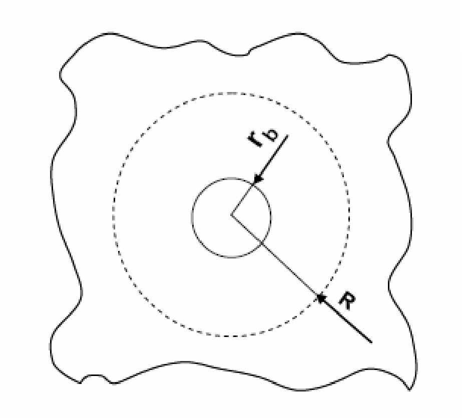

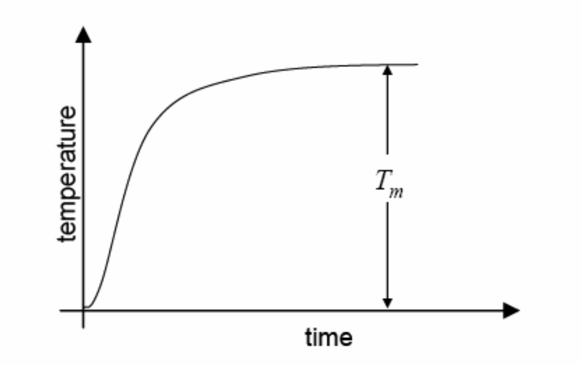

Fig.2. Ideal model Fig.3. Ideal temperature response

This maximal value of the temperature response is used to calculate the thermal conductivity of the material by the relation (1):

$$\lambda = \frac{q}{4\pi r_b T_m (t \to \infty)} \qquad (1)$$

where λ *[Wm⁻¹K⁻¹]* is the thermal conductivity, q *[W]* is the heat flux, r_b *[m]* is the heat source radius and T_m *[K]* is the stabilized temperature value.

In order to obtain a picture on long time thermal conductivity change, testing of the material property is performed by cycles. Each cycle consists on the measuring of the ball temperature (obtaining the base line), the generation of a constant heat until obtaining the stabilized temperature value after some time, and a stabilization stage produced when the heat generation is interrupted.

Results of each cycle are stored in the data logger and transferred into computer, obtaining automatically the thermal conductivity value for each measuring cycle. [3]

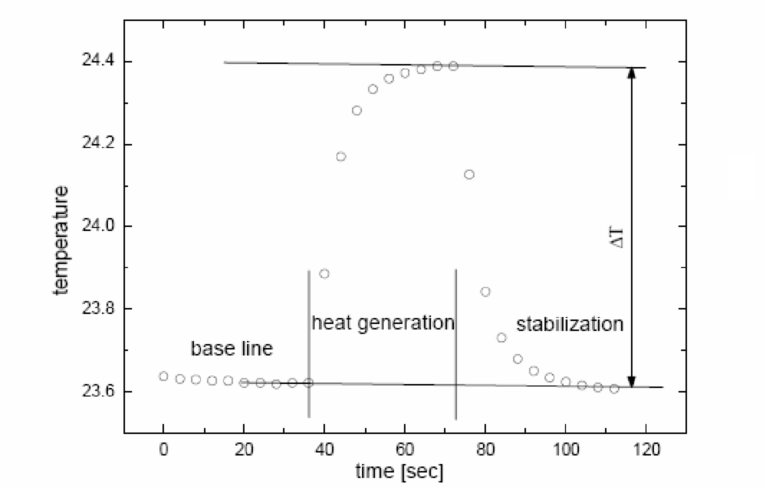

Fig.4.Measuring cycle

Epoxy resins

Epoxy resins are polyether resins containing more than one epoxy group in each molecule. This epoxy group can be found in the middle of the chain, but usually it is in the terminal position. The three members ring is much tensioned, so it reacts easily with a lot of molecules, especially with the ones that give protons. These reactions allow the extension of the chain and the cross-linking. This polymerization is also called curing process. [4]

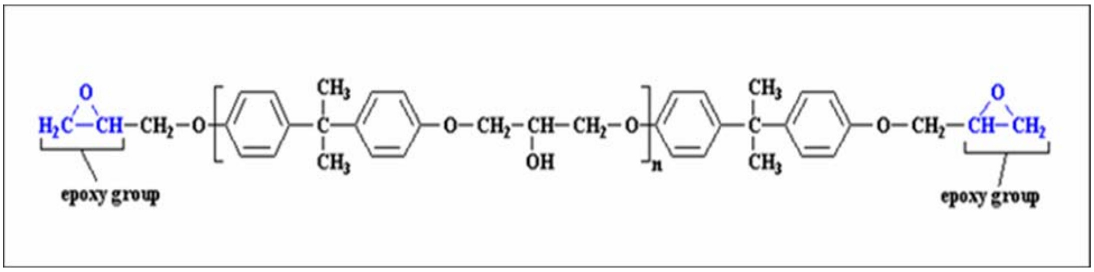

Fig.5.Epoxy resin structure

During the curing process different physical changes can be detected. First, blocks of polymers are formed and then, the blocks are cross-linked obtaining the cured epoxy resin with high molecular weight and viscosity.

As a consequence of the aforementioned changes, the heat capacity, the main free path of phonons and the velocity of phonons are affected, altering the thermal conductivity of the system as well. The problem is to know which of these processes is the predominant in each step of the curing process.

In the first step, a strong change of the configuration entropy is observed due to formation of chain blocks that suppresses reorientation jumps. Therefore heat capacity strongly decreases as the number of blocks increases.

During the cross-linking of the resin the viscosity is increasing. Thus the shear module is increasing as well, the sound velocity is growing and this effect causes growth of thermal diffusivity.

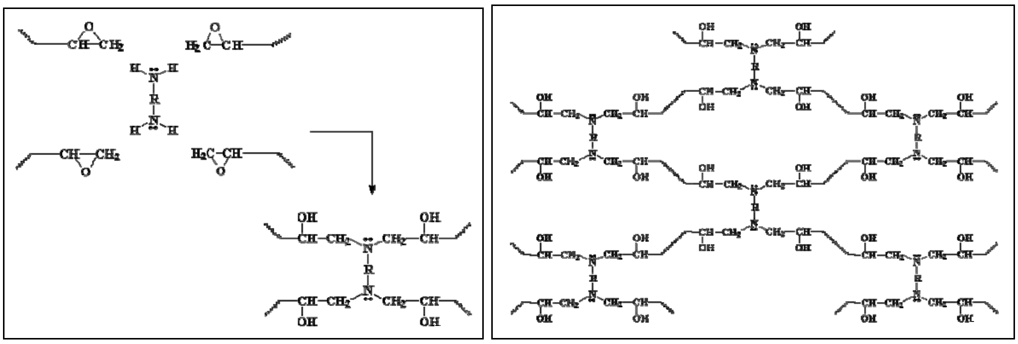

Fig.6.Left: formation of blocks. Right: epoxy resin cross-linked

For this experiment we used an epoxy resin based on bisphenol A and an aliphatic diamine as hardener. The sample was prepared by the Polymer Institute of the Slovak Academy of Science.

2. System

A system was prepared in order to realize the measurements. The sample was put inside a metallic recipient, and the hot ball sensor was placed in the middle of this recipient.

A first chamber was placed over the recipient and a second chamber was placed over the first one to have an isothermal process. The temperature inside the chamber is controlled by a thermostat.

The hot ball sensor is connected to an electronic unit that realizes the required functionalities to obtain data on thermal conductivity and to store the corresponding data. Those data are transferred to a computer.

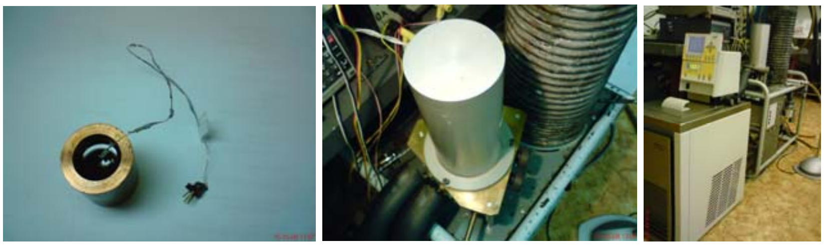

Fig.7.Picture of the hot ball sensor inside the sample

3. Experiment

The calibration of the hot ball sensor is based on the relation (2):

$$ {}^{q}\!\big/_{T_m} = 4\pi r_b \lambda = A\lambda \tag{2} $$

The ratio q/T_m is a linear function of thermal conductivity that will be tested using certified materials, namely porofen, calcium, PMMA and glycerol. A calibration function was obtained.

In order to start the monitoring of the curing process, the temperature was set at 70°C. When this temperature was stabilized, the mixture of the epoxy resin was put in the recipient and the hot ball sensor was introduced in the middle of the mixture. Room temperature values of the thermal conductivity were taken by RTM instrument. Then, the recipient was put into the preheated chamber and the monitoring started using the RTM instrument.

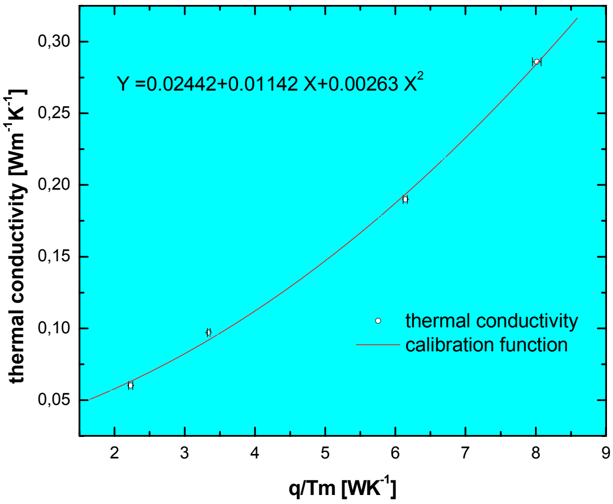

material	**q/Tm**	**lambda**	**error**
Porofen	2,2296	0,06	0,03
Calcium	3,3426	0,097	0,02
PMMA	6,1418	0,19	0,03
Glycerol	8,0134	0,286	0,06

Fig.8.Calibration function

The figure 9 shows changes of the thermal conductivity and temperature during the experiment. The experiment started at room temperature. First, we could observe how the thermal conductivity was going to higher values. It was due to an increasing of the structural entropy of the system because of the increase of the temperature, increasing also the thermal conductivity of the initial mixture of the two components. After some time, the thermal conductivity started to go to lower values again. It is supposed that in this stage of the polymerization blocks of the polymer start to be formed. This formation decreases the configurationally entropy, decreasing the heat capacity as well.

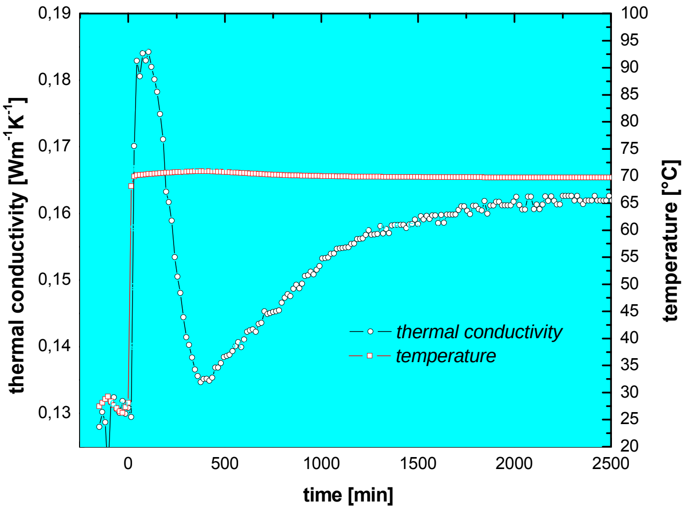

Fig.9.Variation of the thermal conductivity during curing process of the epoxy resin

After this effect, we can observe that that the thermal conductivity is going to higher values. It is in this stage when the cross-linking is taken place. While the three-dimensional net is being formed, the viscosity of the system is increasing, increasing the shear module. It means a growing of the sound velocities. The thermal conductivity increases until a stabilized value.

4. Conclusions

With this experiment we want to present the application of the Hot Ball method to monitoring curing process of an epoxy resin.

For the experiment, an epoxy resin based on bisphenol A has been used, and an aliphatic diamine was used as hardener for the cross-linking. Nowadays, the 80-90% of the commercial epoxy resins is based on bisphenol A.

During the curing process we could observe several physical changes and we were able to determine them monitoring the thermal conductivity using the Hot Ball method.

In a first step, the formation of structural blocks decreases the structural entropy, decreasing as well the specific heat.

In a second step of the curing process, the cross-linking increases the thermal conductivity due to growth of the shear module.

The Hot Ball method has been used as well for monitoring of different technological processes, i.e. vulcanization process of a rubber, water diffusion through porous materials or concrete stiffening.

References

[1] INSTITUTO DE CIENCIA Y TECNOLOGÍA DE POLÍMEROS. Ciencia y Tecnología de Materiales Poliméricos, Volumen II, Ed. CSIC, Madrid, 2004. p 133-141. ISBN 84-609-0968-9.

[2] KUBICAR, L.; VRETENAR, V.; STOFANIK, V.; BOHAC, V., BAGEL, L. Thermophysical sensors: Theory and application of the hot ball, in Proc. of Twenty-Ninth International Thermal Conductivity Conference, Proceedings of Seventeenth International Thermal Expansion Symposium, June 24-27, 2007, edited by John R. Koening, Heng Ban, Lancaster, Pennsylvania, DEStech Publication, Inc., 412-425

[3] KUBICAR, L.; VRETENAR, V.; STOFANIK, V.; BOHAC, V. Thermophysical Sensors: Theory and Realiability of the Hot Ball, Proceedings of the Asian Thermophysical Conference, 21-24 August, 2007, Fukuoka, Japan, sent for publication to Int. J of Thermophysics

[4] CLAYTON A. MAY. Epoxy resins. Chemistry and Technology. Yoshio Tanaka eds., Marcel Dekker Inc., New York 1973

Diffusivity determination from measurement of the time development temperature inside a sample

František Čulík, Jozefa Lukovičová

Slovak University of Technology, Faculty of Civil Engineering

Department of Physics

Abstract: *The conditions are discussed under which the non steady temperature field inside a cuboids or a slab of the thickness l can be considered as 1D problem. In this case we introduce two solution of the 1D heat conduction equation under constant temperature* T_s *at the border planes of the slab as well as at a constant initial temperature* T_0 *inside the slab. Knowledge of the time development temperature from experiment in a plane inside the slab parallel to the border planes permits us to determine thermal diffusivity a2 of the slab. To this aim the solutions of the 1D heat conduction eq. represented by infinite series it is possible to cut off after first n terms and to omit the rest. Such finite series well approximate time development of the temperature in two cases: in the short period of the time* $t << \ell^2/a$ *and in the long period of the time* $t >> \ell^2/a$.

Keywords: *temperature field in a slab, diffusivity determination*

1. Introduction

First we shall consider a cuboidal sample. It is assumed that the temperature at the border surfaces is constant equal to Ts and initial temperature inside the sample is also constant and is equal to $T_0 \neq T_s$. This problem is not a new one but it is still relevant. It has appeared simultaneously with the knowledge that the non steady-temperature field offers a chance for determination some thermal quantities like thermal diffusivity a2, thermal conductivity λ, specific heat capacity c.

In this article a simple method will be demonstrated for determination those characteristics.

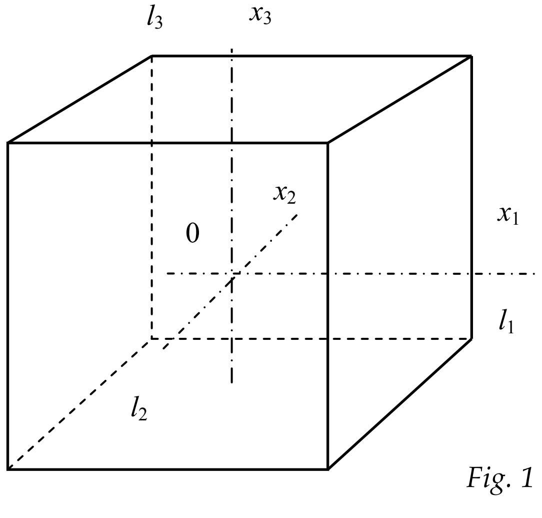

Fig. 1

Fig.1 shows a cuboidal sample with edges l1, l2, l3 and the coordinate system. Origin of the coordinate system is located at the centre of the sample with axes orthogonal to the border surfaces. Temperature at the border surfaces stays constant and is equal to Ts. Initial temperature inside the cuboids is also constant and is equal to T_0.

1a. Three-dimensional temperature field inside a block

The border conditions mentioned above are

$$T\left(x_1 = l/2, x_2, x_3, t\right) = T\left(x_1 = -l/2, x_2, x_3, t\right) = T\left(x_2 = l_2/2, x_1, x_3, t\right) =$$
$$T\left(x_2 = -l_2/2, x_1, x_3, t\right) = T\left(x_3 = l_3/2, x_1, x_2, t\right) = T\left(x_3 = -l_3/2, x_1, x_2, t\right) = T_s, \ t > 0 \qquad (1.1)$$

and the initial condition is

$$T\left(x_1, x_2, x_3, t = 0\right) = T_0 \ , \quad -l_i/2 < x_i < l_i/2 \ , \ i = 1,\ 2,\ 3 \ , \ t > 0 \qquad (1.2)$$

Solution $T\left(x_1, x_2, x_3, t\right)$ of 3D heat conduction equation

$$\frac{\partial T}{\partial t} - a^2 \nabla^2 T = 0 \qquad (1.3)$$

by the method of variable separation assuming it obeys boundary (1.1), and initial (1.2) conditions is given as [1]

$$\frac{T\left(x_1, x_2, x_3, t\right) - T_s}{T_0 - T_s} =$$
$$= \left(\frac{4}{\pi}\right)^3 \sum_{n_1, n_2, n_3 = 1}^{\infty} \frac{\left(-1\right)^{n_1 + n_2 + n_3 + 3}}{\left(2n_1 - 1\right)\left(2n_2 - 1\right)\left(2n_3 - 1\right)} \exp\left[-\pi^2 a^2 \left(\frac{\left(2n_1 - 1\right)^2}{l_1^2} + \frac{\left(2n_2 - 1\right)^2}{l_2^2} + \frac{\left(2n_3 - 1\right)^2}{l_3^2}\right) t\right] \times$$
$$\cos\left(2n_1 - 1\right)\pi \frac{x_1}{l_1} \cos\left(2n_2 - 1\right)\pi \frac{x_2}{l_2} \cos\left(2n_3 - 1\right)\pi \frac{x_3}{l_3} \qquad (1.4)$$

Threefold infinite sum contains terms (in the second line behind the sum) which with increase of trinity natural numbers n_1, n_2, n_3 as well as with increase of the time t decrease. Space distribution of temperature inside the block at the instant of time t is determined by the product of three cosine functions. This product represents even function of space variables $x_i,\ i = 1,2,3$.

We see that each term in infinite sum exponentially decreases with characteristic time equal to $\tau_i = \left\{\frac{l_i}{a\pi\left(2n_i - 1\right)}\right\}^2$ and amplitude decrease is proportional to $\frac{1}{2n_i - 1}$. The time $\tau = \left(\frac{l_i}{2a}\right)^2$ is called the relaxation time. Here $a^2 = \lambda/c\rho$ is the diffusivity, λ -thermal conductivity and $c\rho$ is the heat capacity density of a body.

Because, the centre of the sample coincides with coordinate origin the time development of temperature at that point is given by the same formula (1.4) in which last three $\cos\left(\gamma_i\right)$ functions are equal to one.

In a case of a cube $l_1 = l_2 = l_3 = l$ at the center of a cube triple infinite sum can by reduce to one sum. The time development temperature at that place then is given by the relation

$$\frac{T(x_1,x_2,x_3,t)-T_s}{T_0-T_s}=\left(\frac{4}{\pi}\right)^3\left\{\sum_{n=1}^{\infty}\frac{(-1)^{n+1}}{(2n-1)}\exp\left[-\frac{(2n-1)^2\pi^2a^2}{l^2}t\right]\right\}^3 \tag{1.5}$$

where l represents length of the cube edge. For all times for which inequality

$$t>>-\frac{l^2}{8\pi^2a^2}\ln 3\tilde{\varepsilon}=(-0.0012\ln 3\tilde{\varepsilon}) \tag{1.6}$$

is fulfilled - where $\tilde{\varepsilon}$ is smaller of two numbers 1 and $\varepsilon/9$ - at the center of a cube arises a regular regime with relative uncertainty ε. Proof of this inequality is given in [1]

1b. Transition to one dimensional temperature field -1D

Next we shall introduce and discuss the solution of 1D heat conduction equation under the same border and initial conditions along x axis as before. To treat 3D problem as 1D one, the following condition are to be fulfilled.

At the border planes $x_2=\pm l_2/2$ and $x_3=\pm l_3/2$ the thermal flow does not exist (or at least is negligible small if compare with flow along x_1 axis through two surfaces which area is equal to l_2l_3). A perfect thermal isolation is an idealization because it does not exist. In a thin slab $l<<l_{2,}l_3$. This also supports preceding assumption. Such a slab (or layer) is considered as infinite one. See *Fig. 2.*

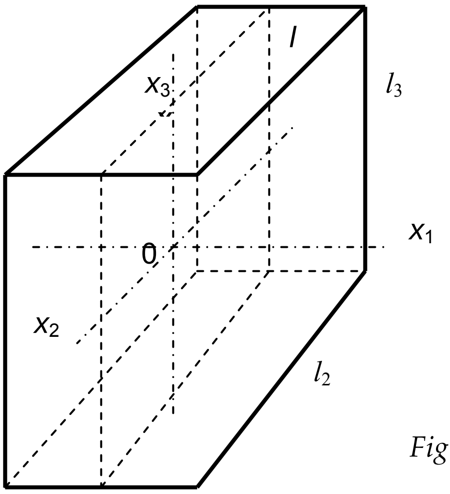

Fig. 2

In this case we have border conditions

$$T(x_1=\pm l/2)=T_s,\ \partial_{x_2}T(x_2=\pm l_2/2)=\partial_{x_3}T(x_3=\pm l_3/2)=0,\ l_1=l \tag{1.7}$$

and initial condition

$$T(x_1,t=0)=T_0,\ -l/2<x_1=x<l/2 \tag{1.8}$$

The solution obeying these conditions we introduce in two forms [2], [4]. The first one is

$$\theta=\frac{T(x,t)-T_s}{T_0-T_s}=\frac{4}{\pi}\sum_{n=1}^{\infty}\frac{(-1)^{n+1}}{(2n-1)}\cos\frac{(2n-1)\pi x}{l}\exp\left[-(2n-1)^2\frac{\pi^2a^2}{l^2}t\right] \tag{1.9}$$

Addition $(T_s-T_0)/(T_0-T_s)=-1$ to both sides of that relation transforms it to the form

$$1-\theta=\frac{T_0-T(x,t)}{T_0-T_s}=1-\frac{4}{\pi}\sum_{n=1}^{\infty}\frac{(-1)^{n+1}}{(2n-1)}\cos\frac{(2n-1)\pi x}{l}\exp\left[-(2n-1)^2\frac{\pi^2a^2}{l^2}t\right] \tag{1.9`}$$

These expressions are useful for long period of time $a^2t/l^2 >> 1$ when it is possible to approximate the infinite series by keeping only first n-terms. (It is due to validity of Leibnitz theorem.) We see the smaller is the thickness l of a sample the shorter that time interval t will be. The second form of that solution takes the form

$$1-\theta=\frac{T_0-T(x,t)}{T_0-T_s}=\sum_{n=1}^{\infty}(-1)^{n+1}\left\{\operatorname{erfc}\frac{(2n-1)-2x/l}{4\sqrt{a^2t/l^2}}+\operatorname{erfc}\frac{(2n-1)+2x/l}{4\sqrt{a^2t/l^2}}\right\} \tag{1.10′}$$

This expression can be rewritten into equivalent form (using the same trick as in (1.9`))

$$\theta=\frac{T(x,t)-T_s}{T_0-T_s}=1-\sum_{n=1}^{\infty}(-1)^{n+1}\left\{\operatorname{erfc}\frac{(2n-1)-2x/l}{4\sqrt{a^2t/l^2}}+\operatorname{erfc}\frac{(2n-1)+2x/l}{4\sqrt{a^2t/l^2}}\right\} \tag{1.10}$$

which can be useful for narrow time interval (0,t) when the relation $a^2t/l^2 << 1$ is valid. Then it is possible to approximate the infinite series by keeping only first n-terms.

Both expressions can be obtained by Laplace transformation of the temperature applying to time variable t. (See [2]: (1.9), p. 89, formula (25); (1.10) p. 91, formula (28)).

2. Thermal flux, power and thermal losses

Thermal flux through the border planes at $x=\pm l/2$ of a slab is determined as

$$q\left(x=\pm\frac{l}{2},t\right)=-\lambda\frac{\partial T(x=\pm l/2,t)}{\partial x} \tag{2.1}$$

Insertion (1.9`) in this relation leads to

$$q\left(x=\pm\frac{l}{2},t\right)=\mp\frac{4\lambda(T_0-T_s)}{l}\sum_{n=1}^{\infty}\exp\left[-(2n-1)^2\frac{\pi^2a^2}{l^2}t\right] \tag{2.2}$$

The thermal power

$$P(t)=\frac{4\lambda(T_0-T_s)l_2l_3}{l}\sum_{n=1}^{\infty}\exp\left[-(2n-1)^2\frac{\pi^2a^2}{l^2}t\right]$$

determines the heat passing through the border surface of the area l_2l_3 per unit time.

The heat added to (if $T_0<T_s$) or released by the slab (if $T_0>T_s$) necessary to transfer it into thermal equilibrium is equal to

$$Q=2\int_0^{\infty}P(t)\,dt=\frac{8\lambda(T_0-T_s)l_2l_3}{l}\frac{l^2}{\pi^2a^2}\sum_{n=1}^{\infty}\frac{1}{(2n-1)^2}\int_0^{\infty}\exp(-\varsigma)d\varsigma=$$

$$\frac{8(T_0-T_s)l_2l_3lc\rho}{\pi^2}\sum_{n=1}^{\infty}\frac{1}{(2n-1)^2}=\frac{8}{\pi^2}(T_0-T_s)Mc\sum_{n=1}^{\infty}\frac{1}{(2n-1)^2}=Mc(T_0-T_s)$$

where the relation $\sum_{n=1}^{\infty}\frac{1}{(2n-1)^2}=\frac{\pi^2}{8}$ was accounted [3]

$Q=Mc(T_0-T_s)$ where mass of the slab is $M=\rho l l_2 l_3$ (2.3)

and the mass density is ρ.

This relation is useful for measurement mean value of specific heat capacity in temperature interval T_0-T_s. Result (2.3) is in accord with the thermodynamic first law.

2.1 Dimensionless quantities

We met above the fractions:

$$\theta=\frac{T(x,t)-T_s}{T_0-T_s} \tag{2.4}$$

The dimensionless temperature. It changes in interval of $(0,1)$.

$$\xi=\left(\frac{x}{l/2}\right) \tag{2.5}$$

The dimensionless coordinate. The change of it lies in the interval of $(-1,1)$.

$$Fo=\frac{a^2}{(l/2)^2}t \tag{2.6}$$

The dimensionless time. This is called Fourier Number. It changes in the interval of $(0,\infty)$.

Because, dimensionless temperature θ is a function of dimensionless coordinates ξ and Fo only it does not contain parameters a2 or l of an investigated specimen explicitly. In this sense it is the universal function $\theta(\xi,Fo)$ of the variables ξ, Fo. One can find plots of this function e.g. in monograph [2]. They may be useful in some practical applications.

3. Problem of diffusivity calculation

Because we are not able to invert the series (1.9) or (1.10) and to express diffusivity a2 as a function of relative temperature θ and the thickness of the layer l analytically in a closed form then we are referred to apply approximate methods of calculation this quantity.

In the paper [5] we have presented simple formula for thermal diffusivity calculation as follows

$$a^2 = \left(\frac{l}{2}\right)^2 \frac{(Fo)_r}{t_r} \tag{3.1}$$

As can be seen three data are needed to obtain the value of diffusivity:

Firstly l – it is the thickness of the layer.

Secondly (Fo)r – it is appropriate Fourier number. If the plot of the function $\theta = \theta(x = 0, Fo)$ is available then for given value of θ say $\theta = N$ (where $0 < N < 1$) the ordinate Fo in that plot is that one for which functional value θ equals N. This ordinate is given as root of the equation $N = \theta(x = 0, Fo)$ and approximate value of it shows that plot.

Thirdly – it is the value of the time tr. If the temperature of a layer is continuously measured in time at the central plane located at x = 0 then the dependence of relative temperature

$$\theta_{\exp} = \theta\left(x = 0, \frac{a^2 t}{(l/2)^2}\right) \tag{3.2}$$

is known as well as the corresponding plot. It is assumed that this course of relative temperature coincides during the time of measurement with theoretical one determined by the relation (1.9) or (1.10) in the same time interval. Then the relation (3.2) holds. If we choose equal value of $\theta_{\exp} = N$ as before then solving the equation $\theta\left(x = 0, (2a/l)^2 t\right) = N$ for t we obtain value tr as a root of that equation. Approximate value of tr can also be found out analyzing the plot of the function $\theta_{\exp}(t)$ (3.2).

Now, we are going to search for values of (Fo)r and tr with intention to demonstrate the upper outlined procedure.

In a long time approximation Fo >1 at x = 0 it is enough to take a few first terms of the series (1.9`). For the sake of simplicity we shall consider two terms only. Now, we draw the graph of the function

$$f = 1 - \theta \approx 1 - \frac{4}{\pi}\exp\left(-\frac{\pi^2}{4}Fo\right) + \frac{4}{3\pi}\exp\left(-\frac{9\pi^2}{4}Fo\right) \tag{3.3}$$

The curve f = f(Fo) resulting from theory is depicted in fig. 3. In *Fig. 3* the plot of the relative temperature *f* and the interval of *Fo* values are shown. This function results from the theory which we have presented above. Down the fig. 3 the coordinates of the points of intersection are quoted.

Dependence fexp = fexp (t) resulting from experiment is plotted in fig. 4. In *Fig. 4* on the left the plot of experimental dependence relative temperature f_{exp} versus *t* in the time interval showed is depicted. The thickness of the layer was *l* = 2 cm. Down, the fig. 4 the coordinates of the points of intersection are also given.

Plot[{1-1.2732©-2.467Fo+0.4244©-22.201Fo,0.99,0.999},{Fo , 1.5 , 3 } ,AxesLabel→{Fo,f}]

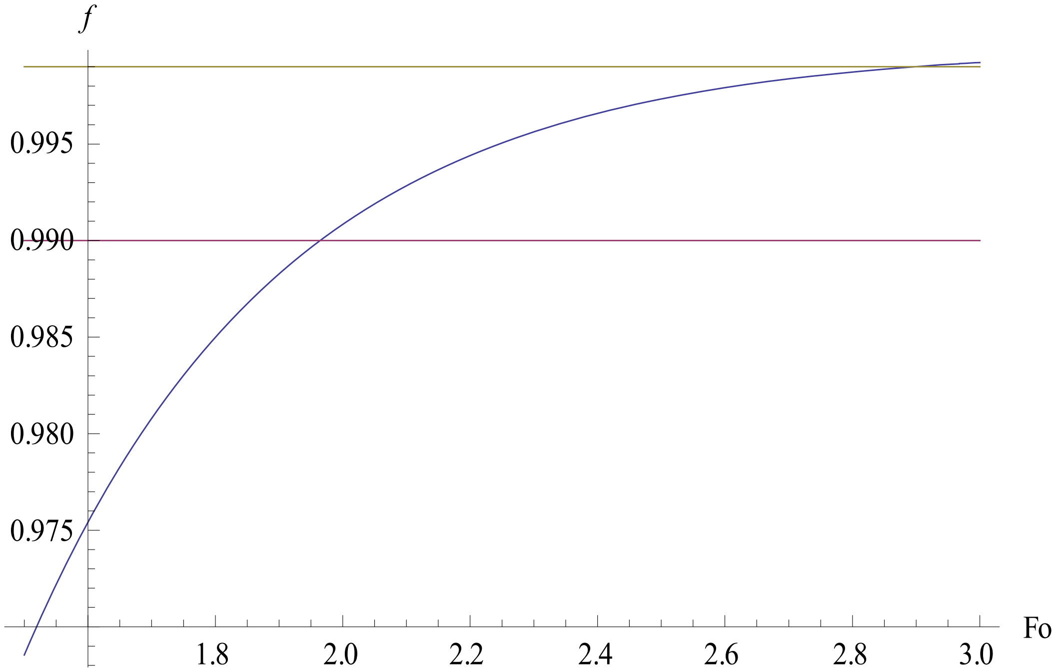

(1.965, 0.99), (2.89797, 0.999)

Fig. 3

Plot[{1-1.2732©-0.523 t+0.424©-4.707t, 0.99, 0.999},{ t , 6.5 ,16},AxesLabel→{t[s],f_{exp} }]

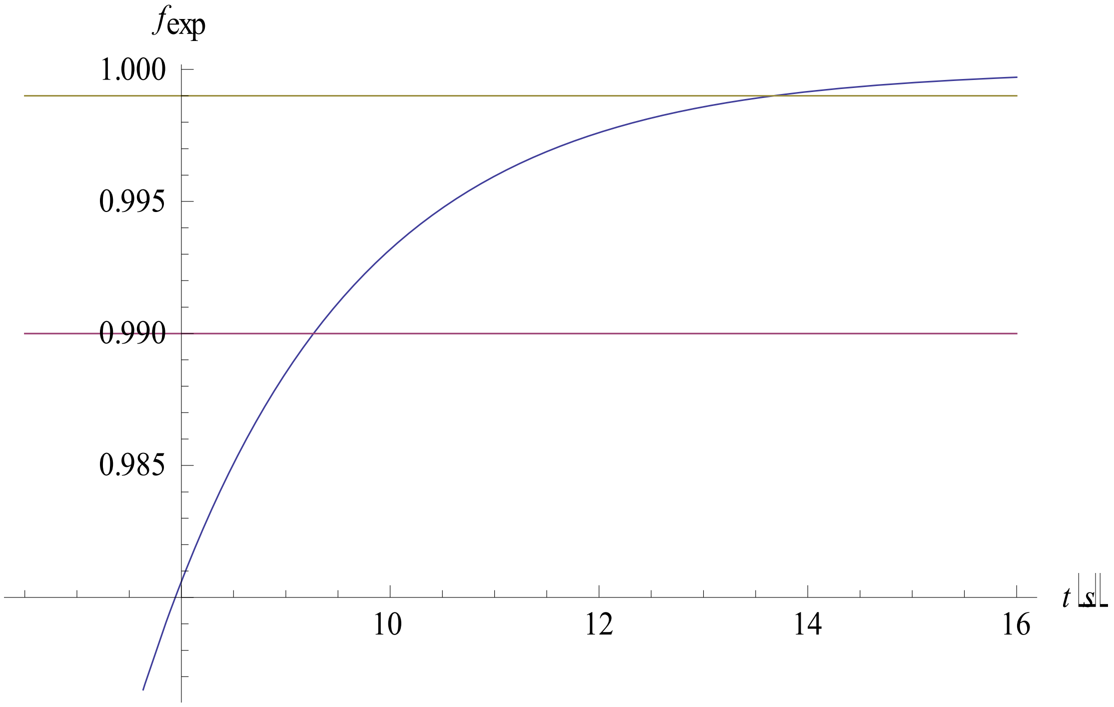

(9.266, 0.99) (13.6698, 0.999)

Fig. 4

Substitution of ordinates of the intersection points into relation (3.1) and l = 2 cm gives

$$a^2 = 10^{-4}\mathrm{m}^2\left(1.965/9.266\ \mathrm{s}\right) = 21.206\times10^{-6}\mathrm{m}^2\mathrm{s}^{-1}$$

and

$$a^2 = 10^{-4}\mathrm{m}^2\left(2.898/13.670\ \mathrm{s}\right) = 21.199\times10^{-6}\mathrm{m}^2\mathrm{s}^{-1}$$

The value of diffusivity a2 = 21.2□$10^{-6}\mathrm{m}^2\mathrm{s}^{-1}$ was measured and published in work [5] using the extended pulse transient method for SiC specimen of the thickness l = 2.84 mm, ρ = 3242 kg.m-3 and c = 672 J.m-1K-1, then λ = a2cρ = 46.187 W.m-1.K-1.

In that paper square pulses of thermal power were considered in which the change of temperature is considered discontinuous. Evidently, this is an approximation. Indeed, the change of temperature is anytime continuous. The theory of the pulses of thermal power at a continuous change of the temperature is developed in article [7]. This may be more accurate for the extended pulse transient method.

Notice.

Experimental dependence of relative temperature fexp = fexp (t) was not available for us. The plot in fig.4 was constructed using some data from work [5] with respect to the formula (3.2). Our intention was to obtain relevant value of a2 and to show that presented method really works.

Procedure for diffusivity determination in short time approximation - provided that formula (1.10`) is applied - is similar to that which has been applied in a case of long time approximation. Which one is to be used it depends e.g. on the thickness l of an investigated specimen. The bigger is l the larger is the time needed for acquirement equal temperature at the central plane at x = 0. Consequently, for larger l that would be more appropriate the long time approximation.

4. Conclusions

It is known that into non-steady temperature field enter diffusivity a2, geometrical characteristics of the investigated specimen (as the length of edges, radius and so on), as well as some parameters included in corresponding initial temperature distribution and border conditions. If the local temperature time dependence in known from experiment then this functional dependence can be utilized for determination thermal diffusivity. Usually temperature field is given as an infinite series. Diffusivity emerges in each term of that series.

So, the problem arises how to extract diffusivity a2 from this series? In this article an approximate method is suggested to this aim. It utilizes both numerical and graphical analysis of the local time dependence given by the theory as well as known from measurement on a particular sample. Finally, simple formula (3.1) is presented enabling immediate diffusivity calculation.

If all parameters entering the temperature field are known the heat (added or released) in relaxation process can also be calculated. In that process a sample undergoes transition from non- equilibrium state determined by initial temperature distribution to the final equilibrium state at the constant temperature Ts.

5. Acknowledgement

This work was supported by the VEGA 1/4204/07 grant of Slovak Grant Agency.

6. References

[1]. B. M. BUDAK, A. A. SAMARSKIJ, A.N. TICHONOV Collection of Problems on Mathematical Physic (in Russia, Sbornik zadač po matematičskoj fizike), Moscow, publisher: Nauka, 3rd edition, 1980, pp. 455-456

[2]. A. V. LYKOV Theory of Thermal Conductivity (in Russia, Teorija teploprovodnosti), Moscow, 1967, publisher: Vysšaja škola,(1.9) formula (25) p. 89, 1.10) formula (28), p. 91).

[3]. I. S. GRADSTEIN; I. M. RISHIK, Tables of Integrals, Sums, Series and Products (in Russia, Tablicy integralov, summ, riadov i proizvedenij), publisher FM, Moscow1963, p. 21.

[4]. CARSLAW H. S.; JAEGER J. C. Conduction of Heat in Solids, 2 Ed., OXFORD, At the Clarendon Press. London 2003

[5] ČULÍK F.; BANÍK I.; LUKOVIČOVÁ J. Temperature field in a solid body restricted by two parallel planar surfaces, Proceedings of Thermophysics 2008, pp. 26-35 October 2008, Meeting of the Thermophysical Society

[6]. VRETENÁR V. Extended version of Pulse transient method, Proceedings of Thermophysics, 2005, Contents, pp. 92-103, October 2005, Meeting of the Thermophysical Society

[7]. ČULÍK F. I.; BANÍK I. Determination of temperature field created by planar heat source in a solid body consisting of three parts in mutual thermal contact, International Journal of Thermal Sciences 48 (2009) pp. 204-208. ELSEVIER. Available online at www.sciencedirect.com

Moisture transport through porous materials monitored by the Hot Ball Method

Laura Casares García, Ľudovít Kubičár

Institute of Physics SAV, Dúbravská cesta 9, SK-845 11 Bratislava, Slovakia

Abstract *Cultural and historical monuments are predominantly constructed of porous materials, where moisture plays a dominant role in their deterioration. Considering this fact, we performed experimental measurements of moisture diffusion through porous materials as sandstone.*

Our experimental studies are focused on a 17% porosity sandstone piece (dimensions 100x50x50mm) from Sander Schilfsandsteingbruch (Germany). A new hot ball method technique was used for monitoring moisture transport.

Our sandstone block has been used for one-dimensional diffusion experiments in which water was diffused through a 50x50mm base surface, while side surfaces remained isolated for moisture transport. Three processes were studied, drying, saturation through a step-wise regime and water-pulse regime. With our work we were able to characterize and calibrate the sample, and to study the changes in moisture transport with temperature.

Keywords: *moisture diffusion, sandstone, hot ball method*

1. Introduction

Porous structures belong to a branch of materials which have a great number of applications in science, civil engineering and industry. On one hand their excellent thermal insulating properties make them ideal materials for building purposes and on the other hand broad physical and chemical processes take place on their pores, namely freezing/thawing, dissolution, condensation/evaporation, absorption/desorption, moisture transport, saturation/drying. In this paper we will focus on the last ones.

In addition, cultural and historical monuments are predominantly constructed of porous materials, where moisture plays a dominant role in their deterioration [1]. Castles, cathedrals and other buildings are attacked by environment due to water, heat, pollutant and underground water. Two factors influence property of an object, namely worsening the thermal insulation due to diffusion of moisture and degradation of material structure due to freeze-thaw process of the moisturized structure. Therefore, information regarding moisture transport through sandstone materials will represent a basic assumption for achieving a better understanding and prevention of the aforementioned processes.

Nowadays there are different experimental methods for measuring thermophysical properties [2,3,4]. However, only transient methods allow us to obtain information in short enough measuring times so the information obtained corresponds to the thermodynamic state of real applications. The technique of transient methods has motivated the construction of a whole range of new innovative laboratory instruments, as for example hot ball sensors which are the base of our experiment. These sensors in connection with the RTM monitoring system give local information on temperature and thermal conductivity [5,6]. As thermal conductivity of porous structures is a function of the pore content, this system can be used for monitoring moisture spreading.

With this new technique approach to moisture diffusion through sandstone materials we hope to show a clear view of the relation between sandstone porosity and moisture diffusion rates, and make some progress in the understanding of thermal conductivity changes with moisture in sandstones.

2. Experimental method

2.1 Experimental technology

The measuring technique used in our experiment is the hot ball method for measuring thermal conductivity. This transient method consists of a small ball which operates both as a heat source and a thermometer. A constant heat flux q from the spherical source of radius r_b into the infinitive medium for times t >0 is assumed. Then the temperature in the surrounding medium will be increased while measured with the thermometer, until a stabilized temperature is reached, T_m [5,6]. At that point we can calculate the material's thermal conductivity with the relation:

$$\lambda = \frac{q}{4\pi r_b T_m (t \to \infty)} \tag{1}$$

where λ [W m-1 K-1] is the thermal conductivity, q [w] is the heat flux, r_b [m] is the heat source radius and Tm [K] is the stabilized temperature value. Figures 1 and 2 show the ideal model and the real hot ball sensors respectively.

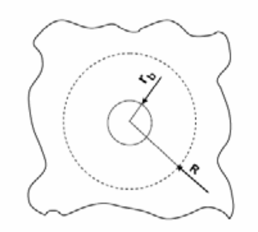

Fig.1. Ideal model

Fig.2. Hot ball sensors

It should be said that these hot ball sensors are varnished to prevent any damage from penetration of moisture when placed in the water-saturated specimen.

Data acquired through the hot ball sensors is stored and transferred to computer with RTM instruments. These electronic units are based on a data logger in connection with the appropriate microcomputer and suitable software. Every measurement produces one cycle with different points consisting of the measured temperature before switching on the heating (base line), the temperature after the start of the heating until stabilization and then back to the base line. We can observe this in Figure 3. Each of these cycles will give us one thermal conductivity value and they will be repeated one after each other every 30 minutes providing data of how thermal conductivity changes with time [5, 6].

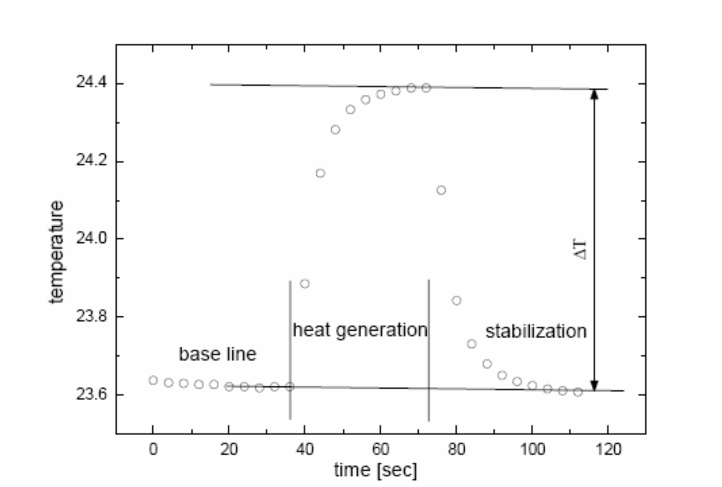

Fig.3. RTM measuring cycle

The isothermal processes are performed thanks to an isolated chamber equipped with a thermostat and a vacuum pumping machine. This chamber consists of two plates connected to the thermostat and between which the specimen is placed. Physical contact between the specimen and the plates will allow the heat flow. With this chamber we are able to keep the desired steady temperature and accelerate the processes thanks to vacuum.

2.2 Specimen

In our experiment we use a sandstone specimen (dimensions 100x50x50mm) with 17.8% published porosity cut from "Hermannsberg", the Sander Schilfsandsteingbruch Hassberge (Germany). Basic characteristics are given in Table 1.

Preparation of the sample for the experiment was the following. First three holes were drilled at different heights in the specimen for the insertion of the hot ball sensors (2.5cm deep with ratios of 0.2cm) and covered with varnish to prevent any watering of the sensors. Then when it was dry, the hot ball sensors (previously varnished as well, to make sure no water could penetrate) were placed in each hole with standard epoxy and put into a recipient to cure. Last step was to cover the sample lateral surfaces with the same epoxy making sure the upper and bottom surfaces were not covered.

After, we waited until everything was completely dry. At this point the experiment was ready to start.

Table 1. Basic characteristics

Dimensions (cm^3)	h_1=10.09 h_2=5.09 h_3=5.08
Hole dimensions (cm^3)	h_1=2.5 r=0.2
Estimated Volume (cm^3) (considering holes)	260
Published porosity (%)	17.8
Calculated porosity (%)	12.8
Published bulk density (kgm^{-3}) of sandstone dry water saturated	2175 2315

2.3 Measuring procedure

In our experiment we perform three different kinds of processes: drying regime, step-wise regime for saturation and water-pulse regime.

Drying

In the drying process the specimen was placed in the isolated chamber and subjected to higher temperatures from 60ºC to 95ºC with vacuum. This process had to be implemented in stages to avoid further damage on porous structure. When the specimen is saturated a sudden change in temperature may affect the water contained in the porous entailing porous damage. For this purpose our first step was to increase the temperature up to 60ºC for 1 to 3 days and then up to 90-95ºC in vacuum for 12-24h. If the sample is water-saturated this last step should be repeated. In order to improve the contact with the heater plates the drying was performed with the sample lying in horizontal position inside the chamber. After every increase in temperature the sample was brought back to 25ºC and weightened.

Saturation

Saturation state was reached through a step-wise water regime in a room at approximately 25ºC. For this purpose the specimen was placed in a bigger glass with permanent water until no more water was able to penetrate. This moment was recognized by stabilized thermal conductivity values in all sensors. The process was performed in stages, each of them followed by stabilization in the due sensor's signal.

1. First, the water level in the glass was 22mm high (just under the bottom sensor), until signal from the bottom hot ball was stabilized.
2. Then more water was added up to the middle sensor
3. Water up to the top sensor
4. Water up to the top edge

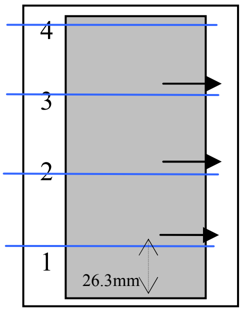

Water-pulse regime

The water-pulse regime consists of applying a controlled small amount of water to the sample. It was performed in the isolated chamber first at 25ºC and then at higher temperatures. The amount of water was controlled with a pipette and placed on a bit of cotton lying on some sand pieces (to create space for water transport), and all in a small tray. The specimen was put in vertical position on top of the cotton piece. Everything was placed in the isothermal chamber before the experiment was started to guarantee a uniform temperature. A small bit of cotton with sand was also placed on top of the specimen between the sample top surface and the heater plate inside the chamber to provide some space for gas evacuation from the sample.

During the whole study data was being acquired through RTM devices and transferred to computer every 1-2 days. The RTM devices were also placed inside of the isolated chamber during drying and water-pulse regime processes. They obtained data on thermal conductivity, temperature and moisture.

In this way, the water spreading was studied through RTMs data and they allowed us to know if water inside the sample had reached each sensor without interfering with the water transport process.

Only after every important process the specimen was weight to avoid further interference with the experiment.

3. Experimental data and results

3.1 Characterization

From the drying and saturation processes we acquire enough data to characterize the sample. Hot ball sensors are constantly measuring thermal conductivity values around each sensor so that they provide us with values for dry and water saturated stages. Weight values from the dry and water saturated sandstones together with the specimen's dimensions will give us the bulk density for both dry and water saturated states. Considering these bulk density differences we can obtain the porosity of our sandstone sample as:

$$\phi = \frac{\rho_{WS} - \rho_D}{\rho_W} \cdot 100 \tag{2}$$

where ρ_{WS} is the water saturated bulk density, ρ_D is the dry bulk density and ρ_W is the density of distilled water at 25ºC which we take as 997 kgm-3.

Table 2 shows these results for our sandstone specimen.

Table 2 Calibration data for the sandstone piece from Sander Schilfsandsteingbruch (Germany)

	Apparent thermal conductivity [W m-1 K-1]		***Density (kg/m3)***	***Porosity (%)***
	Bottom sensor	***Middle sensor***		
DRY	***0.35***	***0.29***	***2202***	***12.8***
WATER SATURATED	***0.70***	***0.34***	***2330***	

3.2 Calibration

From the step-wise regime for saturation we are able to calibrate each sensor. This will give us a relation between moisture and thermal conductivity for each sensor which applied to data from the saturation process would enable us to observe the saturation curves for both sensors in each sample.

With data from the weight and thermal conductivity before and after the saturation process, assuming it as linear, we obtain the calibration graphics adjusting to the equation:

$$M = a + b\lambda, \tag{3}$$

with M being the moisture weight and λ thermal conductivity.

During the whole saturation process our RTM's are obtaining data on thermal conductivity in each sensor every 30 minutes. Using the previous moisture-thermal conductivity relations for each sensor (3) on the (thermal conductivity versus time) saturation graphics we can recalculate the moisture change in time during the saturation process. Graphics 1 shows the calibration and saturation processes for our specimen.

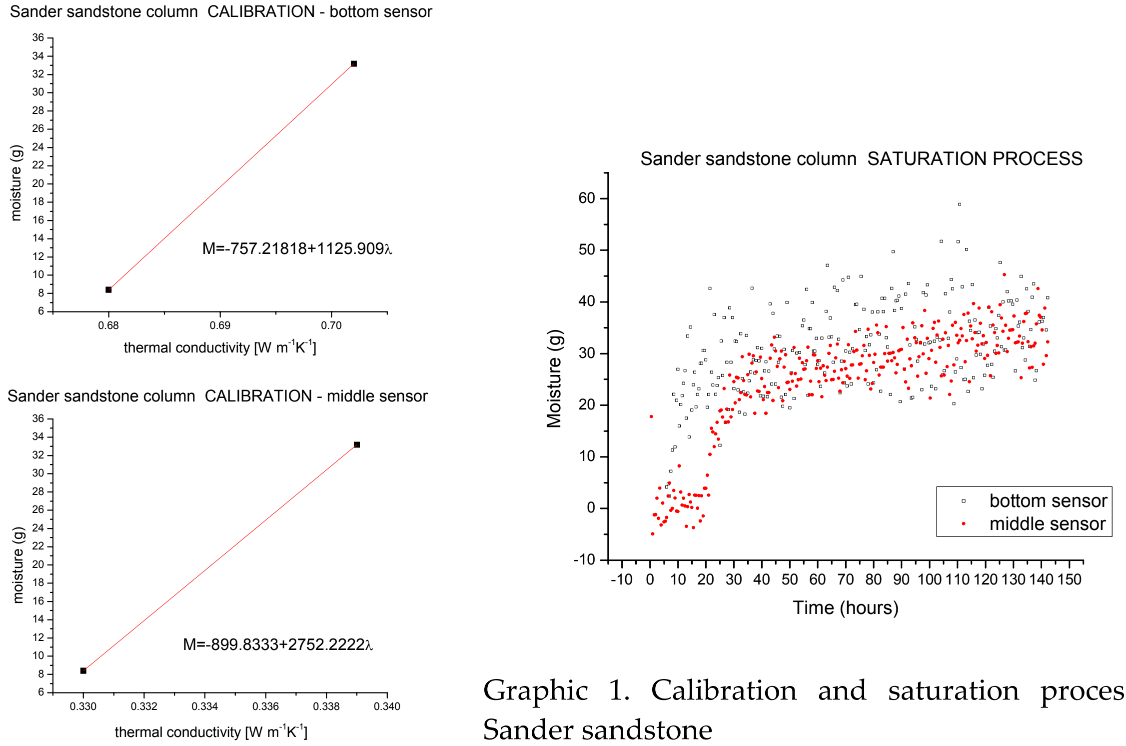

Graphic 1. Calibration and saturation processes of Sander sandstone

3.3 Changes in diffusion with Temperature

Another part of our study was to perform some experiments in the water-pulse regime with the same amount of water but applying different temperatures. Three experiments were performed, at 25, 30 and 40ºC in which the sample was lying on a 10ml watered cotton tray. Data is showed in Graphic 2.

However the initial and final conditions of the specimen were not exactly the same due to the difficulty for noticing the sample's weight at every time with our experimental configuration.

Once the specimen had been put together with the watered tray in the isolated chamber, the RTMs were left there getting data for 16-20 hours. Our goal was to stop the experiment at the exact time when the initial moisture transport regime was finished (the initial steep curve) and before we start to lose water by evaporation. At that estimated moment we opened the chamber and weighted the sample, but then the amount of water inside varied from 7 to 9 ml.

Besides, the initial specimen's weight for each experiment was only similar because our drying method was not too accurate. This can be easily observed in the graphic considering that the 25ºC experiment was the first one performed and the initial amount of water inside the sample was about 3.5ml.

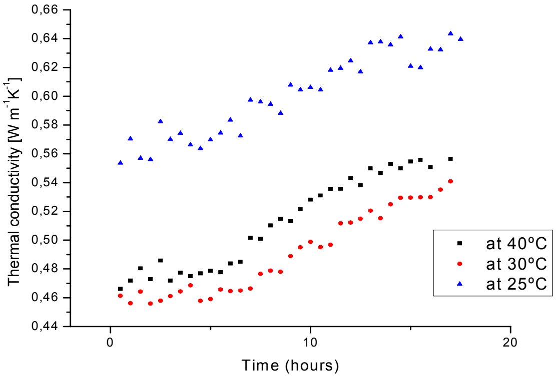

Graphic 2. 10ml water-pulse regime for Sander sandstone at different Temperatures

4. Discussion

The obtained porosity value for our sample (12.8%) is found to be lower than the published one. This is easily explained as our weight data from the sensors was obtained once the specimen had been varnished and it included the three sensors. In the same way density values in Table 2 do not match accurately the published data which shows lower values for dry and water saturated sandstone.

Our calibration graphics show how moisturizing increases thermal conductivity. We can also see how the saturation process in sandstone takes place with similar saturation curves for each height (sensor) in our specimen as the water level is rising.

From Graphic 2 we can observe higher values in thermal conductivity in the 25ºC experiment. This must be due to a higher amount of water inside the sample, which can be checked if we observe the positive slope of the calibration graphics previously studied.

At the same time, if we compare the slopes obtained for the thermal conductivity-time graphics for each temperature we can see that they are very similar. This suggests that moisture transport in these initial stages is not strongly affected by the temperature.

Conclusions

This investigation shows a new application of the hot ball method. We believe moisture diffusion monitored by the hot ball method to be a highly successful way for moisture transport analysis through porous materials.

In this study we have found that moisturizing increases thermal conductivity. Furthermore, we have proved that moisture transport in the initial stages is not highly affected by the temperature up to 40ºC. Future experiments at higher temperatures could be performed.

References

[1] L'. KUBIČÁR, V. VRETENÁR, V. BOHÁČ, P. TIANO, Thermophysical analysis of sandstone by pulse transient method, 2006, International Journal of Thermophysics Vol.27, Mo.1, January 2006, DOI: 10.1007/s10765-006-0042-5

[2] PEL L. Moisture transport in porous building materials, Ph.D. thesis, Eindhoven University of Technology, The Netherlands (1995)

[3] KOPINGA K. and PEL L. One dimensional scanning of moisture in porous materials with NMR, Rev. Sci. Instrum. 65, 3673-3681 (1994)

[4] ROELS S., CARMELIET J., Analysis of moisture flow in porous materials using microfocus X-ray radiography, International Journal of Heat and Mass Transfer 49, 4762-4772, (2006)

[5] L'. KUBIČÁR, V. VRETENÁR, V. ŠTOFANIK, V. BOHÁČ and L. BAGEL', (2008), Thermophysical sensors: Theorhy and application of the hot ball, in Proc. of Twenty-Ninth International Thermal Conductivity Conference, Proceedings of Seventeenth International Thermal Expansion Symposium, June 24-27, 2007, edited by John R. Koenig, Heng Ban, Lancaster, Pennsylvania, DEStech Publication, Inc.,412-425

[6] L'. KUBIČÁR, V. VRETENÁR, V. ŠTOFANIK, V. BOHÁČ, (2008), Thermophysical sensors: Theory and application of the hot ball, Int. J. of Thermophysics, sent for publication.

Relationship between relative permittivity and thermal conductivity moisture dependence of calcium silicate boards

Matus Holubek[1]**, Peter Mihalka**[2]**, Peter Matiasovsky**[2]

[1]Slovak Technical University, Faculty of Civil Engineering, Radlinskeho 11, 813 68
Bratislava, Slovakia, e-mail: holubek@svf.stuba.sk

[2]Institute of Construction and Architecture, Slovak Academy of Sciences, Dubravska
cesta 9, 845 03 Bratislava, Slovakia, e-mail: usarmat@savba.sk

Abstract: *The relative permittivity of calcium silicate as a function of the moisture content was determined using a standard TDR equipment. The obtained results were compared with available results of thermal conductivity measurements for the same material. A similarity between both material properties as the functions of their moisture content was found. The moisture dependences of both analysed parameters are determined by the pore volume structure of the material. The parallel power function models of effective thermal conductivity and relative permittivity based on the information on moisture contents relevant to the transport and on the regularity of pores filled with water enabled the analysis of the performed measurements.*

Keywords: *Relative permittivity, thermal conductivity, moisture content, calcium silicate, material pore structure*

1. Introduction

The moisture content of a porous building material can be determined from the measurement its relative permittivity. The relative permittivity is the parameter analogous to the thermal conductivity and dependent on the moisture content too. As both these parameters depend on the portion and configuration of particular – solid – gaseous – liquid phase components, both of them can be determined from the pore structure parameters of a given material. The Mercury Intrusion Porosimetry (MIP) is the standard testing method for pore structure parameters determination. The pore structure based models of thermal conductivity and relative permittivity are based on expression of transport properties as the power functions of particular transport relevant component volumes. The exponents of these functions are given by the fractal dimensions of relevant component volumes, expressing their regularity. The measured thermal conductivity and the relative permittivity values for calcium silicate boards were analysed with use of the proposed pore structure parameters based models.

2 Pore structure analysis

The mercury intrusion porosimetry is based on the premise that a non-wetting liquid will only intrude capillaries under pressure. The relationship between the pressure and capillary radius is described by Washburn as [1]:

$$P = \frac{-2\sigma\cos\theta}{r} \tag{1}$$

where: P is the pressure, ⊚ is the surface tension of the liquid, ⊚ is the contact angle of the liquid, r is the radius of the capillary.

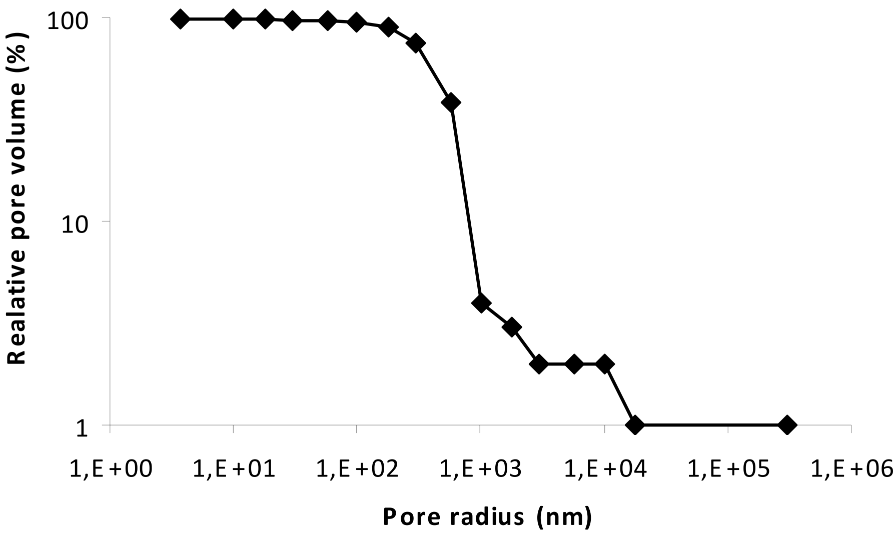

Figure 1: Pore size distribution curve in double logarithmic representation for calcium silicate

For the calcium silicate board with bulk density of 250 kg/m3 the relative pressure-volume data were determined by the 2002 mercury intrusion porosimeter and the micropore unit 120 of ERBA Science, enabling the determination of pores with radii from 3.7 nm up to 0.06 mm. The pore size distribution was determined from the volume intruded at each pressure increment. Total porosity was determined from the total volume intruded. The specific surface area of pores was calculated from the pore radii and the pore volumes. The obtained cumulative pore size distribution curve for calcium silicate is in figure 1.

The pore volume - pore size distribution curve in a double logarithmic representation can be divided into the pore space fractions characterized by a constant slope and indicating the ranges of self-similarity. The slope of each fraction gives the fractal dimension FD of the pores in the fraction.

The mean fractal dimension of a relevant pore volume consisting of i fractions is calculated according to the relationship:

$$FD_m = \frac{\sum_i FD_i \cdot \log\left(r_{\max i} / r_{\min i}\right)}{\log\left(r_{\max} / r_{\min}\right)} \tag{2}$$

where rmaxi, rmini are the maximum and minimum pore radii of particular fractions, rmax, rmin are maximum and minimum pore radii of the relevant volume.

3 Transport parameters model

Generally the effective transport parameter can be expressed by a power function model in which the transport parameter Ki of the ith continuous material component (solid, gaseous, liquid) contributing mostly to the transport can be approximated according to the relation [4]:

$$K_i = k_i\left(\Phi_i - \Phi_{i,crit}\right)^{n_i} \tag{3}$$

where: ni =1+FDmi, FDmi is the mean fractal dimension of the component volume, ki is the transport parameter of the component, ◎i is the component volume, ◎i,crit is the critical volume of the component needed for a connected network to be formed through the material, the term ◎i ◎◎◎i,crit is the relevant volume portion considered.

The critical volume is also known as the critical threshold volume for connectivity percolation. The critical volume value is specific for particular transport processes. The volume participates on the transport only if some critical minimum part of the volume is present. If ◎◎◎◎◎◎i,crit, the component volume portion or the pore volume fraction is not percolated in the material volume. In such a case it is necessary to take into consideration the serial interconnection of the component volume with other components.

The exponent ni expresses the deviations of real pores from parallel components model, their regularity.

At equilibrium material moisture contents corresponding to the environment with the relative humidity higher than ca 97 %, the capillary condensation is dominant. The equilibrium moisture content corresponding to these and higher humidities is dependent on the capillary pressure and is expressed by retention curve. The capillary pressure value is proportional inversely to the radius of the largest capillaries filled with water and it is expressed by Laplace equation:

$$p_c = -\frac{2 \cdot \sigma_w}{r} \tag{4}$$

where ◎w is the surface tension of water.

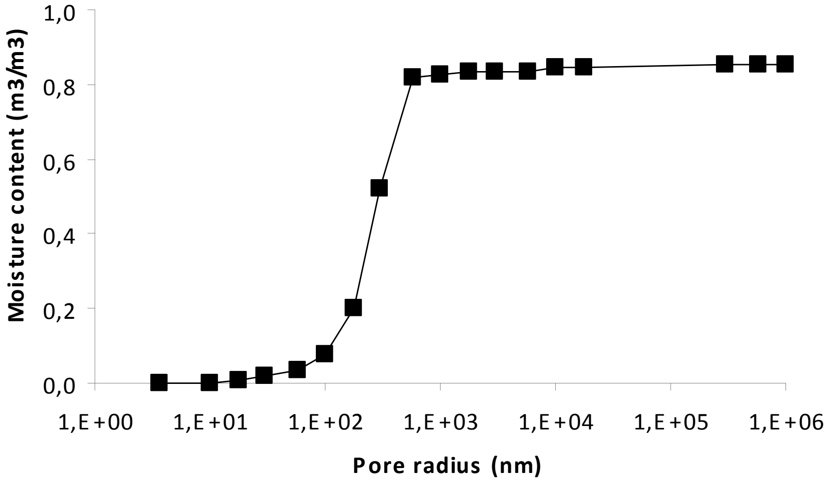

Figure 2: Moisture adsorption curve modelled from MIP results

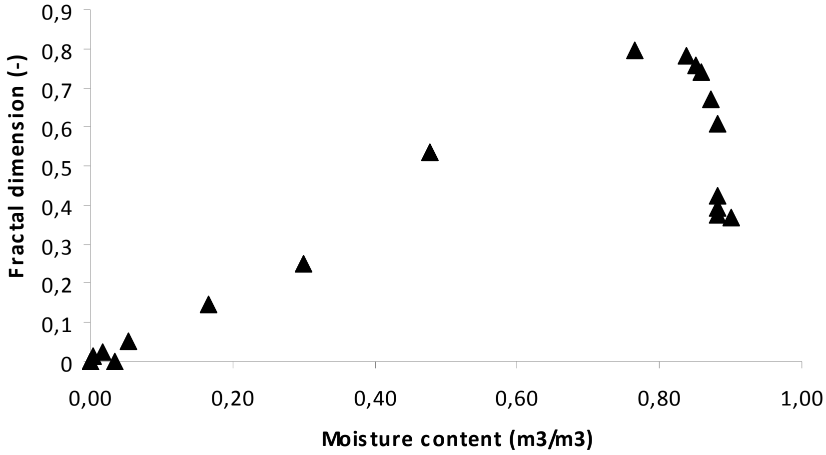

Figure 3: Mean fractal dimension of calcium silicate board moisture content

To combine the MIP and water retention techniques for the pore size analysis we can assume that at given capillary pressure a sum of the intruded mercury volume and the volume occupied by water equals the total porosity of the specimen in a case of calcium silicate. Then the water filling process according to equation (4) can be modelled from the mercury intrusion data. The resulting modelled water filling curve is in figure 2. With use of this curve the mean fractal dimensions corresponding to the relevant moisture contents uw can be determined according to equation (2) from the fractal dimensions determined by MIP for particular pore radii fractions. The results for the calcium silicate are in figure 3. The material parameter dependent on the moisture content can be then calculated from this dependence with use of equation (3).

3.1 Thermal conductivity

The results of the measurements of thermal conductivity of the calcium silicates as a function of the moisture content were published in [2]. In figure 4 there is the thermal conductivity-moisture dependence for a material with the bulk density of 250 kg/m3. The dependence has a bilinear character - its first part is steep due to the moisture shrinkage process in solid matrix during the relative humidities below 95 % corresponding to the moisture contents smaller than 0.025 m3/m3. This moisture content represents the volume critical for the percolation of the material component with the highest thermal conductivity. The results of the measurements for the moisture contents higher than 0.025 were compared with the effective thermal conductivity model based on equation (3) and specified in the form of equation (5).

$$k_{ef}(u_w) = k_s \cdot (1 - \Phi) + k_a \cdot (\Phi - u_w) + k_w \cdot (u_w - u_{crit})^{1+FD_m} \tag{5}$$

where: ks, ka and kw are the thermal conductivities of solid matrix, air and water equal to 1.42, 0.025 and 0.6 W/m.K respectively, uw is the actual moisture content and ucrit is the critical moisture content,◎◎ is the total porosity.

The comparison gives almost the identity of the measured and modelled data.

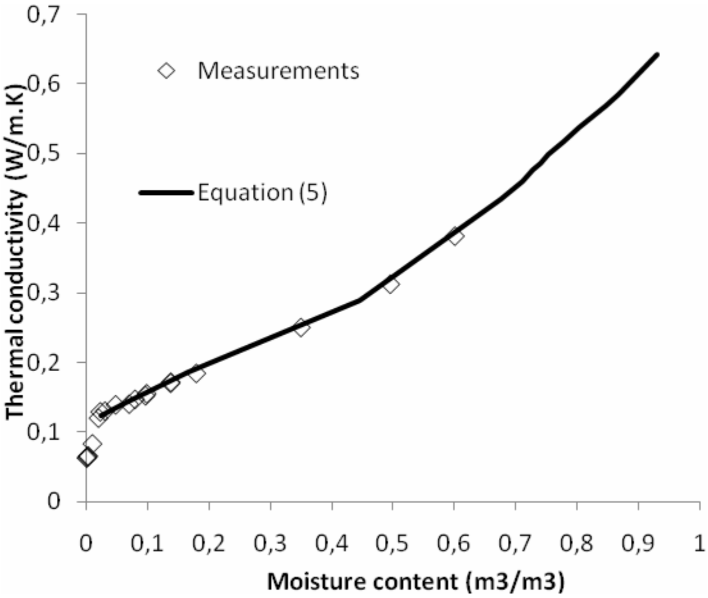

Figure 4: Comparison of measured and modelled moisture dependences of thermal conductivity

3.2 Relative permittivity

The relative permittivity of calcium silicate with various moisture content was measured by [3] and these results were complemented by the own measurements. The effective permittivity model based on equation (3) was specified into the form of equation (6). The comparison of the measurements and the model approximation is in figure 5.

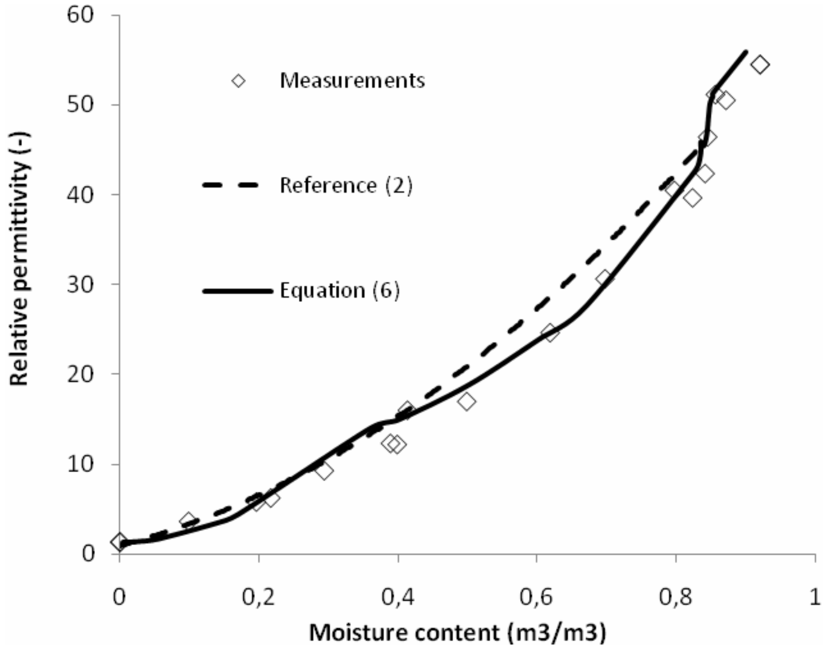

Figure 5: Comparison of measured and modelled relative permittivities

The effective permittivity is given by the parallel configuration the permittivities of solid matrix ◎m, air ◎a and water ◎w equal to 2.3, 1.2 and 80 respectively, at a given degree of saturation uw.

$$\varepsilon_{ef}(u_w)=\varepsilon_s\cdot(1-\Phi)+\varepsilon_a\cdot(\Phi-u_w)+\varepsilon_w\cdot(u_w-u_{crit})^{1+FD_m} \tag{6}$$

The critical volume in equation (6) is equivalent to the critical moisture content, equal to 0.17 m3/m3, for a given calcium silicate. In the moisture content interval 0 – 0.17 the water adsorbed on the surface of pores is predominant and therefore the mean fractal dimension equal to 0.8 (figure 3), corresponding to the volume of pores relevant for the water vapour adsorption, i.e. the pore surface area, was used.

The comparison of the measured and modelled relative permittivity data shows a good similarity and confirms the significant correlation between pore size distribution and fractal properties of the analysed material.

4 Conclusions

The thermal conductivity and relative permittivity of calcium silicate at various moisture contents can be modelled by the power function of relevant moisture content.

The power function exponent is given by the mean fractal dimension of pores filled with water.

Acknowledgement

Authors wish to thank the APVT-51-030704 and APVV-0744-07 projects for the financial support of this work.

References

[1] MATIASOVSKY P.; BAGEL L. Compatibility of BET nitrogen and water adsorption/desorption isotherms of interior plasters. In Proceedings of 4th International Building Physics Conference/Editors Bayazit N.T.; Manioglu, G.K. Yilmaz Z. Istanbul, Technical University Istanbul. p. 11-16. ISBN 978-975-561-350-5

[2] KORONTHALYOVA O.; MATIASOVSKY P. Thermal Conductivity of Fiber Reinforced Porous Calcium Silicate Hydrate-based Composites. Journal of Thermal Envelope and Building Science. 2003. 27(1). p. 71 – 89. ISSN 1097-1963

[3] PAVLIK z.; MIHULKA j. TDR Method – Effective Tool for Moisture Measurement in Porous Materials Containing Salts. In Proceedings of 2nd Confernce on Experimental and Computational Methods for Directed Design and Assessment of Functional Properties of Building Materials. Prague, CTU. 2008. p. 145 – 150. ISBN 978-80-01-04184-0

[4] MATIAŠOVSKÝ, Peter – KORONTHÁLYOVÁ, Oľga. Analysis and modelling of effective thermal conductivity of dry porous building materials. In Proceedings of the 8th Symposium on Building Physics in Nordic Countries / editor Carsten Rode Danish Society of Engineers, IDA, Copenhagen 2008. p. 285-291. ISBN 978-87-7877-265-7

Computational modelling of coupled heat and moisture transport with hysteretic hydric parameters

Jan Kočí[1], Jiří Maděra[1], Eva Vejmelková[1], Robert Černý[1]

[1]Czech Technical University in Prague, Faculty of Civil Engineering, Department of Materials Engineering and Chemistry, Czech Republic

Abstract: *A computational model of coupled heat and moisture transport in porous building materials taking into account hysteresis of hydric parameters is presented. A practical application of the model shows that the hysteretic moisture transport and storage parameters can be considered as quite important in service life analyses of multi-layered systems of porous building materials.*

Keywords: *moisture transport, hysteresis, computer simulation*

Introduction

Heat and moisture transport calculations are quite common in service life analyses of multi-layered systems of building materials. They make it possible to identify potential weak points in building envelopes from the hygro-thermal point of view, thus allow to react to possible danger in time and prevent excessive damage caused for instance by accumulation of liquid water in specific parts of a structure. Although it is known for years that moisture transport and storage parameters of many porous materials may exhibit considerable hysteresis, most of the calculations are still performed with parameters measured during the adsorption phase which is an apparent consequence of difficulties the experimentalists face in the measurements of some parameters in desorption phase.

In this paper, the effect of hysteresis of moisture transport and storage parameters on calculated moisture and relative humidity fields is investigated for a characteristic case of concrete wall with exterior thermal insulation, and the possible consequences of neglecting hysteresis of these parameters for service life calculations are analyzed.

Mathematical model

The diffusion model proposed by Künzel [1] was used for description of coupled heat and moisture transport. The heat and moisture balance equations were formulated in the form

$$\frac{\mathrm{d}H}{\mathrm{d}T}\frac{\partial T}{\partial t} = \mathrm{div}\left(\lambda \,\mathrm{grad}\, T\right) + L_v \mathrm{div}\left[\delta_{\mathrm{p}} \mathrm{grad}\,(\varphi\, \mathrm{p_s})\right], \tag{1}$$

$$\frac{\partial \rho_v}{\partial \varphi}\frac{\partial \varphi}{\partial t} = \mathrm{div}\left[D_\varphi \mathrm{grad}\,\varphi + \delta_p \mathrm{grad}\left(\varphi\; p_s\right)\right], \tag{2}$$

where H is the enthalpy density, Lv heat of evaporation, λ thermal conductivity, T temperature, ρv partial density of moisture, φ relative humidity, δp permeability of water vapor, ps partial pressure of saturated water vapor,

$$D_{\varphi} = D_{w} \frac{\mathrm{d}\rho_{v}}{\mathrm{d}\varphi} \tag{3}$$

is the liquid water transport coefficient, DW capillary transport coefficient (moisture diffusivity).

The inclusion of cyclic wetting and drying processes into the model was done using different moisture transport and storage parameters functions in wetting and drying phase and calculating the path between the parameter functions corresponding to wetting and drying in every time step.

For describing the path between the adsorption and desorption isotherms an empirical procedure was chosen which follows Pedersen's hysteretic model [2]. The actual value of moisture content, w, is determined using equation

$$w = w_{p} + \xi\left(\varphi_{a} - \varphi_{p}\right), \tag{4}$$

where ◎a is the actual value of relative humidity and ◎p the value of relative humidity from previous calculation step, ◎◎is the slope of the hysteretic parameter which is calculated as

$$\xi = \frac{a_{d}\left(w_{p} - w_{a}\right)^{2} \xi_{d} + a_{a}\left(w_{p} - w_{d}\right)^{2} \xi_{a}}{\left(w_{d} - w_{a}\right)^{2}}, \tag{5}$$

w_P is the value of moisture content from previous calculation step, wa and wd are values of moisture content for adsorption and desorption cycles, □a and ◎d the values for tangent adsorption and desorption in the points wa and wd, aa and ad the correction coefficients. An example of the calculation of the path between the adsorption and desorption isotherms is given in Figure 1.

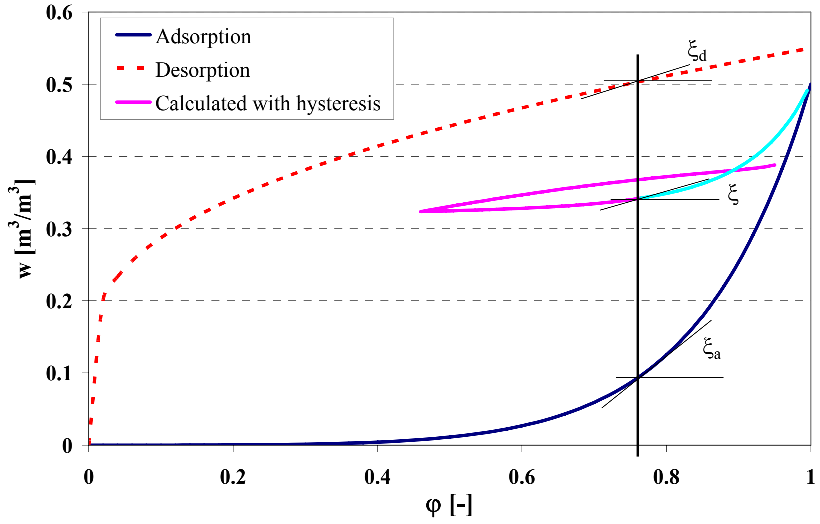

Figure 1: Example of application of hysteresis to sorption isotherms during drying and wetting cycles

In the case of moisture diffusivity, a modification of (5) was necessary in order to express the hysteretic effect in more accurate way. The modified equation can be expressed as

$$\xi = \frac{a_d\left(\ln\kappa_p - \ln\kappa_a\right)^2 \ln\xi_d + a_a\left(\ln\kappa_p - \ln\kappa_d\right)^2 \ln\xi_a}{\left(\ln\kappa_d - \ln\kappa_a\right)^2}, \tag{6}$$

where ⊚p is the value of moisture diffusivity from previous calculation step.

Materials and building envelope

A simplified building envelope system was chosen for the investigation of the effect of hysteresis on the calculated moisture and relative hunidity fields. The load-bearing structure was made of high performance concrete containing metakaolin (600 mm). Mineral wool (140 mm) was used as exterior thermal insulation. Lime-cement plaster (10 mm) was on both exterior and interior side. The building envelope was exposed from inside to constant conditions (temperature equal to 21 °C and relative humidity equal to 55 %) and from outside to climatic conditions corresponding to the reference year for Prague (Fig. 2).

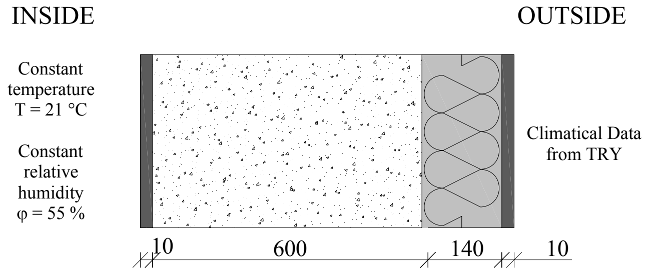

Figure 2: Scheme of the studied envelope including boundary conditions

The initial conditions were chosen as follows: relative humidity 89 % and constant temperature profile equal to 21 °C.

Table 1: Basic parameters of materials of the studied building envelope

Parameter	Unit	HPCM	MW	LCP	LPMH
ρ	[kg/m^3]	2366	170	1550	1745
w_{hyg}	[m^3/m^3]	0.107	0.0073	0.03	0.024
w_{sat}	[m^3/m^3]	0.13	0.89	0.40	0.33
λ_{dry}	[W/mK]	1.56	0.055	0.70	0.84
λ_{sat}	[W/mK]	2.09	1.20	2.40	2.40
κ	[m^2/s]	see Fig. 4	5.1E-10. e3.12w	7.3E-7. e3.2w	3.9E-8
c	[J/kgK]	730	1000	1200	610
μ	[-]	21	45	7	13

The basic material parameters of concrete (HPCM), mineral wool (MW), lime-cement plaster (LCP) and hydrophobized lime plaster modified by metakaolin (LPMH) are shown in Table 1 where the following symbols were used: ϱ – bulk density, c – specific heat capacity, μ – water vapor diffusion resistance factor, λdry – thermal conductivity in dry conditions, λsat – thermal conductivity in water saturated conditions, ⊚ - moisture diffusivity, whyg – hygroscopic moisture content by volume, wsat – saturated moisture content by volume. Fig. 3 presents the sorption isotherms of concrete used in the simulations. The data were obtained by experiments performed at the Department of Materials Engineering and Chemistry, Faculty of Civil Engineering, Czech Technical University in Prague [3, 4].

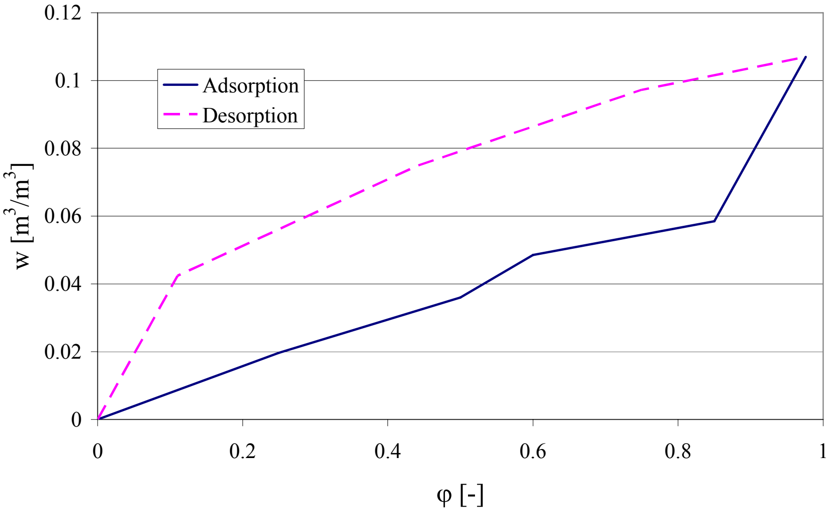

Figure 3: Sorption isotherm of concrete

Fig. 4 presents the moisture diffusivity of concrete. Moisture diffusivity vs. moisture function for adsorption was derived according to (7)-(9), where two input parameters were used, the normalized pore distribution curve f(r), Rmin < r < Rmax, and the average value of moisture diffusivity κav determined in a common sorptivity experiment [5], and the tortuosity effect was linearized for the sake simplicity, i.e., an assumption of n=1 was adopted,

$$\kappa_r(w) = \left(\frac{w}{w_{sat}}\right)^n \frac{R_{\max}^2 f(R_{\max})}{R^2 f(R)} \frac{\int_{R_{\min}}^{R} r^2 f(r) dr}{\int_{R_{\min}}^{R_{\max}} r^2 f(r) dr}, \tag{7}$$

$$\kappa\left(\frac{2}{3} w_{sat}\right) = \kappa_{av}, \tag{8}$$

$$w(R) = w_{sat} \int_{R_{\min}}^{R} f(r) dr. \tag{9}$$

Contrary to the sorption isotherms, where desorption curves can be obtained by common experimental techniques, the desorption curve of moisture diffusivity had to be set empirically as for its experimental determination no quite reliable techniques are available at present. Based on the results of experiments and computational analyses described in [6], it was estimated to be one order of magnitude lower than the adsorption curve.

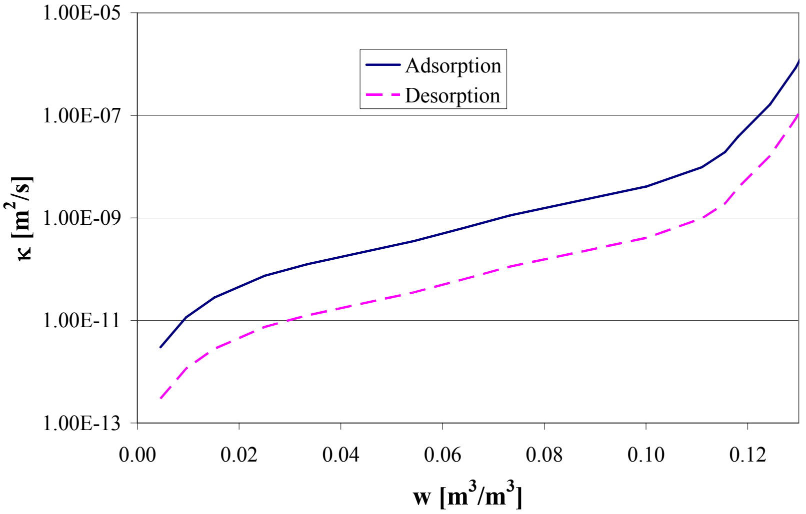

Figure 4: Moisture diffusivity of concrete

The moisture transport and storage parameters of mineral wool insulation and exterior and interior plasters were assumed to be the same in both adsorption and desorption phase. The water vapor adsorption and moisture diffusivity of mineral wool are so low that hysteretic effects are within the error range of experimental methods in any case. The thickness of renders is much lower as compared to both concrete and mineral wool so that the effect of hysteresis in their hygric parameters on moisture transport in the wall as a whole is supposed to be neglected.

Results of computer simulations and discussion

Three different simulations were performed, combining the effects of hysteresis of moisture transport and storage parameters, namely the simulation with hysteresis of sorption isotherm only, hysteresis of moisture diffusivity only and hysteresis of both sorption isotherm and moisture diffusivity. The calculations without hysteresis were done as well for the sake of comparison, using the data for adsorption phase which is usual in computational simulations where hysteresis is neglected.

Hysteresis of sorption isotherm

Figs. 5a, b show moisture content and relative humidity profiles calculated for January 1, which can be considered as characteristic for the winter period. The calculation with hysteretic effects led to increase of moisture content in the envelope, whereas relative humidity was significantly lower.

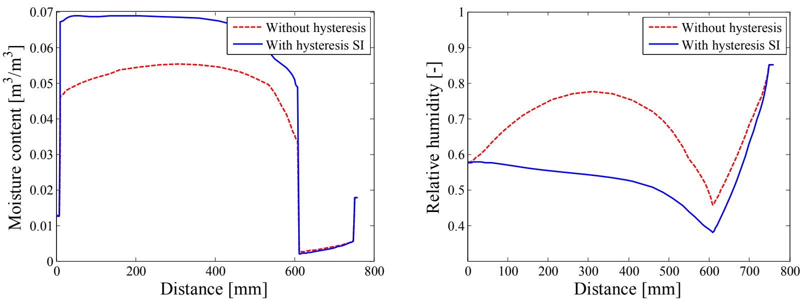

Figures 5a, b :Moisture content (a) and relative humidity (b) profiles for January 1

Figs. 6a, b summarizes the moisture and relative humidity fields during the whole simulated time period of 5 years calculated with hysteresis.

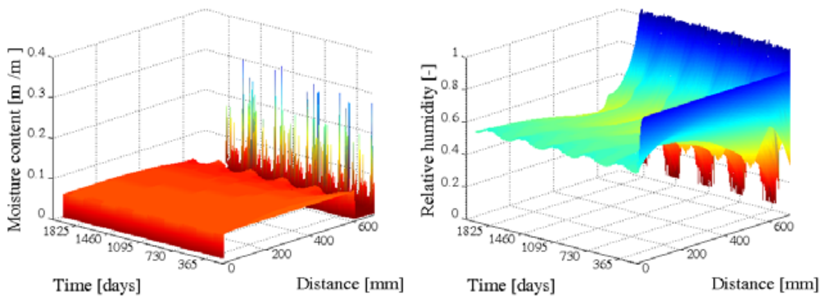

Figures 6a, b: Moisture content (a) and relative humidity (b) fields during a 5-year period

Hysteresis of moisture diffusivity

The moisture and relative humidity profiles for January 1 (Figs. 7a, b) show that both moisture content and relative humidity calculated with hysteresis were higher, which was a consequence of lower moisture diffusivity in drying phase.

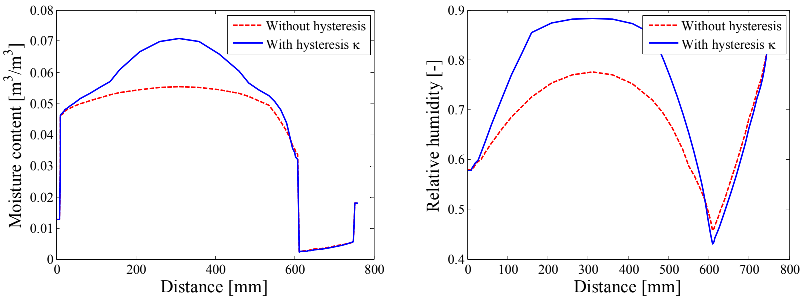

Figures 7a, b: Moisture content (a) and relative humidity (b) profiles for January 1

Figs. 8a, b show the moisture and relative humidity fields during the whole simulated time period of 5 years calculated with hysteresis.

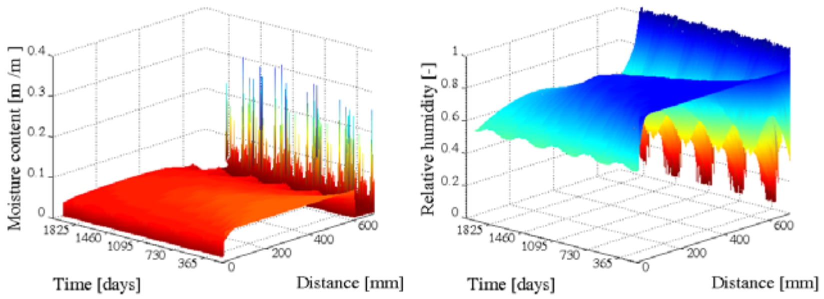

Figures 8a, b: Moisture content (a) and relative humidity (b) fields during a 5-year period

Hysteresis of both sorption isotherm and moisture diffusivity

The moisture and relative humidity profiles (Figs. 9a, b) were very similar to the simulations presented in 4.1, which meant that the hysteretic effect of sorption isotherm had remarkably higher influence on simulation results.

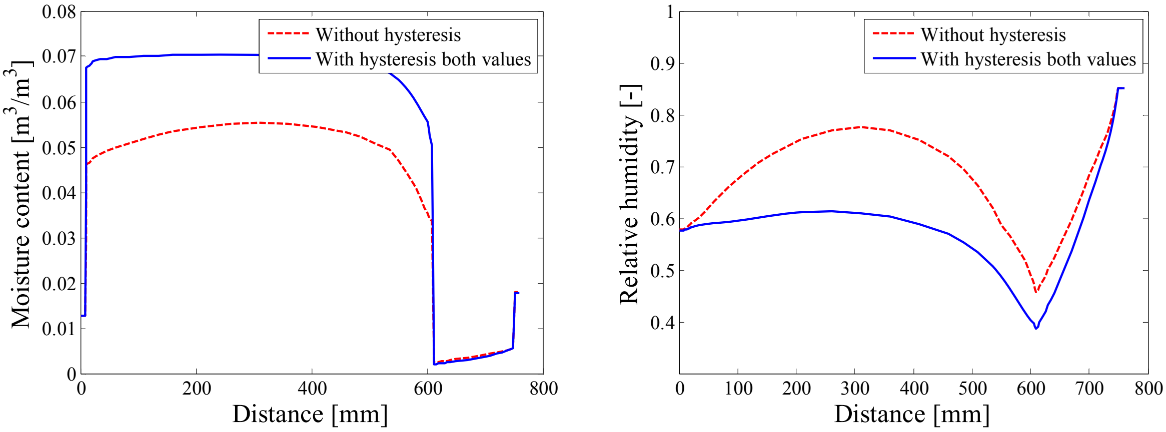

Figures 9a, b: Moisture content (a) and relative humidity (b) profiles for January 1

Figs. 10a, b present the moisture and relative humidity fields during the whole simulated time period of 5 years calculated with hysteresis.

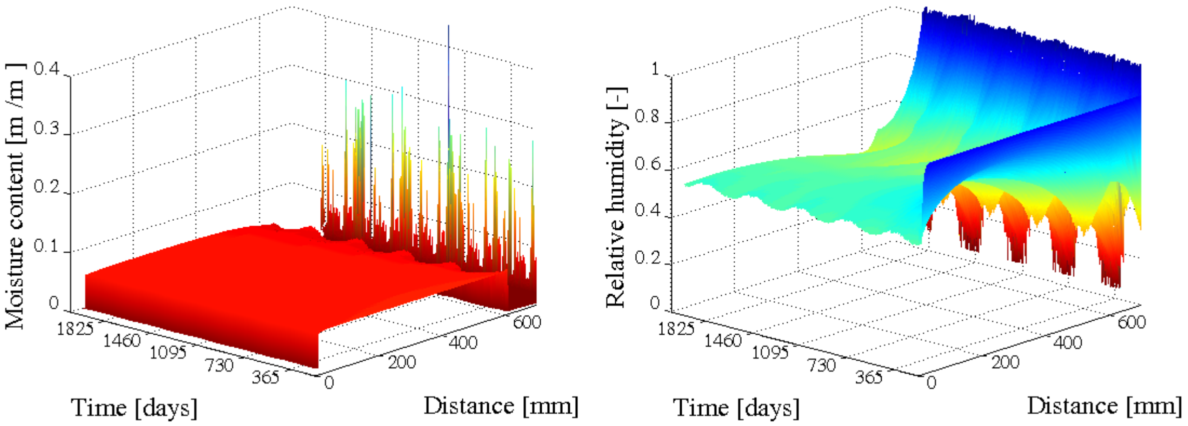

Figures 10a, b: Moisture content (a) and relative humidity (b) fields during a 5-year period

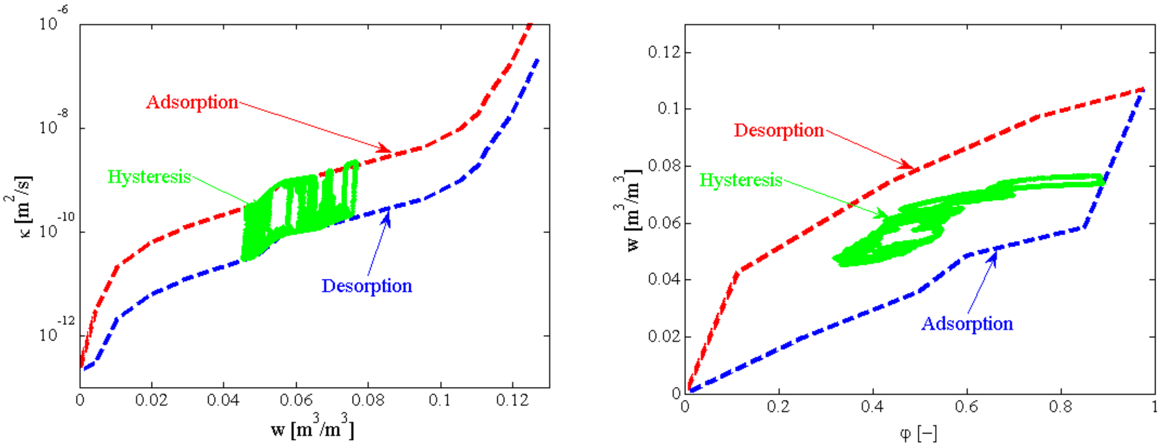

Figures 11a, b: Calculation of hysteresis of moisture diffusivity (a) and sorption isotherm (b)

Figs. 11a, b show how the hysteretic effects were manifested in the values of moisture diffusivity and sorption isotherm of concrete used by the model during the whole time period of 5-years simulation. While the water vapour sorption parameters were mostly near to the center line of the area demarcated by the adsorption and desorption curves, the moisture diffusivities oscillated between the maximum and minimum values.

Comparison of the effects of hysteresis of moisture transport and storage parameters

Figs. 12a, b present a comparison of the effects of hysteresis of moisture transport and storage parameters on moisture content and relative humidity for a characteristic locality in concrete, 1 cm from the interface between concrete and thermal insulation. As for the relative humidity profiles, it is obvious that all values came close each other in the 5th year of simulation. Moisture content profiles were quite different. Results of simulation without hysteretic effect and with hysteresis of moisture diffusivity only were very similar, but they differed from the other simulations in a significant way. Besides, the yearly oscillations of water content were not steady yet after 5 years. Involving hysteretic effects of both moisture diffusivity and sorption isotherm caused the highest increase of moisture content in the chosen point. Similar results were also obtained for other points within the concrete part of the wall.

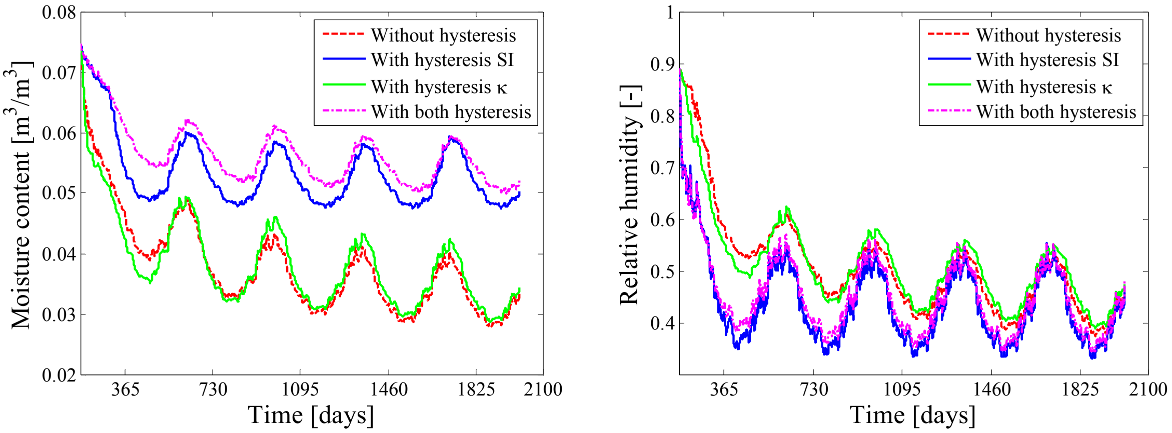

Figures 12a, b: Moisture content (a) and relative humidity (b) in a characteristic locality in concrete, 1 cm from the interface between concrete and thermal insulation

Conclusions

The computer simulations of coupled heat and moisture transport in this paper have shown that the application of hysteretic moisture transport and storage parameters can be considered as quite important in service life analyses of multi-layered systems of porous building materials. The results indicated very significant differences in moisture and relative humidity profiles calculated using the model with hysteretic parameters and without hysteresis. As the differences were always on the dangerous side, it can be concluded that neglecting the hysteretic effects while desorption is in progress can lead to underestimation of damage risk due to water presence in a structure which is rather undesirable in any service life analysis.

Acknowledgement

This research has been supported by the Czech Ministry of Education, Youth and Sports, under project No MSM 6840770031.

References

[1] KÜNZEL, H. M., Simultaneous Heat and Moisture Transport in Building Components, PhD Thesis, IRB Verlag Stuttgart, 1995.

[2] PEDERSEN, C. R., Combined Heat and Moisture Transfer in Building Constructions, PhD Thesis, Report 214. Thermal Insulation Laboratory, TU Denmark, 1990.

[3] VEJMELKOVÁ, E. & ČERNÝ, R., Application of Alternative Silicate Binders in the Production of High Performance Materials Beneficial to The Environment. Proceedings of the 2008 World Sustainable Building Conference [CD-ROM]. Balnarring, Victoria: ASN Events Pty Ltd, 2008, p. 520-525, 2008.

[4] PernIcová, R., PAVLÍKOVÁ, M., PAVLÍK, Z. & ČERNÝ, R., Vliv metakaolinu na mechanické, tepelné a vlhkostní vlastnosti vápenných omítek. Metakaolin 2007. Brno: VUT FAST, s. 70-77, 2007

[5] ČERNÝ, R. & ROVNANÍKOVÁ, P., Transport Processes in Concrete, 1. ed. London: Spon Press, pp. 26–29, 2002.

[6] PEL L., ČERNÝ, R. & PAVLÍK Z, Moisture and Ion Transport. WP5 2-Years Report of the EU 6th Program Project SSPI-CT-2003-501571. TU Eindhoven, Eindhoven, 2006.

Effect of water vapour permeability moisture dependence on simulation of dynamic moisture response

Olga Koronthalyova

Institute of Construction and Architecture, Slovak Academy of Sciences, Dubravska c. 9

SK-845 03 Bratislava, Slovak Republic

Abstract: *In simulations of an isothermal moisture flow the surface flow effects can be involved in the moisture dependent water vapour permeability. Generally, the water vapour permeability is function of moisture content but it is often modeled as vapour permeability / relative humidity relation using the standard cup method measurements results. In this work the effect of the used water vapour permeability function on the reliability of simulation results was evaluated for the case of drying of capillary porous material in the hygroscopic range.*

The simply experiment, consisting in monitoring of isothermal 1-D drying of the chosen building materials (burnt clay bricks, autoclaved aerated concrete) was done. In the following simulations of the drying process different expressions of vapour permeability moisture dependence were used. On the base of the comparison of the measured and simulated results the suitability of the used water vapour permeability functions was determined and the consequences for simulation of dynamic moisture response were discussed.

Keywords: *water vapour permeability, moisture dependency, capillary porous material, hygroscopic range*

Introduction

In simulations of an isothermal moisture flow the surface flow effects can be involved in the moisture dependent water vapour permeability. Generally, the water vapour permeability is function of the moisture content but it is often modelled as vapour permeability / relative humidity relation. It is due to the fact that the standard cup methods are based on steady-state water vapour flow through the specimen which undergoes the water vapour partial pressure difference. Therefore the expression of the vapour permeability / relative humidity relation is possible directly while for the expression of the vapour permeability / water content relation an additional information about the water adsorption curve is necessary.

In this work the effect of the used water vapour permeability function on the reliability of simulation results was evaluated for the case of a drying of the capillary porous material. The evaluation was based on a comparison of the measured and the simulated course of the moisture content during isothermal 1-D drying of the tested materials -burnt clay brick and autoclaved aerated concrete.

Method

Measurements

The tests were done for two capillary porous building materials: burnt clay brick and autoclaved aerated concrete (AAC). The materials were characterised by the basic materials properties as are the bulk density, the open porosity, and the capillary moisture content. The bulk density was calculated from volume and mass of the dried out specimens (oven drying at 105°C). The capillary moisture content was determined from a time-controlled capillary water uptake experiment [3] and the open porosity was obtained from the water saturation test.

The water vapour permeability was determined by the standard dry/wet cup method [1]. The applied relative humidity differences were: 0 / 53%, 53 / 84 % and 53 / 100%. In determination of the nonlinear water vapour permeability from the measured steady state vapor flow, the simplified approach, based on assumption of the constant water vapor resistance factor corresponding to the mean value of the applied relative humidity values on the both sides of the sample was used.

The adsorption and the first desorption curve (from 98 % RH) were determined by conditioning samples in dessicators with saturated salt solutions at constant temperature (23°C). The samples were oven dried beforehand at 105 °C.

The isothermal 1-Ddrying test consisted in the regular monitoring of the drying samples mass. The specimens were sealed on all but two surfaces by the epoxy resin in order to guarantee 1D water vapour flow. The dimensions of the brick sample were 0.2308 x 0.115 x 0.05615 m with the active surface area of 0.053 m^2, the cylindrical-shaped AAC sample had the diameter of 0.19 m, the thickness of 0.264 m and the active surface area was 0.05668 m^2. The samples were moistened by spraying to the moisture content corresponding approximately to the 98% RH, wrapped in PE foil and stored in laboratory for about 3 months (brick) or 1 month (AAC) in order to obtain homogenous moisture content distribution in the specimen. After the homogenization the samples were unwrapped and placed into air-conditioned laboratory with temperature 23°C and relative humidity 53 %. The process of drying was monitored by the regular weighting of the samples.

Simulations

The 1D simulation tool WUFI (version 2.2) was used for calculations of the moisture content in samples. The standard value of the interior surface film coefficient for diffusion $\beta_v = 2.5 \cdot 10^{-8}$ s · m^{-1} was considered. The 1 hour time step and the computational mesh size of 0.7 mm were used.

Results and discussion

The basic material parameters of the brick and AAC are in Table 1. The water vapour resistance factor relative humidity dependence was approximated by the relation (Fig. 1):

$$\mu(\varphi) = \frac{1}{(a + b \cdot \exp(c \cdot \varphi))} \tag{1}$$

Where ϕ is the relative humidity [-], *a, b, c* are parameters. The values of the parameters were: $a = 0.072$, $b = 0.0028$, $c = 4.66$ and $a = 0.0775$, $b = 0.003$, $c = 5.0$ for the brick and the AAC respectively.

The obtained vapour permeability / relative humidity dependence was transformed to vapour permeability / moisture content dependence, using the moisture content / relative humidity

Table 1: Basic material properties of burnt clay brick and autoclaved aerated concrete

Material	**Bulk density [kg/m^3]**	**Open porosity [-]**	**Capillary moisture content [kg/m^3]**	**μ value [-]**		
				0 / 53 %	**53 / 84 %**	**53 / 100 %**
Brick P	1377	0.42	0.38	12	7.1	5.9
AAC	500	0.80	0.28	11		5

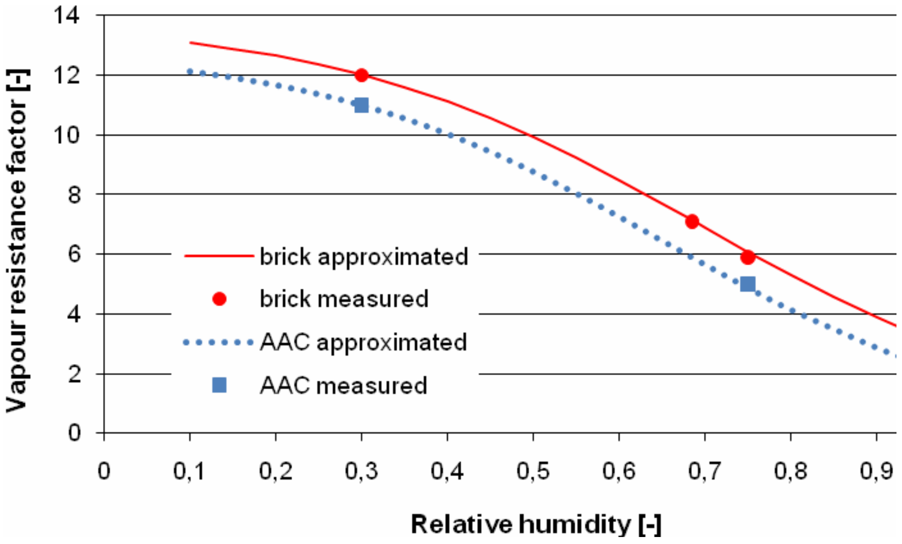

Figure 1: Measured μ-values and the approximations of their humidity dependences.

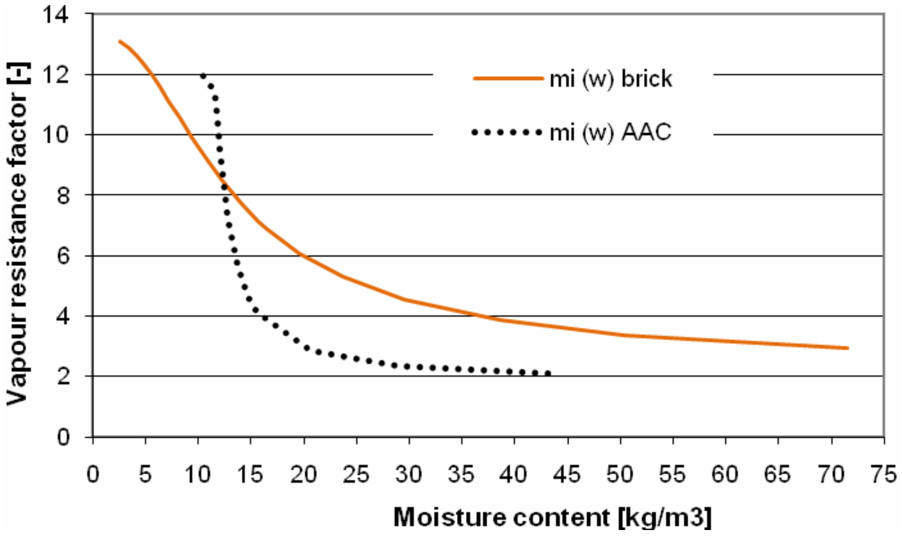

Figure 2: Constructed μ-values moisture content dependences.

relation determined from the measured main adsorption isotherm. The calculations were done for the moisture content ranges corresponding to the relative humidity interval from 10 to 98%. The resultant curves for the tested materials are shown in Fig. 2. With the aim to evaluate the actual differences between the vapour permeability values during the adsorption and desorption process the obtained vapour permeability / moisture content dependence and the measured first desorption isotherm (from 98 %) were used for the expression of the water vapour permeability / relative humidity relation during the first desorption from 98 %. The comparison between the vapour permeability / relative humidity dependences during the adsorption and the desorption process are shown in Fig. 3.

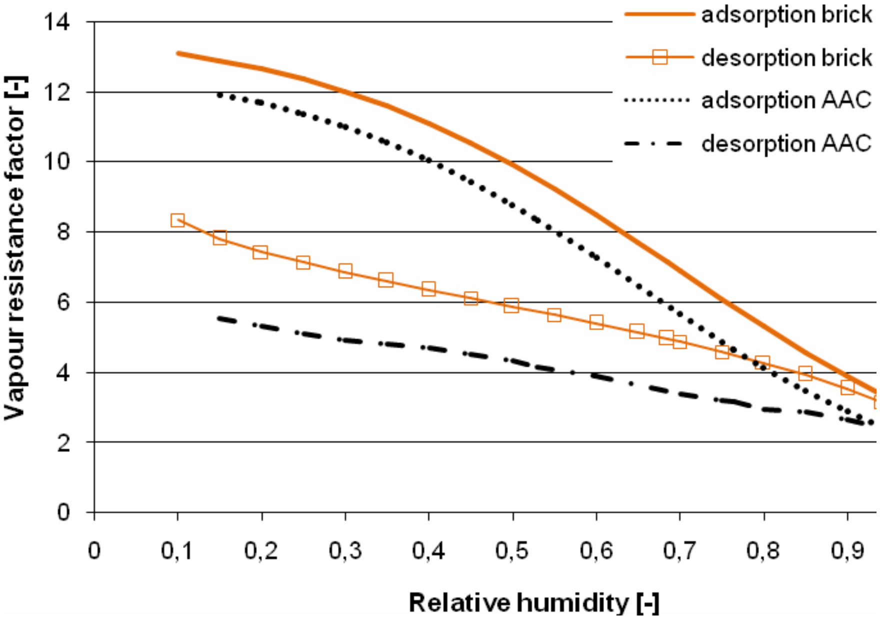

Figure 3: Comparison of the obtained μ-value / relative humidity dependence for the process of adsorption and desorption (from 98 %).

It can be seen from Fig. 3 that for both materials the differences between the adsorption and desorption μ-value / relative humidity dependence are noticeable for the relative humidity values lower than 80%. The differences are most significant in the range of the low RH values (below 50 %).

In the simulation of the drying process the moisture content / relative humidity relation was expressed using the measured first desorption isotherm from 98 %. The simulations were repeated with two various constant μ-values (corresponding to the dry cup and the wet cup value), with the μ-value expressed as the relative humidity function μ (RH) (Eq. 1) and with the μ-value expressed as the moisture content function μ (w) (Fig. 2).

The comparison of the simulation results with the measurement is presented in Figs. 4 and 5. For both tested materials the simulation with constant dry-cup μ-value underestimated significantly the rate of the drying. On the other hand the simulation results with the constant wet-cup μ-value, the μ (RH) and the μ (w) differed only slightly and the agreement with the

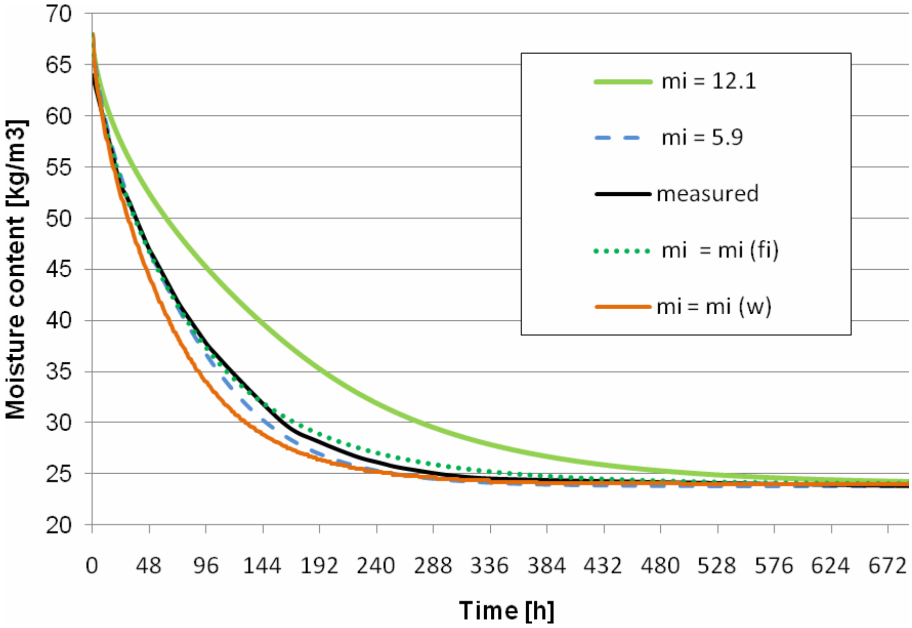

Figure 4: Comparison of the measured and simulated drying courses in the case of brick.

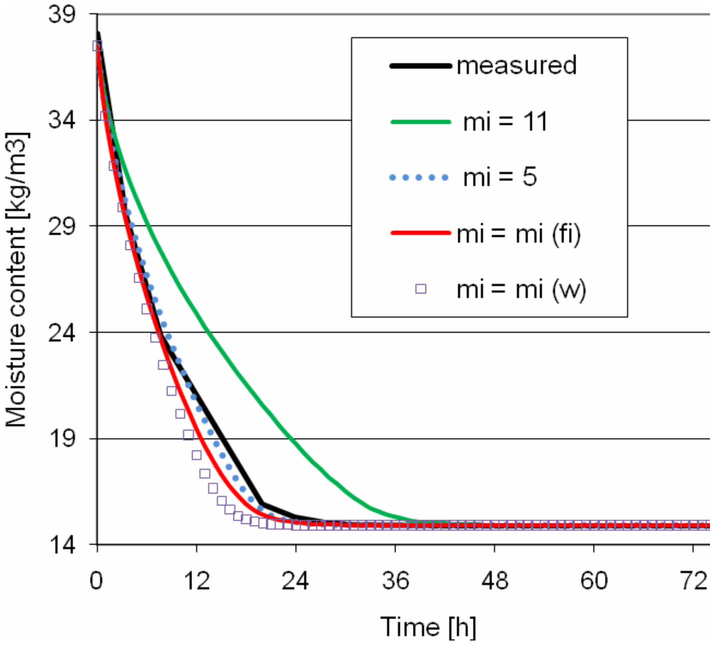

Figure 5: Comparison of the measured and simulated drying courses in the case of AAC.

measured drying course was quite acceptable. In the case of brick an insignificant overestimation of the drying rate was noticed for the μ (w) function while the use of the μ (RH) function resulted in a small underestimation of the drying rate in the range of lower moisture contents. In the case of AAC the use of the μ (RH) as well as μ (w) resulted in a small overestimation of the drying rate and the best agreement with the measured drying course was achieved with the constant wet-cup μ-value.

In the evaluation of the differences between the measured and simulated drying courses it is important to take into account that the results of the simulation are very sensitive to the used adsorption / desorption curve and the discrepancy between the measured and simulated results can be also caused by the deviation of the used desorption curve from the actual one.

The small differences between the results obtained with the constant (wet-cup) vapour permeability and the moisture content / relative humidity dependent vapour permeability were partly due to relatively weak μ-value moisture dependence in the corresponding intervals of moisture content (Fig. 2).

The overestimation of the drying rate in the case of applying the moisture content / relative humidity dependent vapour permeability can be caused by the used vapour permeability / relative humidity function (Eq. 1, Fig. 1), based on an extrapolation in the range of high relative humidity. Therefore an experimental evaluation of water vapour permeability in the range of higher relative humidity should be done. The applied simplified method of the determination of the nonlinear water vapour permeability from the measured steady state vapor flow could also contribute to the overestimation of the resultant vapour permeability values [2].

Conclusions

The effect of the used water vapour permeability function on the reliability of simulation results was evaluated for the case of a drying of two capillary porous building materials: burnt clay bricks and autoclaved aerated concrete The evaluation was based on comparison of the measured and the simulated course of the moisture content during isothermal 1-D drying.

In the range of considered relative humidity (98-53%) the differences between the results obtained with constant (wet cup) vapour permeability and moisture content/relative humidity dependent vapour permeability were not significant. It was partly due to the fact that for both tested materials the vapour permeability moisture dependence in the corresponding intervals of moisture content was not very strong.

The used expression of the moisture content/relative humidity dependent vapour permeability should be verified in the range of higher relative humidity.

Acknowledgements:

The financial support of Slovak Grant Agency VEGA (Grant No 2/7113/27) was gratefully acknowledged.

References

[1] EN ISO 12572:2001 Hygrothermal performance of building materials and products – Determination of water vapour transmission properties. CEN 2001, pp. 32.

[2] DERLUYN, h.; janssen, h.; diepens, j.; derome, d.; carmeliet, j. Hygroscopic Behavior of Paper and Books. Journal of Building Physics. 2007. 31(1). p. 9-34.

[3] ROELS, S. et al. Interlaboratory Comparison of Hygric Properties of Porous Building Materials. Journal of Building Physics. 2004. 27. p. 307–325.

Thermophysical analysis of porous system

Ľudovít Kubičár[1], Vladimír Štofanik[1], Viliam Vretenár[1], Vlastimil Boháč[1], Peter Dieška[2]

[1]Institute of Physics SAS, Bratislava

[2]Fakulty of Informatic and Electrical Engieneering, STU, Bratislava

Abstract: *Paper discusses application of the instrument RTB (Thermophysical tester) for thermophysical analysis of the porous materials. Here, thermophysical analysis means the measuring specific heat, thermal diffusivity and thermal conductivity at the specific thermodynamic condition. Thermodynamic condictions are given by temperature and the specific degree of moisture. In addition investigation of the propagation of freezing/melting front will be demonstrated by monitoring system RTM in connection with Thermophysical Tester RTB. We discuss a possibility of experimental study of the moisture transport in porous materials. A detailed characterization of the Thermophysical tester RTB and the monitoring system RTM will be presented. Measuring regimes of these instruments will be discussed considering above mentioned effects.*

Keywords: *thermal conductivity, thermal diffusivity, specific heat, moisture, transient method, hot ball method*

Introduction

Over the last twenty years a new class of transient methods for measuring thermophysical properties has been spread in research laboratories as well as in technology. Principal differences between classical and transient methods lie in varieties of specimen sizes, measuring time, and number of measured parameters. A number of experimental methods have been developed for the investigation of heat transport through porous structures. Generally these can be divided into two groups, namely methods that use a steady state measuring regime [1, 2] and methods using a transient one [3, 4]. A highly innovative measuring technique, the pulse transient method, is used for determination of specific heat, thermal diffusivity and thermal conductivity. A new hot ball method is used for the monitoring of moisture diffusion in a real environment. Two different instruments based on pulse transient method and the hot ball method has been developed and in the meantime the production has started.

The goal of this work is the presentation of application of these instruments for various research areas connected with porous structures [5, 6, 7].

Principle of instruments

Thermophysical Tester RTB is based on pulse transient method. Scheme of the instrument RTB is shown in Figure 1 (left) and photo in Figure 1 (right)

Figure 1. Instrument RTB. Scheme of the instrument (left) and photo (right)

The instrument is composed of a chamber where temperatures and surrounding atmosphere is controlled. The chamber is universal and can be used for a set of various research areas. Temperature is programmable controlled through thermostat. Vacuum pump allows changing of surrounding atmosphere or realization of the experiment under vacuum. Electronic unit contains current sources, A/D and D/A converters and timers for measuring and driving of different sensors. A communication protocol is compiled allowing data transfer and control of functionality of the electronic unit. USB and TCP/IP communication channels are at disposal.

Monitoring system RTM is based on the hot ball method. The principle of the hot ball is shown in Figure 2 together with the measuring signal [8]. A heat source in the form of a small ball starts to produce with constant rate of heat and simultaneously measures the temperature response of the surrounding medium in time (Figure 1 (right)). The temperature response stabilizes at a constant value T_m after some time. T_m is used to determine the thermal conductivity of the surrounding structure. A sphere with radius R during the temperature stabilization to T_m. Thus, the determined thermal conductivity corresponds to the material within this sphere. Therefore, an average value is to be determined for inhomogenous materials.

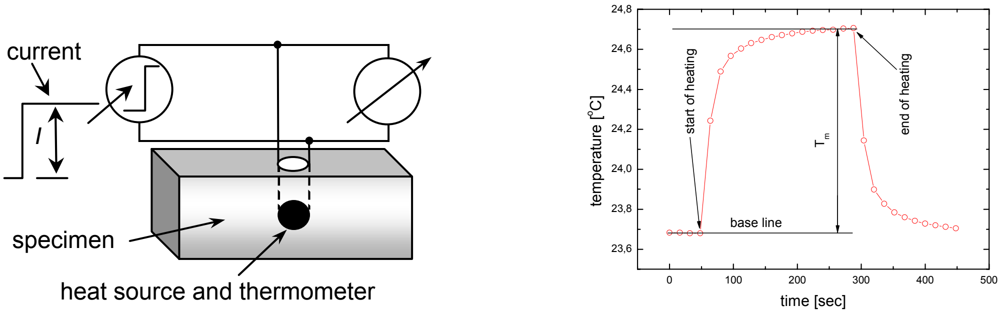

Figure 2: Principle of the hot ball method (right) and its temperature response (left).

A simple instrument was constructed that consists of a data logger, a microcontroller connected with A/D converter for temperature measurement and a D/A converter in connection with current source for heat generation. The instrument can be pre-programmed through USB channel by a PC computer. Principle of the instrument together with a photo is shown in Fig.3.

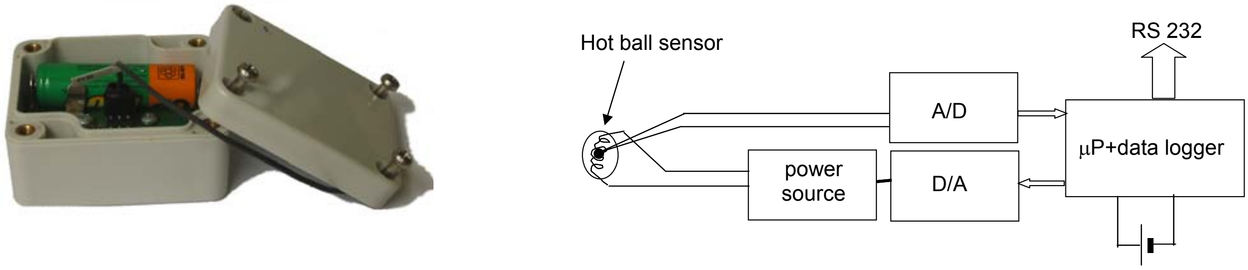

Figure 3: Scheme of the RTM instrument (right) and a photo (left).

Application area of instruments

We list application area of the Thermophysical Tester RTB and Monitoring system RTM for investigation of the thermophysical properties of porous structures. The following research problems can be solved:

- Measuring specific heat, thermal conductivity and thermal diffusivity at specific thermodynamic conditions (stage of moisture, temperature, environmental atmosphere, etc).
- Measuring freezing and thawing anomalies of the specific heat, thermal conductivity and thermal diffusivity
- Propagation of the thawing/freezing front in porous structure
- Diffusion of water in porous structure
- Absorption/desorption on pore surfaces and properties of medium in pores
- Dynamic of drying process
- Process of freeze through of porous structures
- Monitoring of technology processes (concrete setting, polymerization, etc.)

We present some interesting application of the Thermophysical tester RTB and the Monitoring system RTM.

Measuring specific heat, thermal diffusivity and thermal conductivity at the specific thermodynamic conditions. Pulse transient method in connection with the RTB instrument (Figure 1) is used for measuring thermophysical parameters. The principle of the method is shown in Figure 4 together with the specimen set. The specimen consists of three parts (I, II, III). A planar heat source is clamped between the first and the second parts. The heat pulse is produced by Joule heat in the planar electrical resistor of the source. One junction of a thermocouple is placed between the second and the third parts and measures the temperature response to the heat pulse. The specimens are preconditioned to obtain the desired thermodynamic condition. Drying or moisturize procedure is used for this purpose.

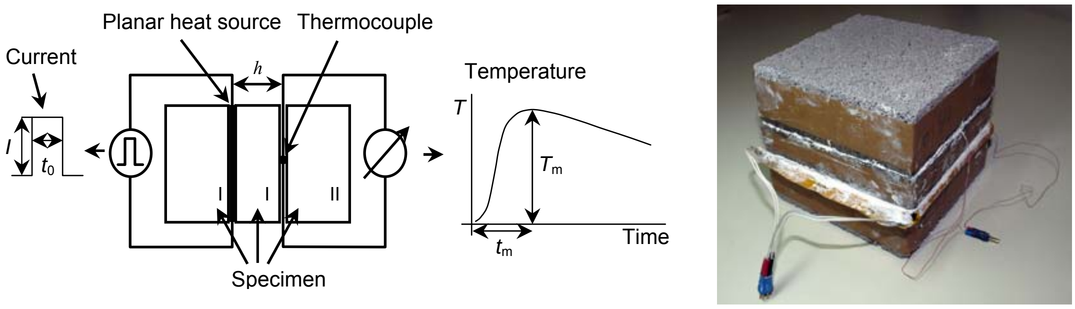

Figure 4: Principle of the pulse transient method (left) and the specimen set up (right)

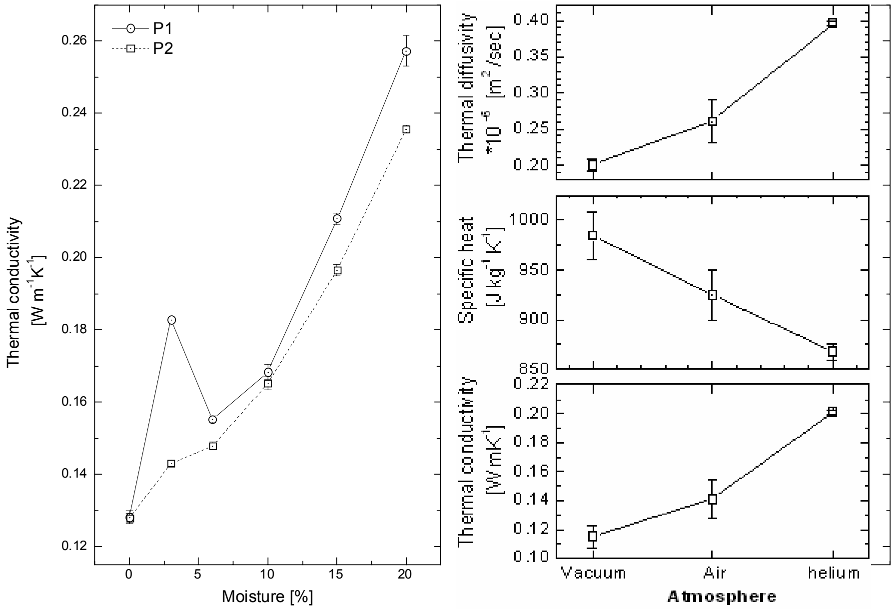

Figure 5: Thermal conductivity of the aerated concrete at 25oC that are moisturized to different degrees (left) and thermophysical parameters of porofen for different atmosphere (right).

Figure 5 shows data on thermal conductivity of aerated concrete on the left side that were moistured to different stages. Similar plots can be obtained for thermal diffusivity and specific heat. Thermophysical parameters of Porofen (Figure 5) having porous structure are significantly influenced by pore content. Effects corresponding to freezing/thawing, absorption/desorption, etc can be investigated depending on pore content and temperature [5].

Propagation of freezing/thawing fronts in porous structures. The freeze through of the walls always starts from the surface and propagates into the wall volume. Then basic characteristics have to be determined to describe process of freezing or thawing. Principle of investigation of the propagation of freezing front is shown in Figure 6. Instrument RTB is used for this investigation providing the appropriate control program is used. The specimen (Figure 4) is preconditioned i.e. a specific moisture degree is reached. Then the specimen set up is cooled to -10oC to freeze all water in the pores. The temperature of the specimen holder in instrument RTB (Figure 1 right) is set (e.g. -2.3 oC) and the frozen specimen set is fixed in the holder. An appropriate heat flux is chosen due to heat production in the heat source and the temperature of the thermocouple starts to be scanned. The frozen water in pores starts to thaw at the place of heat source and this front propagates into the specimen volume. Figure 7 shows anomaly monitored by the thermocouple during pass of thawing front. The thawing front reached thermocouple during time that is shown in Figure 7. This plot is obtained by derivation of the curve shown in Figure 7 left.

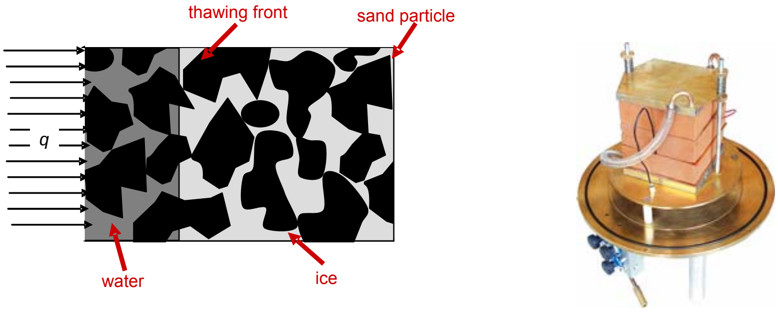

Figure 6: Model of the propagation of thawing front (left). Chamber of the RTB instrument was used for this investigation.

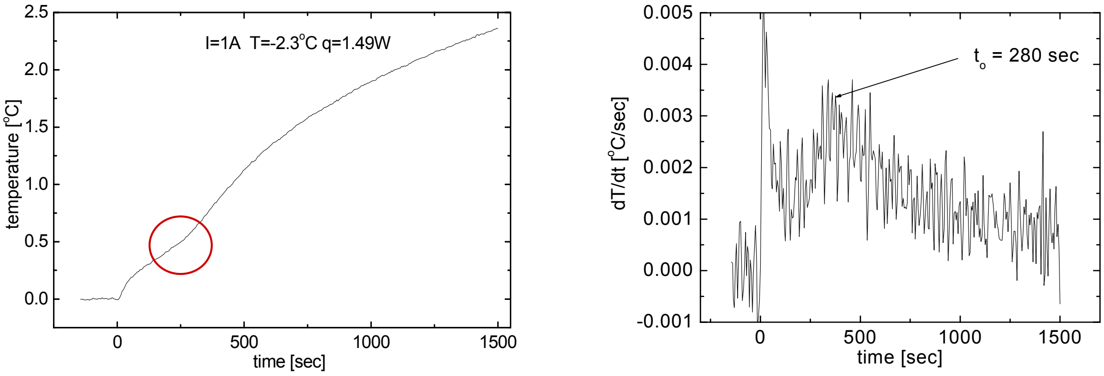

Figure 7: Monitored temperature by thermocouple during the pass of the thawing front (left) and the evaluation of the time required for it.

Monitoring of water into the porous structure. A combination of the RTB and RTM instruments is used for investigation of the water diffusion. Principle of the experiment is shown in Fig.7 left. A porous structure (stone) is fixed into the chamber of the instrument RTB (Figure 8). Side surfaces of the stone are painted by waterproof varnish while top and bottom surfaces are clean. A dish is put between the heat exchanger of the chamber and the stone to fill it with the specified amount of water. Paper is fixed together with several pieces of sand powders to allow water penetration at the bottom and air outlet at the top. Hot ball sensors are fixed in the stone (Figure 8 middle and right) The specimen is dried. The temperature of the holder together with the stone specimen is set up. Then the specified amount of water is put into the dish and monitoring of diffusion starts. Figure 9 show diffusion process of water into the sandstone. Conditions of experiments can be changed like atmosphere, vacuum and temperature.

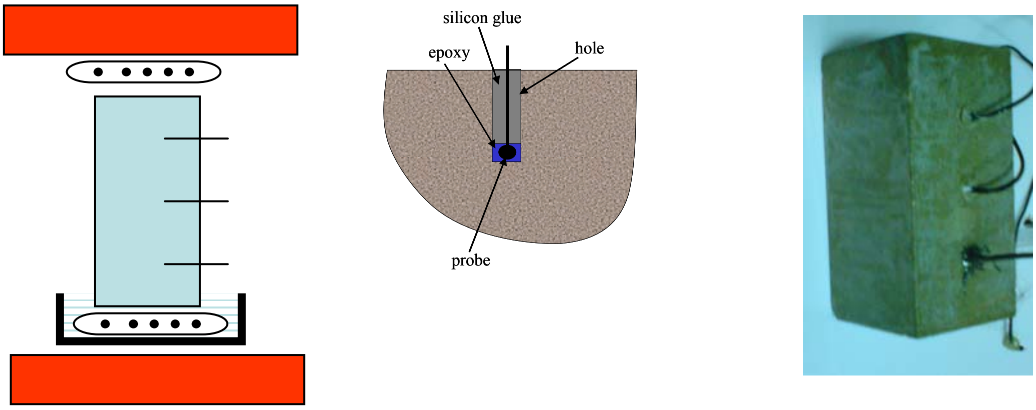

Figure 8: Scheme of the experiment for monitoring of diffusion in the porous structure (left), fixing of hot ball sensor in the stone structure (middle) and photo of stone specimen together with the sensors (right).

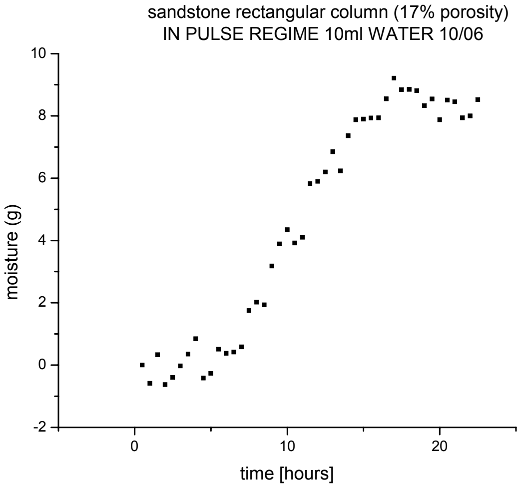

Figure 9: Difusion of moisture into the sandstone specimen.

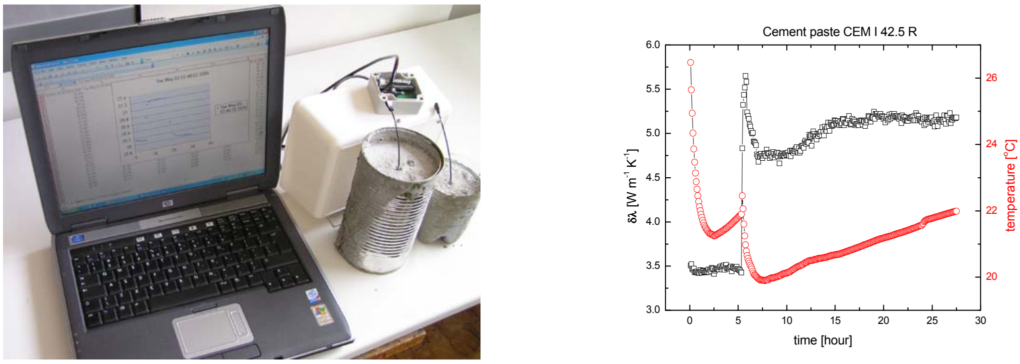

Figure 10: Photo of experimental setup for monitoring of concrete setting (left) and the temperature and thermal conductivity measured during setting process.

Setting of concrete mixture. RTM instrument can be used in laboratory as well as in environment for monitoring of concrete setting. The instrument can be preprogrammed and placed at the appropriate poit of the construction building.An example of monitoring is shown in Figure 10. The setting process is accompanied by an exothermic reaction therefore a peak of temperature is found while thermal conductivity strongly increases. A hardening of concrete can be seen after setting process has finished. The RTM instrument is constructed to fulfill environmental and industrial exposition.

Conclusions

Paper presents applicability of the thermophysical tester RTB and the monitoring system RTM in various area of technology. Thermal conductivity, thermal diffusivity and specific heat of the porous structures can be easy determined providing that thermodynamic conditions are set up like temperature and the surrounding atmosphere and pressure. Freezing and thawing effects can be studied in detail. Instruments can be combined to reach more sophisticated experimentation in area of the propagation of freezing/thawing fronts and in area of moisture diffusion in porous system. Combination of instruments allow comfortable setting the required thermodynamic conditions like, surrounding atmosphere, surrounding pressure and the temperature. A monitoring of the concrete setting was shown. Clear endothermic effects together with the strong increase of the thermal conductivity was found. Both effects correspond to setting process.

Acknowledgements:

The paper was supported by the project APVV – 0497 – 07, the project MVTS - MAFINCO and by the VEGA project 2/5100/25

References

[1] R.P. TYE: Thermal Conductivity, (Academic Press, London, New York, 1968)

[2] K.D. MAGLIĆ, A. CEZAIRLIYAN and V.E. PELETSKY: Compendium of Thermophysical Property Measurement Methods in Recommended Measurement Techniques and Practices, Vol.2, Plenum Press, New York and London (1992)

[3] J. KREMPASKÝ: Meranie termofyzikálnych veličín (VEDA SAV, Bratislava 1969), in Slovak

[4] Ľ. KUBIČÁR and V. BOHÁČ, in: Proc. of 24th Int. Conf on Thermal Conductivity / 12th Int. Thermal Expansion Symposium, October 26-29, (1997), p. 135

[5] Ľ. KUBIČÁR, V. VRETENÁR and V. BOHÁČ, Solid State Phenomena Vol. 138 (2008) pp 3-28

[6] Ľ. KUBIČÁR, V. VRETENÁR, V BOHÁČ, V ŠTOFANIK, P DIESKA, Engineering Geology 2009, submitted for print

[7] Ľ. KUBIČÁR, V. BOHÁČ, V. VRETENÁR, V. ŠTOFANIK, P. DIESKA, C. C. ANÍBARRO, Ľ. BAGEĽ, I., NOVAK, I. CHODAK, Proc. of 30th Int. Conf on Thermal Conductivity / 18th Int. Thermal Expansion Symposium, August 29 – September 2, Pittsburgh, 2009

Computational modelling of temperature and moisture profiles in a multi-layered system of building materials

Jiří Maděra[1], Jan Kočí[1], Robert Černý[1]

[1]Czech Technical University in Prague, Faculty of Civil Engineering, Department of Materials Engineering and Chemistry, Prague, Czech Republic

Abstract: *Computational modelling of temperature and moisture profiles in a multi-layered system of building materials is performed using TRANSMAT computer code developed at the Czech Technical University in Prague. A characteristic example of a building envelope with lightweight load-bearing material is chosen. The effect of both exterior render and thermal insulation material on the hygrothermal performance of the wall is clearly demonstrated.*

Keywords: *computational modelling, building envelope, temperature and moisture*

Introduction

In spite of the autoclaved aerated concrete (AAC) is a structural material commonly used around Europe, high frequency of AAC structures defects has become well known among the potential investors what leads in consequence to the weakening of the position of AAC on the European building materials market which is unfortunate because the material can be considered as environmentally friendly and has considerable potential for future applications.

The design of AAC building envelopes has mostly been done by empirical rules for construction until now. As a result, approaches to design have differed case by case and failures have resulted as a result of incorrect specifications and errors in construction. Typical failure examples are cracking of both external and internal finishes, detachment of renders from the AAC block (sometimes with the AAC itself), cracks around windows and doors, frost failure of external render.

The current standards cannot help to the designers in preventing failure. Moisture analysis in both Czech and European codes is restricted to water vapor transport in steady-state conditions. This presents a risk for a designer as water suction, water vapor convection, and the cross effects between heat and moisture transport are not considered and this can often lead to the underestimation of the amount of liquid water in the envelope or the condensation zone can appear in another place than predicted by the standard calculation.

In this paper, hygrothermal conditions in characteristic types of AAC-based building envelopes are simulated using the methods of computational modeling which can provide more detailed and accurate information than the application of oversimplified methods in current standards, and thus can allow qualitatively better service life estimates.

Materials and building envelopes

In the computer simulations of temperature and relative humidity fields we have solved four different building envelopes, based on AAC load-bearing structure and two types of external thermal insulation with two different plasters. The first insulation was hydrophobic material on mineral wool basis with low value of hygroscopic moisture content (MW), with the thickness of 50 mm. The other insulation was material with higher value of water vapor diffusion resistance factor on polystyrene basis (EPS), with the thickness of 60 mm. As the external finish either cement plaster (CP) or lime-cement plaster (LCP) was considered. All the investigated envelopes were rendered by lime-cement plaster on their interior side (see Fig. 1). Two of the envelopes were designed without thermal insulation layer in order to show the impact of thermal insulation on the hygrothermal performance.

Envelope A:		
LCP	(1)	15 mm
AAC	(3)	375 mm
LCP	(4)	5 mm

Envelope B		
CP	(1)	15 mm
AAC	(3)	375 mm
LCP	(4)	5 mm

Envelope C		
LCP	(1)	5 mm
MW	(2)	50 mm
AAC	(3)	375 mm
LCP	(4)	5 mm

Envelope D		
LCP	(1)	5 mm
EPS	(2)	50 mm
AAC	(3)	375 mm
LCP	(4)	5 mm

The basic parameters of materials of the described building envelope are shown in Table 1 [1, 4]. Here, ρ is the bulk density, θ_{hyg} the maximum hygroscopic moisture content, θ_{sat} the moisture content corresponding to water saturation, λ_{dry} the thermal conductivity corresponding to dry sample, λ_{sat} the thermal conductivity corresponding to water saturation, κ the moisture diffusivity, c the specific heat capacity and μ the water vapor diffusion resistance factor.

Table 1. Basic material parameters of AAC and renders

		AAC	**CP**	**LCP**
ρ	[kg/m^3]	500	2100	1550
θ_{hyg}	[m^3/m^3]	0.046	0.04	0.03
θ_{sat}	[m^3/m^3]	0.79	0.22	0.40
λ_{dry}	[W/mK]	0.092	1.34	0.70
λ_{sat}	[W/mK]	1.17	1.45	2.40
κ	[m^2/s]	3.5E-9·$e^{1.45\theta}$	3.1E-11·$e^{3.2\theta}$	7.3E-7·$e^{3.2\theta}$
c	[J/kgK]	1100	1000	1200
μ	[-]	5.9	45	7

Table 2. Basic material parameters of thermal insulations

		EPS	MW
ρ	[kg/m^3]	50	170
θ_{hyg}	[m^3/m^3]	0.001	0.0073
θ_{sat}	[m^3/m^3]	0.97	0.89
λ_{dry}	[W/mK]	0.04	0.055
λ_{sat}	[W/mK]	0.56	1.20
κ	[m^2/s]	2.1E-11·$e^{0.0475\theta}$	5.1E-10·$e^{3.12\theta}$
c	[J/kgK]	1300	840
μ	[-]	50	3

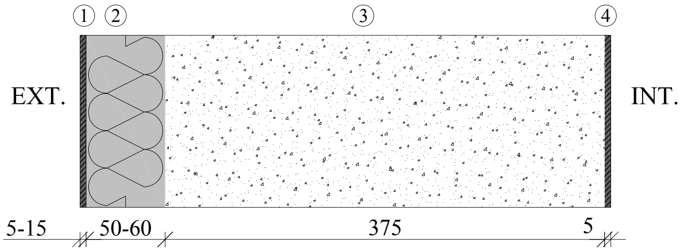

Figure 1: Buildings envelope used for calculations

Numerical Solution by TRANSMAT Code

For the calculations we employed the computer simulation tool TRANSMAT 4.3 [3] which was developed at the Faculty of Civil Engineering, Czech Technical University in Prague. The construction of the code is based on the application of the general finite element computer simulation tool SIFEL (SImple Finite ELements) developed in the Department of Mechanics, FCE CTU. The moisture (1) and heat balance (2) equations were formulated according to Künzel's model [2].

$$\frac{d\rho_v}{d\varphi}\frac{\partial\varphi}{\partial t} = div\left[D_\varphi grad\varphi + \delta_p grad(\varphi p_s)\right], \tag{1}$$

$$\frac{dH}{dT}\frac{\partial T}{\partial t} = div(\lambda gradT) + L_v div\left[\delta_p grad(\varphi p_s)\right], \tag{2}$$

where ρ_v is partial moisture density, φ the relative humidity, δ_p the water vapor permeability, p_s the partial pressure of saturated water vapor in the air, H the enthalpy density, L_v the latent heat of evaporation of water, λ the thermal conductivity and T is the temperature. The liquid water transport coefficient is defined as (3)

$$D_\varphi = \kappa\frac{d\rho_v}{d\varphi}. \tag{3}$$

The proper initial and boundary conditions of the model are crucial factor affecting the reliability of the calculations. The initial moisture content of AAC was assumed 10% by mass (common conditions for AAC use by the Czech building industry) and temperature 21 °C. In the computer simulations, the analyzed building envelopes were exposed from inside to constant conditions (temperature equal to 21°C and relative humidity equal to 55 %) and from outside to the climatic conditions corresponding to the reference year for Prague. As the starting point in the calculations three different dates (T1 = 29th July, T2 = 28th August and T3 = 29th September) were chosen to analyze the effect of time period when the masonry is walled.

Computational Results

We have chosen two critical profiles in the assessment of the hygrothermal performance of the envelopes, A-A′ and B-B′. For the envelopes A and B, where the thermal insulation is missing, the profile A-A′ was set between load-bearing structure and external plaster. For the other envelopes the profile A-A′ was between load-bearing structure and thermal insulation. In these profiles we have calculated the dependence of relative humidity and temperature on time. The profile B-B′ was set as a cross section from exterior to interior to show the temperature and relative humidity fields across the envelope.

Envelope A

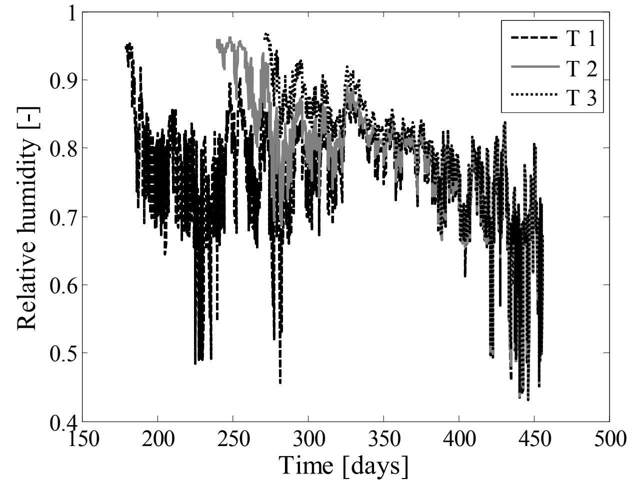

Figure 2. Relative humidity in profile A-A′

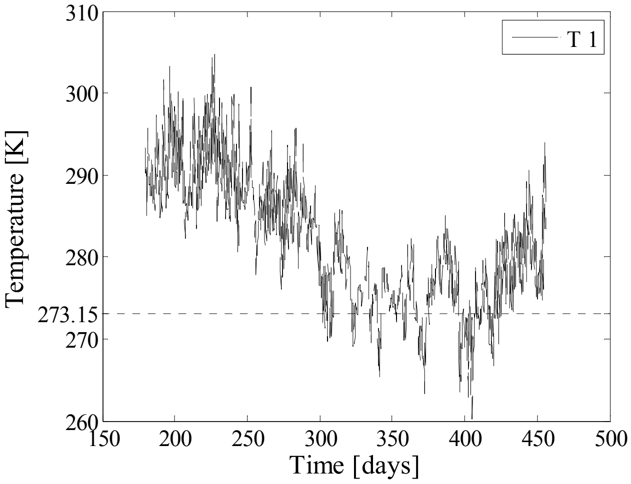

Figure 3. Temperature in profile A-A′

Figure 2 shows a dependence of relative humidity on time. During the winter period (approximately days 330 to 420) the values of relative humidity within the envelope are acceptable. In addition, the high volume of pores in the lime-cement plaster allows the envelope to breath, which leads to fluctuation of relative humidity inside the construction.

The time development of temperature in profile A-A′ shown in Figure 3 indicates the danger of water freezing/thawing in winter period where the temperatures are mostly under the freezing point. Together with high level of relative humidity inside the construction this could lead to destruction of AAC.

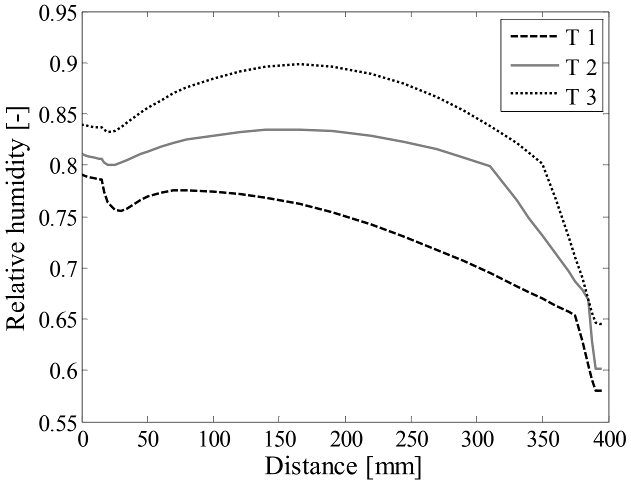

Figure 4. Relative humidity in profile B-B′

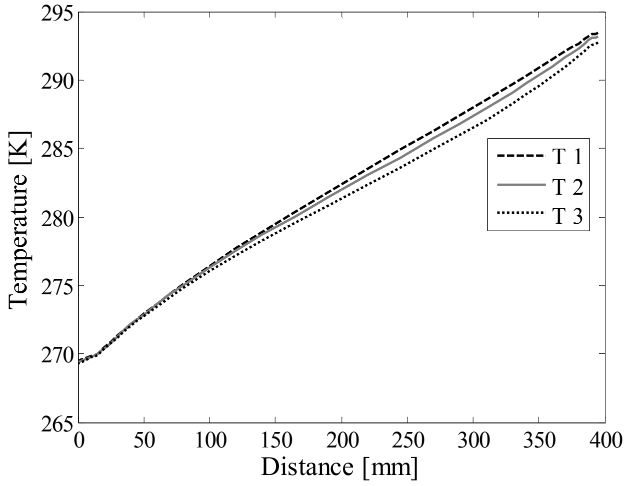

Figure 5. Temperature in profile B-B′

Fig. 4 shows a comparison of the relative humidity profiles in the envelope for 20th November as characteristic for the winter period. It is obvious that the later the wall is made the more water is retained in the construction during the winter time.

In all cross section diagrams shown further in this paper the position 0 mm represent the exterior surface of the building envelope.

The temperature in profile B-B′ is continuously increasing from the exterior to the interior due to missing thermal insulation. At the interface between external plaster and AAC the temperature is again below the freezing point.

Envelope B

Figure 6 presents a dependence of relative humidity on time. During the winter period the level of relative humidity within the envelope is acceptable only for T1 (start time 29th June). The other simulations T2 and T3 are not suitable because of too high level of relative humidity.

The time development of temperature in profile A-A′ is shown on Figure 7. The freezing/thawing cycles are well perceptible.

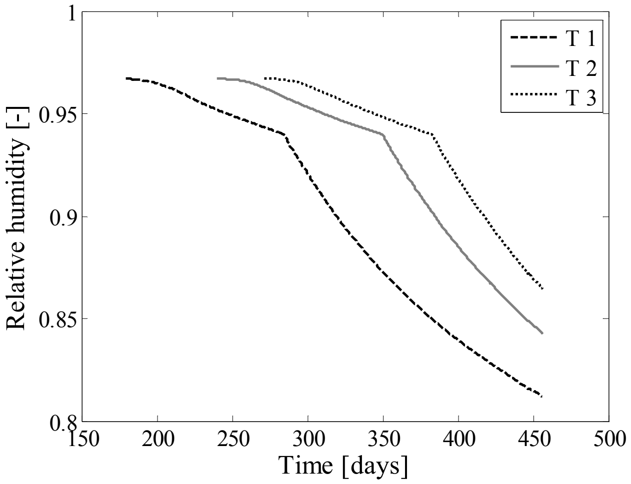

Figure 6. Relative humidity in profile A-A′

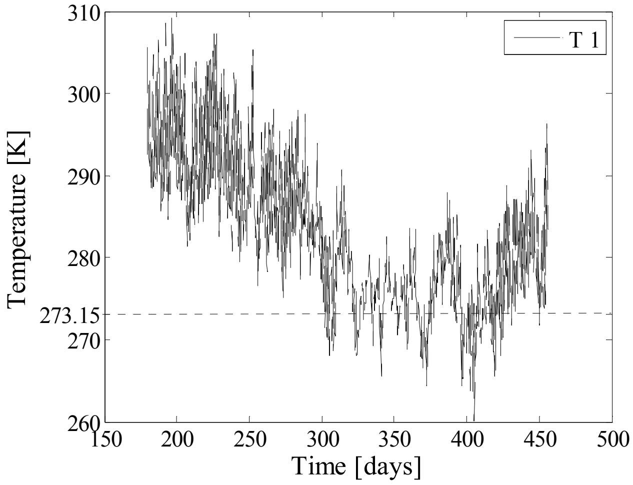

Figure 7. Temperature in profile A-A′

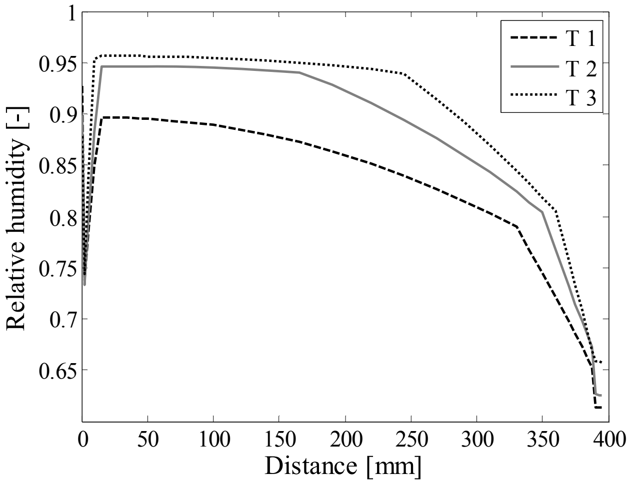

Figure 8. Relative humidity in profile B-B′

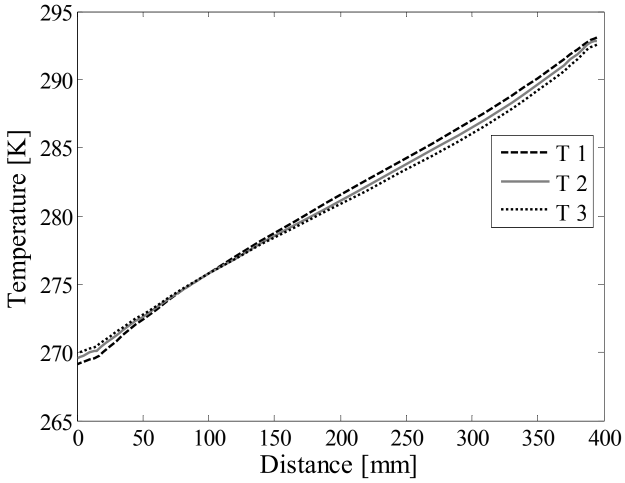

Figure 9. Temperature in profile B-B′

Figs. 8, 9 show the cross section of the envelope without thermal insulation rendered by lime-cement plaster. In Fig. 8 the negative effect of cement plaster on the whole construction is clearly evidenced. Due to the CSH gels in this material the total porosity of the plaster is very low. This is the reason why the initial water is held inside the construction and it is very difficult to evaporate.

Envelope C

Figs. 10, 11 show the time development of temperature and relative humidity of the envelope with thermal insulation on mineral wool basis. Although the level of relative humidity is quite high (see Fig. 10), taking into account the non-freezing temperature beyond the thermal insulation (see Fig. 11) this does not present any danger of water freezing/thawing inside the construction.

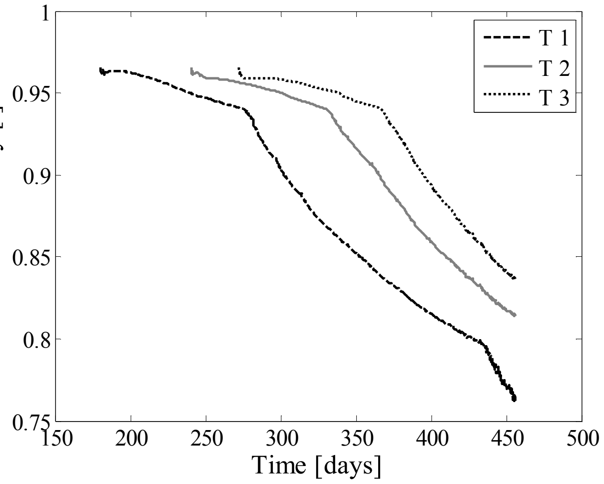

Figure 10. Relative humidity in profile A-A′

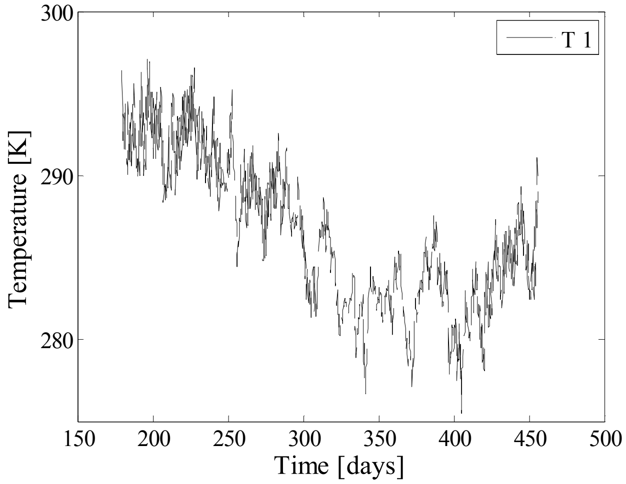

Figure 11. Temperature in profile A-A′

The impact of thermal insulation is obvious on Fig. 13. The temperature of whole AAC element is in the winter period above the freezing point, which is substantial factor prolonging the durability of the construction and preventing possible failures.

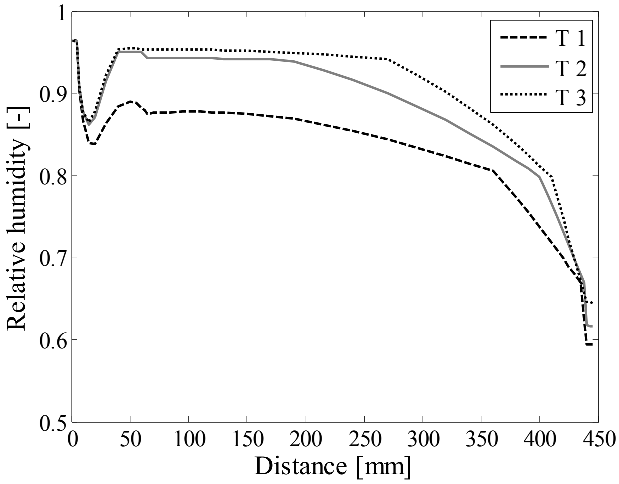

Figure 12. Relative humidity in profile B-B′

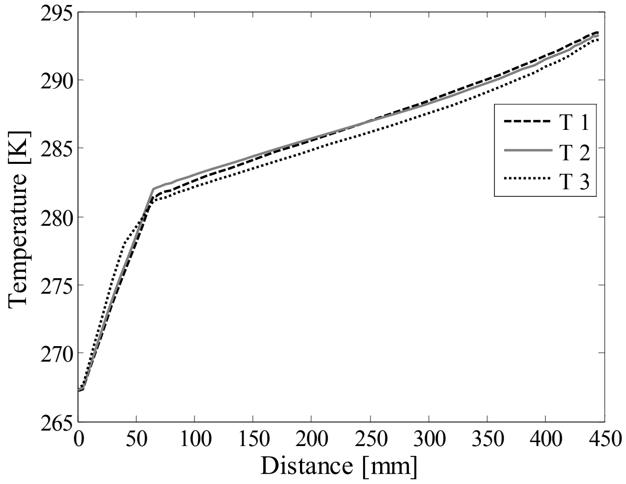

Figure 13. Temperature in profile B-B′

Envelope D

Figs. 14, 15 present the time development of temperature and relative humidity of the envelope with thermal insulation on polystyrene basis. Although the level of relative humidity is quite high (see Fig. 14), together with non-freezing temperature beyond the thermal insulation (see Fig. 15) this does not present any danger of water freezing/thawing inside the construction.

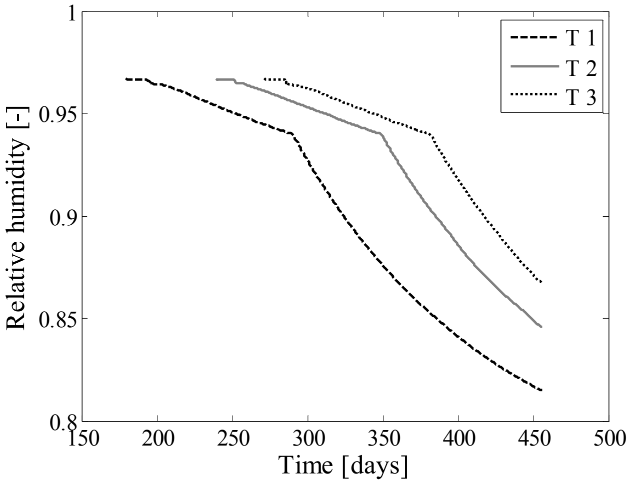

Figure 14. Relative humidity in profile A-A′

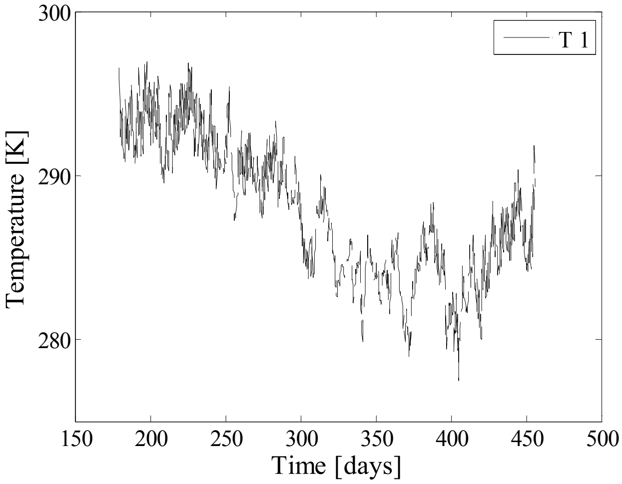

Figure 15. Temperature in profile A-A′

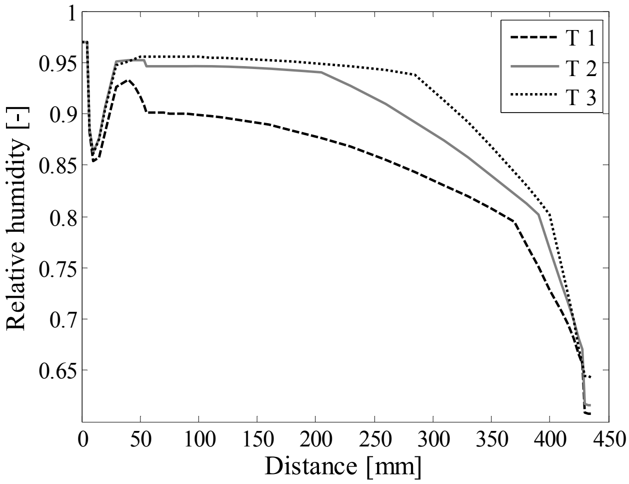

Figure 16. Relative humidity in profile B-B′

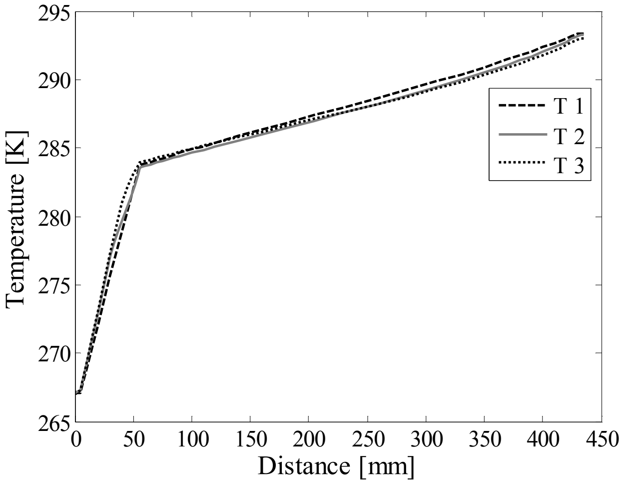

Figure 17. Temperature in profile B-B′

Figs. 16, 17 show relative humidity and temperature field across the envelope D on 20th November. Although the temperature inside the AAC element is above the freezing point, it would be desirable to start walling in the end of June (T1) to give the construction enough time to dry out.

Conclusions

The calculation results presented in this paper showed different hygrothermal behaviour of different building envelopes depending on their structure. When lime-cement plaster as external render was used we were practically not restricted by the period of walling. Using of cement plaster brought complications and it was not suitable especially for construction in the second half of year because the envelope had not enough time to dry out. The water was then held inside during winter and it could undergo freezing/thawing cycles.

All the investigations showed as the most suitable the envelopes C and D, where external thermal insulation was used. The values of relative humidity in the envelope were still rather high, but the temperatures were above the freezing point, so that the freezing/thawing cycles were practically excluded.

Acknowledgement

This research has been supported by the Czech Ministry of Education, Youth and Sports, under project No MSM 6840770031.

References

[1] JIŘIČKOVÁ M., 2004. Application of TDR Microprobes, Minitensiometry and Minihygrometry to the Determination of Moisture Transport and Moisture Storage Parameters of Building Materials, Prague: Czech Technical University.

[2] KÜNZEL H. M., 1995. Simultaneous Heat and Moisture Transport in Building Components, PhD Thesis, IRB Verlag Stuttgart

[3] MADĚRA, J., ČERNÝ, R., 2005. TRANSMAT – a Computer Simulation Tool for Modeling Coupled Heat and Moisture Transport in Building Materials, Proceedings of Workshop 2005 - Part A,B, Prague: CTU, pp. 470-471.

[4] ROELS S., CARMELIET J., HENS H., ADAN O., BROCKEN H., ČERNÝ R., PAVLÍK Z., HALL C., KUMARAN K., PEL L., PLAGGE R., 2004. Interlaboratory Comparison of Hygric Properties of Porous Building Materials. Journal of Thermal Envelope and Building Science 27: 307-325.

Application of computational modelling on the service life assessment of building envelopes

Jiří Maděra[1],Václav Kočí[1],Eva Vejmelková[1] and Robert Černý[1]

[1] Department of Materials Engineering and Chemistry, Faculty of Civil Engineering, Czech Technical University in Prague, Thákurova 7, 166 29 Prague 6, Czech Republic

Abstract: *A computational modeling approach is used for an assessment of the service life of exterior renders of building structures, the identification of the number of frost cycles in a real structure being the key assessment factor. A concrete wall with different types of concrete, thermal insulation materials and renders is under consideration. Conclusions on the most advantageous material composition with respect to the service life of exterior renders are drawn.*

Keywords: *Computational analysis, coupled heat and moisture transport, concrete wall, thermal insulation system*

Introduction

Degradation of exterior renders is caused by many factors. The most principle are chemical and mechanical corrosion. As a mechanical corrosion we can assume the influence of weather conditions, particularly the destruction effect of freezing water which is contained in the exterior renders. Phase conversion of this water goes along with volume increase and this is the main mechanism leading to material destruction.

Different exterior render can be frost-resistant in varying degrees which depends on its material characteristics. The frost resistance could be defined by experimental methods.

However, more complicated is to determine the amount of freezing cycles which arise during the year in the investigated exterior render applied on real building structure. Freezing cycle can appear only when two conditions are met. The first condition is the presence of overhygroscopic (liquid) moisture, the second a temperature below water freezing point. So we have to observe the hygrothermal performance of the exterior render and compare the thermal and hygric state in parallel. Computational analysis is the best instrument for this operation. The amount of freezing cycles depends in the first instance on climatic conditions and material composition used in building envelope.

Based on experimental and computational results we can then design optimal material composition of building envelope with respect to its service life.

Computational simulations

Building envelope

In this paper we assumed concrete wall made from different types of concrete (CF, CM, CS or CR) provided by thermal insulation system (EPS or mineral wool). The wall is provided by lime-cement plaster on interior side and by modified lime plaster on exterior side. By the same token we assumed the cases when the thermal insulation system is not present. To compare different hygrothermal behaviour of concrete in dependence on its modification we made simulation of simple concrete wall only. The material combination is shown in Figure 2.

Hygrothermal performance was investigated in exterior plaster in a point just under the surface and in concrete in a point close to the interface with render.

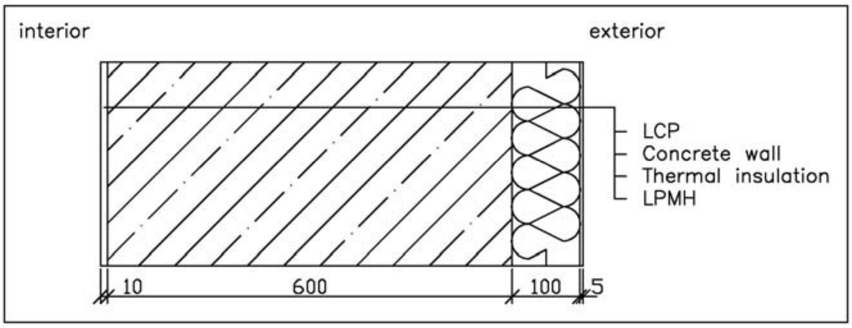

Figure 1: Scheme of building envelope

Input parameters

As the input parameters we need to know characteristics of used materials, boundary and initial conditions.

Basic material characteristics of analyzed materials are shown in Tables 1, 2 and 3. We used following symbols: ϱ – bulk density [kg/m^3], ψ – porosity [%], c – specific heat capacity [J/kgK], μ – water vapour diffusion resistance factor [-], λ_{dry} – thermal conductivity in dry conditions [W/mK], λ_{sat} – thermal conductivity in water saturated conditions [W/mK], κ - moisture diffusivity [m^2/s], w_{hyg} – hygroscopic moisture content by volume [m^3/m^3]. All these parameters were measured in laboratory of transport processes at the Department of Materials Engineering and Chemistry, Faculty of Civil Engineering, Czech Technical University in Prague [1] [2].

Table 1: Basic material characteristics of concretes

	CF	CM	CS	CR
ϱ [kg/m^3]	2356	2366	2334	2380
ψ [%]	12.5	13.0	9.7	12.3
c [J/kgK]	692	728	720	672
$\mu_{dry\ cup}$ [-]	44.63	32.44	17.70	15.80
$\mu_{wet\ cup}$ [-]	17.18	20.99	8.99	6.60
λ_{dry} [W/mK]	1.550	1.565	1.632	1.660
λ_{sat} [W/mK]	1.940	2.085	2.077	2.085
κ [m^2/s]	6.49e-9	4.09e-9	3.77e-9	7.15e-9
w_{hyg} [m^3/m^3]	0.074685	0.106943	0.089000	0.083300

Table 2: Basic material characteristics of plasters

	LCP	LPMH
ϱ [kg/m^3]	1550	1745
ψ [%]	40	33
c [J/kgK]	1200	610
μ [-]	7	10
λ_{dry} [W/mK]	0.700	0.845
λ_{sat} [W/mK]	2.40	2.40
κ [m^2/s]	7.3e-7	3.9e-8
w_{hyg} [m^3/m^3]	0.040	0.024

Table 3: Basic material characteristics of thermal insulation materials

	EPS	Mineral wool
ϱ [kg/m^3]	50	170
ψ [%]	97	89
c [J/kgK]	1300	840
μ [-]	50	3
λ_{dry} [W/mK]	0.040	0.055
λ_{sat} [W/mK]	0.560	1.200
κ [m^2/s]	2.1e-11	5.1e-10
w_{hyg} [m^3/m^3]	0.001	0.0073

Initial and boundary conditions should be as realistic as possible. Therefore, we used climatic data in exterior for Prague in the form of a Test Referent Year (TRY), which contains average climatic data for 30 years. On interior side we used constant value of relative humidity 55% and temperature 21°C. The simulation started on 1 July and was done for 5 years.

In the determination of service life of exterior renders, we also have to know their durability under freeze/thaw conditions. Here, we employed the data measured by P. Rovnaníková for lime-cement plaster (LCP) and hydrophobic lime plaster modified by metakaolin (LPMH). The frost resistance data of concretes - concrete modified by fly ash (CF), metakaolin (CM), slag (CS) and reference concrete without any modification (CR) – measured by M. Ondráček and M. Sedlmajer were used for the assessment of the service life of concrete walls. The data are summarized in Table 4.

Table 4: Number of freezing cycles causing damage of material

	LCP	LPMH	CF	CM	CS	CR
Number of freezing cycles	> 103	40	> 100	> 100	> 100	> 100

Computational model

The computations were accomplished by the computational program TRANSMAT 7.1, which was developed at the Department of Material Engineering and Chemistry, Faculty of Civil Engineering, Czech Technical University in Prague on the basis of the general finite element package SIFEL. The mathematical formulation of coupled transport of heat and moisture leads to a system of partial differential equations, which are solved by finite element method. In the particular case in this paper, Künzel's model was used [3]:

$$\frac{d\rho_v}{d\varphi}\frac{\partial\varphi}{\partial t} = div\left[D_\varphi grad\varphi + \delta_p grad\left(\varphi p_s\right)\right] \tag{1}$$

$$\frac{dH}{dT}\frac{\partial T}{\partial t} = div\left(\lambda gradT\right) + L_v div\left[\delta_p grad\left(\varphi p_s\right)\right] \tag{2}$$

where ρ_v is the partial density of moisture, φ relative humidity, δ_p permeability of water vapour, p_s partial pressure of saturated water vapour, H enthalpy density, L_v heat of evaporation, λ thermal conductivity and T temperature,

$$D_\varphi = D_w \frac{d\rho_v}{d\varphi} \tag{3}$$

is liquid moisture diffusivity coefficient, D_W capillary transport coefficient.

Results of computational simulation

The results are summarized in a set of figures. Every figure shows time dependence of moisture and temperature at the same time during fourth year of simulation. This is advantageous with regard to interpretation of simulation results. There are two horizontal lines in each figure which represent hygroscopic moisture content and temperature of freezing point.

From the vast number of figures produced in computational simulations only the most representative are chosen, rest of them is only described.

At the beginning, hygrothermal properties of simple concrete wall are analyzed. This allows us to get real image about differences in hygrothermal behaviour of different types of concrete in dependence of their modifications. Analysis of other building envelopes then follows which utilizes the previous knowledge.

Simple concrete wall

The most predisposed type of concrete to creation of freezing cycles is the reference concrete. However, due to low moisture content during the studied period there is not any freezing cycle. As we can see on Figure 3, overhygroscopic moisture content is reached only in summer month when the temperature is above zero.

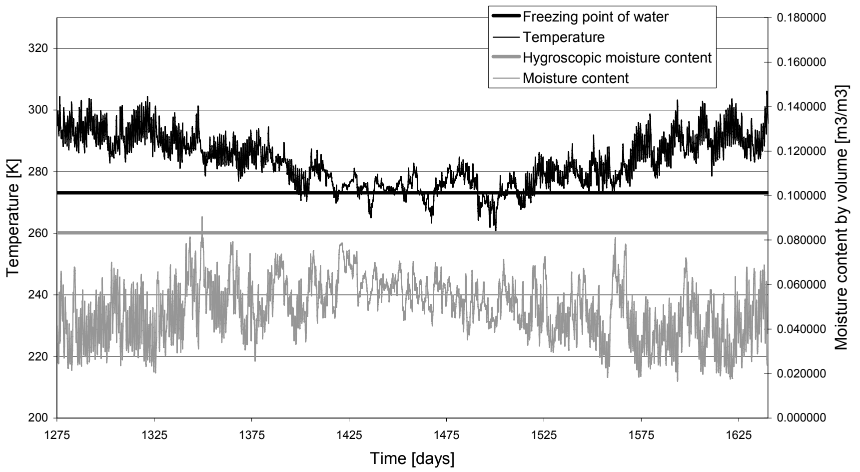

Figure 2: Hygrothermal performance of concrete, simple concrete wall (CR), 2 mm under the surface

In concrete modified by fly ash, the overhygroscopic moisture content is reached once per a reference year, but as in the previous case this happens in summer month so there are not any possibilities of creation of freezing cycles.

In other types of concrete the overhygroscopic moisture content is not reached at all.

Concrete wall without thermal insulation system

If we consider concrete wall provided only by plasters, the worst material combination is to use reference concrete without any modifications. This material combination leads to creation of two freezing cycles in exterior plaster. The cycles took 2 and 13 hours and arisen in 325th and 326th day of reference year (Figure 4). Other types of concrete do not give suitable conditions for freezing of water.

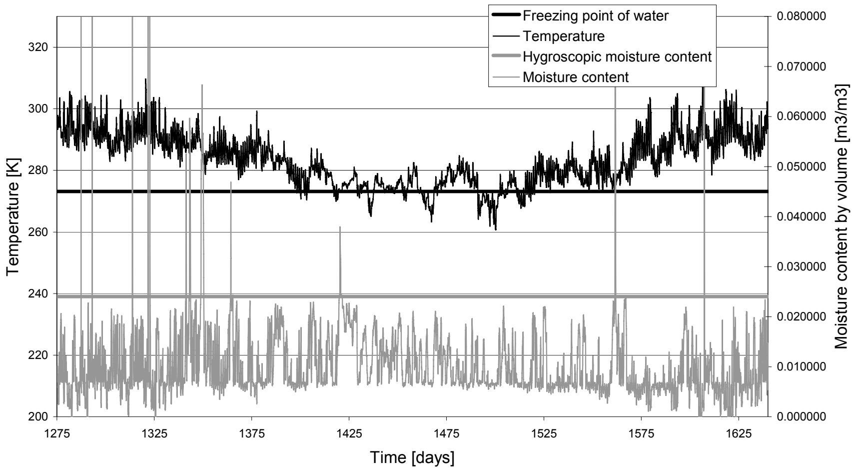

Figure 3: Hygrothermal performance of exterior plaster, concrete wall (CR) provided by exterior plaster, 2 mm under the surface

In all cases, the water contained in concrete does not get frozen. All the results are similar to result on Figure 5.

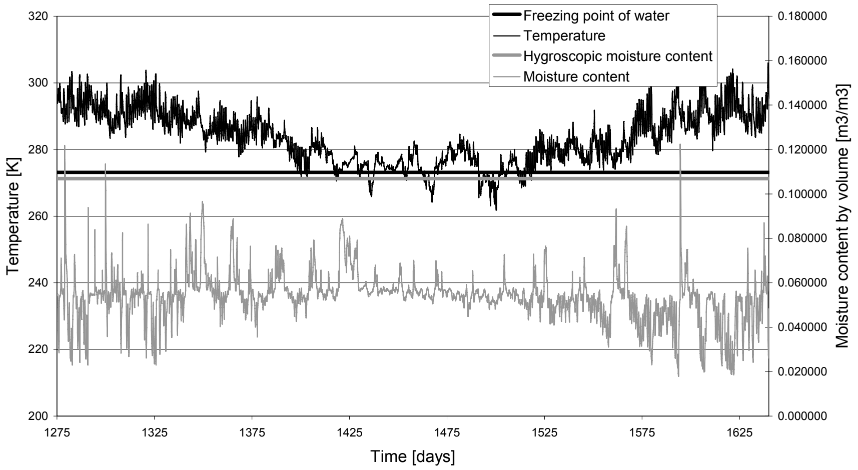

Figure 4: Hygrothermal properties of concrete, concrete wall (CM) provided by exterior plaster, 2 mm from material interface

Concrete wall provided with thermal insulation system

EPS as the insulation material provided with plaster reliably keeps the concrete wall from effects of freezing cycles no matter which type of concrete is under consideration.

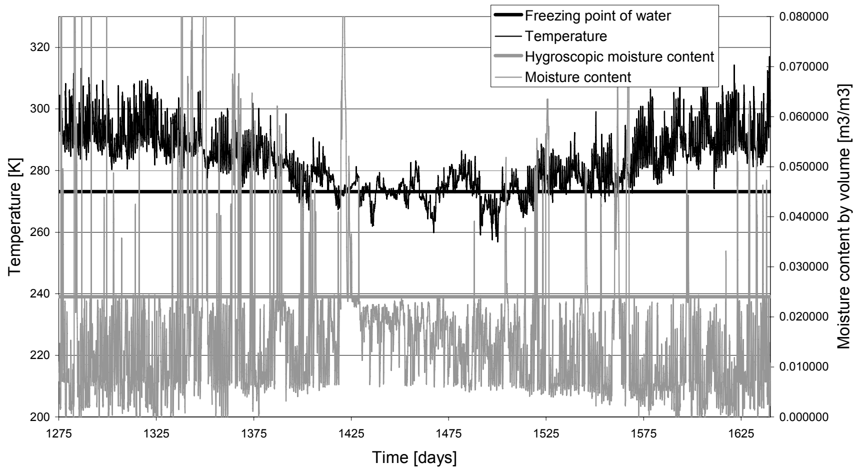

Figure 5: Hygrothermal performance in exterior plaster, concrete wall (CS) provided by EPS with exterior plaster, 2 mm under the surface

Nevertheless, disadvantage of this material combination lies in abnormal strain of exterior plaster caused by weather conditions. In the simulation we counted more than 25 freezing cycles in every material combination in exterior plaster per reference year (Figure 6).

Duration of freezing cycles is different. The longest one takes 36 hours, the shortest one only 1 hour. Single cycles are separated by tiny temperature or moisture fluctuations which raise their final number.

Mineral wool has the same effect as EPS and protects the concrete wall from increase of moisture content and decrease of temperature at the same time. This prevents water in the wall getting overhygroscopic and getting frozen. Anyway, exterior plaster applied on mineral wool is abnormally exposed too. The number of freezing cycles during one reference year is little bit smaller then in plaster applied on EPS and counting about 25 cycles in every material combination (Figure 7).

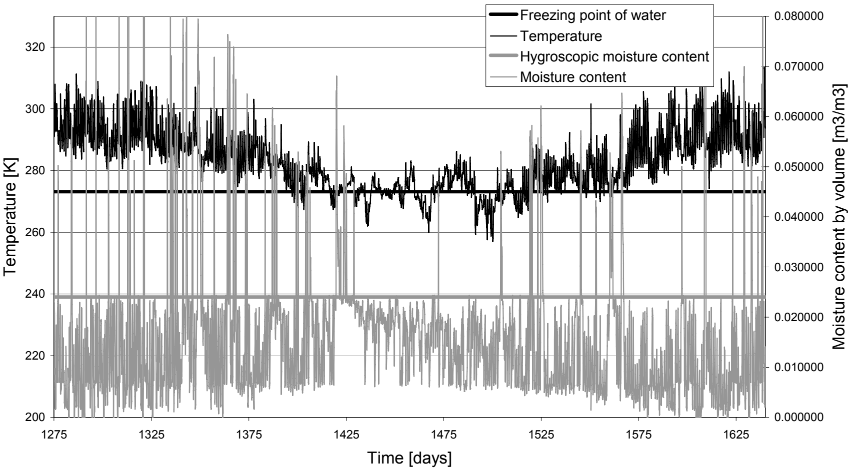

Figure 6: Hygrothermal performance in exterior plaster, concrete wall (CF) provided by mineral wool with exterior plaster, 2 mm under the surface

As we can see, the cycles are separated by tiny moisture and temperature fluctuations, too.

Discussion

In an assessment of the impact of freezing cycles on service life of exterior renders, it is not enough to consider only the frost resistance determined in the laboratory. It is important to realize, that the number of freezing cycles depends on material combination, not only on material characteristics of used materials. As important as the freezing cycles' time is the lag between two cycles. If the freezing cycles' time is too short, water can not solidify into ice and can not disrupt the structure of plaster. By the same token, if the lag between two cycles is too short, ice can not melt back into water and then refreeze again, so its destruction effect can be neglected and we can consider both as one.

When we evaluate the number of freezing cycles taking these considerations into account, we get new number of freezing cycles which is reduced (Table 5).

Table 5: Number of freezing cycles after reduction

	LCP	CF	CM	CS	CR	EPS	MW	LPMH
Simple concrete wall	-	0	-	-	-	-	-	-
	-	-	0	-	-	-	-	-
	-	-	-	0	-	-	-	-
	-	-	-	-	0	-	-	-
Concrete wall provided with exterior plaster	0	0	-	-	-	-	-	0
	0	-	0	-	-	-	-	0

	0	-	-	0	-	-	-	0
	0	-	-	-	0	-	-	2
Concrete wall provided with EPS and exterior plaster	0	0	-	-	-	0	-	20
	0	-	0	-	-	0	-	20
	0	-	-	0	-	0	-	19
	0	-	-	-	0	0	-	20
Concrete wall provided with mineral wool and exterior plaster	0	0	-	-	-	-	0	20
	0	-	0	-	-	-	0	21
	0	-	-	0	-	-	0	19
	0	-	-	-	0	-	0	21

In this computer simulation only the liquid moisture appearance caused by rain was considered. However, there can be locations on building, which are exposed to water originating from other sources. This can be the case of a socle part of building and places with bad construction details solution. In these cases, the number of freezing cycles during one year could be much higher.

Although simple concrete wall built from all the types of investigated concrete does not show indications of freezing of the contained moisture, the wall made from reference concrete is very close to it. As we considered only reference year which is based on long-term average of relative humidity and temperature, the freezing cycles cannot be completely excluded in every particular year; in real weather conditions deviations from the average values may appear which could lead to creation of some freezing cycles. Basically, this is caused by the lowest value of moisture diffusivity of reference concrete which does not allow for a relatively fast release of contained moisture.

Considering the wall provided with exterior plaster only, the reference concrete gives us the worst results again. There are some freezing cycles in all types of concrete, however water contained in exterior plaster applied on reference concrete gets frozen twice a reference year. This determines the service life of plaster approximately to 15 years. In rest of cases, damage caused by weather conditions is not the main cause of degradation.

If we investigate concrete wall provided with thermal insulation system, namely EPS or mineral wool, due to propitious thermal insulating properties the temperature in the concrete will never drop below zero which makes freezing of water impossible. However, both materials of thermal insulation have very low value of moisture diffusivity. Therefore, the moisture can not be transported to concrete in sufficient amount and its level remains relatively high for long time. Pull of low temperature causes then freezing of this water. Surface layer (2 mm) of exterior plaster will resist only for 2 years. But overall thickness of the plaster is 5 mm, so the service life could be doubled.

Conclusions

Comparing all the results obtained in this paper, from the point of view of frost resistance the best option is to use concrete modified by fly ash. Although in most of cases, concrete is not the material which will be damaged by freezing of water, its type has still relatively high influence on service life of other materials of the wall, renders in particular.

Nowadays, most of concrete buildings are provided with thermal insulation. Based on results of this simulation, more advantageous is to use EPS, but the differences between EPS and mineral wool are not too high. So, the sole criterion of water freezing in the exterior render is not the decisive one for a choice of thermal insulation material.

Acknowledgement

This research has been supported by the Czech Ministry of Education, Youth and Sports, under project No MSM 6840770031.

References

[1] VEJMELKOVÁ E. and ČERNÝ, R., 2008, Application of Alternative Silicate Binders in the Production of High Performance Materials Beneficial to the Environment. Proceedings of the 2008 World Sustainable Building Conference [CD-ROM]. Balnarring, Victoria: ASN Events Pty Ltd.: 520-525.

[2] PERNICOVÁ R. et al., 2007, Vliv metakaolinu na mechanické, tepelné a vlhkostní vlastnosti vápenných omítek. Metakaolin 2007. Brno: VUT FAST, 2007: 70-77.

[3] KŰNZEL H.M., 1995, Simultaneous Heat and Moisture Transport in Building Components, Ph.D. Thesis. IRB Verlag, Stuttgart.

Analysis of water vapour sorption process in static dessicator method

Peter Matiasovsky[1], Zuzana Takacsova[2]

[1] Institute of Construction and Architecture, Slovak Academy of Sciences, Dubravska cesta 9, Bratislava, Slovakia, e-mail: usarmat@savba.sk

[2] Slovak Technical University, Faculty of Civil Engineering, Radlinskeho 11, 813 68 Bratislava, Slovakia

Abstract: *The specimens of characteristic interior finish materials were placed in static dessicators to obtain the sorption isotherms. The time courses of water vapour adsorption/desorption for particular specimens were measured by gravimetric method in weekly intervals. An analytical solution of the diffusion equation describing the sorption process was applied in an analysis of the obtained results. A possibility to determine water vapour transport parameters, like the sorption capacity and the surface transport coefficient, from the sorption courses was given by the actual boundary conditions, defined by the Biot number. The dynamics of the sorption process in the static dessicators is determined by very low values of the effective surface water vapour sorption coefficient given by a decrease of the water vapour diffusion rate through the dessicator plate, with a smaller surface transfer at high relative humidities.*

Keywords: *Water vapour sorption, equilibrium moisture content, dessicator method*

1. Static dessicator method

The dessicator method is a standard technique to obtain equilibrium moisture contents of porous materials placed in vacuum dessicators. The dessicator (figure 1) is a jar divided into two spaces: the lower containing the saturated salt solution maintaining a required relative humidity and the upper where the tested material specimens are placed. The spaces are

Figure 1: Vacuum dessicators with various salts saturated solutions

Figure 2: Ceramic dessicator plate

separated by a perforated ceramic plate (figure 2). The perforations have a circular form and their surface area represents only 5 % of the plate as a whole. During the sorption process the water vapour diffuses between the upper and lower spaces and the rate of the diffusion is determined by the water vapour permeability of the ceramic plate.

The water vapour sorption isotherms at 20°C temperature were measured by the static dessicator method. The samples were placed in sealed dessicators containing saturated solutions of the salts: $LiCl.H_2O$, $CaCl_2.2H_2O$, $NaBr.2H_2O$, $NaCl$ and KNO_3, maintaining the atmospheres of 32 %, 60 %, 75 % and 95 % relative humidities respectively. The equilibrium moisture content was determined by the gravimetric method.

2 Sorption process

A 1D water vapour sorption process in a material can be described by the diffusion equation in the form:

$$\frac{\partial c}{\partial t} = \frac{D}{\mu\sigma} \cdot \frac{\partial^2 c}{\partial x^2} \tag{1}$$

where: c is the concentration of water vapour in the air of pores ($kg.m^{-3}$), s is the amount of adsorbed water in the volume of material ($kg.m^{-3}$), D is the diffusion coefficient of water vapour in air ($m^2.s^{-1}$), t is the time (s), μ is the diffusion resistance factor (-) and $\sigma$is the moisture capacity [1]:

$$\sigma = \frac{M_\infty}{V \cdot c_s \cdot \Delta\varphi} \tag{2}$$

where: V is the volume of specimen (m^3), c_s is the concentration of saturated water vapour ($kg.m^{-3}$), M_∞ is the difference of material equilibrium moisture contents (kg), $\Delta\varphi$ is the change the air relative humidity (-).

The moisture capacity σ is determined from the difference of equilibrium moisture contents of the specimen at the beginning and at the end of the sorption process and from the difference of the ambient relative humdities, defining the humidity step. The experiments were performed for the following sequences of humidity steps: 0 → 32 → 95 → 32 %, 0 → 60 → 95 → 60 % and 0 → 75 → 90 → 75 % and 12 materials: lime-cement and lime-gypsum mortars, gypsum plates and wooden materials were tested.

2.1 Analytical solution

The solution of equation (1) for the specimen of the thickness d under the constant initial conditions and the boundary conditions of the third kind has the form [2]:

$$M(t) = M_\infty \left\{ 1 - \sum_{n=1}^{\infty} \frac{2Bi^2}{\pi_n^2 \left(Bi^2 + Bi + \pi_n^2 \right)^2} \exp\left(-\frac{\pi^2 D}{\mu \cdot \sigma \cdot d^2} t \right) \right\} \tag{3}$$

The eigenvalues ◎n are calculated from the solution of the transcendent equation, expressing the relationship between Biot number Bi and ◎n, considering the same boundary conditions on both surfaces:

$$\tan \pi_n = \frac{2\pi_n \cdot Bi}{\pi_n^2 - Bi^2} \tag{4}$$

where the Biot number is equal to:

$$Bi = \frac{\beta \cdot d \cdot \mu}{D} \tag{5}$$

where is ◎ the surface film water vapour transfer coefficient.

2.2 Solution for small Biot numbers

If Bi ◎ 0, or < 0.1 in practice, the adsorption process is controlled by the surface film water vapour transfer and all terms of the sum for n > 1 can be neglected. The time course of the adsorbed water vapour mass increase has then the exponential character with the ultimate value M_∞.

$$M(t) = M_\infty \left\{ 1 - \exp\left[-\frac{\beta \cdot S \cdot V \cdot c_s \cdot \Delta\varphi}{M_\infty} \cdot t \right] \right\} \tag{6}$$

The logarithm of function (6) has a linear character:

$$\ln\left(1 - \frac{M(t)}{M_\infty} \right) = -\left[\frac{\beta \cdot S \cdot V \cdot c_s \cdot \Delta\varphi}{M_\infty} \right] \cdot t \tag{7}$$

Knowledge of the tangent of function (7) enables to determine the surface water vapour transfer coefficient ◎ from the water sorption course.

3 Results

The measured adsorption and desorption courses for the parallelepiped shape specimens with the dimensions of 0.1 x 0.1 x 0. 02 m were analysed. At given dimensions the specimens, and under the assumption that the effective surface film water vapour transfer coefficients in dessicators are decreased by the perforated plates, the specimens were considered as the infinite plates and the sorption process could be solved as 1D problem with use of solution (7).

In figures 3 – 4 there is an example of the adsorption and desorption time courses and their logarithms for chosen lime-cement plaster after 35 ◎ 95 % and 35 ◎ 95 % relative humidity changes. All analysed time courses of sorption could be expressed as the exponential functions.

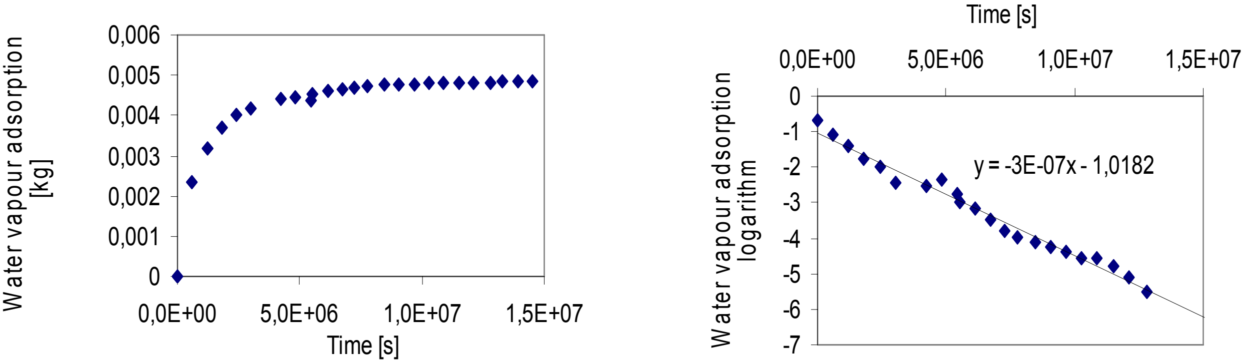

Figure 3: Exponential adsorption time course – lime-cement plaster, 32 ✈ 95 % relative humidity change

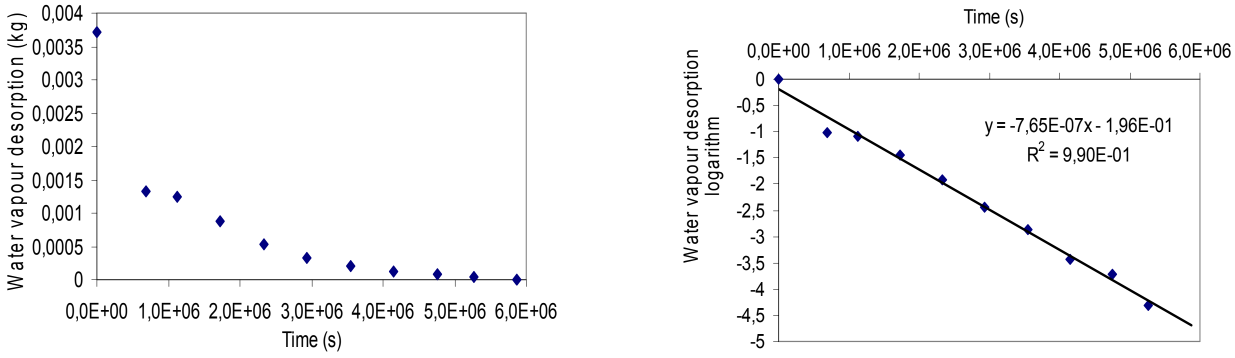

Figure 4: Exponential desorption time course – lime-cement plaster, 95 ✈ 32 % relative humidity change

From the logarithms of the sorption courses the exponents, expressing the speed of sorption process, were determined. The inverse values of the exponents represent time constants of the process. The sorption time constant is defined as the value reaching the 63 % of the ultimate moisture change. In figure 5 there is a distribution of the occurrence of the time constant values for all analysed materials. The most frequent values lie in interval 0 - 30 hours that means the sorption experiments lasted approximately 1 – 3 months. The great values, more than 50 hours, were observed for the gypsum and wooden materials. In a case of gypsum materials the time constants were high during desorption. This phenomenon can be explained by the hydration changes, typical for these materials. The woods have a large time constants in general, which is given by their moisture capacities.

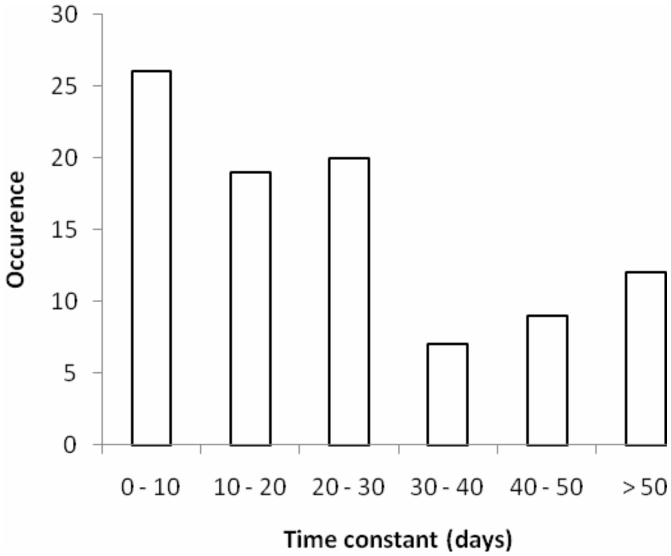

Figure 5: Distribution of sorption time constants occurrence

The surface water vapour transport coefficients were determined from the known sorption exponents. The most frequent values are in the interval with the order of magnitude 1.10-5 m.s-1. These values correspond to the values usual under laboratory free convection conditions reduced by the factor of 0.05 – due to the barrier represented by dessicator plate. The higher values, of the order of magnitude 1.10-6 m.s-1, correlate with the high - 75 and 95 % relative humidities.

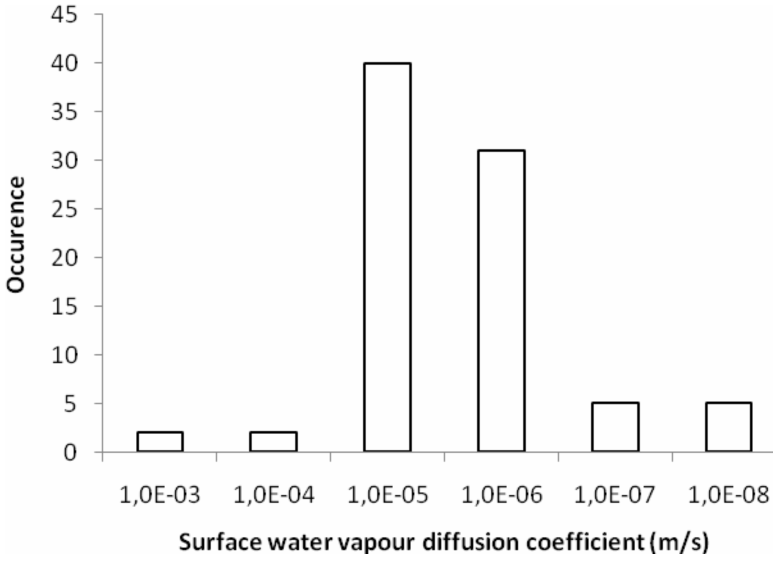

Figure 6: Distribution of surface water vapour diffusion coefficients occurrence

4. Conclusions

The dynamics of water vapour sorption process in a vacuum dessicator is determined by the surface water vapour diffusion coeficient between the dessicator environment and the sample.

The surface water vapour diffusion coefficient values in dessicators can be identified from the exponential curve of a sorption in time. Long sorption times are given by the surface water vapour diffusion coefficients smaller than in laboratory free convection conditions. Their values are equal or lower than 1.10^{-5} $m.s^{-1}$.

The dynamics of water vapour sorption process in a vacuum dessicator can be evalueated by the time constants of the process. The most frequent values lie in the interval 0 – 30 hours. Higher values are typical for gypsum and wooden materials.

Acknowledgement

Authors wish to thank the APVT-51-030704 and APVV-0744-07 projects for the financial support of this work.

References

[1] KUENZEL H. M.; Kiessl K. Bestimmung des Wasserdampfdiffusionwiederstandes von mineralischen Baustoffen aus Sorptionsversuchen. In Bauphysik. 1990. 12(5) p. 140-144. ISSN 0171-5445

[2] LUIKOV A. V, Heat-Conduction Theory [in Russian], Vysshaya Shkola, Moscow, 1967. 2-3-5/64-65-6.

[3] MATIASOVSKY P.; Bagel L. Compatibility of BET nitrogen and water adsorption/desorption isotherms of interior plasters. In Proceedings of 4th International Building Physics Conference/Editors Bayazit N.T.; Manioglu, G.K. Yilmaz Z. Istanbul, Technical University Istanbul. p. 11-16. ISBN 978-975-561-350-5

A statistical mechanical description of phases and first-order phase transitions

Igor Medveď

Department of Physics, Constantine the Philosopher University, Tr. A. Hlinku 1, 949 74 Nitra, Slovakia

Abstract: *We briefly review the Pirogov-Sinai theory that allows one to rigorously study phases and first-order phase transitions from a statistical mechanical point of view. We wish to demonstrate that it is a powerful tool that may be used in various applications from materials physics to physical chemistry and biology.*

Keywords: *Phase, phase transition of first order, Pirogov-Sinai theory*

1 Introduction

Phase transitions are intriguing phenomena that we often met in practice. The melting of solids, dehydroxylation in kaolinite, $\alpha \rightarrow \beta$ transition in quartz, condensation of gases, phenomena of ferromagnetism and antiferromagnetism, order-disorder transitions in alloys, or transition from a normal to a superconducting material are all examples of phase transitions.

There are basically two ways to describe phase transitions. First, one says that a phase transition occurs if thermodynamic functions have discontinuities or singularities. If it is a discontinuity in the first derivative of a thermodynamic potential (such as specific energy e, magnetization m, or density ρ), the *phase transition* is *of first order*; we will focus on this type of phase transition in the following. Second, one says that a phase transition occurs if there is a macroscopic instability with respect to boundary conditions: keeping, for instance, the temperature and pressure of a system constant, a change in the external conditions leads to dramatic changes in macroscopic quantities (like e, m, or ρ). Thus, changing forces acting near the boundary (that is small with respect to the system volume) causes a change in the macroscopic state of the system. Under such conditions, the free energy (and/or other boundary-condition *in*dependent thermodynamic functions) cannot be a smooth function.

However, the proof of existence of phase transitions in realistic systems at the microscopic level is still an open problem, although the procedure is in principle clear. Indeed, it should basically run as follows. Consider a system of N interacting particles with the Hamiltonian of the form,

$$H_N(\vec{r}_1, \vec{p}_1, \ldots, \vec{r}_N, \vec{p}_N) = \sum_{k=1}^{N} \frac{p_k^2}{2m_k} + \sum_{1 \le k < j \le N} U(|\vec{r}_k - \vec{r}_j|), \tag{1}$$

where U is a realistic (e.g., the Lenard-Jones) potential, and its grand-canonical partition function

$$Z_N(V, \beta, z) = \sum_{N=0}^{\infty} \frac{z^N}{N!} \left(\frac{2\pi}{\beta h}\right)^{3N/2} \left(\prod_{k=1}^{N} m_k^{3/2}\right) \int_{V^N} e^{-\beta \sum\limits_{1 \le k < j \le N} U(|\vec{r}_k - \vec{r}_j|)} d^{3N} r, \tag{2}$$

where h is the Planck constant and $\beta = 1/kT$ (with k being the Boltzmann constant and T being the temperature). Suppose we wish to study a liquid-vapor transition in the system. Then we need to show that the density

$$\rho(\beta, z) = z \frac{\partial}{\partial z} \lim_{V \to \infty} \frac{1}{V} \log Z_N(V, \beta, z) \tag{3}$$

has a jump at some value $z = z(\beta)$, providing β is sufficiently large (T is small). It has turned out that this simply formulated problem is in fact extremely hard to solve.

In this paper we briefly describe a statistical mechanical approach that allows one to rigorously prove the existence of first-order phase transitions and study them in quite a detail.

2 Lattice models

Since it is hard to study phase transitions in realistic systems, one instead considers models that are simpler: on the one hand, they can be studied to a reasonable extent; on the other hand, they are non-trivial (they can exhibit a phase transition). A common type of such simple models are *lattice models*. In them particles lie at sites of a regular lattice in space and cannot move. Thus, there are no momentum variables, and the Hamiltonian contains only a potential energy. Usually, one uses a pair potential that decays sufficiently fast at infinity; most often it is just of a finite range.

The simplest lattice model that exhibits phase transitions is the standard *Ising model* [1]. It was introduced to crudely simulate the structure and behavior of a (domain in a) magnet. Each particle of the model can be in only two states: it has “spin up” (denotes as +) or “spin down” (denoted as –), see Fig. 1(a). The interaction is limited to nearest neighbors with an interaction potential ϕ such that either $\phi = -1$ (+1), say, if the neighboring spins are equal (unequal), or $\phi = +1$ (–1), say, if the neighboring spins are equal (unequal). The former case corresponds to a ferromagnet, while the latter one to an antiferromagnet. Equivalently, the model may be interpreted as corresponding to a one-component lattice gas (simulating a binary alloy, for instance), in which case the two states of a particle at a site x are “particle occupies x” and “x is vacant”, see Fig. 1(b).

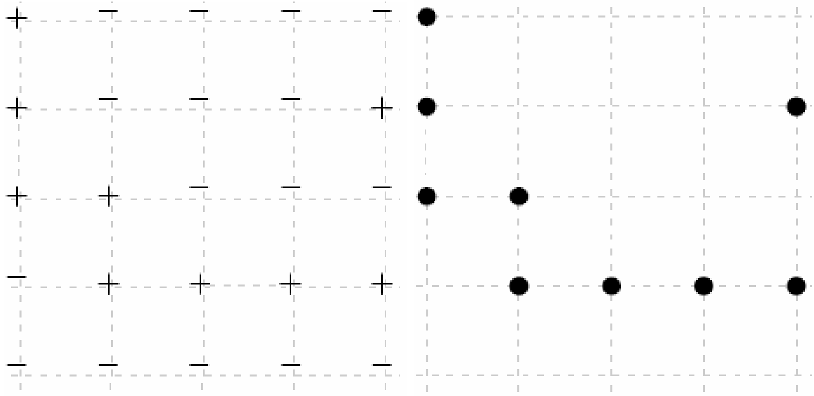

(a) (b)

Figure 1: The Ising model on a square lattice representing (a) a magnet, (b) a lattice gas

Since its introduction in 1925 the Ising model and its various modifications have been used in many practical applications. To name few of the latest ones, let us mention that it served as a model of a mixed ferromagnetism and antiferromagnetism for Fe-Cr steel [2], $LiHoF_4$ magnetic material [3], antiferromagnet dysprosium pyrogermanate ($Dy_2Ge_2O_7$) [4], ferromagnetic-to-paramagnetic phase transition of $La_{0.75}Sr_{0.25}MnO_3$ [5], Fe-Al alloys [6], or alloys in general [7].

At sufficiently low temperatures the standard ferromagnetic Ising model undergoes a first-order phase transition. The corresponding jump is in the magnetization as an external magnetic field H changes across $H = 0$ (i.e., the system is spontaneously magnetized at $H = 0$). This may be proved by the famous *Peierls argument* [8]: one shows that a macroscopic instability occurs by using a geometric language of *contours* as follows. A microscopic configuration of spins on a lattice corresponds to one collection of contours that represent the (connected components of the) boundaries separating the regions of plus and minus spins. In other words, contours represent energetic barriers between the plus and minus regions. Then it is quite straightforward to show that if the spins external to the system are fixed to be all pluses (minuses), then a spin inside the system is very likely to be also plus (minus), provided T is sufficiently small [9].

Another often used example of a lattice model is the *Potts model*. In a sense it is a generalization of the Ising model from two to $q \geq 2$ spins. Thus, a particle at a site x has a "spin" σ_x that attains one of the values 1, 2, …, q. The interaction is again limited to nearest neighbors and, for the ferromagnetic case, the interaction potential $\phi = -1$, say, if the spins are equal, whereas $\phi = 0$, say, if the spins are unequal. It is known that this model exhibits, for q large, a first-order phase transition at some $\beta = \beta_t$, with q ordered phases coexisting for $\beta \geq \beta_t$ (at low T) and one disordered phase existing for $\beta \leq \beta_t$ (at high T). The notion of contours is again very useful is arriving at this conclusion. Out of the many latest applications of the Potts model we may mention the modeling of ferromagnetic Ni-Mn-X alloys (X = In, Sn, Sb) [10], ice I (ordinary ice) [11], texture formation during electrodeposition processes [12], texture-controlled grain growth during annealing [13], grain growth in materials [14], solid-state sintering of powder compacts [15], or nanoparticle sintering [16].

3 Pirogov-Sinai theory

A generalization of the Peierls argument and of the language of contours for studying lattice models was done by Pirogov and Sinai [17]. Their theory has been broadly extended since (see [18] for the references on this issue). The *Pirogov-Sinai theory* became a very convenient tool especially in the situations when no symmetry-related techniques can be used. It is a perturbative theory (the perturbations are carried out around ground states) in which microscopic configurations are represented geometrically as regions of ground states separated by boundaries (see Fig. 2(a)), i.e., by contours that correspond to energetic barriers. The main results of the theory may be briefly summarized as follows.

A low temperature *phase* typically looks as a perturbation of the ground states: it is a "see" of a ground state with "islands" of non-ground states. A linear size of the islands is ~log L, where L is a linear size of the system. The islands are spread around with a volume density that is not zero but of the order $e^{-\beta}$. Therefore, a phase typically looks as is depicted in Fig. 2(b) and not Fig. 2(a). In addition, each ground state gives rise to only a single low temperature phase (a one-to-one correspondence between the ground states and phases).

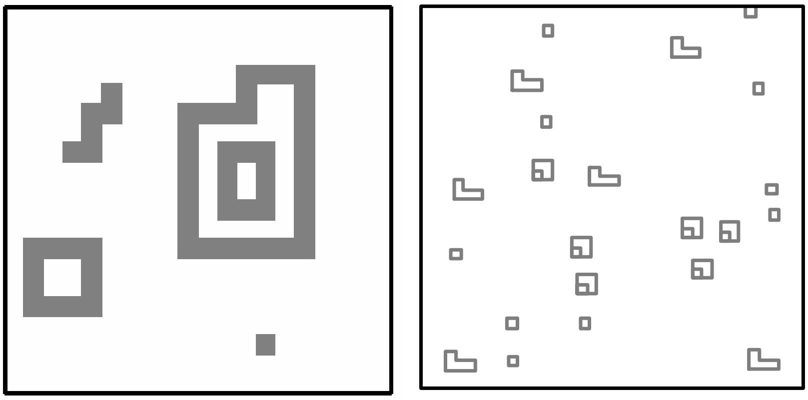

(a) (b)

Figure 2: Schematic pictures of contours (gray) separating ground state regions (white): (a) possible contours, (b) typical contours at low T

The Pirogov-Sinai theory also enables one to construct low temperature *phase diagrams* of the models. It is able to introduce "meta-stable" free energy densities f_n for each phase $n = 1, \ldots, N$. By comparing the densities f_n the phase diagram can be obtained (analogously to a ground state diagram that is obtained by comparing energy densities e_n). Thus, if f_n is minimal of all N free energy densities, the n-th phase is stable (for given values of thermodynamic parameters). The coexistence of two or more phases occurs at those points or lines/surfaces, where several phases are stable (two or more free energy densities are minimal). In addition, since free energy densities f_n are very close to the ground state energy densities e_n (the difference being of the order $e^{-\beta}$), the phase diagram is only a small ($\sim e^{-\beta}$) deformation of the ground state diagram.

Finally, the theory enables us to detect *phase transitions*. Starting from the observation that the true free energy density f is equal to the minimum of all "meta-stable" free energy densities, $f = \min\{f_1, \ldots, f_N\}$, it immediately follows that, for example, across a coexistence line of phases n and m the one-sided derivatives of f do not coincide, $f'_- = f_n' \neq f_m' = f'_+$, implying that a first-order phase transition takes place here.

By now there are several puzzling problems to which the Pirogov-Sinai theory has been successfully applied, such as the finite-size effects (the details of the rounding of the phase transition discontinuities and singularities) or the Lee-Yang zeros of partition functions (see references given in [18] for more details). The models that are covered by the theory include, besides the standard Ising and Potts model, many other models with a finite-range potential and even quantum perturbations of classical models, systems with continuous spins, and continuous systems. There are actually only three basic conditions under which the theory is applicable: (i) sufficiently low temperatures, (ii) finite number of ground states, and (iii) contours (i.e., the boundaries between ground states) represent sufficiently high energetic barriers so that the energy of a contour is proportional to the contour size (the Peierls condition). The last condition can be verified directly or sometimes by the method of an m-potential [19]. Although the theory applies rather generally to a large number of systems, the introduction of contours is basically a model dependent problem (even for a given model one may use several types of contours according to the properties to be studied). Nevertheless, there are canonical prescriptions how contours may be constructed.

3.1 Our results

We have recently applied the Pirogov-Sinai theory to study first-order phase transition spikes in the current density vs. electric potential plots of underpotential deposition (UPD). This is the deposition of a metal ion on an electrode made from a different, more noble metal (for example, Cu on Au or on Pt) at electric potentials larger than the equilibrium Nernst potential (at which a bulk deposition occurs). Under these conditions only a (sub)monolayer is deposited (no bulk deposition takes place), and ordered phases commensurate with the electrode surface structure are often observed. Thus, it is appropriate to simulate the deposition process by the behavior of a two-dimensional lattice-gas model. In our studies [20-24], we provided relations of macroscopic quantities (the spike area, position, width, asymmetry) to microscopic quantities (the interaction energies between ions). Our theory of UPD spikes is based on the finite-size effects.

We also used the Pirogov-Sinai theory to study chiral segregation in two dimensional molecular systems (on thin layers). Chiral segregation occurs in an equimolar mixture of a chiral molecule and its mirror image whenever two phases are formed, each containing the molecules of only one chiral type (without using an external preference of either chiral type). It is often required in practice to maintain control over chirality of molecular systems and produce molecules of a specific chiral type. Using the Pirogov-Sinai theory, we showed that chiral segregation can occur in two-dimensional systems of simple (tetrahedral) chiral molecules within a suitable range of intermolecular interactions [25, 26].

Acknowledgment

This work was supported by the grants VEGA 1/0302/09 and VEGA 1/0216/09 and by the FCVV Initiative of the Constantine the Philosopher University under grant I-06-399-01.

References

[1] ISING, E. Beitrag zur theorie des ferromagnetismus. Z. Phys. 1925. 31. p. 253.

[2] ACKLAND, G. J. Ordered sigma-type phase in the Ising model of Fe-Cr stainless steel. Phys. Rev. B. 2009. 79. p. 094202.

[3] TABEI, S. M. A.; GINGRAS, M. J. P.; KAO, Y.-J.; YAVORSKII, T. Perturbative quantum Monte Carlo study of LiHoF4 in a transverse magnetic field. Phys. Rev. B. 2004. 70. p. 144411.

[4] KE, X.; DAHLBERG, M. L.; MOROSAN, E.; FLEIRMAN, J. A.; CAVA, R. J.; SCHIFFER, P. Magnetothermodynamics of the Ising antiferromagnet Dy2Ge2O7. Phys. Rev. B. 2008. 78. p. 104411.

[5] KIM, D.; ZINK, B. L.; HELLMAN, F. Critical behavior of La0.75Sr0.25MnO3. Phys. Rev. B. 2002. 65. p. 214424.

[6] AGUIRRE CONTRERAS, W. R.; ZAMORA, L. E.; PÉREZ ALCÁZAR, G. A.; PLASCAK, J. A. Magnetic properties of Fe-Al alloys through Ising and Heisenberg models with a nonlinear exchange interaction. Phys. Rev. B. 2005. 72. p. 052402.

[7] BLUM, V.; HART, G. L. W.; WALORSKI, M. J.; ZUNGER, A. Using genetic algorithms to map first-principles results to model Hamiltonians: Application to the generalized Ising model for alloys. Phys. Rev. B. 2005. 72. p. 165113.

[8] PEIERLS, R. On ising's model of ferromagnetism. Proc. Camb. Phil. Soc. 1936. 32. p. 477.

[9] GRIFFITH, R. B. Peierls proof of spontaneous magnetization in a two-dimensional Ising ferromagnet, Phys. Rev. 1964. 136. p. A 437.

[10] BUCHELNIKOV, V. D.; ENTEL, P.; TASKAEV, S. V.; SOKOLOVSKIY, V. V.; HUCHT, A.; OGURA, M.; AKAI, H.; GRUNER, M. E.; NAYAK, S. K. Monte Carlo study of the influence of antiferromagnetic exchange interactions on the phase transitions of ferromagnetic Ni-Mn-X alloys (X=In,Sn,Sb). Phys. Rev. B. 2008. 78. p. 184427.

[11] MUGURUMA, C.; OKAMOTO, Y.; BERG, B. A. Thermodynamics of two lattice ice models in three dimensions. Phys. Rev. E. 2008. 78. p. 041113.

[12] CAVALCANTI, W.; SANTOS, M.; FIGUEIREDO, W. Growth model with a finite number of orientations on a linear substrate. Phys. Rev. E. 2004. 69. p. 021608.

[13] IVASISHIN, O. M.; SHEVCHENKO, S. V.; VASILIEV, N. L.; SEMIATIN, S. L. 3D Monte-Carlo simulation of texture-controlled grain growth. Acta Mater. 2003. 51. p. 1019.

[14] MULHERAN, P.; HARDING, J. H. A simple statistical model for grain growth in materials. Acta Metall. Mater. 1992. 39. p. 2251.

[15] BRAGINSKY, M.; TIKARE, V.; OLEVSKY, E. Numerical simulation of solid state sintering. Int. Jour. Solids Struct. 2005. 42. p. 621.

[16] QIU, F.; EGERTON, T. A.; COOPER, I. L. Monte Carlo simulation of nano-particle sintering, Powder Technol. 2008. 182. p. 42.

[17] PIROGOV, S.; SINAI, Ya. G. Phase diagrams of classical lattice systems. Theor. Math. Phys. 1975. 25. p. 1185; and Phase diagrams of classical lattice systems. Continuation. Theor. Math. Phys. 1976. 26. p. 39.

[18] KOTECKÝ, R. Phase transitions: on a crossroads of probability and analysis. In Highlights of Mathematical Physics. Providence, American Mathematical Society. 2002. p. 191.

[19] HOLSZTYNSKI, W.; SLAWNY, J. Peierls condition and number of ground states. Comm. Math. Phys. 1978. 61. p. 177.

[20] HUCKABY, D. A.; MEDVEĎ, I. Shapes of voltammogram spikes explained as resulting from the effects of finite electrode crystal sizes. J. Chem. Phys. 2002. 117. p. 2914.

[21] MEDVEĎ, I.; HUCKABY, D. A. Voltammogram spikes interpreted as envelopes of spikes resulting from electrode crystals of various sizes: Application to the UPD of Cu on Au(111). J. Chem. Phys. 2003. 118. p. 11147.

[22] MEDVEĎ, I.; HUCKABY, D. A. A statistical mechanical study of current spikes due to phase transitions at electrode-electrolyte interfaces. J. Stat. Phys. 2007. 129. p. 335.

[23] MEDVEĎ, I. A formula for the profile of voltammogram spikes in the quasistatic regime. J. Chem. Phys. 2008. 129. p. 124701.

[24] MEDVEĎ, I.; HUCKABY, D. A. Phase transitions at electrode-electrolyte interfaces interpreted as a result of finite-size effects. Fluid Phase Equil. In press.

[25] MEDVEĎ, I.; TRNÍK, A.; BELKASRI, A. K.; HUCKABY, D. A. Low temperature phases of the Andelman–de Gennes model of chiral discrimination: Rigorous results J. Chem. Phys. 2007. 126. p. 154512.

[26] MEDVEĎ, I.; TRNÍK, A.; HUCKABY, D. A. Chiral segregation in three microscopic statistical-mechanical models. Phys. Rev. E. 2009. 80. p. 011601.

Analysis of moisture hysteresis of building materials in hygroscopic range

Peter Mihalka[1]**, Peter Matiasovsky**[1]

[1]Institute of Construction and Architecture, Slovak Academy of sciences, Dubravska cesta 9, SK-845 03, Bratislava, email: usarmipe@savba.sk

Abstract: *The moisture hysteretic behaviour of building materials in a hygroscopic range was investigated. Based on the available main adsorption/desorption curves and primary scanning curves, the functions of the hysteretic factor [2] for investigated materials were treated. Following the hysteretic factor similarity, the parameters of the hysteresis model proposed by [1] were determined.*

Keywords: *Water vapour sorption, hysteresis, hysteretic factor, scanning curves*

Introduction

The differences between adsorption and desorption isotherm are affected mainly by pore structure properties, such as the specific surface area, the pore size distribution and the total porosity. During the drying, less of water is released from the material than water is absorbed during wetting and this phenomenon is called sorption hysteresis. The shape of the sorption curves is similar but the desorption isotherm has higher values of water content than the adsorption isotherm. This phenomenon is called hysteresis. In most of simulation tools, the process of the alternate water vapour adsorption and desorption in building constructions is controlled by one function, usually by the middle of adsorption and desorption isotherms. In a case of hysteretic materials, the process of adsorption and desorption is not the same. The equilibrium moisture content during the desorption process is higher than the moisture content during adsorption at the same relative humidity.

The hysteretic behaviour of some hygroscopic building materials was investigated. Based on hysteretic model parameters and shape of hysteresis loop, the materials were classified into two groups.

Theory

In the hysteretic material the moisture capacity is given the by slope of the scanning sorption curves. The scanning curves always lie between the main adsorption and desorption isotherms, figure 1a. The moisture capacity during scanning is always lower than the moisture capacity of the main adsorption curve and generally it is lower than the moisture capacity of main desorption curve, figure 1b.

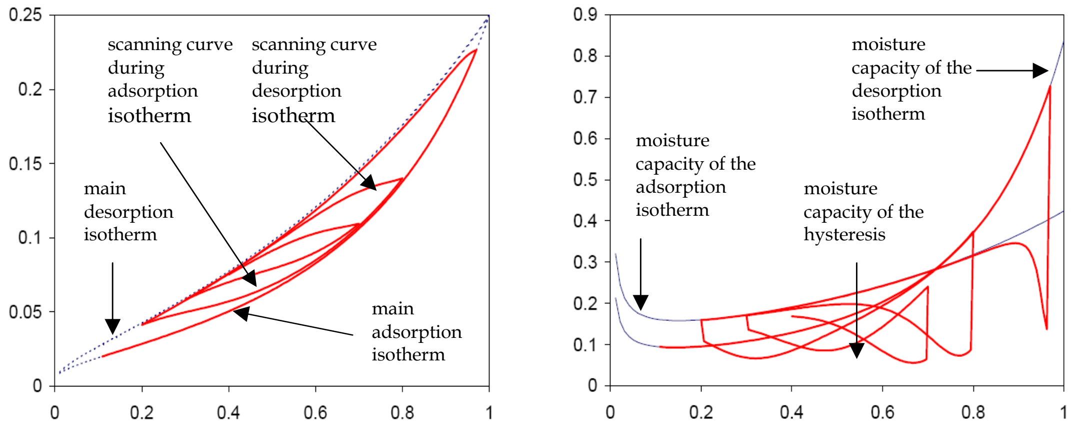

a *b*

Figure 1: Moisture hysteresis. a – scanning curves, b – moisture capacity

A simple empirical model describing the scanning curves was done by Pedersen [1]. In this model the moisture capacity in the hysteresis region is represented by the slope of the scanning curves:

During adsorption:

$$\xi_{hys} = \frac{\gamma_a \cdot (u - u_{adsorption})^A \cdot \xi_{desorption} + (u - u_{desorption})^A \cdot \xi_{adsorption}}{(u_{desorption} - u_{adsorption})^A} \tag{1}$$

During desorption:

$$\xi_{hys} = \frac{(u - u_{adsorption})^D \cdot \xi_{desorption} + \gamma_d \cdot (u - u_{desorption})^D \cdot \xi_{adsorption}}{(u_{desorption} - u_{adsorption})^D} \tag{2}$$

where

ξ_{hys} – the moisture capacity (slope of scanning curve) at given relative humidity

u – the water content (kg/kg)

$u_{adsorption}$ – the water content calculated from main adsorption isotherm (kg/kg)

$u_{desorption}$ – the water content calculated from main desorption isotherm (kg/kg)

$\xi_{adsorption}$ – the moisture capacity at given relative humidity calculated from main adsorption isotherm

$\xi_{desorption}$ – the moisture capacity at given relative humidity calculated from main desorption isotherm

γ_a, A – the parameters of hysteresis during adsorption

γ_d, D – the parameters of hysteresis during desorption.

Originally [1], parameters A and D = 2.0, γ_a and γ_d = 0.1 were proposed. The analysis of a previous work [4], [5], [6] and [7] shows the different values for the different hygroscopic building materials.

The water content during scanning between the equilibrium adsorption and desorption can be approximated as:

$$u = u_o + \xi_{hys} \cdot \Delta\varphi \tag{3}$$

or:

$$u = u_o + \Delta\varphi \cdot \left(\frac{\gamma_a \cdot (u - u_{adsorption})^A \cdot \xi_{desorption} + (u - u_{desorption})^A \cdot \xi_{adsorption}}{(u_{desorption} - u_{adsorption})^A} \right) \tag{4}$$

$$u = u_o + \Delta\varphi \cdot \left(\frac{(u - u_{adsorption})^D \cdot \xi_{desorption} + \gamma_d \cdot (u - u_{desorption})^D \cdot \xi_{adsorption}}{(u_{desorption} - u_{adsorption})^D} \right) \tag{5}$$

Chatterjee [2] proposed hysteretic factor, which describes the ability of the material to have the hysteretic behaviour.

$$f(\varphi) = \frac{u_{sat} - u_{desorption}(\varphi)}{u_{sat} - u_{adsorption}(\varphi)} \tag{6}$$

where:

$f(\varphi)$ – the hysteretic factor at given relative humidity (-)
u_{sat} – the saturated moisture content (kg/kg)
$u_{adsorption}(\varphi)$ – the moisture content from adsorption isotherm (kg/kg)
$u_{desorption}(\varphi)$ – the moisture content from desorption isotherm (kg/kg).

Results

Based on available measured main adsorption, desorption and scanning curves, the parameters of the described hysteresis model were approximated. The optimal parameters for the analysed hygroscopic materials for different scanning ranges are listed in table 1.

Table 1: Optimal parameters of the used hysteresis model

Material	Scanning range	Adsorption		Desorption	
		◎a	A	◎d	D
Concrete wc=0,55, 2300 kg/m3 [3]	90%◎45%, 43%◎95%	0.8	2.0	0.1	2.0
Cellular concrete 510 kg/m3 [3]	43%◎91%	0.75	1.05	-	-
Cellular concrete 500 kg/m3 [6]*	94%◎12%	-	-	0.97	2.0
	75%◎12%	-	-	0.87	2.0
Lightweight concrete 640 kg/m3 [3]	44%◎95%	0.40	2.0	-	-
Sandstone 1700 kg/m3 [3]	94%◎65%	-	-	0,6	2,0
Sandstone 1800 kg/m3 [3]	43%◎85%, 98%◎20%	0.60	2.0	0.9	2.0
Sandstone 1830 kg/m3 [3]	43%◎95%	0.70	2.0	-	-

Gypsum board [4]*	79,5%◎33%	-	-	0.68	1.6
Asbestos cement [3]	95%◎40%, 40%◎95%	0.95	2.0	0.6	2.0
Cork 200 kg/m3 [3]	97%◎21%	-	-	0.97	1.05
Pine 510 kg/m3 [3]	43%◎95%	0.70	1.1	-	-
Spruce 420 kg/m3 [3]	44%◎95%	0.70	1.2	-	-
Spruce 420 kg/m3 [5]	44%◎95%	0.40	1.0	-	-
Yellow poplar [5]	44%◎95%	0.68	1.15	-	-
Wood wool board 610 kg/m3 [3]	43%◎91%	0.75	1.05	-	-
Paper [2]	90%◎15%	-	-	0.40	1.0
	80%◎15%	-	-	0.50	1.0
	75%◎15%	-	-	0.70	1.0
	45%◎90%	0.60	1.0	-	-
	60%◎90%	0.60	1.0	-	-

Note: *- real desorption isotherm was not given

The hysteretic factor as a function of relative humidity is in figure 2.

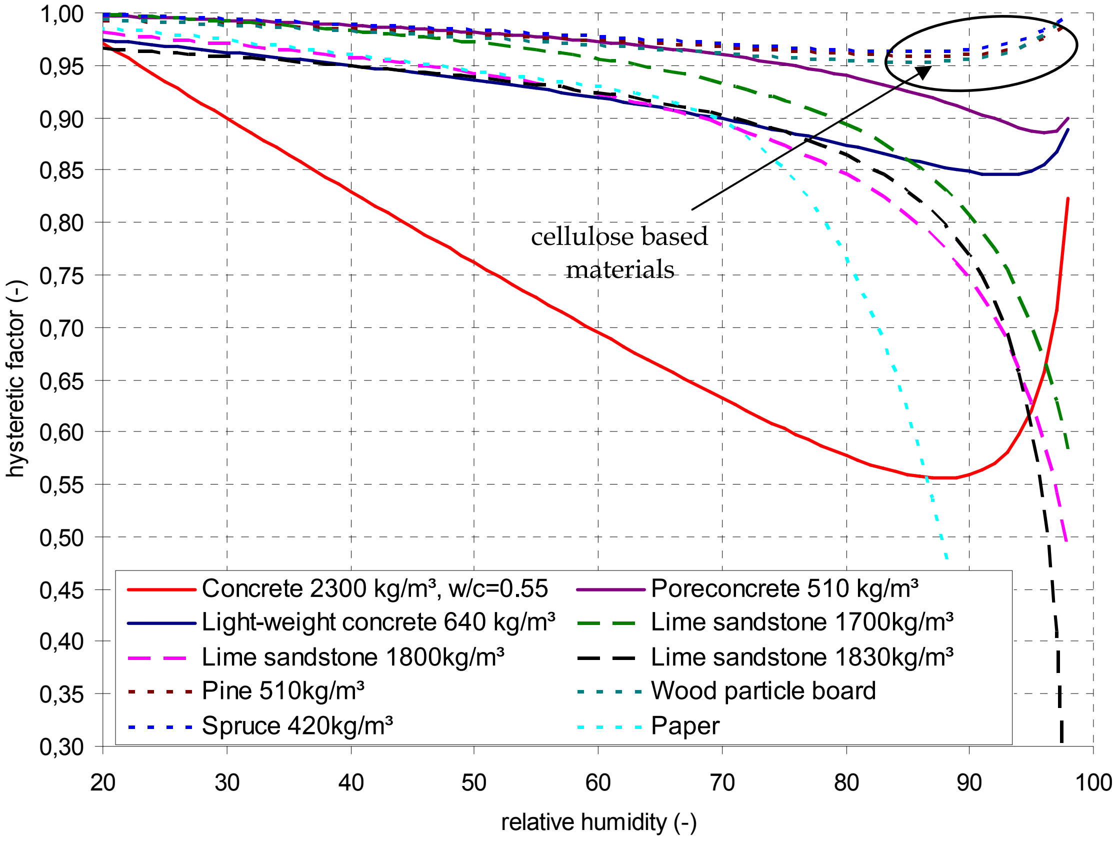

Figure 2: Hysteretic factor

All analysed cellulose based materials are characterized by a flat course of the scanning curves - the parameters *A* and *D* are close to 1.0 except the paper. The hysteretic factor reaches values above 0.95. The saturated water content of the paper was determined by the extrapolation of the main adsorption and desorption curves [2], as the hysteretic factor was not determined with a correct value of the saturation moisture content, the hysteretic factor drops.

For all other materials the hysteretic factor above the relative humidity of 60 % falls down, for these materials the values of parameters *A* and *D* closed to 2.0 are characteristic. For the aerated concrete, with the bulk density of 510 kg/m^3, the hysteretic factor falls down to the value of 0.88 at the relative humidity 95 %. This fact corresponds to the low value of the parameter *A*.

The parameters *A* and *D*, constant in the analysed range, have the same value for adsorption and desorption process. The parameters γ_a and γ_d are slightly different, however, the paper has the equal values for adsorption and desorption processes. For concrete and asbestos cement, the equality is lost and the values are dependent on the scanning range.

Knowledge of one of the main sorption isotherms and the sorption hysteresis parameters enables to determine the other main sorption isotherm. The equilibrium moisture content of the main adsorption or desorption curve can be approximated using equations (1) and (2). The scanning curve will be approximated with any function, derivation of which represents a moisture capacity of the scanning curve at given relative humidity. If the parameters *A* and *D* are equal to 1.0, equations (1) and (2) will be simplified into a linear form. In a case when *A* and *D* equal 2.0, the equations have a quadratic form, they have 2 roots and one of them having no physical sense is neglected.

Collecting the materials into two separated groups based on the similarity of the parameters *A* and *D* is useful for selection of the calculation method for the main adsorption or desorption isotherm modelling.

Conclusions

Based on the available measured main water vapour adsorption/desorption isotherms and scanning curves, the parameters of sorption hysteresis model has been approximated. From the analysis of the hysteretic model parameters and the hysteretic factor function, the materials were collected into two groups. For all materials with the parameters A and D close to 1.0, the flat course of the hysteretic factor is characteristic. This is typical mostly for the cellulose based materials. For all other materials, the parameters A and D close 2.0 are typical. The hysteretic factor at the relative humidity higher than 60 % significantly falls down.

Knowledge of the sorption hysteresis data and parameters enables to complement the missing main sorption curves. The proposed procedure will be used in a next work.

Acknowledgement

Authors wish to thank the APVT-51-030704 and APVV-0744-07 projects for the financial support of this work.

References

[1] PEDERSEN, C.R. Combined heat and Moisture transfer in Building Constructions, PhD Thesis, Thermal Insulation, Technical University of Denmark, report 214

[2] CHATTERJEE, S.G. Comparison of domain and similarity models for chatacterizing moisture sorption equilibria of paper. In Ind.Chem.Res. vol.40, 2001, pp. 188-194

[3] HANSEN, K.K. Sorption isotherms, a catalogue, Building materials laboratory, The Technical University of Denmark, 1986

[4] KWIATKOWSKI, J.; WOLOSZYN, M.; ROUX, J-J. Modelling of hysteresis influence on mass transfer in building materials, Building and Environment, Elsevier, 2009, pp.633-642, ISSN 0360-1323

[5] FRANDSEN, H.L. Modelling of Moisture transport in Wood, State of Art and Analytic Discussion, Aalborg University, 2005, ISSN 1395-7953 R0502

[6] KORONTHÁLYOVÁ, O. et al. Simulation of dynamic moisture response of autoclaved aerated concrete. In Proceedings of 8th Symposium on Building Physics in the Nordic Countries, Danish society of Engineers, IDA, Copenhagen 2008, pp. 817-824, ISBN 978-87-7877-26-7.

[7] MIHÁLKA, P. et al. Simulation of hysteretic behaviour at dynamic moisture. In Proceedings of Thermophysics 2008, Vydavateľstvo STU, Bratislava 2008, pp.110-118, ISBN 978-80-227-2968-0

Thermodilatometry of ceramics using the simple push-rod dilatometer

Jana Moravčíková

Faculty of Natural Sciences, Constantine the Philoshopher University in Nitra, Tr. A. Hlinku 1, SVK 949 74 Nitra, Slovak Republic email: jana.moravcikova@ukf.sk

Abstract: *This paper describes a dilatometer of the own construction designed for education and its calibration. The example of dilatometry of the quartz crystal is shown.*

Keywords: *Thermodilatometry, Push-rod Dilatometer, Ceramic*

Introduction

The dimensions of major material increase by the increasing temperature. This relates with difference between attachment forces and detachment forces effecting between pairs of interactive atoms in the crystal lattice. Asymmetry of the vibration amplitude between each pair of atoms causes that their middle distance is increasing by increasing temperature. The vibration period is divided unequal; the particles are longer time more distant as are closer to each other. It shows like the increasing the dimensions of the body by increasing the temperature [1]. Some sudden length variations can be observed when the phase transition occurs inside a solid sample: it corresponds to a change in the structure. Thermodilatometry is a technique which consists in measuring the length of a sample as function of the temperature.

Thermodilatometric analysis plays important role in ceramic research. It allows the forecast of the changes in the sample made from input minerals. When ceramic powder is heated, the densification and sintering process can be observed and studied through thermodilatometry. The experimental study of the influence of additives and raw materials, reaction kinetics, phase transitions, glaze development, and thermal shock are next abilities of thermodilatometry. Because dilatometric patterns of most raw ceramic constituents are known, the dilatometric curve can be useful for estimation the composition of the green sample [2-4].

A survey of dilatometric results obtained for fired ceramics show that their relative thermal expansion is $\Delta l/l_0 < 1$ % in the temperature region 20 – 1300 °C. If sintering of the green sample takes place, one can expect contraction $\Delta l/l_0 > 12$ % in this temperature region. Also some phase changes are accompanied with large shrinkage, e.g. intensive rebuilding of the crystal lattice at dehydroxylation and creation of the new phase at 950 °C in clay ceramics. As it follows from that, a large scale of the measurement, rather than extreme sensibility, is necessary for thermodilatometry of the green ceramics. A resolving power of 1 × 10-6 m is fully sufficient for most investigations. A push-rod dilatometer with linear variable displacement transducer (LVDT) and alumina carrier elements (tube or rods) meets these requirements very well.

A low-cost dilatometer was developed in our laboratory for education goals [5]. Then the dilatometer was improved in many ways and used for thermodilatometry of kaolin-base ceramics. This paper describes the dilatometer and its calibration.

Principle of the push-rod dilatometer

The push-rod dilatometer, see Fig. 1, exploits a differential method, which is based on measuring the difference between the expansion of alumina rods, which thermal expansion is known, and the sample made from material, which thermodilatometric behavior is unknown.

The parts A and B of the all rods expand during heating. As the all alumina rods are in the same temperature fields subsistent to the parts A and B, they expand equally and do not give rise to the transducer signal. Wherefore, only the central part C is important. The initial length l_0 of the sample is as long as the alumina rods parallel to the sample. At higher temperature the carrier alumina rods and the unknown sample expand, but the sample has a different linear thermal expansion coefficient. This causes a movement of the push-rod, which is measured by the differential transformer as displacement Δd. The displacement is proportional to the change of the electrical output signal of the transducer ΔU and we can write

$$k\Delta U = \Delta l_s - \Delta l_{ar} \tag{1}$$

where Δl_s is the change of the length of the sample and Δl_{ar} is the change of the length of the carrier alumina rods at the temperature t.

The relative expansion of the alumina rod is known for the whole temperature range. If we mark l_0 the initial length of the sample, then the relative expansion of the sample could be calculated from the known values of $\Delta l_{ar} / l_0$ and the measured values of ΔU. For the relative expansion of the sample $\Delta l_s / l_0$ we obtain from Eq. (1)

$$\frac{\Delta l_s}{l_0} = \frac{k\Delta U}{l_0} + \frac{\Delta l_{ar}}{l_0} + \frac{(k\Delta U)_{se}}{l_0} \tag{2}$$

where the one term is added on the right side. It represents an influence of the systematic errors.

If the relative expansion of the sample is known, the linear thermal expansion coefficient can be calculated as

$$\alpha = \frac{1}{l_0}\frac{\Delta l_s}{\Delta t} \tag{3}$$

where Δt is temperature interval and Δl_s is a gain of the length of the sample in this interval.

Push-rod dilatometer

Different techniques of measurement of thermal expansion of solid materials are shortly described in [6-9] but no design of the dilatometric cell is similar to that used in this work. A similar construction was described in [10]. A dilatometric cell of the construction described below (Fig. 1) consists of four carrier alumina rods (with diameter 3.0 mm) that are fastened to two holders made of duralumin and the push-rod and supporting rod. The LVDT (INPOS, ZPA Jinonice, Czech republic) is fixed to the one holder (see Fig. 1). The construction is light and no one holder is firmly connected with the frame of the apparatus. The dilatometric cell freely passes through windows of the furnace with the ceramic fiber insulation. The furnace is made from porous alumina bricks and silicon carbide rods are used as heating elements. Central part of the dilatometric cell with the sample is located in the furnace. A view on the perpendicular section of the dilatometric cell with arrangement of the rods, sample and push-rod can be seen in Fig. 2. The sample is placed between two rods: one of them is push-rod and the other is supporting rod, which is fastened to the second holder. The push-rod can be shifted together with the sample and supporting rod with a zeroing screw. The LVDT measures the changes of the pushrod position Δd, i.e. the changes of the length of the sample. A dilatometric arrangement is at Fig. 3.

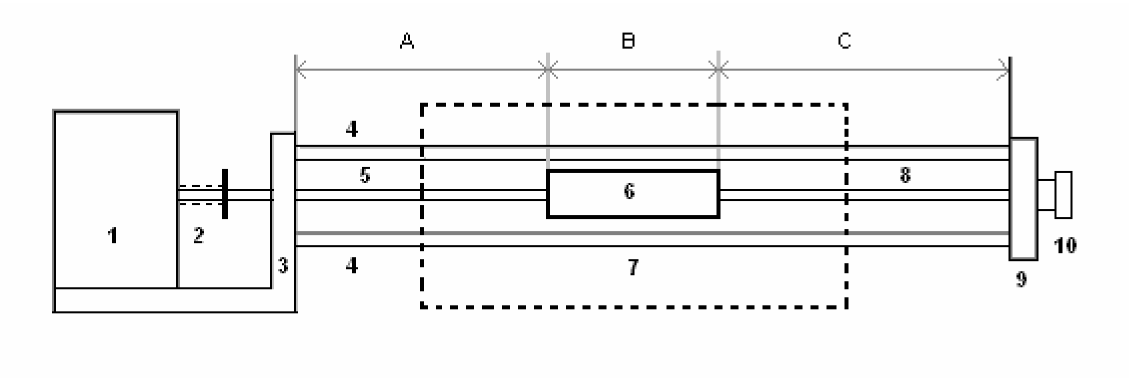

Figure 1: Schematic diagram of dilatometer. 1 – inductive transducer, 2 – spring, 3 – holder, 4 – carrier alumina rods, 5 – push-rod, 6 – sample, 7 – furnace, 8 – supporting rod, 9 – holder, 10 – micrometric zeroing screw

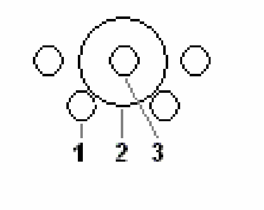

Figure 2: Perpendicular section of the dilatometric cell. 1 – four carrier rods, 2- sample, 3 – push-rod

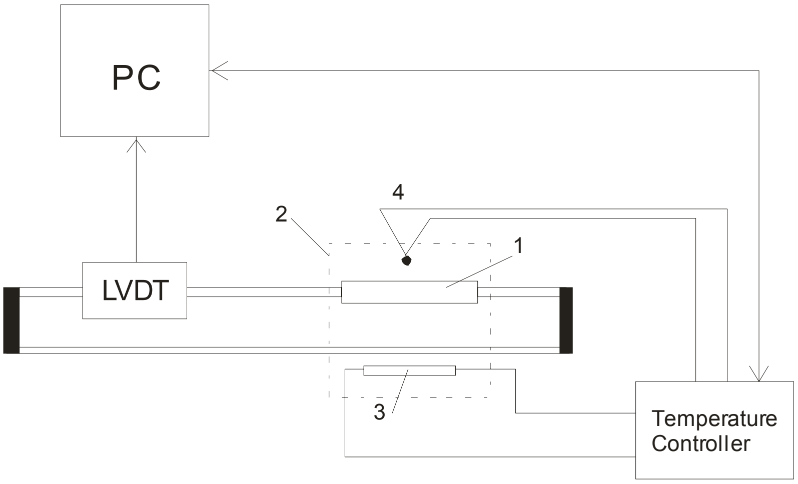

Figure 3: Scheme of dilatometer: 1 – sample, 2 – furnace, 3 – heating elements, 4 – thermocouple

The working temperature range of the dilatometer is 20 – 1200 °C, ambient atmosphere is the static air. The temperature is measured by thermocouple Pt-PtRh10%, which is placed beside the sample, and is controlled with temperature controller Clasic Clare 4 (Czech republic). Output signals of the LVDT and the temperature are stored by PC.

Calibration of LVDT

A purpose of this calibration was to determine the constant k in Eq. (1) and to test a linearity of the LVDT, Fig. 4. The calibration was performed by micrometric screw. The value of the constant $k = 2.600 \pm 0.004$ µm/mV. The high value of the correlation coefficient $R = 0.9998$ makes possible to consider the relationship $\Delta U(\Delta l)$ as linear. The span of the dilatometer is 6 mm.

Calibration of the dilatometric cell

The push-rod dilatometer visible in Fig. 1 is based on the comparison of the expansion of the sample to expansion of the carrier rods. Because this method is not absolute, the calibration of the instrument is necessary [11]. The calibration of the differential push-rod dilatometers is based on the measurement of the samples made from reference materials [11-15].

The calibration was performed using the reference sample with dimensions ∅5 × 30.00 mm made of steel X10 NiCrMoTiB 1515 delivered by Physikalisch-Technische Bundesanstalt, Berlin. This material has been intensively studied in the recent past, e.g. in [16, 17]. Results of round robin test we used as the reference dilatometric curve [18], which can be expressed by the polynomial function

$$\left(\frac{\Delta l}{l_0}\right)_{ref} = -4\times10^{-22}t^3 + 2\times10^{-7}\,t^2 + 0.0018t - 0.045 \tag{4}$$

where t is a temperature in °C and $(\Delta l / l_0)_{ref}$ is in %. Correlation coefficient of the fitting is R=1.

The reference sample was measured 5 times at heating rate 5 °C/min. The results are shown in Fig. 4, where the difference between the measured values $(k\Delta U)/l_0$ and the dilatometric curve of the reference steel sample $(\Delta l / l_0)_{ref}$ can be seen. The difference seems to be large at the first glance. The reason is the omitting the thermal expansion of the carrier alumina rods in the region adjacent to the sample as well as the influence of possible systematic errors on the output signal ΔU.

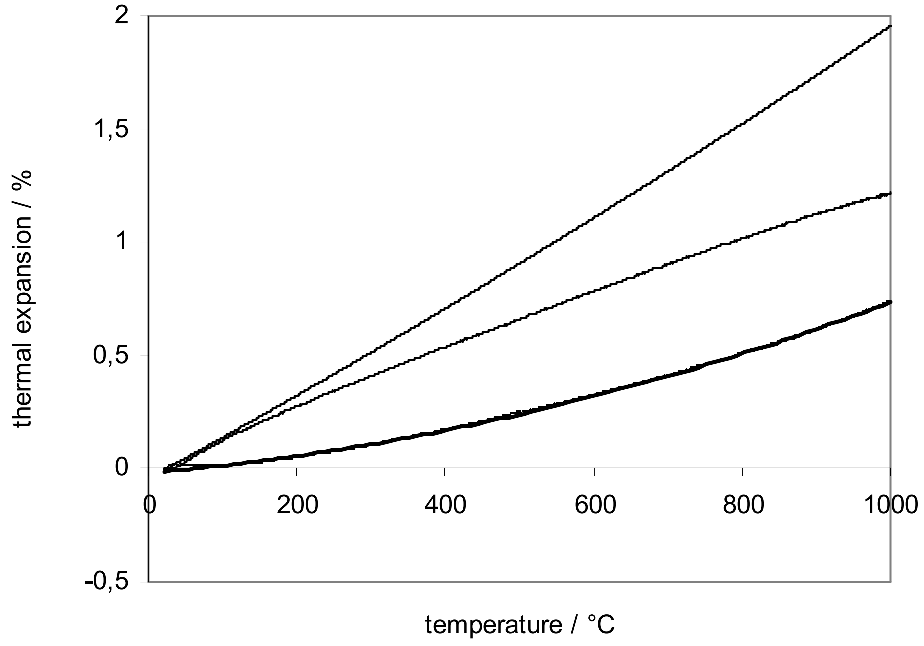

Figure 4: Dilatometric curve of the steel reference sample plotted from reference values [16] (upper line), mean curve of the measured results $k\Delta U / l_0$ *(middle line), and correction function (lower line)*

The next step is searching for the correlation function, which is a difference between the values of $(\Delta l / l_0)_{ref}$ and the mean function gained from the average measured values. Both functions are plotted in Fig. 4. The correction function $(\Delta l / l_0)_{cor}$ includes not only the correction of the thermal expansion of the carrier alumina rods, but also hidden systematic errors of the apparatus. Then the Eq. (2) becomes simpler

$$\frac{\Delta l_s}{l_0} = \frac{k\Delta U}{l_0} + \left(\frac{\Delta l}{l_0}\right)_{cor} \tag{5}$$

We used the polynomial fitting to obtain the analytical expression of the correction function. The function has the form

$$\left(\frac{\Delta l}{l_0}\right)_{cor} = 5\times10^{-7} t^2 + 3\times10^{-4} t - 0.0178 \tag{6}$$

where t is a temperature in °C. Correlation coefficient of the fitting is $R = 0.9996$.

A correct work of the dilatometer was verified by measurement of the quartz crystal (from locality Banska Bela, Slovakia) along c axis. The results were compared with [19] where the results of four independent measurements are presented, see Fig. 5.

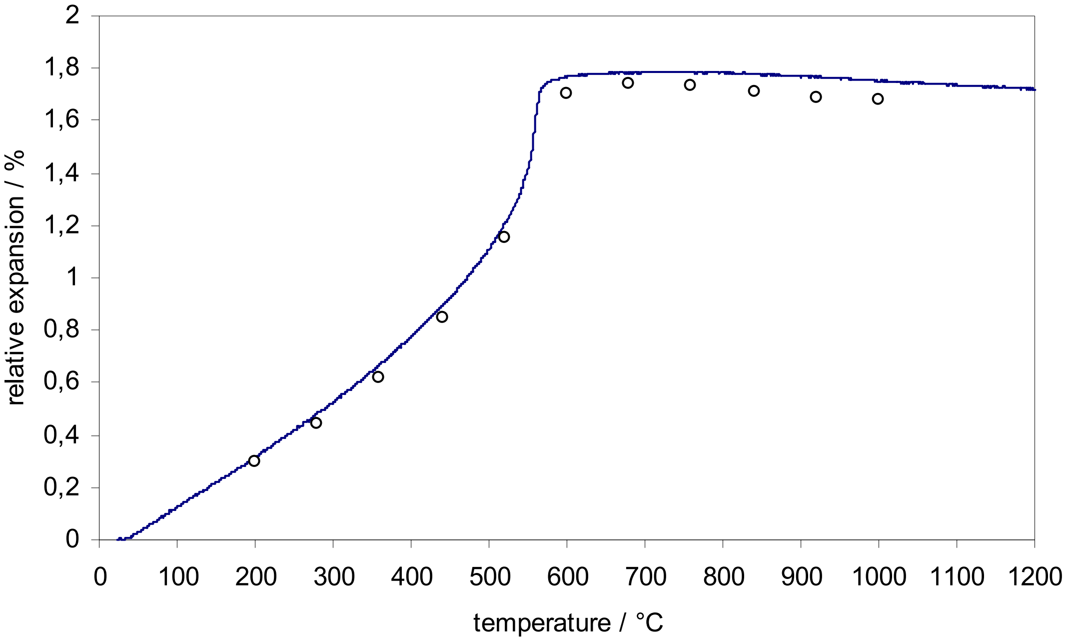

Figure 5: Dilatometric curves of quartz crystal. Points are main values from three sets of data [19], line-measured curve

Conclusion

The construction of the push- rod dilatometer for education was described. The calibration of the dilatometer was carried out by the steel X10 NiCrMoTiB 1515_reference sample. A correct work of the dilatometer was verified by measurement of the quartz crystal compared with results from literature.

This dilatometer was used in several research projects, mainly for dilatometry of ceramics [20-22].

References

[1] DEKKER, A. J. Fyzika pevných látek, Academia, Praha, 1966

[2] CURTIS, W.F. Firing studies of Al2O3 porcelains by irreversible thermal dilatometry. In MS Thesis. Alfred NY, School of Ceramic Engineering of Alfred University.1978.

[3] ŠAŠEK, L. Laboratory methods for silicate materials, SNTL – Alfa, Praha – Bratislava, 1981.

[4] ŠŮCHA, L. ; VRBSKÝ, J. Analytická příručka I., SNTL. Praha. 1979. p.271-325

[5] ŠTUBŇA, I. Škoľnyj dilatometr do 650 °C. In Sb. Problemy fiziki i technologii ee prepodavanija. Lipeckij Gosud. Pedag. Universitet, Lipek. 2000. p. 120-123

[6] JAMES, J.D. ; SPITTLE, J.A. ; BROWN, S.G.R. ; EVANS, R.W. A review of measurement techniques for thermal expansion coefficient of metals and alloys at elevated temperatures. Meas. Sci. Technol. 2001. 12. p. R1-R15

[7] TAYLOR, R. E. Thermal expansion of solids. Materials Park OH, ASM Int.,1998

[8] KAMSEU, E. ; LEONELLI, C. ; BOCCACCINI, D. Non-contact dilatometry of hard and soft porcelain compositions. Journal of Thermal Analysis. 2007. 88. p. 571-576

[9] LECLERC, F. New applications of the thermodilatometry in the characterization of ceramics. Journal of Thermal Analysis. 1992. 38. p. 515-522

[10] AGARWAL, G. ; SPEYER, R. F. ; HACKENBERGER, W.S. A novel programmed shrinkage dilatometer for optimized sintering of powder ceramics. Journal of Thermal Analysis. 1997. 49. p. 1297-1304

[11] ASTM E 228-95: Standard test method for linear thermal expansion of solid materials with a vitreous silica dilatometer.

[12] VALENTICH, J. Calibration of tube type dilatometers. J. Thermal Analysis. 1977. 11. p. 387-403

[13] YAMADA, N.; ABE, R.; OKAJI, M. A calibration method for measuring thermal expansion with a push-rod dilatometer. Meas. Sci. Technol. 2001. 12. p. 2121-2129

[14] VALOVIČ, Š. Calibration of the differential dilatometer. Acta Univ. Tyrnaviensis, C. 2002. 6. p. 129-134

[15] ZMATUJI, A. N.; LIFAMOV, I. I.; SHEVCENKO, E. B.; SHERSTYUKOV, N. G. Metrological foundations of dilatometry. Measurement techniques. 1968. 11. p. 1014-1017

[16] RICHTER, F. VGB Kraftwerkstechnik. 1988. 68. p. 1061-1072

[17] VOZÁR, L.; HOHENAUER, W. Uncertainty of Thermal Diffusivity Measurements Using the Laser Flash Method. Int. J.Thermophysics. 2005. 26. p. 1899-1915

[18] RUDTSCH, S. Intercomparison between thermophysical property measurements on an austenitic stainless steel. Int. J. Thermophysics. 2005. 26. p. 855-867

[19] RAZ, U.; GIRSPERGER, S.; THOMPSON, A. B. Thermal expansion, compressibility and volumetric changes of quartz obtained by single crystal dilatometry to 700 °C and 3,5 kilobars (0,35 GPa). Expansion and compressibility changes of quartz http://e-collection.ethbib.ethz.ch/eserv/eth:25671/eth-25671-01.pdf

[20] ŠTUBŇA, I.; TRNÍK, A.; VOZÁR, L. Thermomechanical and thermodilatometric analysis of green alumina porcelain. Ceramics International. 2008. 34. p. 1181-1185

[21] ŠTUBŇA, I.; VÁŽANOVÁ, A.; VARGA, G.; HRUBÝ, D. Simple Push-Rod Dilatometer for Dilatometry of Ceramics. Research and Teaching of Physics in the Context of University Education. 2007. p. 69-74

[22] VARGA, G.; ŠTUBŇA, I. Dilatometry of stove tile ceramic material Letovice. Építőanyag. 2008. 60. p. 13-14

The influence of heating rate on thermal field in cylindric ceramic samples

Ján Ondruška, Anton Trník, Libor Vozár

Department of Physics, Constantine the Philosopher University, Nitra, Slovakia

Abstract: *Heating of traditional clay electroceramics causes the elimination of physically and chemically bonded water. This process depends on the size and heating rate of a sample. We show the influence of the surface temperature and the difference between the surface and the bulk temperature.*

Keywords: *dehydroxylation, cylindric sample, thermal field*

Introduction

Elimination of the physically and chemically bonded water depends on the rate of firing as well as on the size of a ceramic sample [1]. These processes start on the surface of the sample at the same temperature, regardless of the heating rate or sample size. However, the next spread of these processes inside the sample depends on the sample radius and heating rate [1]. This is most evident in samples of large dimensions that are typically used in electroceramic industry. The liberation of physically bonded water starts at the temperature ~30 °C and if water molecules are dissociated, water drives off eventually at 200 °C – 250 °C [2].

The process of the loss of chemically bonded water from the kaolinite crystals, called dehydroxylation, starts at temperature ~400 °C [3, 4]. A temperature range 450 °C – 600 °C is often considered for dehydroxylation region [7]. This interval is valid for small samples with mass less than 1 g. For large samples this interval depends on the sample size and heating rate and its upper limit is shifted to higher temperatures. Thermophysical and mechanical properties of the kaolin-base ceramics are substantially changed during dehydroxylation [5, 6]. Therefore, it is essential to have a rather detailed knowledge of this process, especially in industrial applications, where good control over mechanical and thermophysical properties of large samples is crucial.

In this paper we study temperature differences in a cylindrical ceramic body during its heating in the dehydroxylation region. In our opinion, it is the first step for explaining the distribution of the dehydroxylation products in a large sample.

Samples and methods

The samples were prepared from the wet plastic ceramic mass prepared for manufacturing high-voltage insulators. The initial composition of the ceramic material consists of 48 wt. % of kaolin and clay, 30 wt. % of alumina and 22 wt. % of feldspar. The samples have a cylindrical shape of diameter 80 mm and 120 mm length. The four holes (∅2 mm) in which thermocouples Pt-PtRh10 were placed were bored into the sample as shown in Fig.1.

First, the samples were dried in the furnace at the isothermal regime at 150 °C for 8 hours. The temperature 150 °C was reached by a linear heating with the heating rate 0.5 °C/min. Then the samples were cooled down to the room temperature and the main experiment was performed during the linear heating with rates of 1.0, 1.5, 2.0, 2.5, and 3.0 °C/min up to 900 °C. During the heating, the temperatures were measured in the distances $r = 0$, 1, 2, and 3 cm from the middle of the sample, see Fig. 1. One thermocouple was placed close to the sample surface.

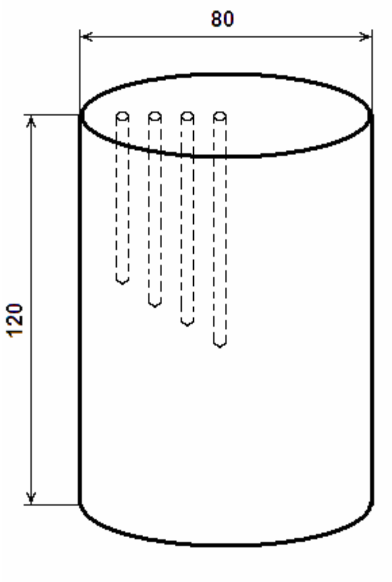

Figure 1: A cylindrical sample with holes for thermocouples. The dimensions are in mm

Results and discussions

The liberation of the physically and chemically bonded water is a process associated with a mass loss. In large cylindrical samples we must take into account not only the diffusion of water through the kaolinite crystals, but also the transport of water through pores and micropores of the ceramics. The diffusion of water is the main control mechanism in dehydroxylation range [8, 9].

Figures 2 – 6 describe the temperature distribution in a cylindrical sample in four different points. For each curve we can define two important peaks. The first one marks the elimination of the physically bonded water. The second peak corresponds to dehydroxylation. This process, when the kaolinite crystals are transformed into metakaolinite crystals, is endothermic [10]. During this process the hydroxyl groups in kaolinite are liberated and connecting together so as water molecules can escape from the crystal and then from the sample.

The first peak of curves in Fig. 2 – 6 indicate, the elimination of the physically bonded water is a two-step process. In the first step water is liberated from the pores of the material. In the second step water bonded directly on the surface of the crystals is liberated. This bond, realized by the van der Vaals forces, is stronger and a higher temperature is needed to liberate water molecules. Evidently, the elimination of the physically bonded water is an endothermic process.

Figures 2 – 6 show that the starting temperature of any of these two processes depends on the heating rate as well as on the place inside the sample. The deeper is the thermocouple, the later the starting temperature is observed. That is, the starting temperature is shifted to higher temperatures in the interior of the sample. It is caused by the growing pressure of the water vapor inside the sample.

Figures 7 – 10 describe the temperature change in the same place in the sample, but with different heating rates 1.0 °C/min, 1.5 °C/min, 2.0 °C/min, 2.5 °C/min, 3.0 °C/min. As depicted, the processes start in the surface layers at the same temperature regardless of the heating rate. However, the heating rate influences the starting temperatures inside the sample. We obtained interesting results, as Fig. 7 shows. The curves are strictly dependent on the heating rate. If the heating rate is slow, the liberation of the physically bounded water finishes sooner than dehydroxylation starts. Nevertheless, at the higher heating rates dehydroxylation starts even if the liberation of the physically bonded water is still running, see Figs. 7 – 10.

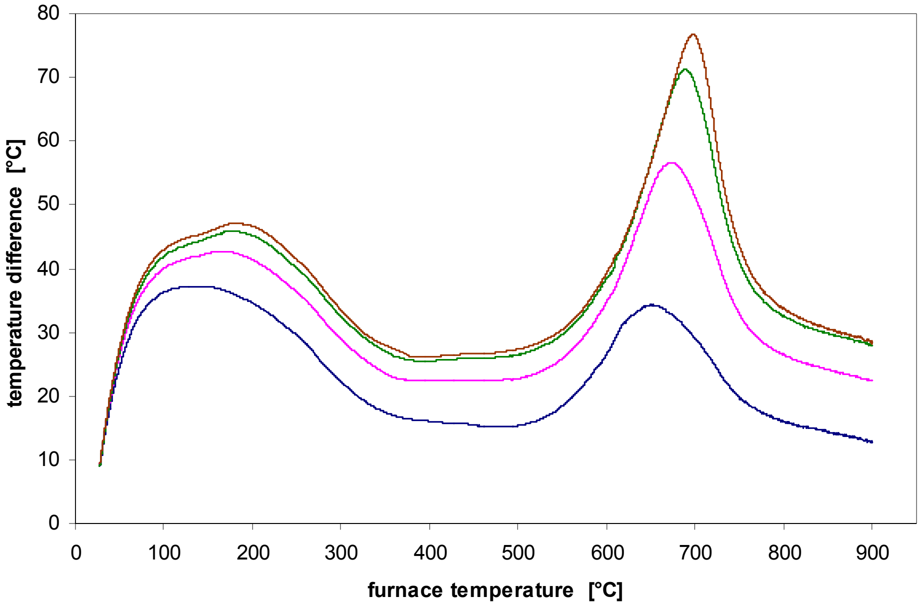

Figure 2: The temperature difference between the temperature on the surface of the sample and in different radii. From the top: r = 0 cm, 1 cm, 2 cm and 3 cm with heating rate 1 °C/min

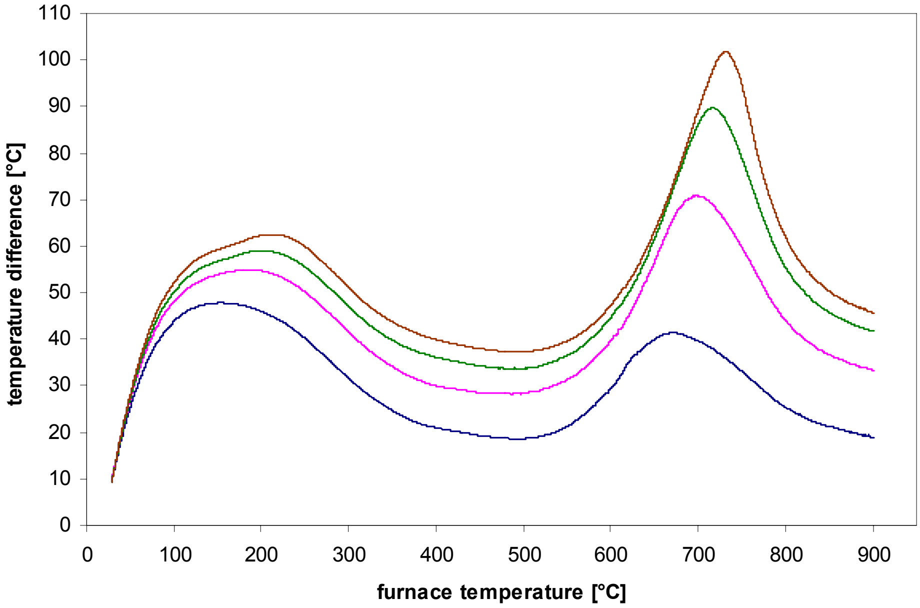

Figure 3: The temperature difference between the temperature on the surface of the sample and in different radii. From the top: r = 0 cm, 1 cm, 2 cm and 3 cm with heating rate 1.5 °C/min

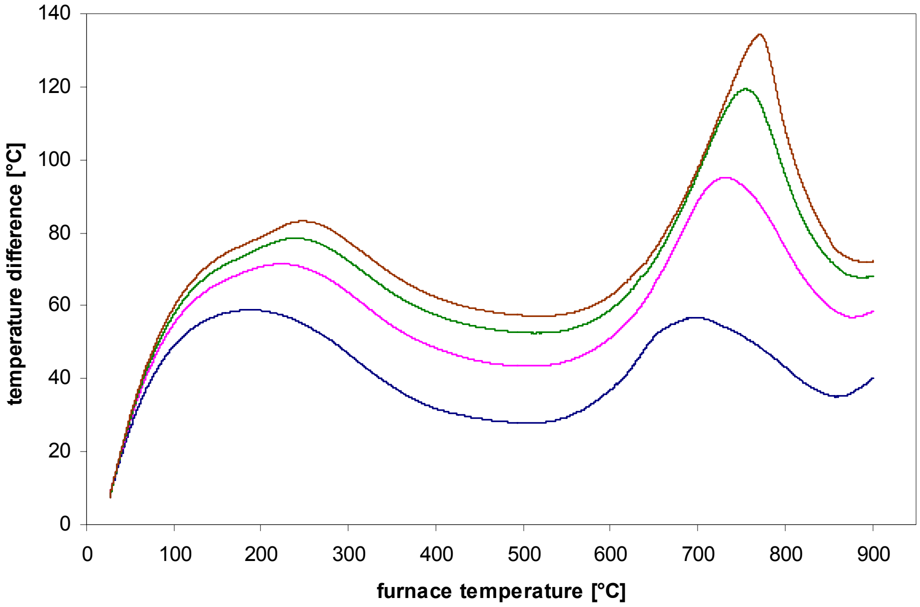

Figure 4: The temperature difference between the temperature on the surface of the sample and in different radii. From the top: r = 0 cm, 1 cm, 2 cm and 3 cm. Heating rate 2 °C/min

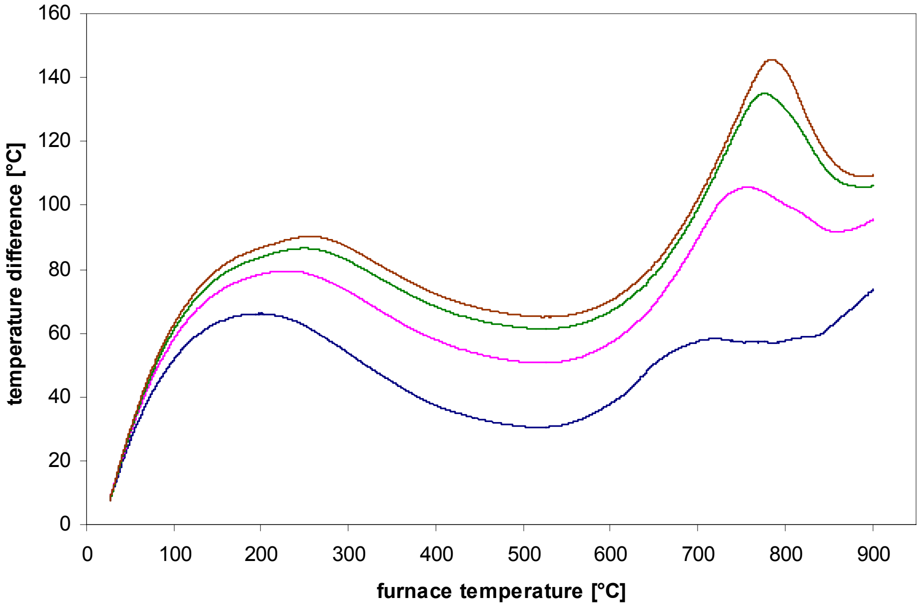

Figure 5: The temperature difference between the temperature on the surface of the sample and in different radii. From the top: r = 0 cm, 1 cm, 2 cm and 3 cm. Heating rate 2.5 °C/min

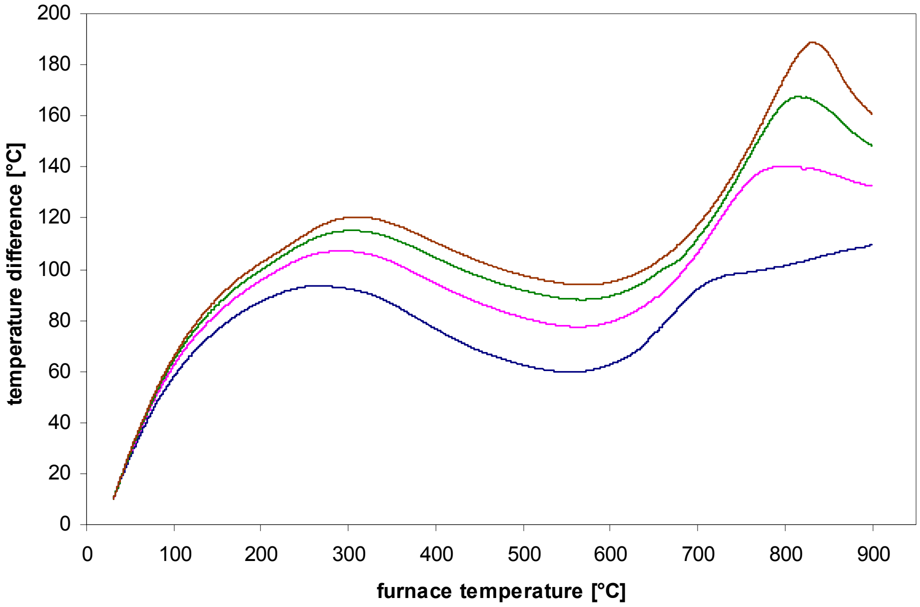

Figure 6: The temperature difference between the temperature on the surface of the sample and in different radii. From the top: r = 0 cm, 1 cm, 2 cm and 3 cm. Heating rate 3 °C/min

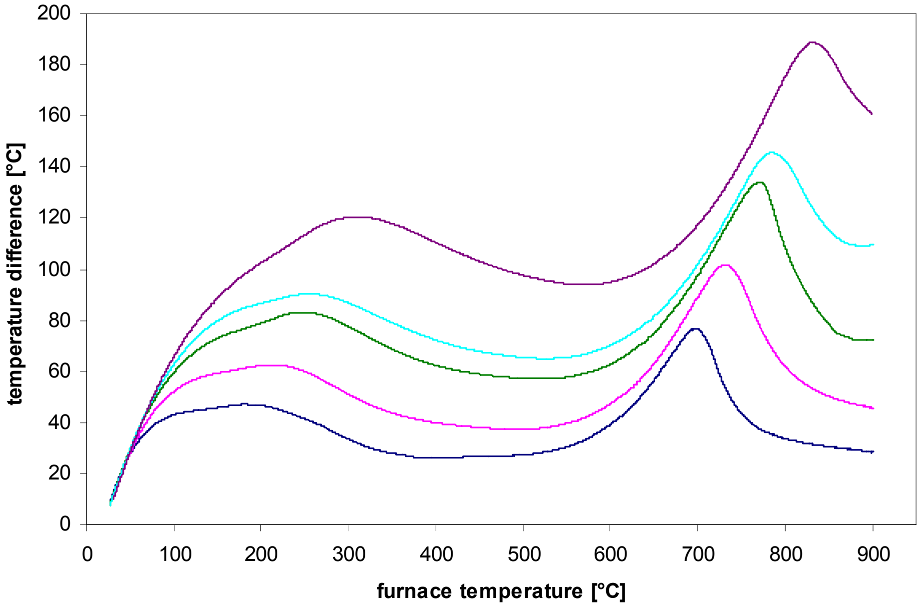

Figure 7: The temperature difference between the temperature on the surface and in radius r = 0 cm with different heating rates. From the top: 3.0 °C/min, 2.5 °C/min, 2.0 °C/min, 1.5 °C/min, 1.0 °C/min.

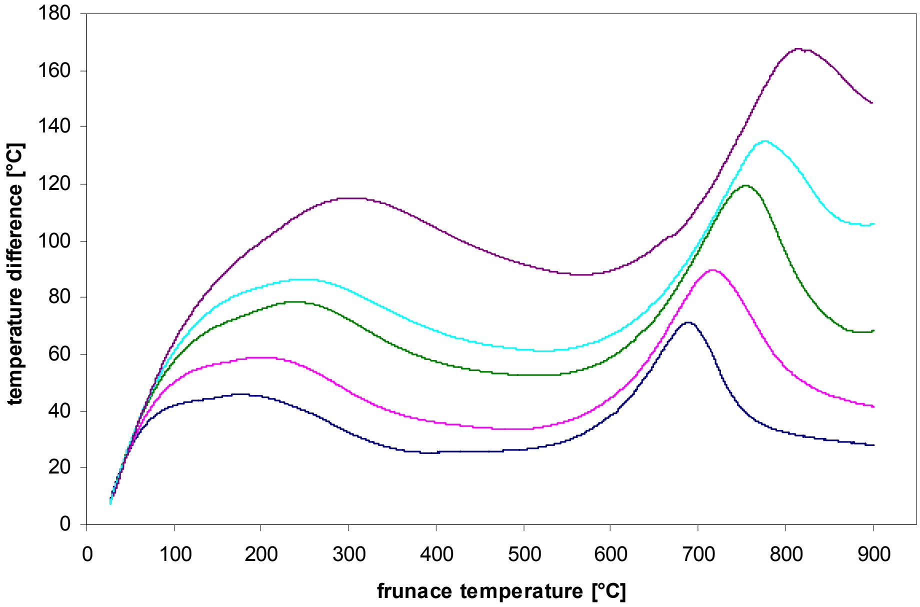

Figure 8: The temperature difference between the temperature on the surface and in radius r = 1 cm with different heating rates. From the top: 3.0 °C/min, 2.5 °C/min, 2.0 °C/min, 1.5 °C/min, 1.0 °C/min.

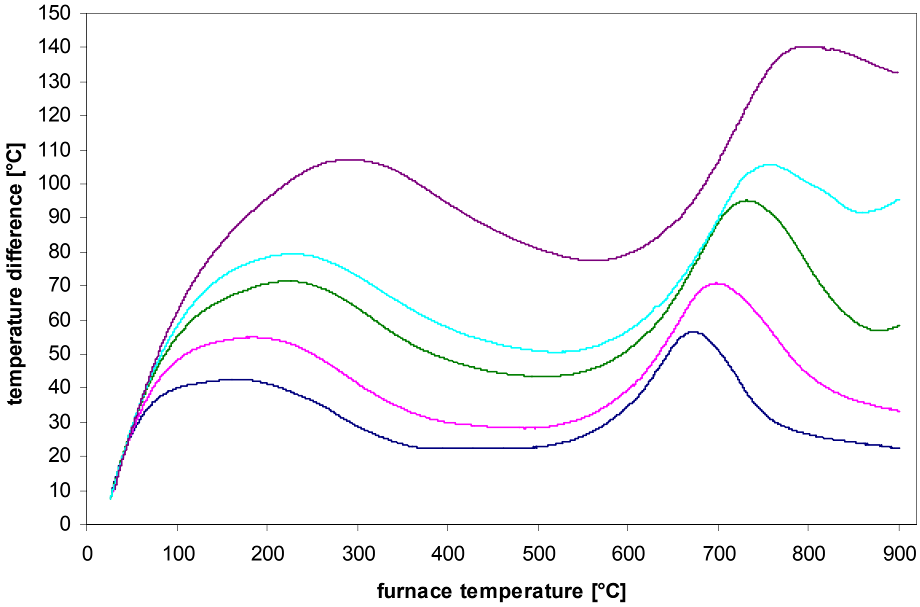

Figure 9: The temperature difference between the temperature on the surface and in radius r = 2 cm with different heating rates. From the top: 3.0 °C/min, 2.5 °C/min, 2.0 °C/min, 1.5 °C/min, 1.0 °C/min.

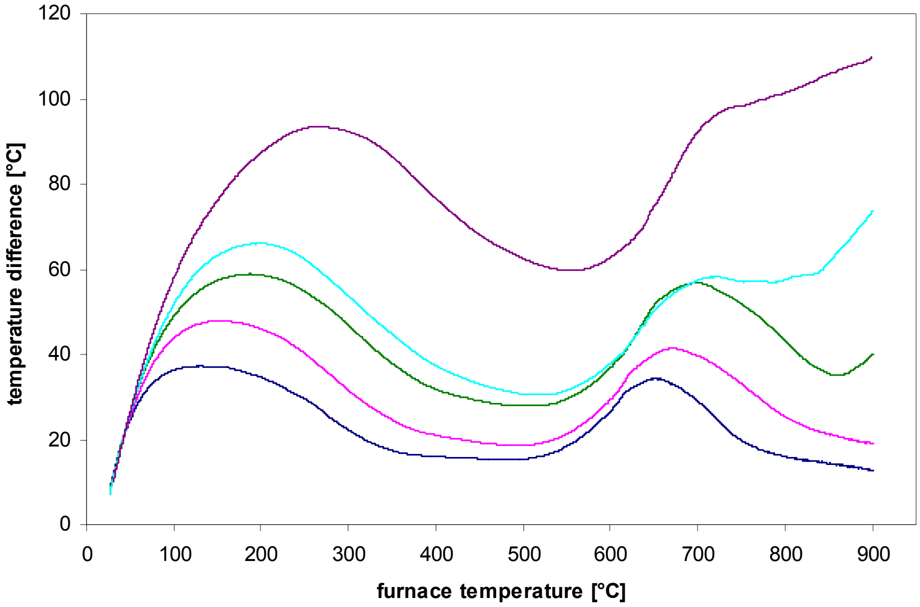

Figure 10: The temperature difference between the temperature on the surface and in radius r = 3 cm with different heating rates. From the top: 3.0 °C/min, 2.5 °C/min, 2.0 °C/min, 1.5 °C/min, 1.0 °C/min.

Conclusion

The elimination of the physically and chemically bonded water depends on a sample's diameter and heating rate of firing of the ceramic sample. These processes start on the surface of the sample and spread across to its center. While the liberation of the physically bonded water in the center of the sample is still running, or just finishing, the dehydroxylation process starts on the samples surface. The experiment showed that the temperature of the start of dehydroxylation and its maximum rates vary from the surface to the centre of the sample.

Acknowledgement

This work was supported by grants VEGA 1/0302/09 and UGA I-09-304-01 and FCVV initiative of the Constantine the Philosopher University under grant I-06-399-01. The authors appreciate the cooperation with the ceramic plant PPC Čab, Slovakia, a member of the international PPC Insulators group.

References

[1] ŠTUBŇA, I., VOZÁR, L. The influence of the sample size on low-temperature processes in green electroceramics, Industrial Ceramics 25, 2005, p. 110-112

[2] KOZÍK, T. et al. The temperature dependence of the electric conductivity of unfired porcelain mixture. Ceramics – Silikáty, 36 1992, p. 69-72

[3] BRINDLEY, G. W. – SHARP, J. H. – PATTERSON, J. H. – NARAHARI, B. N. Kinetics and mechanism of dehydroxylation process, I. temperature and vapor pressure dependence on dehydroxylation of kaolinite, The American Mineralogist, 52, 1967, N1-2, 201-211

[4] ČÍČEL, B. – NOVÁK, I. – HORVÁTH, I. Mineralogy and crystallochemistry of clays, SAV Bratislava, 1981

[5] CARTY, W. M. - SENAPATI, U. Porcelain – Raw Materials, Processing, Phase Evolution, and Mechanical Behavior. Journal of the American Ceramic Society, 81[1], 1998, p. 3-20,

[6] KOZÍK, T. - ŠTUBŇA, I. Mechanical strength of the ceramic material in the dehydroxylation temperature region. Silikáty, 25, 1981, p. 237-241

[7] ŠTUBŇA, I., VARGA, G., TRNÍK, A. Investigation of kaolinite dehydroxylation is still interesting. Épitőnyag – Building materials, 58, 2006, p. 6-9

[8] GLIKSMAN, M. E. Diffusion In Solids, Rensselaer Polytechnic Institute, John Wilez and sons, Inc., New York, 2000

[9] ŠTUBŇA, I. Dehydroxylation of Electroceramic Cylindrical Bodies, DIDMATTECH ’95, UKF Nitra, 1995

[10] VARGA, G. The structure of kaolinite and metakaolinite, Épitőnyag – Building materials, 59, 2007, p. 6-9

Experimental analysis of water and nitrate transport in porous building materials

Zbyšek Pavlík[1], Lukáš Fiala[1], Milena Pavlíková[1] and Robert Černý[1]

[1] Department of Materials Engineering and Chemistry, Faculty of Civil Engineering, Czech Technical University in Prague, Thákurova 7, 166 29 Prague 6, Czech Republic

Abstract: *Water and nitrate transport is analyzed experimentally in several characteristic types of porous building materials. The main practical outcome is the determination of two principal transport parameters, namely the moisture diffusivity and nitrate diffusion coefficient. It is shown that the possible neglect of nitrate diffusion in the liquid phase is apparently wrong because the moisture diffusivity calculated from nitrate concentration profiles under this assumption is one to two orders of magnitude higher than moisture diffusivity calculated from moisture profiles.*

Introduction

Historical masonry always contains certain amount of water soluble salts that can originate from the following sources: salts are primarily present in building materials, salts can be formed by chemical reaction or decomposition (e.g. dolomitic lime or pure lime, that were in the past very often used in building masonry, in presence of gypsum and moisture creates magnesium sulphate), salt can also come from materials used during reconstruction or renovation of building (e.g., low quality cements, water glass-based impregnations and infusions, de-icing agents added to mortars to enable work in wintertime, etc.), in urban areas huge amounts of sodium and calcium chlorides are still used as de-icing agents for roads and pavements maintenance during the winter period, although it is very well known that they do not only destroy building materials, roads and corrode the metals but they are also harmful for plants and trees, nitrates in building materials are in most cases of biological origin, they are found in objects where animal excrements were present (e.g., former stables, pigeons and bats excrements), high amounts of nitrates and nitrites were also found in buildings with leaking or broken sanitation and sewage pipes (the nitrates are formed by conversion of carbamide to nitrates), various water-soluble salts can be transported to masonry from ground water, especially in case of historical buildings, where horizontal water-proof insulation is often missing, salts originated by chemical reaction with air pollutants (e.g. sulphates formed by reaction of carbonates with sulphur oxides that are the components of acid rains).

Salts are from the chemical point of view binary or multi-component compounds consisting of simple or complex cations and anions. Only specific group of salts represents real danger in building practice or restoration. In light of danger for building materials and components, the salt solubility is the most important criterion. In corrosive processes only those salts take part, which are well soluble in water, whereas the influence of insoluble salts is more or less negligible.

The most frequent salts that cause damages of building materials and structures are sulphates, chlorides and nitrates and in some particular cases also water-soluble carbonates.

The destructive effect of water-soluble salts is the consequence of two main processes – crystallization and salt hydration in porous materials. Salt crystals can gradually fill the porous space and the crystallization pressures are exerted on the pore walls. In dependence on temperature, supersaturation rate and pore dimension, the destruction of materials can occur.

The second degradation process evoked by water-soluble salts is related to the salts that enable to bind defined amount of water molecules in their crystal lattice. The formation of hydration products is characteristic by changes of salt volume that are accompanied by hydration pressures. Also in this case, the harmful effect on the durability of building materials can be observed [7].

Because of the evident salt harmful effects on the performance and durability of buildings, the understanding to the mechanisms of coupled moisture and salt transport is quite important issue for building physicist as well as for practitioners.

One of the effective tools, which can help to predict the salt transport and salt induced damage, represents mathematical modelling. To give only a couple of examples, the main reasons for the salt presence in building structures can be identified using computer simulations. The progress of salt accumulation in walls and renders can be predicted and the time of necessary repair estimated. The effect of different desalination methods can be simulated in advance and the application of the particular techniques optimized.

The effectiveness of the application of mathematical modelling in dealing with salt induced damage critically depends on the type of the model used. Salts can be transported in the porous system only in the presence of water. Therefore, modelling the salt ingress into porous materials in the form of coupled water and salt transport is indispensable. As the accuracy of computer simulated data obtained by any model is primarily determined by the accuracy of its input parameters, a choice of a particular model should always be done in a direct link to the available material parameters.

Determination of material parameters for the computational modelling of coupled moisture and salt transport is not an easy task and is probably the milestone in the application of advanced computer codes for specific type of materials and structures.

In this work we focused on the assessment of parameters describing the salt transport in masonry materials originally used in the Central European territory, nominally sandstone and lime mortar.

The assessment of material parameters is done using inverse analysis of experimentally determined salt and moisture concentration profiles assuming diffusion-advection mechanism of salt solution transport including the salt ions bonding on the pore walls. In this model, the moisture transport is described by moisture diffusivity (κ) and salt transport by salt diffusion coefficient (D).

Materials

In this paper, materials that were originally used for historical buildings in the Central Europe territory are studied.

The sandstone originated from Mšené-lázně quarry (Czech Republic). It is siliceous fine-grained material usually used especially for ornamental parts of the architecture, like gothic flowers, romantic shells, and sculptures. The first reference to the extraction of sandstone from the quarry close to Mšené-lázně, a town north-west of Prague, was found in the land register of Roudnice Monastery in 1388 and the quarry is operational to the present [7]. Mšené sandstone is psamitic equigranular rock, about 95% of which is made up of suboval quartz clasts. Other mineral grains are present only as accessories (tourmaline, epidote, muscovite and zircone). Quartz grains reach up to 0.1 mm in diameter, but those of muscovite are larger, up to 0.3 mm. The matrix is formed by clay minerals (mainly kaolinite).

Application of lime-based binders for plasters and mortars can be traced up to ancient world and their use was significant until the end of 19th century. On this account, the properties of lime-based plaster from the point of view of salt transport and storage are studied as well. The composition of the tested plaster mixture is given in Table 1.

Table 1: Composition of tested plaster mixture

Amount [kg]		
Lime CL 90	Sand 0/2 mm	Water
4.80	14.40	4.80

Plaster mixture was prepared using laboratory mixing machine with forced rotation for 3 minutes and then compacted using vibrating machine. Mixture was cast into a standard prism form, after two days all prisms were taken out of forms and then cured for 28 days in high relative humidity environment.

The lime CL 90 was produced by limekiln Mokrá, Czech Republic. Sand 0/2 mm fraction was delivered by Heidelberg Cement Group, Brněnské písky Inc., affiliate Bratčice, normalized according to EN 196-1.

For characterization of the studied materials, their basic properties were measured on water vacuum saturation principle using the Archimedes' weight. The results are presented in Table 2, where ϱ_b is the bulk density, ϱ_{mat} matrix density and ψ total open porosity.

Table 2: Basic material properties of the studied materials

Material	**ϱ_b [kg/m^3]**	**ρ_{mat} [kg/m^3]**	**Ψ [-]**
Sandstone	1807	2627	0.31
Lime plaster	1650	2575	0.36

For the assessment of parameters describing the coupled moisture and salt transport, the experimental measurement of moisture and salt concentration profiles were done.

The arrangement of the experiment for determination of moisture and salt concentration profiles was analogous to standard water suction experiments. The rod-shaped samples with the dimensions of 20 x 40 x 160 mm were first dried at 80°C and 0.1 mbar and water and vapour-proof insulated by epoxy resin on all lateral sides. Then, they were exposed by their 40 x

20 mm face to the penetrating KNO_3 solution (concentration 101.1 kg/m3 of solution). Duration of the experiment was 30, 60 and 90 minutes for three different groups of samples. After this time, the samples were cut into 8 pieces and in each piece water content and nitrate concentration were measured. Moisture content was determined by the gravimetric method using weighing the moist and dried specimens. In the determination of nitrate concentration, the particular samples were after drying first ground by a vibration mill so that grains smaller than 0.063 mm were obtained. Then the ground samples were overflowed by 80°C warm distilled water and leached. The nitrate contents in particular leaches were measured using the pH/ION 340i device with utilization of ion selective electrode (ISE).

Since the applied diffusion-advection model of salt transport takes into the account the effect of salt ions bonding on the pore walls, the nitrate binding isotherms were measured for all the studied materials as well. For the determination of ion binding isotherm, Tang and Nilsson modified absorption method was used. This modification consisted in using the specimens of more realistic dimensions (40 x 40 x 10 mm) instead of crushed specimens [2]. On the basis of the measured ion binding isotherm of KNO_3, the profiles of bound and free nitrates were determined.

Inverse Analysis of Experimental Data

The inverse analysis of experimentally determined moisture and nitrate concentration profiles was done assuming that the salt solution transport is realized on the diffusion-advection principle. In this way, the salt solution transport is described by system of two parabolic equations, whereas one of them describes the salt mass balance and the second one water mass balance (for details see e.g. [5], [8]). Since we have assumed for the simplicity of the studied problem only 1-D salt solution transport, the system of two parabolic equations could be subjected to an inverse analysis in a similar way as for one parabolic equation, provided the initial and boundary conditions were simple enough, and the material parameters D (salt diffusion coefficient) and κ (moisture diffusivity) could be identified as functions of water content and salt concentration. The simplest possibility of such an inverse analysis is an extension of the Boltzmann-Matano treatment [4] under the same assumptions of constant initial conditions and Dirichlet boundary conditions on both ends of the specimen for both moisture content and salt concentration where one of the Dirichlet boundary conditions is equal to the initial condition. The details on the final equations for calculation of moisture dependent moisture diffusivity and salt diffusion coefficient in dependence of salt concentration can be found in [5].

Results and Discussion

The experimentally determined moisture and nitrate concentration profiles are given in Figures 1-2. For the computational inverse analysis it was necessary to smooth the measured data to obtain continuous functions. The linear filtration method was used for that purpose (see Figs. 1-2).

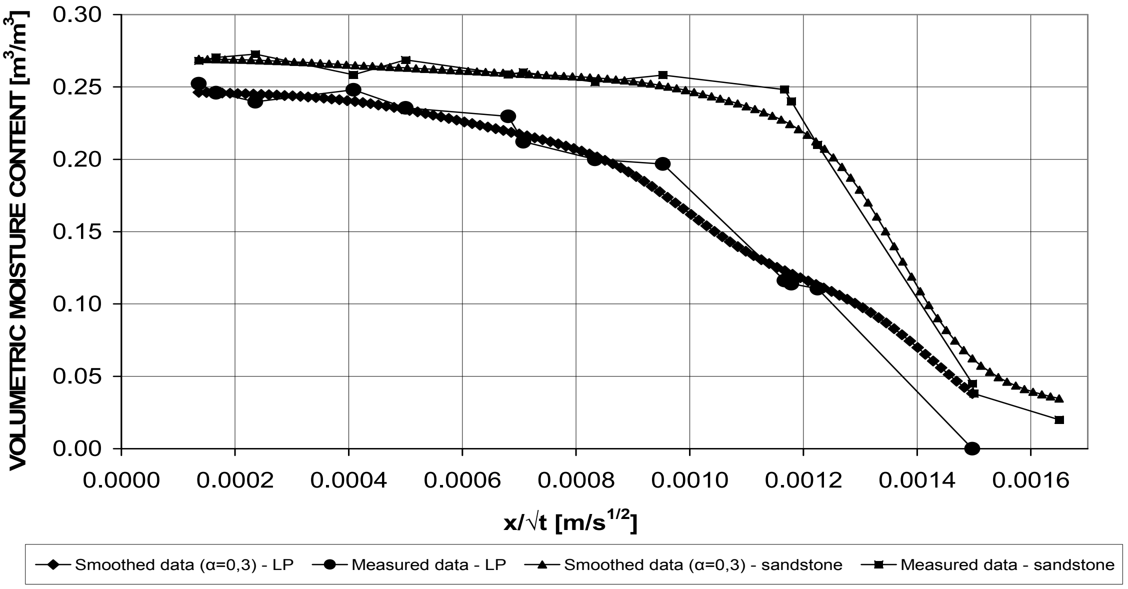

Figure 1: Moisture content profiles measured for penetration of KNO3 solution

The comparison of measured moisture profiles (see Fig. 1) shows that the transport of KNO_3 -in-water solution in sandstone was slightly faster than in the case of lime plaster. This finding is contrary to the measured total open porosity of studied materials, which was for the lime plaster higher by about 5%. However, we can assign these results to the differences in the pore size distribution of particular materials. This observation was proved also by the measurement of total salt concentration profiles presented in Figure 2.

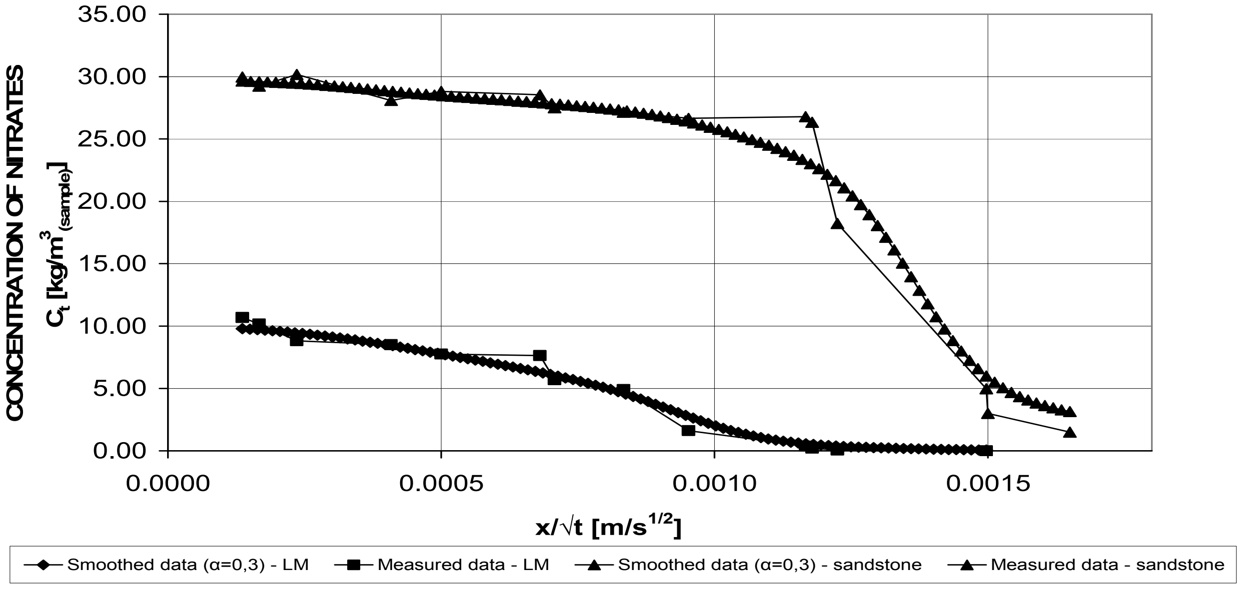

Figure 2: Total nitrate concentration profiles

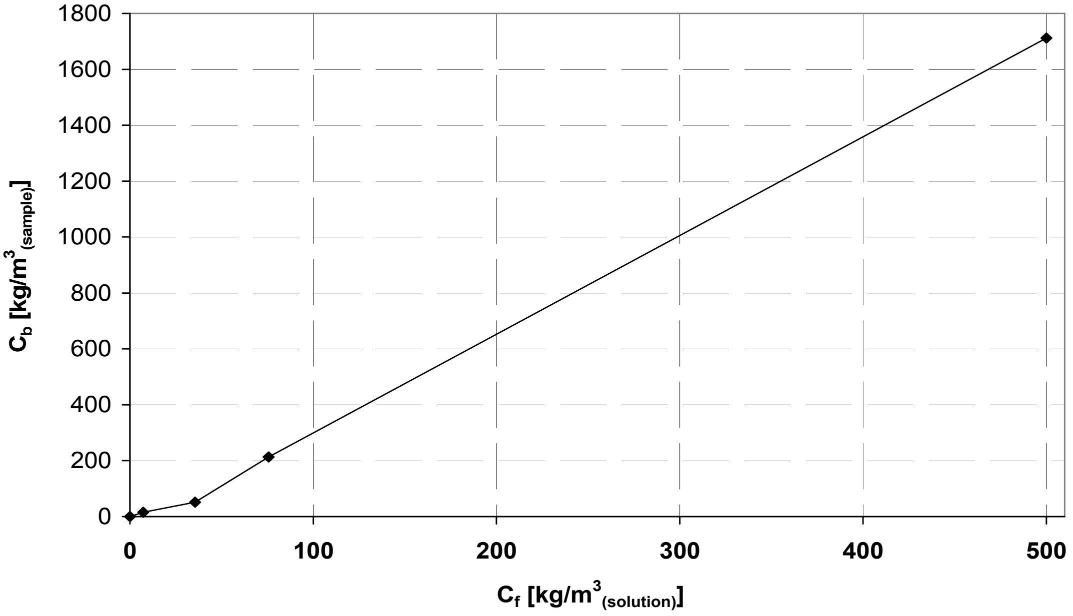

Figure 3: Binding isotherm of KNO3 for the sandstone

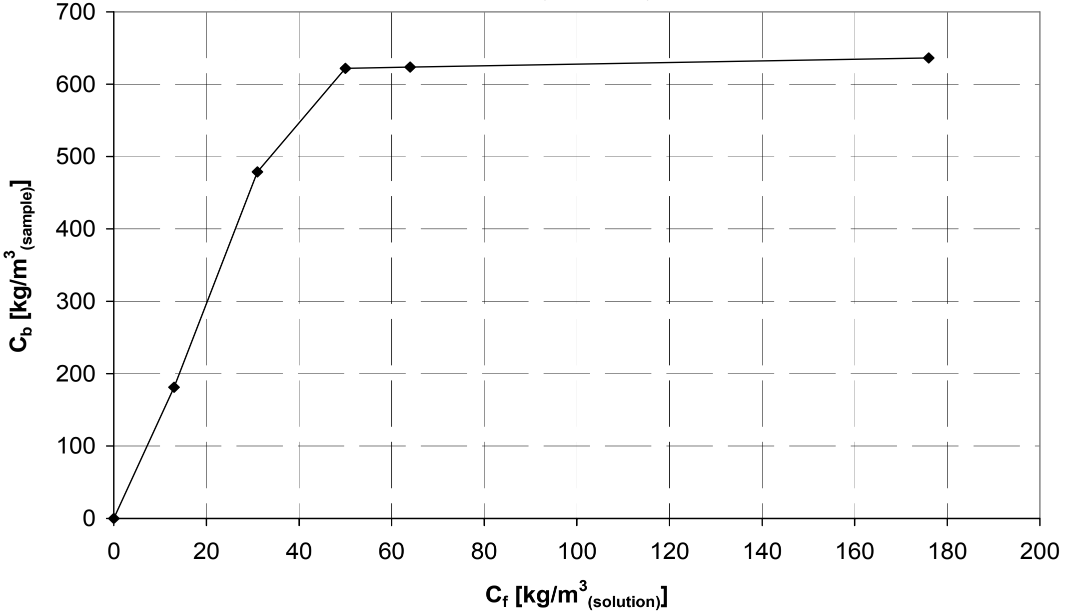

Figure 4: Binding isotherm of KNO3 for the lime plaster

The nitrate binding isotherms measured by modified Tang and Nilsson adsorption method are shown in Figures 3-4. They give evidence of the very high nitrate binding capacity of both studied materials. In the previous works (see e.g. [1], [6]) we have already studied the transport and binding of chloride ions in sandstone. The results presented in these papers clearly show that the binding capacity of Mšené sandstone is completely different for particular salt solutions. On this account there is evident, the obtained results of inverse analysis presented in this paper can be used only for the description of the KNO_3 solution transport and for the other different types of salt solution, additional measurement and calculations are needed.

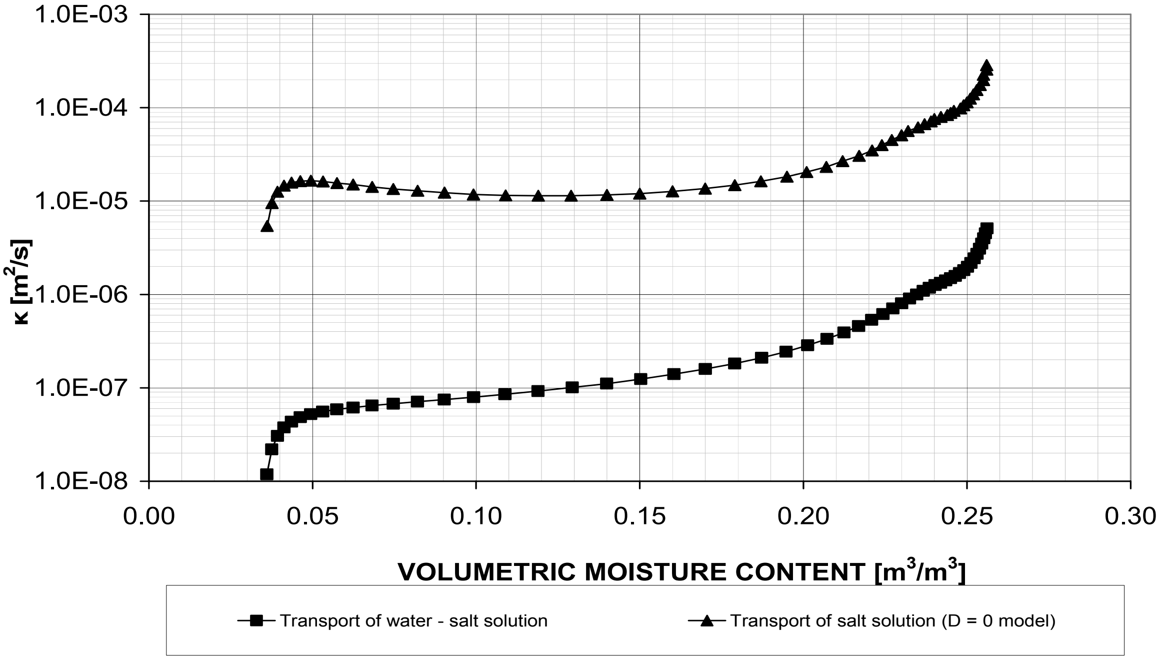

Figure 5: Moisture diffusivity for the studied sandstone

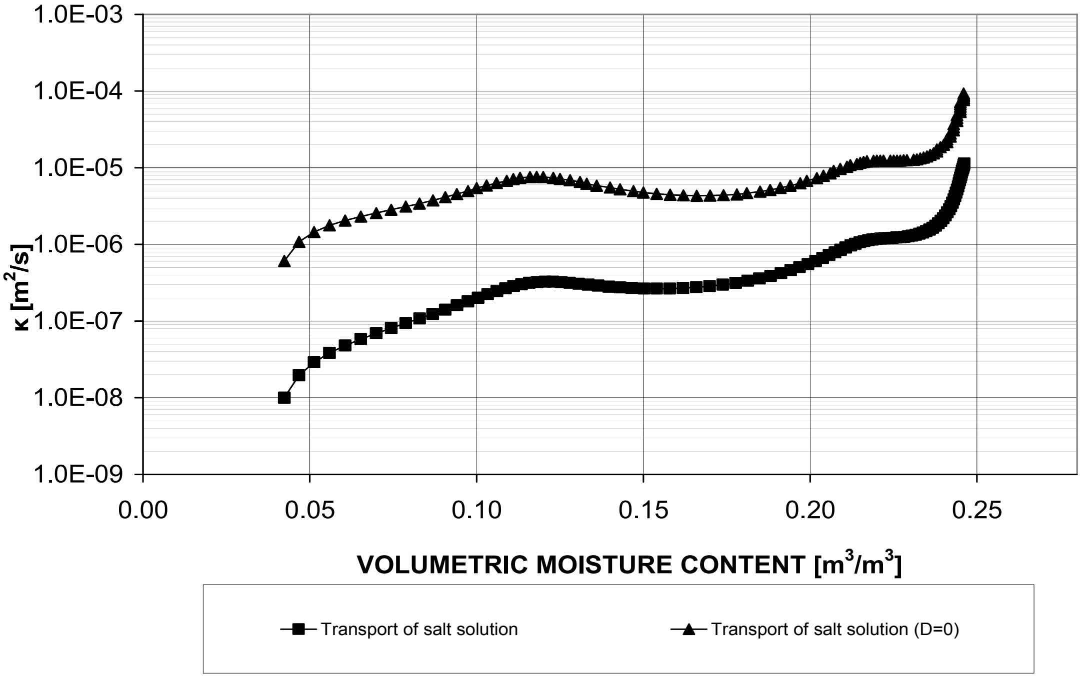

Figure 6: Moisture diffusivity for the studied lime plaster

The results of inverse analysis are presented in Figures 5-8. They show that the possible neglect of nitrate diffusion in the liquid phase is apparently wrong, because the moisture diffusivity calculated from nitrate concentration profiles under this assumption is two to three orders of magnitude higher than moisture diffusivity calculated from moisture profiles.

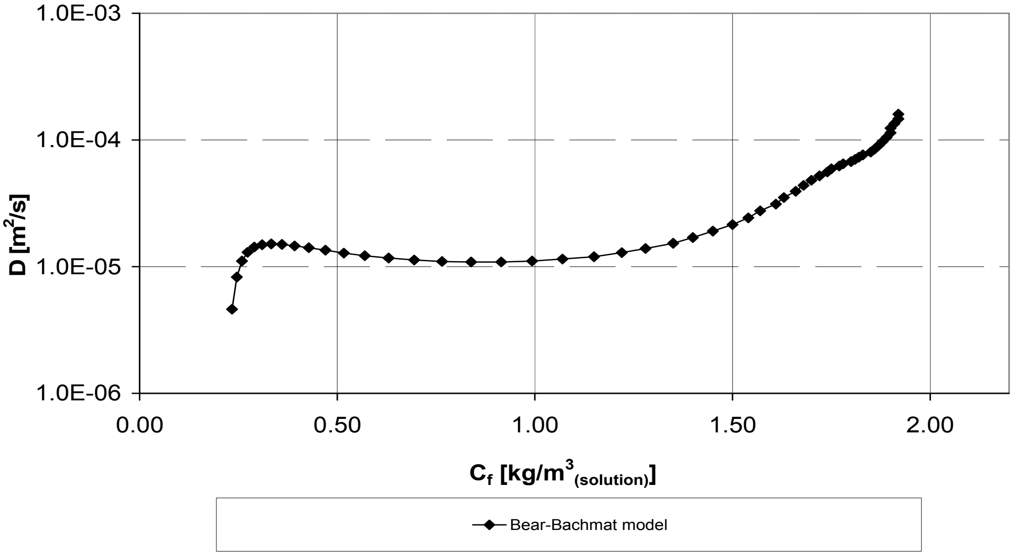

Figure 7: Nitrate diffusion coefficient for the sandstone

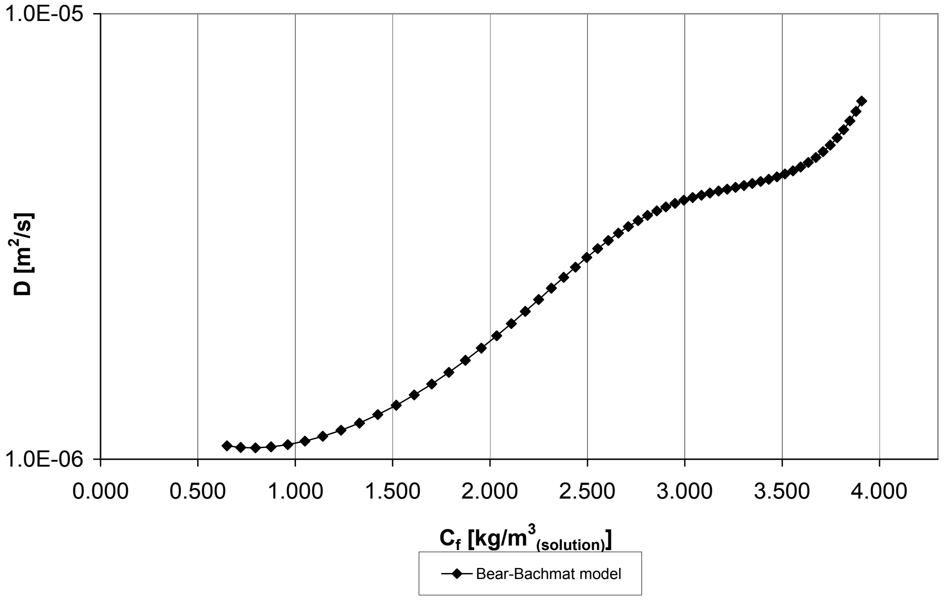

Figure 8: Nitrate diffusion coefficient for the lime plaster

The dependence of nitrate diffusion coefficient on concentration is shown in Figures 7-8. From the quantitative point of view, the calculated nitrate diffusion coefficient is quite high, about three to four orders of magnitude higher than the diffusion coefficients of most ions in free water. Therefore, the common diffusion mechanism is probably not the only driving force for nitrate transport within the liquid phase and some other driving forces are taking place here. This acceleration of nitrate transport can be attributed most probably to surface diffusion on pore walls and/or to osmotic effects [3]. Comparing the results obtained for the sandstone and lime plaster, the calculated concentration dependent nitrate diffusion coefficients correspond to the experimentally determined moisture and nitrate concentration profiles.

Conclusions

The main practical outcome of the presented work represents determination of two main parameters describing the coupled water and nitrate transport in sandstone and lime plaster. The performed experiments and calculations have revealed important fact that different salt solutions are transported in the porous structure of materials with specific velocity. This finding is in agreement with differences in diffusion coefficients of chloride, sulphate and nitrate ions in water (CRC Handbook of Chemistry and Physics, 85th Edition, Ed. David R. Lide, 2004 – 2005, CRC Press). In our opinion, the crucial factor that affects the transport of salt ions is the shape and dimension of their molecules and the pore size distribution curves of the studied materials.

Acknowledgement

This research has been supported by the Czech Ministry of Education, Youth and Sports, under project No MSM 6840770031.

References

[1] FIALA L., PAVLÍK Z., JIŘIČKOVÁ M. & ČERNÝ R. Calculation of Moisture Diffusivity and Chloride Diffusion Coefficient of Sandstone Using Data from a Single Experiment, Symposium Trwalosc Materialów i Konstrukcji Budowlanych [CD-ROM], 103-106, Opole: Politechnika Opolska, 2006.

[2] JIŘIČKOVÁ, M. & ČERNÝ, R. Chloride Binding in Building Materials, Journal of Building Physics 29: 189-200, 2006.

[3] KONIORCZYK, M. & GAWIN, D. Modelling of transportation processes in building materials with different pore structures considering osmosis. Proceedings of the 12th Symposium for Building Physics, Dresden: TU Dresden, 823-830, 2007.

[4] MATANO, C. On the relation between the diffusion coefficient and concentration of solid metals, Jap. J. Phys. 8: 109-115, 1993.

[5] PAVLÍK, Z., JIŘIČKOVÁ M., FIALA L. & ČERNÝ R. Inverse Modeling of Salt Diffusion and Advection in Building Materials, Research in Building Physics and Building Engineering, 155-160, London: Taylor and Francis, 2006.

[6] PAVLÍK, Z., MICHÁLEK, P., PAVLÍKOVÁ, M., KOPECKÁ, I., MAXOVÁ, I. & ČERNÝ, R. Water and Salt Transport and Storage Properties of Mšené Sandstone, Construction and Building Materials 22(8): 1736-1748, 2008.

[7] PAVLÍK, Z., FIALA, L. PAVLÍKOVÁ, M. & ČERNÝ, R. 2008. Determination of Water and Nitrate Transport Properties of Sandstone Used in Historical Buildings, In Cenkler Matbaacilik Tic. Ltd., Durability of Building Materials and Components 11. Istanbul, 773-780, 2008.

[8] Pel, L., Kopinga K. & Kaasschieter E. F. Saline absorption in calcium-silicate brick observed by NMR scanning. J. Phys. D: Appl. Phys., 33: 1380–1385, 2000.

Thermomechanical modelling of maturing concrete mixture

Stanislav Šťastník, Jiří Vala, Jaroslav Nováček

Faculty of Civil Engineering, Brno University of Technology,
Veveří 95, CZ - 602 00 Brno, Czech Republic,
email: stastnik.s@fce.vutbr.cz, vala.j@fce.vutbr.cz, novacek.j@fce.vutbr.cz

Abstract: *Concrete is a natural composite whose properties are determined by hygro-thermo-chemo-mechanical processes at early age of its existence. Namely in the case of massive structures such processes should be controlled carefully to guarantee the optimal behaviour of a structure according to its proposed use. The complete mathematical model of heated concrete, treated as a multi-phase porous material, consists i) of 20 balance equations, coming from the mass, momentum and energy balance laws for continua with microstructure, corresponding to solid concrete, liquid mixture, water vapour and dry air, coming from the mass, momentum and energy balance laws for continua with microstructure and ii) of a set of constitutive relationships, identified by laboratory experiments. Some preliminary simulation results are available.*

Keywords: *Material properties of early-age concrete, thermodynamic principles, hygro-thermo-chemo-mechanical modelling, partial differential equations of evolution.*

Introduction

Quantitative analysis of early-age behaviour of concrete is a rather complicated multi-physical problem. Every reliable thermomechanical model of maturing concrete mixture should include at least a) reversible elastic deformation, b) viscous creep of material and c) volume changes, unlike a) and b) independent of external loads, namely c1) autogenous volume changes, driven by chemical shrinkage of cement particles, c2) subsequent thermal expansion, c3) drying caused by water loss into environment and c4) later carbonation. Three principal internal and external influences are 1) internal hydration heat, generated by the hydration hydraulic processes, 2) ambient temperature variation, connected with ambient humidity variation (natural or artificial ones), 3) external mechanical loads; thus evidently hygro-thermo-chemo-mechanical modelling and simulation is needed.

Moreover, the proper quantitative study such physical and chemical processes should be supported by the multi-scale analysis: especially [4] for samples prepared as mixtures of cement, water and air distinguishes anhydrous-cement scale (from 10^{-8} to 10^{-6} m), cement-paste scale (from 10^{-6} to 10^{-4} m) with growing crystals and capillary phenomena, mortar scale (about 10^{-2} m) with particles included in a seemingly homogenous matrix and macroscale (about 10^{-1} m) for a natural composite. The physical formulations come i) in [1] from common phenomenological relations with a large number of model parameters, ii) in [7] from phenomenological coefficients in Onsager reciprocity relations and Gibbs-Duhem conditions, iii) in [2] and [4] from mechanistic calculations at representative volume elements for multiple scales and, alternatively, iv) in [3] and [5] from thermodynamic conservation principles applied to hybrid mixture theory.

The mathematical and computational homogenization techniques cannot be assigned to i), ii), iii), iv) exactly; their applicability is also limited by reasonable quantitative data from laboratory measurements (at all considered scales) and corresponding observations in situ. In the rough classification, the following approaches can be found in the literature: a) no proper homogenization occurs, macroscopic ad hoc equations are obtained using statistical arguments (with such difficulties as lack of data and low validity), b) "multi-physical" homogenization (often rejected by the mathematical society), derived from the RVE analysis of physical and chemical processes at various scales (using least squares and similar tricks), c) homogenization in standard Lebesgue and Sobolev spaces, e.g. H-, G-, Γ- or two-scale convergence, whose best results refer to ideal periodic structures (in general effective characteristics may not exist), d) homogenization in general Banach spaces, as convergence in Young measures or Σ-convergence for so-called homogenization structures (unfortunately, such formulations lead to formally very complicated and physically non-transparent theories, moreover no software is available), e) homogenization with probability measures, requiring deep knowledge from the theory of stochastic processes.

This paper applies the generalized approach iv), respecting some results of the multiple-scale analysis iii). Its aim is to demonstrate the derivation of the system of evolution equations for 20 physically transparent variables, supplied by initial and boundary conditions, derived from basic principles of classical thermodynamics, without non-physical or additional numerical manipulations. Nevertheless, a lot of question remains open, both in the formal existence theory in appropriate spaces of abstract functions, and in the convergence of homogenization structures and other numerical procedures. Although all constitutive relations are suggested to be able to be identified experimentally, still other potential difficulties may be hidden in the uncertainty of proposed measurements and their sensitivity to unadvisable influences.

Derivation of evolution equations

We shall study the behaviour of a maturing concrete body in the Cartesian coordinate system $x = (x_1, x_2, x_3)$ in the 3-dimensional Euclidean space R^3 in arbitrary time $t \geq 0$. We shall use the simplified notations $\dot{\psi} = \partial\psi/\partial t$ for time derivatives and $\psi_{,i} = \partial\psi/\partial x_i$ for x_i-derivatives where $i \in \{1,2,3\}$. The indices $\varepsilon \in \{s, w, v, a\}$ will refer to the following material phases: solid material s, liquid water w, water vapour v and dry air a. In the case of vector variables with values in R^3 we shall write only ψ instead of (ψ_1, ψ_2, ψ_3), in the case of matrix variables with values in $R^{3\times 3}$ we use the abbreviation ψ for $\psi_{i,j}$, $i, j \in \{1,2,3\}$. The notation δ is reserved for Kronecker symbols everywhere.

The multiphase medium at the macroscopic level can be described as the superposition of all ε-phases, whose material point with coordinates $x_i^{\varepsilon 0}$ in the reference configuration Ω^0 occupies a point with coordinates $x_i^{\varepsilon}(t)$ in the deformed configuration $\Omega(t)$ in R^3 at time t. In the Lagrangian description of the motion the position of each material point can be expressed as $x_i^{\varepsilon}(t) = x_i^{\varepsilon 0} + u_i^{\varepsilon}(x_i^{\varepsilon 0}, t)$ where $u_i^{\varepsilon}(x_i^{\varepsilon 0}, t)$ denotes the displacement at chosen time. Thus

$$F_{ij}^{\varepsilon}(x^{\varepsilon 0}, t) = \frac{\partial x_i^{\varepsilon}(x^{\varepsilon 0})}{\partial x_j^{\varepsilon 0}} = \delta_{ij} + \frac{\partial u_i^{\varepsilon}(x^{\varepsilon 0}, t)}{\partial x_j^{\varepsilon 0}}$$

can be taken as a deformation characteristic, needed later in strain-stress constitutive relations. Moreover, we need also the first and second material time derivatives, following the velocity of ε-constituents, well-known as velocities (displacement rates) $v_i^{\varepsilon}(x_i^{\varepsilon 0}, t)$ and accelerations (velocity rates) $a_i^{\varepsilon}(x_i^{\varepsilon 0},t)$. By the chain rule we have $v_i^{\varepsilon}(x^{\varepsilon 0},t) = \dot{u}_i^{\varepsilon}(x^{\varepsilon 0},t) + u_{i,j}^{\varepsilon}(x^{\varepsilon 0},t) v_j^{\varepsilon}(x^{\varepsilon 0},t)$, $a_i^{\varepsilon}(x^{\varepsilon 0},t) = \dot{v}_i^{\varepsilon}(x^{\varepsilon 0},t) + v_{i,j}^{\varepsilon}(x^{\varepsilon 0},t) v_j^{\varepsilon}(x^{\varepsilon 0},t)$; here the terms $u_{i,j}^{\varepsilon} v_j^{\varepsilon}$ and $v_{i,j}^{\varepsilon} v_j^{\varepsilon}$, applying the Einstein summation rule for all indices $j \in \{1,2,3\}$, can be understood in the sense of scalar products $\operatorname{grad} u^{\varepsilon} \cdot v^{\varepsilon}$, $\operatorname{grad} v^{\varepsilon} \cdot v^{\varepsilon}$ (although the construction of such general grad-operator is not quite trivial).

If ω^{ε} is a source corresponding to a scalar quantity ψ^{ε} then the conservation of a scalar quantity ψ^{ε} in the notation of [6] reads

$$\dot{\psi}^{\varepsilon} + (\psi^{\varepsilon} v_i^{\varepsilon})_{,i} = \omega^{\varepsilon} \ ;$$

the derivative with respect to the i-th space coordinate and the summation should be precised again as above. At the RVE level, for some physical quantities ψ related to a phase ε we must distinguish between their resulting averaged values ψ_{ε} and their intrinsic averaged values ψ^{ε}. The needed relation $\psi_{\varepsilon} = \eta^{\varepsilon} \psi^{\varepsilon}$ contains the volume fraction $\eta^{\varepsilon}(n,S)$, a function of the material porosity n and the saturation S; both n and S are varying substantially during the hydration process. Let ζ be the volume fraction of vapour, contained in the gas (vapour and dry air) phases. We have $\eta^{s} = 1-n$, $\eta^{w} = nS$, $\eta^{v} = n(1-S)\zeta$, $\eta^{a} = n(1-S)(1-\zeta)$ for all particular phases.

We shall assume local thermal equilibrium which implies that, at each (x,t), the temperature T of all phases is the same. The a priori unknown (and mutually independent) variables in our model are now all 12 velocities v_i^{ε}, the (absolute) temperature T and also 4 material densities ρ^{ε} . Assuming that vapour and dry air are perfect gases, we can calculate their pressures as $p^{v}(\rho^{v},T)$ and $p^{a}(\rho^{a},T)$ algebraically from the Clapeyron law. This is not valid for the liquid phase, whose pressure p^{w} is the additional unknown variable. Let us remind that for the total gas pressure $p^{g} = p^{v} + p^{a}$ the capillary pressure can be evaluated as $p^{c} = p^{g} - p^{w}$. In the evaluation of phase changes two crucial quantities occur: the (usually increasing) mass m^{w} of skeleton (and corresponding sink of liquid water mass) and the vapour mass m^{v} caused by (liquid) water evaporation or desorption. Both m^{w} and m^{v} depend evidently (in a complicated way) on T, p^{g}, p^{c}, n, S, water cement ratio, etc. The direct reliable determination of m^{w} from the analysis of chemical reaction occurring in the irreversible process of cement hydration is impossible in practice; thus the hydration kinetics has to be described using some empirical parameter(s). The so-called hydration degree Γ, a normalized variable with values between 0 and 1, is introduced in [3]; its evaluation requires always to solve an auxiliary evolution problem for certain nonlinear ordinary differential equation with experimentally identified coefficients. The time evolution of mass m^{w} can be then determined from the formally simple formula $m^{w} = \Gamma m_{\infty}^{w}$ where m_{∞}^{w} characterizes the final mass of hydrated (chemically combined) water. No similar approach is available to the evaluation of m^{v}; thus we have to consider m^{v} as the further unknown variable. The saturation S is an experimentally determined function of p^{c} and T. The porosity can be obtained from the formula $n = 1-(1-n_0)/\det F^{s}$ where $n_0(x^{s0})$

denotes the porosity in the reference configuration (at $t = 0$). The vapour fraction ζ remains to be calculated from the balance equations.

The available balance equations are 4 mass balance equations and 4 balance equations (for 4 phases) and 12 linear momentum balance equations (for 4 phases and 3 components); thus the complete system of evolution contains 20 equations. We have now 20 unknown fields ρ^{ε} (4 fields), v_i^{ε} (12 fields), T, p^w, m^w and ζ. The remaining variables occurring in the balance equations have to be obtained from appropriate constitutive equations.

The mass balance works with scalar quantities $\psi^{\varepsilon} = \rho_{\varepsilon}$ and corresponding source terms $\omega^s = -\dot{m}^w$, $\omega^w = \dot{m}^w - \dot{m}^v$, $\omega^v = \dot{m}^v$, $\omega^a = 0$. No additional algebraic relations (except the above discussed ones) are needed.

Since all phases are considered microscopically non-polar, the angular momentum balance forces only the symmetry for the partial Cauchy stress tensor τ, i. e. $\tau_{ij} = \tau_{ji}$ for each real matrix τ generated by such stress components; the relation between τ_{ij} and deformation characteristics will be explained later. The formulation of the linear momentum balance in 3 directions is much more difficult. The first step is to introduce $w_i^{\varepsilon} = \rho_{\varepsilon} v_i^{\varepsilon}$ and to choose (for all particular i) $\psi^{\varepsilon} = w_i^{\varepsilon}$. The second step starts with the definition of the total Cauchy stress σ^{ε} (unlike the partial one, τ_{ij}) in the form $\sigma_{ij}^{\varepsilon} = \tau_{ij}\delta^{s\varepsilon} - \delta_{ij} p_{\varepsilon}$ (which generates a symmetrical matrix again) and continues with the setting $\omega^{\varepsilon} = \sigma_{ij,j}^{\varepsilon} + \rho_{\varepsilon}(g_i - a_i^{\varepsilon} + t_i^{\varepsilon})$ where g_i denotes the gravity accelerations g_i and t_i^{ε} the additional (time variable) accelerations due to interactions with other phases; the last term needs more explanation. In practical applications the matrices σ^{ε} (for particular ε) cannot be distinguished frequently; thus the effective (phase-independent) total Cauchy stress $\sigma_{ij} = \tau_{ij} - \delta_{ij}(p_w + p_v + p_a)$ is useful, too. The constitutive relationships for the solid phase, e. g. those between τ and u^s, v^s, etc., needs the multiplicative decomposition into a finite number M of matrix components in the form $F^s = F^{s1} \ldots F^{sM}$ to admit an appropriate relation $\tau(F^{s1},\ldots,F^{sM},\dot{F}^{s1},\ldots,\dot{F}^{sM},\ldots)$. The setting of t_i^{ε} is possible from the Darcy law; for $\varepsilon \neq s$ there holds $\mu^{\varepsilon}\rho_{\varepsilon}(v_i^{\varepsilon} - v_i^s) = K_{ij}^{\varepsilon}(\rho_{\varepsilon}(g_j - a_i^{\varepsilon} + t_j^{\varepsilon}) - p_{\varepsilon,j})$ where the new material characteristics occur: μ^{ε} is the dynamical viscosity and K_{ij}^{ε} refer to the elements of the permeability matrix, depending on ρ_{ε} again.

The energy balance comes from scalar quantities $\psi^{\varepsilon} = w_i v_i / 2 + \rho_{\varepsilon}\kappa^{\varepsilon}$ where κ^{ε} is usually defined as $\kappa^{\varepsilon} = c^{\varepsilon}T$ for the thermal capacities c^{ε}, in general functions of T and p^c, and from source terms $\omega^{\varepsilon} = (\sigma_{ij,j}^{\varepsilon} + q_i^{\varepsilon})_{,i} + \rho_{\varepsilon}(g_i - a_i + t_i^{\varepsilon}) + \tilde{\omega}^{\varepsilon}$ where q_i^{ε} denote the internal heat fluxes. By the Fourier law $q_i^{\varepsilon} = -\lambda_{ij}^{\varepsilon}T_{,j}$ with the thermal conductivity matrices λ^{ε}, in general functions of T and p^c again. All additive terms $\tilde{\omega}^{\varepsilon}$ can be expressed for particular phases, similarly to source terms in mass balance, in the form $\tilde{\omega}^s - = -m^w h^w$, $\tilde{\omega}^w = m^w h^w - m^v h^v$, $\tilde{\omega}^v = m^v h^v$, $\tilde{\omega}^a = 0$; two new characteristics here are the specific enthalpies of hydration h^w and evaporation h^v.

The process of redistribution of the complete set of unknown variables $(\rho^{\varepsilon}, v_i^{\varepsilon}, T, p^w, m^v, \zeta)$, driven namely by the chemical reactions in the mixture, starting from certain a priori known values of these variables at $t = 0$, is substantially conditioned by the boundary conditions. In addition to the heat fluxes q^{ε} (everywhere on Ω), let us introduce also the boundary diffusion fluxes $r_i^{\varepsilon} = \rho_{\varepsilon}(v_i^{\varepsilon} - v_i^s)$. The values of unknown quantities are prescribed on the boundary of Ω (or on its part), i. e. in the form of the Dirichlet, Cauchy, Neumann, Robin, etc. types. The most frequent choices are $\sigma_{ij} \nu_j = \overline{t}_i$ with imposed tractions $\overline{t}_i$, $(\rho_a(v_i^a - v_i^s) + r_i^a)\nu_i = \overline{r}^a$ with imposed air fluxes $\overline{r}^a$, $(\rho_w(v_i^w - v_i^s) + r_i^w + \rho_v(v_i^v - v_i^s) + r_i^v)\nu_i = \overline{r}^w + \overline{r}^v + \beta(\rho_w)$ with imposed liquid water and vapour fluxes $\overline{r}^w$, $\overline{r}^v$ or $(\rho_w(v_i^w - v_i^s)h^v - \lambda_{ij} T_{,j})\nu_i = \overline{q} + \alpha(T)$ with imposed heat fluxes $\overline{q}$; α and β here are some heat and mass exchange functions, respectively.

Computational algorithm and illustrative example

The notation $R = (\rho^s, \rho^w, \rho^v, \rho^a)$, $V = (v_1^s, v_2^s, v_3^s, v_1^w, v_2^w, v_3^w, v_1^v, v_2^v, v_3^v, v_1^a, v_2^a, v_3^a)$, $T = (T, p^w, m^v, \zeta)$ will be now introduced for simplicity. Omitting the technical details (namely the t-step and x-mesh adaptivity), we can apply this idea in the following rough algorithm:

1. set R, V and T by the initial conditions for the zero time,
2. go to the next time step, preserving R, V and T,
3. solve R from the linearized version of (R), evaluate the correction ε_R of R,
4. solve V from the linearized version of (V), evaluate the correction ε_V of V,
5. solve T from the linearized version of (T), evaluate the correction ε_T of T,
6. if ε_R, ε_V and ε_T are sufficiently small, return to 3,
7. if the final time is reached, stop the computation, otherwise return to 2.

The algorithm hides all (discretized) constitutive relations; some of them are rather complicated, as the inequalities in the strain-stress dependencies for the elasto-plastic behaviour, or the determination of hydration degree Γ. The outputs are the (discretized) time distributions of R, V and T; the time distributions of all remaining variables can be completed a posteriori from constitutive relations.

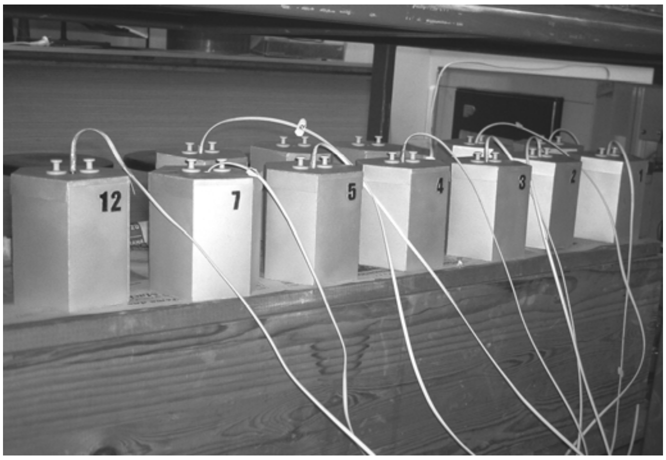

Figure 1: Calorimetric measurements for the identification of hydration heat

The validity of all computational predictions depends strongly on the reliability both of all material characteristics (constants and functions) and of the realistic description of environmental influences by the set initial and boundary conditions. This forces the analysis of a lot of inverse problems with simplified geometrical configuration, but with unknown characteristics. Figure 1 illustrates the calorimetric measurement, useful for the evaluation of hydration heat, consequently of hydration degree (as introduced in [3]). Figure 2 shows the development of hydration-driven changes of specimen length in time for two materials of interest.

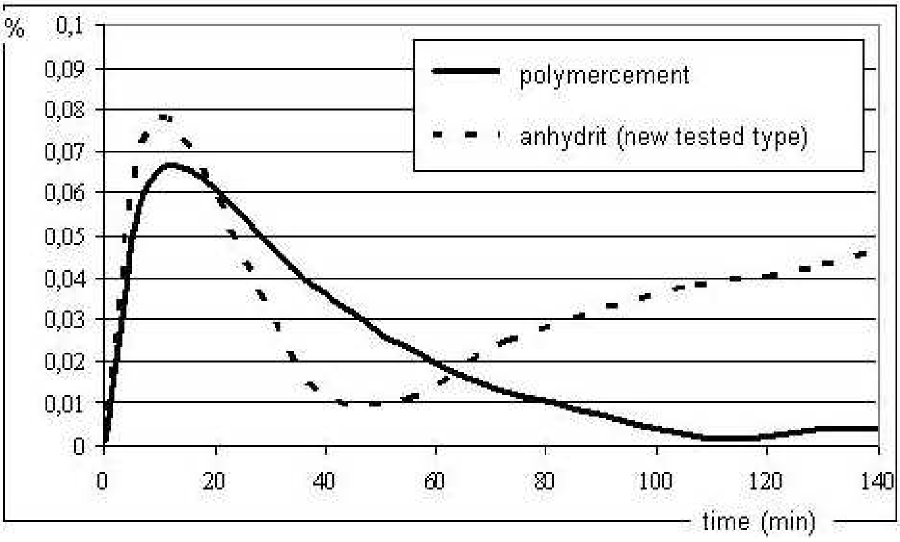

Figure 2: Length changes during hydration of two different material samples

The computational approach has been tested (under a set of rather strong simplifying assumptions, not discussed in this paper properly) on the simulation of the thermal behaviour of the proposed special material depot, surrounded by maturing concrete mixture. Figure 3 documents one time step of such ANSYS-supported simulation; its scale refers to the temperature range between 12 °C and 36 °C.

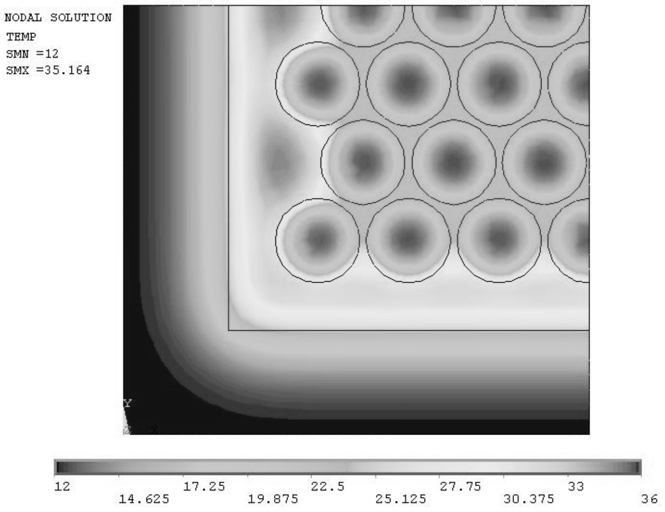

Figure 3: Example of the distribution of temperature in maturing concrete mixture

Conclusion

In this paper we have briefly presented an original computational approach, based on the conservation laws of classical thermodynamics, for the hygro-thermo-chemo-mechanical modelling of behaviour of maturing concrete mixtures. This approach is able to quantify the time development of all fields of interest without physically non-transparent tricks and strange empirical relations ignoring microstructural information.

However, such modelling is difficult, namely because of i) the non-periodic material structure, formed as a result of rather complicated chemical reactions, ii) its different mechanisms of deformation under stress and tension, including the danger of fracturing, iii) the uncertain boundary conditions from external environment, iv) the need of cooperation with the standard or pre-stressed reinforcement of other stiffening particles. The above presented numerical example should be thus understood as the first (but realistic) step in this analysis; both the experimental and theoretical work and the software development is still in progress.

Acknowledgement.

This research has been supported by the Ministry of Education, Youth and Sports of Czech Rep. No. MSM 0021630511.

References

[1] BAŽANT, Z. P. Prediction of concrete creep and shrinkage: past, present and future. Nuclear Engineering and Design. 2001. 203(1). p. 27 - 38. ISSN 0029-5493.

[2] BERNARD, O.; ULM F.-J.; LEMARCHAND, E. A multiscale micromechanics-hydration model for the early-age elastic properties of cement-based materials. Cement and Concrete Research. 2003. 33(9). p. 1293 - 1309. ISSN 0008-8846.

[3] GAWIN, D.; PESAVENTO, F.; SCHREFLER, B. A. Hygro-thermo-chemo/mechanical modelling of concrete at early ages and beyond. International Journal for Numerical Methods in Engineering. 2006. 67(3). p. 299 - 331 (Part I), 332 - 363 (Part II). ISSN 0029-5981.

[4] PICHLER, CH.; LACKNER, R.; MANG, H. A. A multiscale micromechanics model for the autogenous-shrinkage deformation of early-age cement-based materials. Engineering Fracture Mechanics. 2007. 74(1). p. 34 - 58. ISSN 0013-7944.

[5] SANAVIA, L.; SCHREFLER, B. A.; MANG, H. A. A formulation for an unsaturated porous medium undergoing large inelastic strains. Computational Mechanics. 2002. 28(3/4). p. 137 - 151. ISSN 0178-7675.

[6] VALA, J.; ŠŤASTNÍK, S. On the thermal stability in dwelling structures. Building Research Journal. 2004. 52(1). p. 31-56. ISSN 1335-8863.

[7] WATANABE, K.; TADA, S. From simultaneous heat and moisture transfer models to the modeling of deterioration of concrete. Building Research Institute Tsukuba (Japan). 2005. p. 1 - 10. Available at www.texte.co.jp/heat_moisture/Heat_mass_transf.pdf.

Dielectric properties of building materials

Zbigniew Suchorab[1], Henryk Sobczuk[2]

[1]Faculty of Environmental Engineering, Lublin University of Technology,
Nadbystrzycka 40B, 20-618 Lublin, Poland

email: Z.Suchorab@wis.pol.lublin.pl

[2]Faculty of Environmental Engineering, Lublin University of Technology,
Nadbystrzycka 40B, 20-618 Lublin, Poland

email: H.Sobczuk@wis.pol.lublin.pl

Abstract: *Building materials consist of at least three phases: solid, gaseous and liquid. Electrical parameters of building materials strongly depend on water content which has the great influence on them in the electromagnetic field. One of them is the dielectric permittivity ε which is the measure of the material particles interaction with the external, alternate electric field induction. It is generally known that water molecule differs from the other phases of building materials by its polar character which is expressed in the value of dielectric permittivity (80) comparing to air – 1, or solid phase particles (4-8). This difference is often used for estimation of water content in building materials using several measurement techniques and is the most useful using TDR (Time Domain Reflectometry) method. There article is a review of models and formulas describing dielectric permittivity of building materials used for moisture estimation.*

Keywords: *building materials, dielectric properties, TDR, moisture determination*

Introduction

Moisture of building barriers and materials is an important problem of buildings exploitation in moderate climate. It is a typical phenomenon which should be considered both from constructional and sanitary-hygienic point of view. Water is especially harmful for the material structure during winter season due to phase (melting and thawing) and thus volume changes. Also it should be here underlined that water is a good salt ions carrier, which during surface evaporation crystallize increasing its volume and damaging the porous structure of the material.

Above mentioned problems connected with water presence show that measurement of water content in building materials or structures is a very important and required issue which would allow to keep the appropriate water conditions of the buildings. During the years many measurement methods have been developed. These methods can be generally divided into direct and indirect ones.

Moisture determination methods

For moisture determination of building materials both direct and indirect methods can be applied. First of them are very precise, but also time consuming and proving no monitoring potential. Application of the direct methods requires sampling and thus destruction of the barriers. Nowadays they are mainly used for calibration of the other – indirect methods. The most popular among direct techniques is gravimetric method – the samples are weighed before and after drying in 105°C and then the determined mass is recalculated into moisture.

Indirect methods rely on determination of other parameters which are dependent on moisture – for example electric resistance, dielectric permittivity, ability to moderate the neutrons or water potential. Indirect methods are less precise because the determined, indirect parameters often depend on other properties like salinity, temperature or frequency. This should be considered as disadvantage of such an approach. On the other hand, indirect methods offer quick measurements, high monitoring potential, and relatively good accuracy of measurement.

In this paper we focus on the dielectric methods of indirect water content determination. Two of them are of high practical importance: capacitance method and TDR (Time Domain Reflectometry). Both of them determine dielectric permittivity of the measured material.

Dielectric permittivity, often called dielectric constant is a parameter determining water molecules energy released in external, alternate electromagnetic field. For porous materials like rocks or building materials it is a resultant of the permittivities of particular phases (solid, gaseous and finally liquid – water). Porous materials consist of at least three phases: solid, gaseous and liquid. From the electrical point of view they can be treated as weak conductors and water has the greatest influence on their behavior in the presence of the electromagnetic field. This is caused by high dielectric permittivity of water caused by the fact that water and its molecule structure which is a dipole [1].

Relative dielectric permittivity ε expresses the material particles interaction with external, alternate electric field induction which makes water molecules rotate according to the input field to follow its direction. This causes energy storage, which is released after the external field disappears. This energy is expressed as the real part of the dielectric constant ε'. Imaginary part ε'' of the dielectric permittivity represents energy loses caused by ionic conductivity dependent on the salts concentration. Dielectric permittivity of such medium with non-zero electric conductivity is described by the following formula [1]:

$$\varepsilon_{\omega} = \varepsilon'_{\omega} - i\left(\varepsilon''_{\omega} + \frac{\sigma_0}{\varepsilon_0 \omega}\right) \tag{1}$$

ε'_{ω} = real part of dielectric permittivity of medium in relevant frequency ω;

ε''_{ω} = imaginary part of dielectric permittivity of medium in relevant frequency ω;

i = imaginary unit; σ_0 = electrical conductivity; ε_0 = dielectric permittivity of vacuum

(ε_0 = 8,85·10-12 F/m); ω = angular frequency of the external electric field.

Capacitance method for moisture determination

Capacitance method is a dielectric, user friendly method which offers quick and non-destructive water detection. There are several limitations in its exploitation. The most important is accuracy changeability due to chemical composition of the material and also salinity influence [2].

TDR (Time Domain Reflectometry)

Problems of capacitance probes accuracy are caused by low operating frequency of the electromagnetic field. The TDR method works in much higher frequency. In lower frequencies there is high influence of imaginary part of dielectric permittivity (which states for salinity). TDR devices work in the range frequencies of about 1GHz. From the diagram below (Figure 1) it is clearly visible that for that frequencies imaginary part is low, constant and can be neglected. Also it must be underlined here that the real part of the complex dielectric permittivity is relatively high and constant.

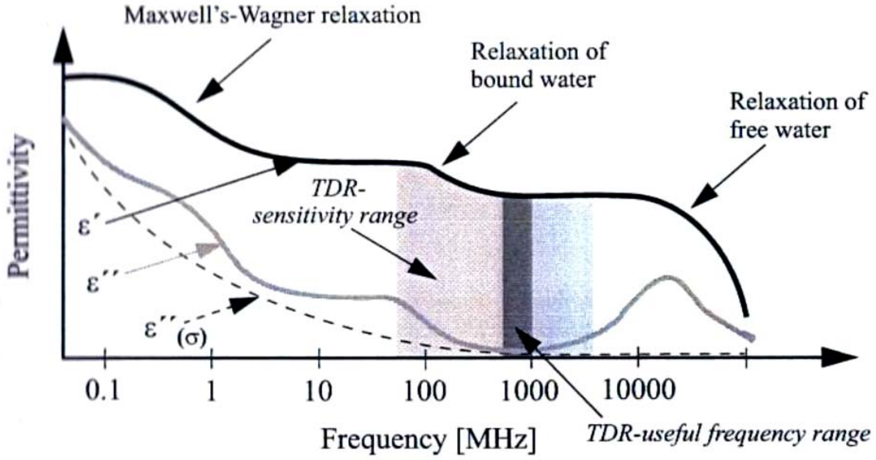

Figure 1: Dielectric permittivity dependence on frequency [3, 4]

Dielectric permittivity can be determined using TDR device with following formula:

$$\varepsilon = \left(\frac{ct_p}{2L}\right)^2 \tag{2}$$

ε – dielectric permittivity (determined parameter), c – light velocity in vacuum [3·108 m·s-1], tp – measured time of signal propagation along waveguide [s], L – lenght of the waveguide [m].

Structure of building materials

Building materials are complicated in structure and their chemical composition. This strongly influences their dielectric parameters that can be read using capaticance or TDR method. They are mainly porous media (with the exception of glass steel etc.) which means that they are formed by at least two phases – solid (mineral) and gaseous in the form of the air gaps. Partially saturated materials (the most natural state) consist of three phases – solid, gaseous and liquid (water). In totally saturated states the air is removed by water which fully fills the pores.

One of the most important parameters characterizing building materials is porosity which is generally defined as a quotient of pores volume and whole sample volume. In case of the porous media like building materials it is a very complicated parameter because it not only depends on volume but also the pores shapes and their distribution (Figures 2 and 3). This directly influences moisture parameters of the materials and thus dielectric.

From the water-air point of view the pores can be divided into the following:

- Closed pores (not available for water and the air) – totally isolated. For example pores in polystyrene or polyurethane foam (insulating materials),
- Open pores – connected with external environment by the system of connections with other pores. Available for migrating water and air – important from the point of view moisture considerations. Among them there are: single side open pores, two sides open pores, joined pores and clusters (arrays of pores).

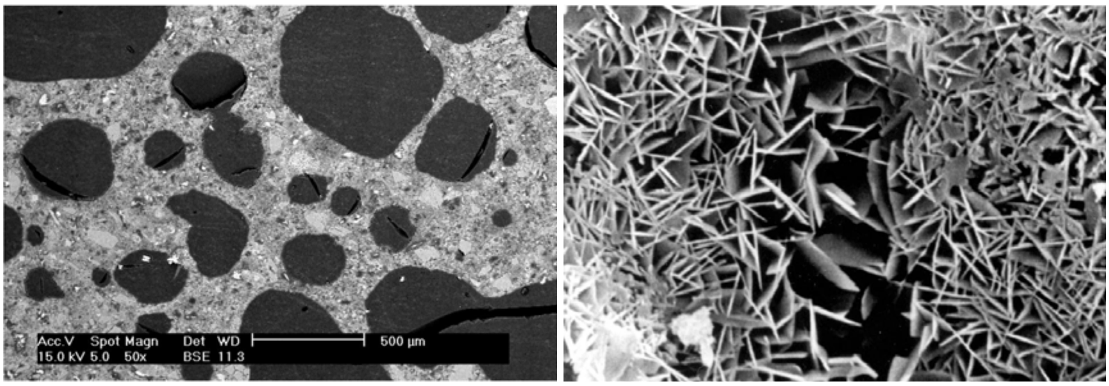

Figure 2. Scanning Electron Microscope photography of aerated concrete. Left - porous structure (spherical macro-pores in black color). Right - microcapillars with flat, needle-shaped crystals, and macro-capilar [5].

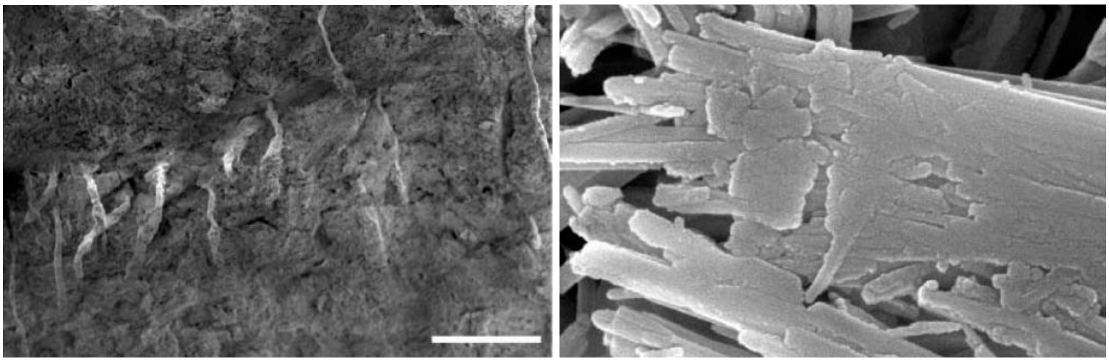

Figure 3. Autoclaved calcium silicate (Calsitherm) photographed using Scanning Electron Microscope [6].

As it was mentioned before water dielectric permittivity is about 80, air 1 and for mineral phase between 4 and 10. Dielectric permittivities of mineral phase are about 10 or less. For basalt it is 12, granite 7-9 and in case of sandstone 9-11 [7].

Dielectric properties of moist building materials

Building materials differ in porosity, density, pores types and distribution but also mineral phase. In case of dry materials dielectric permittivity value is dominated by mineral phase permittivities. In saturation by mineral phase and water. In intermediate (unsaturated) states it depends on the shares of particular phase.

In general the dielectric properties of moist building materials can be described using several models. There are two approaches to describe dielectric parameters of such materials: physical, using physical models, and empirical approach with calibration formulas.

Below there are presented some of the models describing dielectric parameters of building materials.

One of the physical models is power formula proposed by Tinga et al. [8]:

$$\varepsilon_a = \left[\theta \cdot \varepsilon_w^\beta + (1-\phi)\varepsilon_s^\beta + (\phi-\theta)\varepsilon_g^\beta\right]^{1/\beta} \tag{3}$$

εw, εs, εg – dielectric permittivity of the water phase, the solid particle phase and gaseous phase,

θ – volumetric water content, Φ – porosity, β – geometry factor depending on the geometrical order of the 3 phase mixture and their action in the transfer of generated electric field. Has no physical significance [9] (β = -1 for layered materials (layers perpendicular to electromagnetic field), β = 1 for isotropic 2 phase mixtures, β = 0.5 for homogenous and isotropic materials, β = 0.46 for different materials – best fit).

Another physical model is the linear mixing rule by Whalley [10]:

$$\sqrt{\varepsilon_a} = \theta\left(\sqrt{\varepsilon_w} - 1\right) + \frac{\rho_b}{\rho_p}\left(\sqrt{\varepsilon_s} - 1\right) + 1 \tag{4}$$

ϱb – bulk density, ϱp – particle density.

In 1974 Birchak et al. [9] proposed bound water mixing model:

$$\varepsilon_a = \left[(\theta-\theta_{bw}) \cdot \varepsilon_{fw}^\beta + \theta_{bw} \cdot \varepsilon_{bw}^\beta + (1-\phi)\varepsilon_s^\beta + (\phi-\theta)\varepsilon_g^\beta\right]^{1/\beta} \tag{5}$$

θ – total water content, θbw – bond water content, εfw – dielectric permittivity of free water, εbw – dielectric permittivity of bond water.

In the following model, the entire water present in the building material is not only considered as free liquid water with dielectric permittivity equal εw=80. This model also considers bond water which possesses lower dielectric permittivity (εbw) than liquid water.

Other, interesting model for determination of dielectric properties was published by De Loor [11]. It was geometrical pattern mixing rule, based on a dispersion model which described the dielectric properties of four components of the modeled material. This model can be successfully applied for the description of capillary medium like building materials. The mineral particles are the input medium with the inclusions of the other components like air, bound water and free water. The general formula of the model is the following:

$$\varepsilon_m = \varepsilon_S + \sum_{i=1}^{3} \frac{V_i}{3}(\varepsilon_i - \varepsilon_S) \sum_{j=1}^{3} \frac{1}{\left(A_j \dfrac{\varepsilon_i}{\varepsilon^e} - 1\right)} \tag{6}$$

εm, εs, εi, εe, – dielectric permittivities of the mixture, solid mineral particles and the inclusions from tied and free water, air but also effective relative permittivity at border surfaces, Vi –

respective volume of inclusions fractions, Aj – parameter representing the influence of the geometry at the depolarization over ellipsoids factors.

One of the simplest models proposed for dielectric parameters of porous materials description was by Noborio et al. [12].The authors related the volumetric water content to the dielectric constant using a general formula:

$$\theta = a + b\cdot\varepsilon c \qquad (7)$$

a, b and c are the calibration constants depending on material parameters.

As it was underlined before, the structure of building materials is strongly inhomogeneous and application of only physical models may lead to measurement errors or moisture underestimation. That's why for practical use another approach to describe dielectric properties of moist building materials is applied. This approach is based on application of the empirical formulas obtained with laboratory experiments. This enables to avoid the problems with consideration of porous structure of the materials and in most cases provides better results for moisture determination using dielectric methods of measurement.

One of the most common empirical mixing rule was proposed in 1980 by Topp et al [13]. This simple model can be applied for any porous material and correlates material moisture (θ) in the dependence of dielectric permittivity (ε):

$$\theta = \frac{-530 + 292\varepsilon - 5.5\varepsilon^2 + 0.043\varepsilon^3}{10000} \qquad (8)$$

This model was significantly improved by Malicki et al. [14] by considering the bulk density (ϱ) of the measured material which improved the measurements accuracy:

$$\theta = \frac{\left(\varepsilon^{0,5} - 0.819 - 0.168\rho - 0.159\rho^2\right)}{7.17 + 1.18\rho} \qquad (9)$$

Other model that can be found in the literature was proposed by Ren et al. [15]. It presents moisture dependence on dielectric permittivity (sand and clay loam) in the following form:

$$\theta = 8.76\cdot10\text{-}5\varepsilon3 - 4.03\cdot10\text{-}3\varepsilon2 + 7.01\cdot10\text{-}2\varepsilon - 0.161 \qquad (10)$$

Useful formulas describing the dependence between volumetric water content and dielectric permittivity obtained by fitting the TDR readouts to the gravimetric measurements were proposed in [16] for moisture determination of building materials. The calculated formulas for autoclaved aerated concrete with different bulk densities (400, 500, 600 and 700 kg m-3) were the second degree polynomials:

$$\theta400 = -1.0\cdot10\text{-}3\varepsilon2 + 4.26\cdot10\text{-}2\varepsilon - 3.37\cdot10\text{-}2 \qquad (11)$$

$$\theta500 = -7.0\cdot10\text{-}4\varepsilon2 + 3.336\cdot10\text{-}2\varepsilon + 2.02\cdot10\text{-}2 \qquad (12)$$

$$\theta600 = -5.0\cdot10\text{-}4\varepsilon2 + 2.87\cdot10\text{-}2\varepsilon + 6.8\cdot10\text{-}3 \qquad (13)$$

$$\theta700 = -7.0\cdot10\text{-}4\varepsilon2 + 3.29\cdot10\text{-}2\varepsilon - 1.05\cdot10\text{-}2 \qquad (14)$$

Figure 4 presents dependence between dielectric permittivity and moisture of autoclaved calcium silicate, which can be described with the following formula [17]:

$$\theta = -0{,}0002\varepsilon^2 + 0{,}0266\varepsilon - 0{,}0034 \tag{15}$$

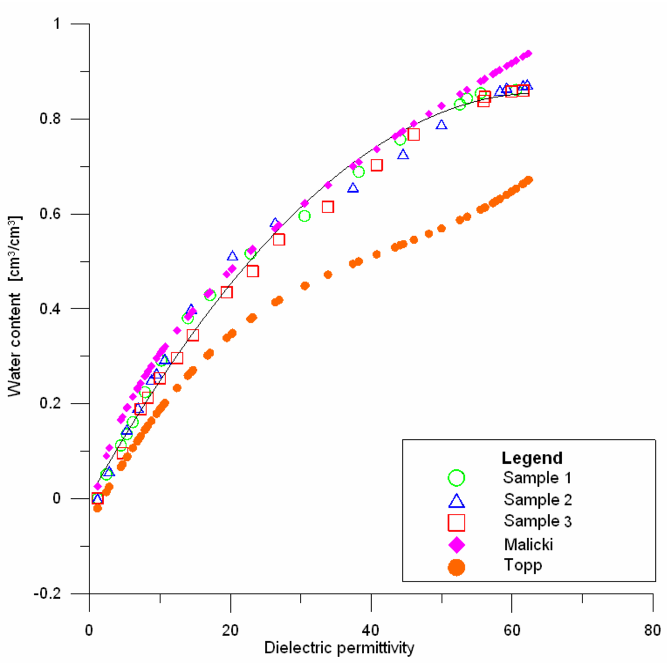

Figure 4. Dependence between dielectric permittivity and moisture read by TDR device in calcium silicate.

For the red brick other empirical model between moisture and dielectric properties (Figure 5) was proposed in [18]:

$$\theta = -0{,}001\varepsilon^2 + 0{,}0408\varepsilon - 0{,}067 \tag{16}$$

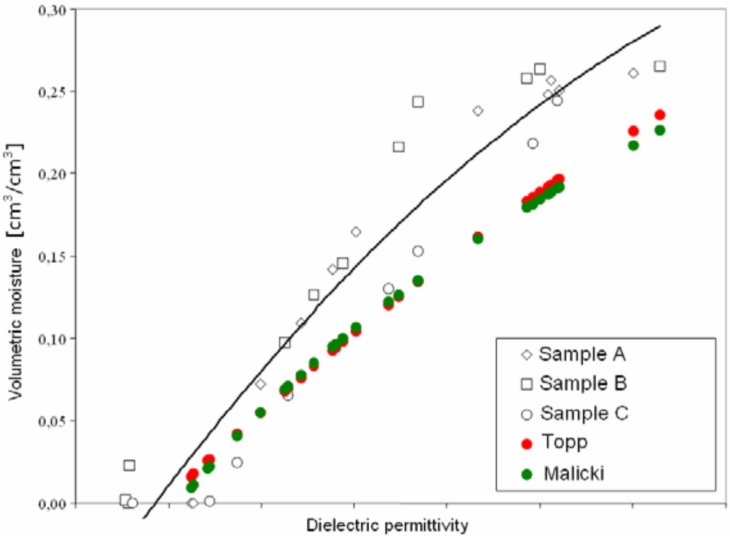

Figure 5. Dependence between dielectric permittivity and moisture read by TDR device ceramic red brick.

Summary

Among the indirect methods of measurement the dielectric methods play important role and knowledge of building materials dielectric parameters enables water content determination on satisfying level.

It should be underlined that building materials are strongly inhomogeneous, differing in structure, density and porosity that's why empirical models of dielectric permittivity are more useful than physical for practical application in the measurements. Empirical approach requires laboratory calibrations and can be time consuming. On the other hand there are many calibration formulas available in the literature which may be applied in dielectric moisture determination in building materials.

Acknowledgement

This work was supported by the Ministry of Science and Higher Education of Poland, Nr: 4952/B/T02/2008/34.

References

[1] SKIERUCHA W.; MALICKI M. A. TDR Method For The Measurement Of Water Content And Salinity Of Porous Media, Institute of Agrophysics PAS, Lublin, 2004

[2] SKIERUCHA W. Influence Of Temperature On Soil Moisture Measurement Using Reflectometric Method (In Polish), Acta Agrophysica PAS Lublin, 122, 2005(5). ISSN 1234-4125

[3] SOBCZUK H.; PLAGGE R. Time Domain Reflectometry Metod in Environmental Measurements, Lublin 2007, Monografie Komitetu Inżynierii Środowiska Polskiej Akademii Nauk vol. 39, ISBN 83-89293-51-X

[4] HILHORST M.A.; DIRKSEN C.E. Dielectric water content sensors: Time Domain versus Frequency Domain. Symposium on Time Domain Reflectometry in Environmental, Infrastructure and Mining Applications, Evanston (Chicago), USA, 2004, pp. 143-153, Spec. Publ. SP19-94

[5] ROELS S.; SERMIJN J.; CARMELIET J. Modelling unsaturated moisture transport in autoclaved aerated concrete: microstructural approach. Building Physics 2002 – 6th Nordic Symposium, Norway, 2002, pp. 167-174, ISBN: 82-91412-02-2

[6] HAMILTON A.; HALL C. Physicochemical characterization of a hydrated calcium silicate board material, Journal of Building Physics, 2005, 29, pp. 9-19, ISSN 1744-2591

[7] DORF R.C., CRC Handbook of Engineering Tables, 2004, CRC Press LLC.

[8] TINGA W.R.; VOSS W.A.G.; BLOSSEY D.F. Generalized approach to multiphase dielectric mixture theory, J. Appl. Phys. 44, 1973, pp. 3897-3902

[9] BIRCHAK J.R.; GARDNER C.G.; HIPP J.E.; VICTOR J.M., High dielectric constant microwave probes for sensing soil moisture, Proc. IEEE, 62, 1, 1974, pp. 93-98, ISSN 0018-9219

[10] WHALLEY W.R. Considerations on the use of Time Domain Reflectometry (TDR) for measuring soil water content, J. Soil Sci. 44, 1993, pp. 1-9

[11] De LOOR G.P., Dielectric properties of heterogeneous mixtures containing water, J. Microwave Power, 3,2, 1968, pp. 67-73, ISSN 0022-2739

[12] NOBORIO K.; HORTON R.; TAN C.S. Time Domain Reflectometry Probe for Simultaneous Measurement of Soil Matric Potential and Water Content. Soil Science Society of America Journal 63, 1999, pp. 1500–1505, ISSN 0361-5995

[13] TOPP G.C.; DAVIS J.L.; ANNAN A.P. Electromagnetic Determination Of Soil Water Content: Measurements In Coaxial Transmission Lines. Water Resour. Res., 16, 1980, pp. 574-582, ISSN: 0043-1397

[14] MALICKI M. A.; PLAGGE R; ROTH, C.H. Improving The Calibration Of Dielectric TDR Soil Moisture Determination Taking Into Account The Solid Soil, Eur. J. Soil Sci., 1996, 47, pp. 357–366, ISSN 1351-0754

[15] REN T.; NOBORIO K.; HORTON R. Measuring Soil Water Content, Electrical Conductivity, and Thermal Properties with a Thermo-Time Domain Reflectometry Probe, Soil Science Society of America Journal 63, 1999, pp. 450–457, ISSN 0361-5995

[16] SOBCZUK H.; SUCHORAB Z. Calibration of TDR Instruments for Moisture Measurement of Aerated Concrete. In: ed. W. Skierucha and T. Walczak, Monitoring And Modelling the Properties of Soil as Porous Medium, Institute of Agrophysics Polish Academy of Sciences, Lublin, 2005, Poland, pp. 158-165, ISBN 83-87385-95-6

[17] SUCHORAB Z., Assessment Of Heat Loss And Moisture Flow In Building Materials (in Polish), PhD thesis, Lublin University of Technology, 2006

[18] SPALITABAKA K.; WRÓBEL K.; SUCHORAB Z. Calibration of TDR method for moisture determination of red ceramic brick (in Polish), Problemy Inżynierii Środowiska, XXVII Międzynarodowe Sympozjum im. Bolesława Krzysztofika AQUA 2007, pp. 148-154, ISBN 978-83-925264-0-7

Thermal, hygric and salt-related properties of high performance concrete

Eva Vejmelková[1],Martin Keppert[1],Milena Pavlíková[1] and Robert Černý[1]

[1] Department of Materials Engineering and Chemistry, Faculty of Civil Engineering, Czech Technical University in Prague, Thákurova 7, 166 29 Prague 6, Czech Republic

Abstract: *Thermal, hygric and salt-related properties of four types of high performance concrete are analyzed. Experimental results show that all four studied materials have very good prerequisites for application in building industry. Their water transport characteristics are very suitable for high performance concrete. The low liquid water transport parameters can guarantee slow water penetration into the material, thus high durability.*

Keywords: *high performance concrete, thermal, hygric, salt-related properties*

Materials

Four different types of high-performance concrete were studied. Three of them contained alternative silicate binders, namely metakaolin (BM), ground granulated blast furnace slag (BS), and fly ash (BP). The fourth was reference mixture with only Portland cement as binder (BR). Table 1 presents the composition of the studied concrete mixtures.

Table 1. The composition of concrete mixtures [kgm^{-3}]

Component	BR	BM	BS	BP
CEM I 42.5 Mokrá	484	440	440	440
aggregates 0-4 mm	812	812	812	812
aggregates 8-16 mm	910	910	910	910
Plasticizer Mapei Dynamon SX	5.3	5.3	5.3	5.3
metakaolin Mefisto	-	44	-	-
ground granulated blast furnace slag Štramberk	-	-	44	-
fly ash Dětmarovice	-	-	-	44
water	188	188	188	188

Experimental methods

Basic characterization experiments

As fundamental physical material characteristics, bulk density ρ_b [kgm^{-3}], porosity [Vol.-%] and matrix density ρ_{mat} [kgm^{-3}] were determined using the vacuum saturation method [4]. Each sample was dried in a drier to remove majority of the physically bound water. After that the samples were placed into the desiccator with deaired water. During three hours air was evacuated with vacuum pump from the desiccator. The sample was then kept under water not less than 24 hours.

From the mass of the dry sample m_d, the mass of water saturated sample m_w, and the mass of the immersed water saturated sample m_a, the volume V of the sample was determined from the equation

$$V = \frac{m_w - m_a}{\rho_w} \tag{1}$$

where ρ_w is the density of water. The open porosity ψ_0, the bulk density ρ and the matrix density ρ_{mat} were calculated according to the equations

$$\psi_0 = \frac{m_w - m_d}{V\rho_w} \tag{2}$$

$$\rho = \frac{m_d}{V} \tag{3}$$

$$\rho_{mat} = \frac{m_d}{V(1-\psi_0)} \tag{4}$$

The measurement of basic parameters took place in a conditioned laboratory at the temperature of 22±1°C and 25-30% relative humidity. In the experiment 6 samples of 50 x 50 x 25 mm were used.

Characterization of pore structure of the studied materials was performed by mercury intrusion porosimetry. This well-known method is based on intrusion of mercury to the porous sample by gradually increasing intrusion pressure while mercury penetrates to smaller pores. The experiments were carried out using the instruments PASCAL 140 and 440 (Thermo Scientific). The range of applied pressure corresponds to pore radius from 2 nm to 2000 μm. Since the size of sample for PASCAL is restricted to volume of cca 1 cm^3 and the studied materials contain aggregates of the same size, the porosimetry measurements were performed on samples without coarse aggregates.

Water vapor and water transport properties

The wet cup method and the dry cup method were employed in the measurements of water vapor transport parameters. The specimens were water and vapor proof insulated by epoxy resin on all lateral sides, put into the cup and sealed by technical plasticine. The impermeability of the plasticine sealing was achieved by heating it first for better workability and subsequent cooling that resulted in its hardening. In the wet cup method the sealed cup containing saturated K_2SO_4 solution (the equilibrium relative humidity above the solution was 97.8%) was placed into an air-conditioned room with 30 % relative humidity and weighed periodically. The measurements were done at 25±1°C in a period of four weeks. The steady state values of mass loss determined by linear regression for the last five readings were used for the determination of water vapor diffusion coefficient [4]. In the dry cup method the sealed cup containing dried $CaCl_2$ (the equilibrium relative humidity above the desiccant was 5%) was placed in an air-conditioned room with 30 % relative humidity. Otherwise the measurement was done in the same way as in the wet cup method.

The water vapor diffusion coefficient D [m^{2}s^{-1}] was calculated from the measured data according to the equation

$$D = \frac{\Delta m \cdot d \cdot R \cdot T}{S \cdot \tau \cdot M \cdot \Delta p_p} \tag{5}$$

where Δm [kg] is the amount of water vapor diffused through the sample, d [m] the sample thickness, S [m^2] the specimen surface, τ [s] the period of time corresponding to the transport of mass of water vapor Δm, Δp_p [Pa] the difference between partial water vapor pressure in the air under and above specific specimen surface, R the universal gas constant, M the molar mass of water, T [K] the absolute temperature.

On the basis of the diffusion coefficient D, the water vapor diffusion resistance factor μ was determined:

$$\mu = \frac{D_a}{D} \tag{6}$$

where D_a is the diffusion coefficient of water vapor in the air.

In the experiment 6 samples of 50 x 50 x 25 mm were used. The liquid water transport was characterized by water sorptivity and apparent moisture diffusivity. The specimen was water and vapor-proof insulated on four lateral sides and the face side was immersed 1-2 mm in the water. Constant water level in tank was achieved by a Mariotte bottle with two capillary tubes. One of them, inside diameter 2 mm, was ducked under the water level, second one, inside diameter 5 mm, was above water level. The automatic balance allowed recording the increase of mass. The water absorption coefficient A [kgm^{-2}s$^{-1/2}$] was calculated using the formula

$$i = A \cdot \sqrt{t} \tag{7}$$

where i [kg/m^2] is the cumulative water absorption, t the time from the beginning of the suction experiment. The water absorption coefficient was then used for the calculation of the apparent moisture diffusivity in the form [1]

$$\kappa_{app} \approx \left(\frac{A}{w_c - w_0} \right)^2 \tag{8}$$

where w_c [kgm^{-3}] is the saturated moisture content and w_0 [kgm^{-3}] the initial moisture content.

In the experimental work 5 specimens of 50 x 50 x 20 mm were used.

Hygric expansion

The hygric strain ε_u [-] was determined using a comparative technique according to the equation

$$\varepsilon_u = \frac{\Delta l}{l_{0,u}} \tag{9}$$

where $l_{0,u}$ is the length at the reference moisture content, Δl the difference between the length at actual moisture content and length at reference moisture content. The lengths were measured using a contact comparator having the accuracy of 0.001 mm.

Chloride binding isotherms

Chloride adsorption isotherms were measured by a modification of the method by Tang and Nilsson [2] based on the adsorption from solution.

In the original version of the method a crushed sample of cement mortar or cement paste dried at 11% relative humidity was put into a cup, then the cup was vacuumed in a desiccator for 2 hours, before being filled with a specific concentration NaCl solution saturated with $Ca(OH)_2$. The volume of the solution inside the cup was calculated from the increment of the mass of the cup and the density of the solution. The cup was covered and stored at 20°C to reach equilibrium. Adsorption equilibrium was typically achieved after 7 days for 25 g samples. Then the inside solution was pippetted to determine the chloride concentration by potentiometric titration using 0.01N $AgNO_3$ and a chloride selective electrode. The bound chloride content C_b (in mg/g) was calculated from the equation

$$C_b = \frac{M_{Cl} V (C_0 - C_1)}{W} \tag{10}$$

where M_{Cl} is the molar mass of chlorine, V the volume of the solution (in ml), C_0, C_1 the initial and equilibrium concentrations, respectively, of chloride solution (in mol/l), and W the mass of the dry sample, which can be calculated from the difference in mass of the sample dried in a desiccator at 11% relative humidity and in an oven at 105°C. The free chloride content C_f (in mol/l), corresponding to the value of C_b calculated from equation (10) was given by

$$C_f = C_1 \tag{11}$$

By performing the experiment with different values for the initial salt concentration C_0, a point wise function $C_b = C_b(C_f)$ can be obtained, which is the ion binding isotherm.

The possible shortage of the method of Tang and Nilsson [2] is that the measuring procedure is developed for crushed samples of cement paste and it is assumed that the content of cement is the main criterion for a possible recalculation to real concrete or cement mortar. In fact, the method is certain idealization of the binding problem assuming that chlorides can get in direct contact with every small grain of hydrated cement. However, in a real concrete specimen (even in cement paste) the interior pore surface where the cement binder is accessible to the chlorides is certainly smaller than the total surface of a crushed specimen. The chloride binding capacity can be then affected by many other factors such as the change in the porous structure and pore distribution due to the application of different aggregates, the presence of various admixtures etc. Therefore, the result obtained by the Tang and Nilsson method can be considered as a certain upper limit to the real chloride binding capacity.

The modification of the Tang and Nilsson adsorption method used in this paper consisted in using the specimens of more realistic dimensions (40 x 40 x 10 mm) instead of crushed specimens [3]. Two specimens were analyzed for each material.

Thermal properties

Thermal conductivity and specific heat capacity were measured using the commercial device ISOMET 2104 (Applied Precision, Ltd.). ISOMET 2104 is equipped with various types of optional probes, needle probes are for porous, fibrous or soft materials, and surface probes are suitable for hard materials. The measurement is based on analysis of the temperature response of the analyzed material to heat flow impulses. The heat flow is induced by electrical heating using a resistor heater having a direct thermal contact with the surface of the sample. In the experimental work 3 cubic samples 70 x 70 x 70 mm were used.

Experimental results and discussion

Basic characterization experiments

The basic physical properties of studied composites measured by the water vacuum saturation method are shown in Figures 1 and 2. The bulk densities of all materials differed only up to about 2% and matrix densities up to 5%. The highest value of porosity achieved the material BM containing metakaolin and the lowest value the material BS with slag admixture. The difference between these two materials was about 34 %.

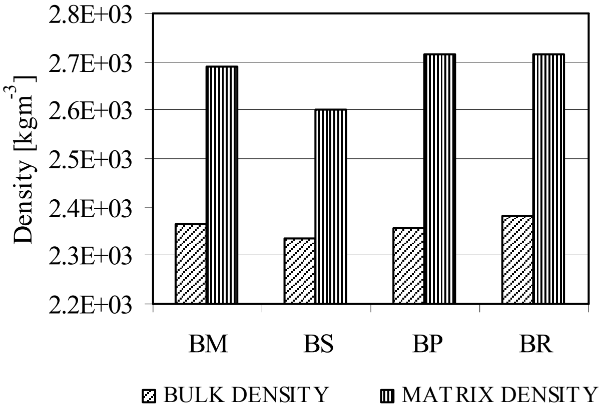

Figure 1. Bulk and matrix density of studied composites

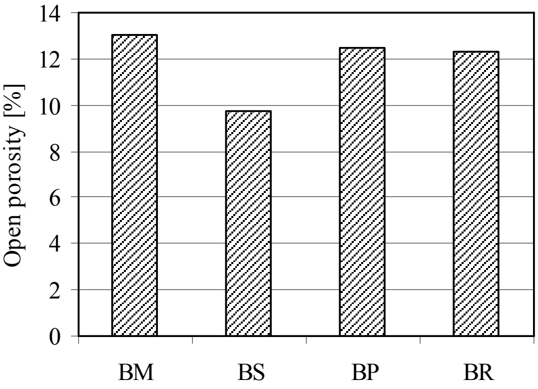

Figure 2. Open porosity of studied composites

Figure 3 shows the cumulative pore volume of the analyzed composites measured by mercury intrusion porosimetry. The results are in a qualitative agreement with the measurements of open porosity by the water vacuum saturation technique. The material with slag addition had substantially lower cumulative pore volume than the other materials.

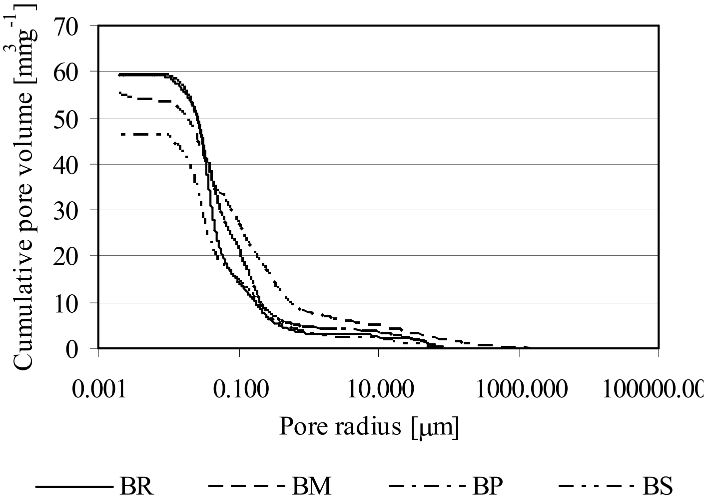

Figure 3. Cumulative pore volume of studied composites

Water vapor and water transport properties

The results of measurements of water vapor diffusion resistance factor μ of the analyzed composites are presented in Figure 4. Comparing the data measured for the four studied materials, we can see that the μ values of BR and BP were in the both ranges of higher and lower relative humidity about 2-3 times higher than for BS and BM. This does not agree with the porosity data in Figures 2 and 3. The material BS with the lowest porosity achieved the lowest water vapor diffusion resistance factor. Possible explanation could be in crack appearance in the specimens of the material with slag addition. In general, such discrepancies could also be explained by the effect of tortuosity of the porous system.

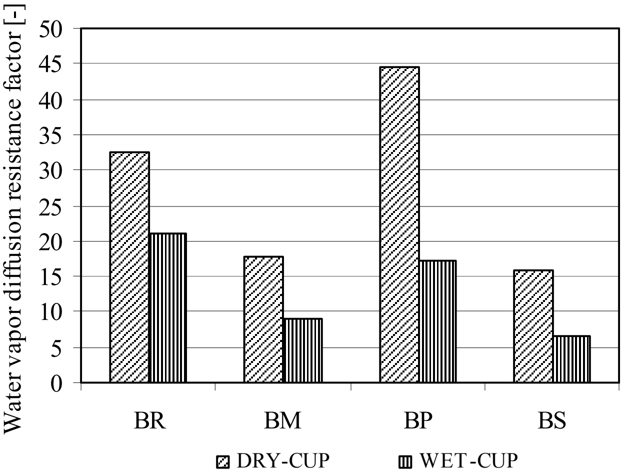

Figure 4. Water vapor diffusion resistance factor of studied composites

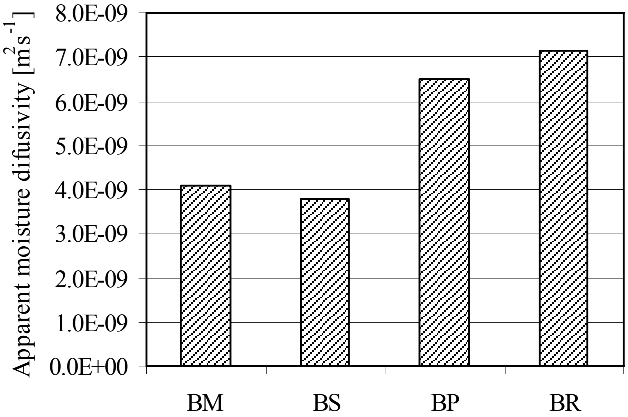

Figure 5. Apparent moisture diffusivity of studied composites

The effect of alternative silicate binders on the liquid moisture transport parameters was pronounced for materials with ground granulated blast furnace slag and metakaolin. The apparent moisture diffusivity of BM and BS (Figure 5) was almost two times lower than for BR.

On the other hand, apparent moisture diffusivity of the material with fly ash achieved nearly the same value as the basic mixture BR. Here the results were in better agreement with the porosity data from Figures 2 and 3 than for water vapor transport parameters. The material with lowest open porosity achieved the lowest apparent moisture diffusivity value. However, the agreement was not perfect either due to some contradictory results in Figures 2 and 3. The material BM with highest open porosity measured by water vacuum saturation method (Figure 2) achieved the second lowest moisture diffusivity. On the other hand, its cumulative pore volume measured by mercury intrusion porosimetry (Figure 3) was second lowest which agrees with the moisture diffusivity value. So, the conclusions are not exactly clear in that respect.

Hygric expansion

Experimental results in Figure 6 show that the highest hygric strain exhibited the material with fly ash addition, the lowest the reference composite material BR. The hygric strain vs. moisture functions of all studied materials had concave character. So, the hygric expansion decreased with increasing moisture content.

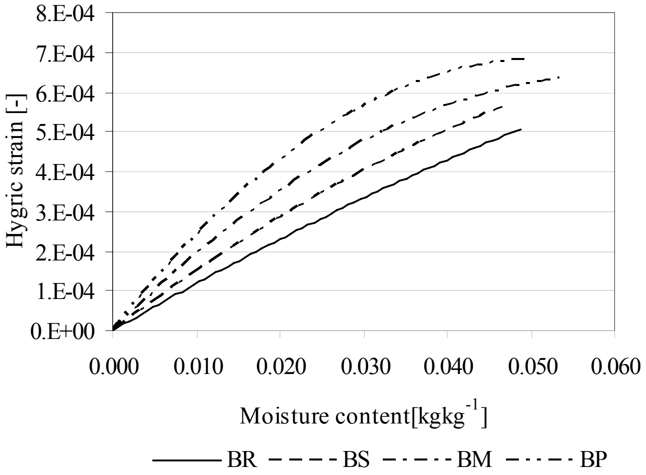

Figure 6. Hygric strain of studied composites

Chloride binding isotherms

Measurements of chloride binding isotherms in Figures 7-10 (the different curves mean different specimens) showed that the highest chloride binding capacity exhibited the material BM with metakaolin addition and the second highest was the material BS with slag. BP and BR had almost two times lower amount of bound chlorides.

The differences were more remarkable in the range of high chloride concentration. The higher chloride binding capability of BM and BS may be related to the slower course of pozzolanic reaction in comparison with Portland cement hydration. The chloride binding test was taking much more time than the other types of tests, approximately 6 months. Therefore, the pozzolanic reaction might already be almost completed after that time – contrary to the measurements of other parameters which were done 28 days after mixing. So, it seems reasonable to complement the measurements done in this paper by the determination of mechanical properties after longer time. This could bring the required explanation.

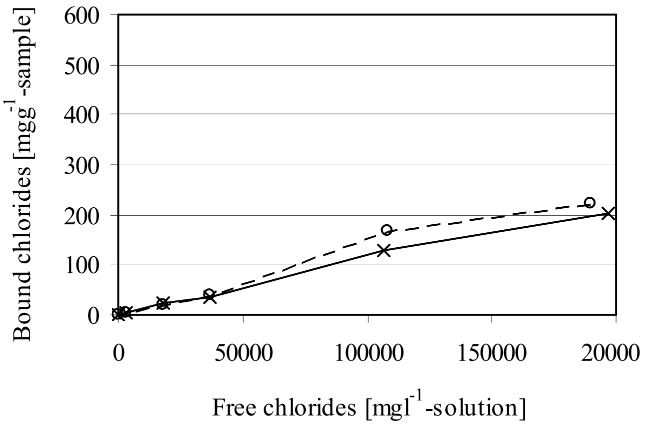

Figure 7. Bound chlorides of the material BR

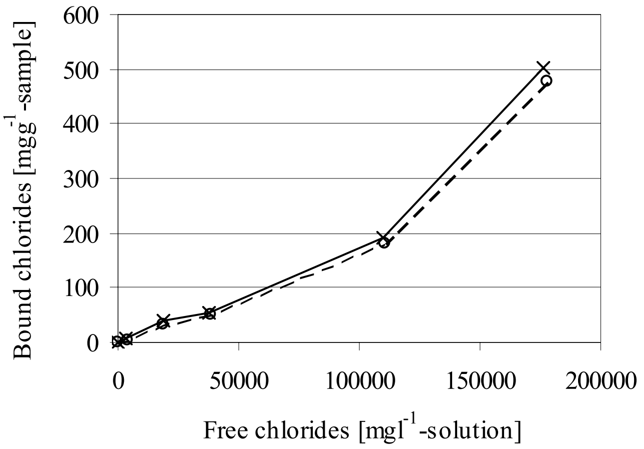

Figure 8. Bound chlorides of the material BM

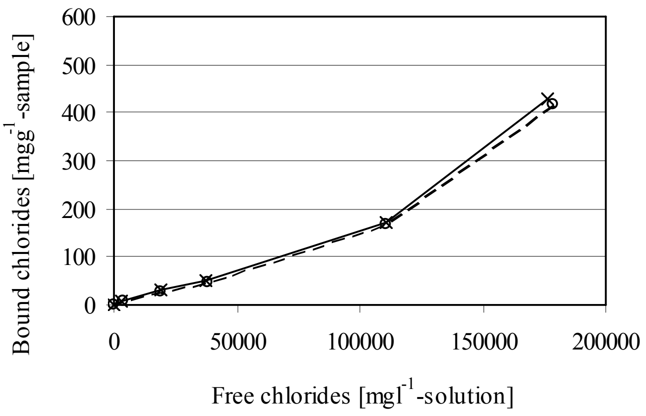

Figure 9. Bound chlorides of the material BS.

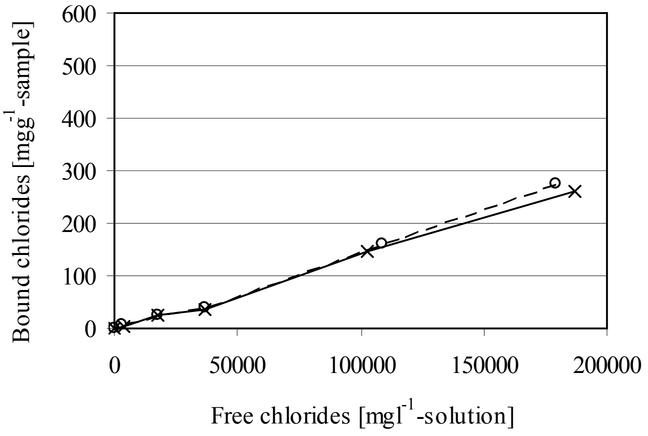

Figure 10. Bound chlorides of the material BP

Thermal properties

The data in Figure 11 show that the dependence of thermal conductivity of all materials on moisture content was similar. The differences were in the whole analyzed moisture range relatively low, up to 10%. The highest thermal conductivity achieved the material BS which was in a qualitative agreement with its lowest open porosity. As for the three other materials, the measured thermal conductivities did not completely agree with the porosity data. This could be explained partially by the possible differences in the topology of the pore system of the particular materials, partially by the low differences in measured thermal conductivity (the error range of the measuring method was ±5%).

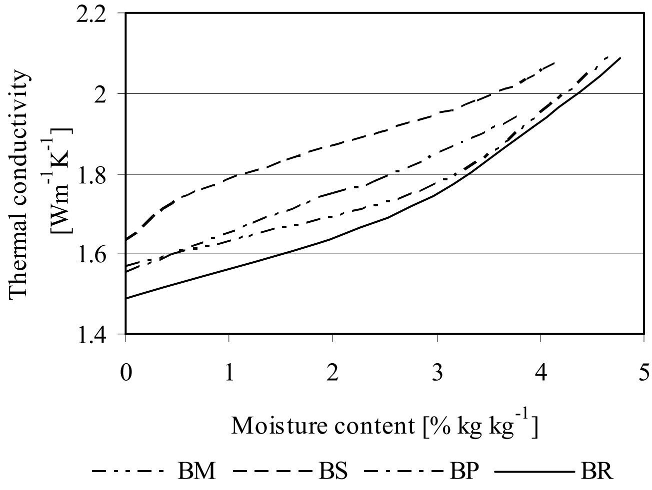

Figure 11. Thermal conductivity of studied composites

The specific heat capacity of BR (Figure 12) was slightly lower than for other materials in the whole range of moisture content. However, the observed differences were within the error range of the measuring method of ±10%. The values of thermal diffusivity (Figure 13) were once again very similar for all materials in whole the moisture range. This reflects the low differences in both thermal conductivity and specific heat capacity data of the investigated materials.

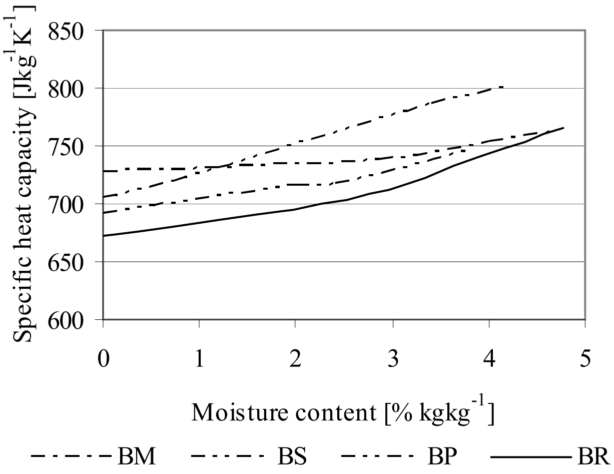

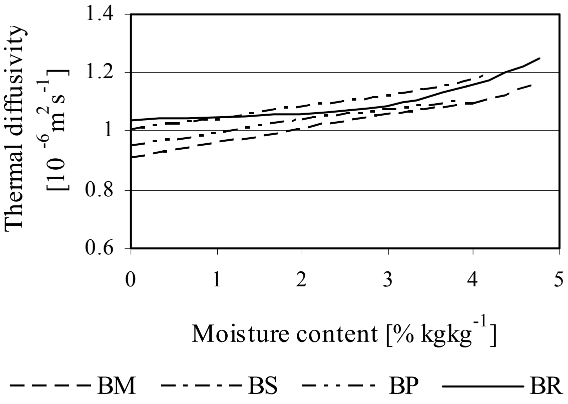

Figure 12. Specific heat capacity of studied composites

Figure 13. Thermal diffusivity of studied composites

Conclusions

Experimental results presented in this paper showed that the replacement of Portland cement in the amount of up to 10% by metakaolin, fly ash or ground granulated blast furnace slag as environmental more friendly alternative binders can be considered a viable alternative in the future production of high performance concrete.

Acknowledgement

This research has been supported by the Czech Ministry of Education, Youth and Sports, under project No MSM 6840770031.

References

[1] KUMARAN M.K., 1994, Report on Measurements to Determine Moisture Diffusivity of Eastern White Pine. IEA Annex XXIV Report T3-CA-92/04.

[2] TANG L.,NILSSON L.O., 1993. Chloride binding capacity and binding isotherms of OPC pastes and mortars. Cement and Concrete Research 23: 247-253.

[3] JIŘIČKOVÁ M. and ČERNÝ R., 2006, Chloride Binding in Building Materials, Journal of Building Physics 29: 189-200.

[4] ROELS S., CARMELIET J., HENS H., ADAN O., BROCKEN H., ČERNÝ R., PAVLÍK Z., HALL C., KUMARAN K., PEL L., PLAGGE R., 2004, Interlaboratory Comparison of Hygric Properties of Porous Building Materials. Journal of Thermal Envelope and Building Science 27: 307-325.

Properties of innovative materials on gypsum basis

Pavel Tesárek, Robert Černý

Czech Technical University in Prague, Faculty of Civil Engineering, Department of Materials Engineering and Chemistry, Prague, Czech Republic

Abstract: *Paper Measurements of basic mechanical, thermal and hygric parameters of calcined gypsum produced using waste flue gas desulphurization gypsum and chemo-gypsum and modified by the addition of plasticizers and hydrophobizers are presented in the paper. Bulk density, matrix density, open porosity, bending and compressive strength, thermal conductivity, volumetric heat capacity, water absorption coefficient, apparent moisture diffusivity, water vapor diffusion coefficient are determined and compared to the properties of hardened gypsum without any admixtures*

Keywords: *gypsum, innovative materials, properties*

Introduction

Calcined gypsum is a historical binder that was used already several thousands years ago. Gypsum was called gatch in Persia, gypsos in Greek, and gypsum in Latin. Iranians, Egyptians, Babylonians, Greeks, and Romans were familiar with the art of working with gypsum plasters, e.g. the decorated interior walls of Pompeii. Gypsum was found in the binder of buildings in the territory of today's Syria dated 7000 BC; it was also used in Cheops pyramid 2650 BC, the palace of Knossos etc. Now is this product known as "stuco", "kettle stucco", plaster of Paris or plaster.

Calcined gypsum as a low-energy material can be produced with advantage from the waste products of either flue gas desulphurization (FGD) in thermal power plants, phosphoric acid, hydrofluoric acid, citric acid and boric acid production in chemical plants or from natural gypsum by its dehydration at the temperatures of 110 to 150°C [16]. Then, β-form of calcined gypsum $CaSO_4 \cdot 1/2H_2O$ is formed according to equation:

$$CaSO_4 \cdot 2H_2O \rightarrow CaSO_4 \cdot 1/2H_2O + 1\ 1/2H_2O \qquad (1)$$

The solid structure of calcined gypsum is created by reverse hydration when gypsum $CaSO_4 \cdot 2H_2O$ is formed again:

$$CaSO_4 \cdot 1/2H_2O + 1\ 1/2H_2O \rightarrow CaSO_4 \cdot 2H_2O \qquad (2)$$

These two phenomena, dehydration (1) and rehydration (2), are basis of gypsum technology. The solid structure of calcined gypsum can then be created by reverse hydration [14].

Amount of impurities in gypsum is given by the purity of calcium sulphate dihydrate in raw material; there are two possibilities:

i. Natural gypsum – main problem is purity of exploited gypsum and segregation process of impurities as clay etc.

ii. Secondary raw materials – problem is with impurities from chemical and other industry applied technologies.

Flue gas desulfurization gypsum and gypsum from chemical production is produced in high amounts. However, the industrial use of gypsum is insufficient considering the amount of its production. Nowadays, it is mostly used for the production of gypsum plasterboards only, and the rest is deposited at waste disposal sites. Due to the very low price and large availability of waste gypsum, the material has a good potential for applications in buildings not only for dividing structures as with the most current gypsum applications but in some cases also for load-bearing structures. One of the reasons for the neglect of the material by building industry is the almost complete lack of knowledge of its properties.

For an extended use of gypsum in buildings some modifications of this material are necessary which are supposed to enhance its original properties and increase its service life. For instance, use of plasticizers or fiber reinforcement can increase the mechanical strength of gypsum products, hydrophobization can protect the material from water penetration, fillers can decrease the necessary amount of binder in a composite material.

Modifications of gypsum are usually performed using polymer materials. Bijen and van der Plas [1] reinforced gypsum by E-glass fibres, and modified the binder by using acrylic dispersion in a mixture with melamine. The results showed that this material had higher flexural strength and higher toughness than glass fiber reinforced concrete after 28 days. A disadvantage of polymers based on carbon chain is a decrease of fire resistance of calcined gypsum elements. Application of hydrophobization admixtures is another way of possible and perspective gypsum modification because the resistance of hardened gypsum against water is still considered a serious problem. In the literature, only applications of lime and artificial resins (polyvinylacetate, urea formaldehyde and melamine formaldehyde) were studied, some inorganic substances such as fluorosilicates, sulfates and silicates were found to increase hardness and impermeability of the surface, see [12]. Colak [2] impregnated the gypsum surface by various epoxy resins and studied the effect of impregnation on mechanical properties and water sorption. While the flexural strength was not changed due to the impregnation, some resins were found to protect gypsum completely from water penetration. However, generally it can be stated that the resistance of hardened gypsum against water is not yet resolved in a satisfactory way.

The primary aim of our research work is the adjustment of basic technologies for the production of modified gypsum, particularly from the points of view of hydrophobization and improvement of mechanical and thermal properties.

Very few information about material properties of gypsum products was published until now. Basic mechanical properties of calcined gypsum (compressive strength, tensile and flexural strength, Young's modulus, Poisson constant) are relatively well known, see, e.g. Klein and Ruffer [7], Singh and Garg [13], Tazawa [15]. Thermal properties of calcined gypsum (thermal conductivity, specific heat, thermal diffusivity) were determined for instance in Danten et al. [5], Mehaffey [10] and Hanush [6]. Among the hydric properties of calcined gypsum, Hanusch [6] introduced the water vapor diffusion resistance factor, Dahl et al. [4] measured sorption and desorption isotherms, Lucas [9] the sorptivity. However, the data sets presented by various investigators for different types of calcined gypsum are mostly incomplete so that their applicability is limited. Complete sets of thermal, hygric and mechanical parameters of practically any type of non-modified and modified gypsum are very rarely available and without their knowledge it is impossible to perform any serious mechanical or hygrothermal analysis of building elements based on these materials. So, determination of a complete set of these parameters is still a very actual problem.

In this paper, several materials based on waste flue gas desulphurization gypsum and two types of waste chemo-gypsum and modified by the addition of plasticizers and hydrophobizers are investigated, and their mechanical, thermal and hygric properties are measured.

Experimental methods

Basic properties

The basic characterization of the studied materials was done using the vacuum water saturation method. In the vacuum water saturation method, bulk density, matrix density and open porosity were measured. Each sample was dried in a drier to remove majority of the physically bound water. After that the samples were placed into a desiccator with distilled water. During three hours air was evacuated with vacuum pump from the desiccators. The specimen was then kept under water not less than 24 hours [11].

From the mass of the dry sample m_d [kg], the mass of water saturated sample m_w [kg], and the mass of the immersed water saturated sample m_a [kg], the volume V [m^3] of the sample was determined from the equation

$$V = \frac{m_w - m_a}{\rho_l} \tag{3}$$

where ρ_l is the density of water.

The open porosity ψ_0 [-], the bulk density ρ [kg/m^3], and the matrix density ρ_{mat} [kg/m^3], were calculated according to the equations

$$\psi_0 = \frac{m_w - m_d}{V\rho_l} \tag{4}$$

$$\rho = \frac{m_d}{V} \tag{5}$$

$$\rho_{mat} = \frac{m_d}{(1-\psi_0)V} \tag{6}$$

Bending strength and compressive strength

The measurement of bending strength was performed according to the Czech standard ČSN 72 2301 [3] on the 40 x 40 x 160 mm prisms. The specimens were demolded 15 minutes after the final setting time and stored in the testing room. Every specimen was positioned in such a way that the sides that were horizontal during the preparation were in the vertical position during the test. The experiment was performed as a common three-point bending test using the WPM 50 kN device. The distance of the supporting cylinders was 100 mm. The bending strength was calculated according to the standard evaluation procedure. The measurements were done at the times of 2 hours, 1 day, 3 days, 7 days, 14 days and 28 days after mixing.

Compressive strength was determined in accordance with the Czech standard ČSN 72 2301 [3] on the halves of the specimens left over after the bending tests. The specimens were placed between the two plates of the WPM 100 kN device in such a way that their lateral sides adjoining during the preparation to the vertical sides of the molds were in contact with the plates. In this way, the imprecision of the geometry on the upper cut off side was not affecting negatively the experiment. The compressive strength was calculated as the ratio of the ultimate force and the load area.

Hygric properties

Moisture transport properties were measured in both hygroscopic and overhygroscopic range.

Moisture diffusivity

The moisture diffusivity was estimated using a water sorption experiment. A common experimental setup was chosen. The specimen was water and vapor-proof insulated on four lateral sides and the face side was immersed 2 mm in the water. Constant water level in the tank was achieved using a bottle placed upside down. The known water flux into the specimen during the suction process was then employed to the determination of the water absorption coefficient.

For the calculation of the apparent moisture diffusivity D_w [m²/s], the following approximate relation [8] was employed:

$$D_w \approx \left(\frac{A}{w_c} \right)^2 \tag{7}$$

where A is the water absorption coefficient [kg/m^{2}s$^{1/2}$], and w_c is the saturated moisture content [kg/m^3].

Water vapor diffusion resistance factor

The water vapor diffusion resistance factor was determined by the standard cup methods (dry and wet). The water vapor diffusion coefficient *D* was calculated at first from the measured data according to the equation

$$D = \frac{\Delta m \cdot d \cdot R \cdot T}{S \cdot \tau \cdot M \cdot \Delta p_p} \tag{8}$$

where *D* is the water vapor diffusion coefficient [m^2/s], Δm the amount of water vapor diffused through the sample [kg], *d* the sample thickness [m], *S* the specimen surface being in contact with the water vapor [m^2], τ the period of time corresponding to the transport of mass of water vapor Δm [s], Δp_p the difference between partial water vapor pressure in the air under and above the specimen [Pa], *R* the universal gas constant [J/mol K], *M* the molar mass of water [kg/mol], *T* the absolute temperature [K].

On the basis of the diffusion coefficient *D*, the water vapor diffusion resistance factor μ was determined,

$$\mu = \frac{D_a}{D} \tag{9}$$

where D_a is the diffusion coefficient of water vapor in the air [m^2/s].

In the dry cup method the sealed cup containing silica gel was placed in a controlled climate chamber with 50% relative humidity and weighed periodically. For wet cup method sealed cup containing water was placed in an environment with the temperature of 25°C and relative humidity of 50%. The measurements were done at 25°C in a period of two weeks.

The steady state values of mass gain or mass loss determined by linear regression for the last five readings were used for the determination of water vapor transfer properties.

Thermal properties

Thermal conductivity λ [W/mK], thermal diffusivity a [m^2/s], and volumetric heat capacity $c\rho$ [J/m^{3}K] were determined using the commercial device ISOMET 2104 (Applied Precision, Ltd.). ISOMET 2104 is a multifunctional instrument equipped with various types of optional probes. Needle probes are for porous, fibrous or soft materials, surface probes are suitable for hard materials. The measurement is based on the analysis of the temperature response of the analyzed material to heat flow impulses. The heat flow is induced by electrical heating using a resistor heater having a direct thermal contact with the surface of the sample. Thermal diffusivity was calculated by device using the equation:

$$a = \frac{\lambda}{c\rho} \tag{10}$$

Materials and samples

The first material, which was used as reference, was β-form of calcined gypsum with purity higher than 98% of flue gas desulphurization gypsum, produced at the electric power station Počerady, Czech Republic. The water/gypsum ratio of 0.627 was chosen which corresponded to the normal consistence according to the Czech standard ČSN 72 2301 [3]. Normal consistence was determined using the slump test. The standard metal cylinder with the diameter of 50 mm and height of 100 mm was fully filled by water and gypsum mixture. Then the mixture was poured out from the cylinder, the slump measured in two perpendicular directions and the average value calculated. The standard slump corresponding to the normal consistence is 180±5 mm. This material which will be denoted as S1 in what follows was classified as G-13 B III according to ČSN 72 2301 [3].

The second material, which was used for reference measurements, was commercially produced gypsum plaster from Gypstrend Inc. – Kobeřice. This plaster is β-form of calcined gypsum with purity 80-95 % and consists of natural gypsum and chemo-gypsum. The commercial name of this material is “Grey gypsum plaster.” The classification of the analyzed gypsum was performed according to the Czech standard ČSN 72 2301 as G 2 B II. Material which was made from grey gypsum plaster without additives was denoted as A1. The modified materials on basis of grey gypsum plaster were denoted as A3 and A5. Material A3 with water/gypsum ratio 0.670 was modified using commercial products Polyfor and Oil MH 15. Polyfor is liquid plasticizer and aeration admixture for plasters without lime. Oil MH 15 is a liquid hydrophobization admixture. Amount of these admixtures for the modified materials A3 and were for Polyfor 1 % by mass and for Oil MH 15 0.3 % by mass.

The second modified material A5 with water/gypsum ratio of 0.917 contained the same additives in the same amount as A3, and in addition it comprised also 3% of expanded pearlite EP 150 by mass.

For the measurements of particular mechanical, thermal and hygric parameters, we used the following samples: bending strength and compressive strength – 3 specimens 40 x 40 x 160 mm, apparent moisture diffusivity – 4 specimens 50 x 50 x 23-25 mm, water vapor diffusion coefficient - 12 cylinders with the diameter 105 mm and thickness 10-22 mm, thermal conductivity and volumetric heat capacity – 6 specimens 70 x 70 x 70 mm.

The all samples were mixed according to the Czech standard ČSN 72 2301 [3].

Experimental results

The basic properties – bulk density, matrix density and open porosity – of the non-modified and modified gypsum are shows in Table 2.

Table 1. Basic physical properties of measured materials

Material	Bulk density [kg/m3]	Matrix density [kg/m3]	Open porosity [-]
S1	**1170**	**1900**	**0.38**
A1	**982**	**2090**	**0.54**
A3	**1021**	**1910**	**0.51**
A5	**791**	**1946**	**0.59**

The bulk density was highest (and the open porosity lowest) for the material S1 (Počerady). This can be explained by its lowest water/gypsum ratio. The differences between the values of bulk density and open porosity of materials based on Kobeřice gypsum reflected besides the water/gypsum ratio also the composition of studied materials (e.g. the effect of expanded pearlite).

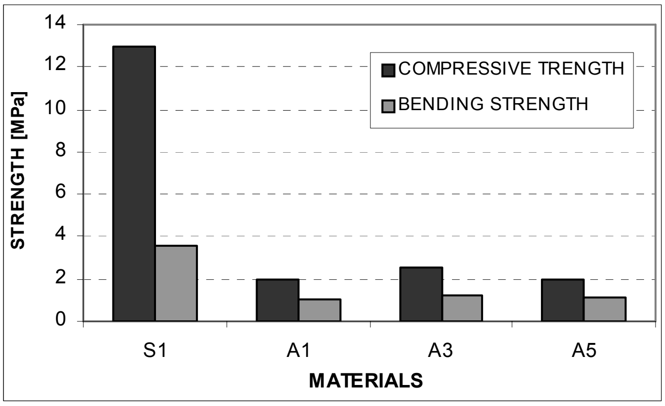

Figure 1. Comparison of compressive and bending strength

The bending and compressive strengths after 2 hours (the time chosen according to ČSN 72 2301) are shown in Figure 1. The results correspond well with the differences in basic physical properties from Table 1. The 2-hours value of compressive strength of the material S1 is more than 6 times higher compared to the materials on Kobeřice gypsum basis, the value of bending strength more than 3 times higher. Among the materials on Kobeřice gypsum basis the best mechanical properties were achieved for the material A3. Compressive strength of this material is about 25 % higher in comparison with A1 and A5, bending strength 20 % higher.

Figure 2 shows typical dependences of water absorption [kg/m^2] on the square root of time [s$^{1/2}$]. Clearly, the effects of water/gypsum ratio (the difference between S1 and A1) and of hydrophobization (A3 and A5 against S1 and A1) are very significant.

Table 3 shows the quantification of experimental results of the 1-D water absorption experiment in the form of water absorption coefficient and apparent moisture diffusivity. We can see that for the materials A3 and A5 the water absorption coefficient is 15-30 times lower than for the reference materials S1 and A1, the apparent moisture diffusivity by even 2-3 orders of magnitude. So, the effect of the hydrophobization admixture Oil MH15, which was used for modification of the materials A3 and A5, on water transport was quite remarkable.

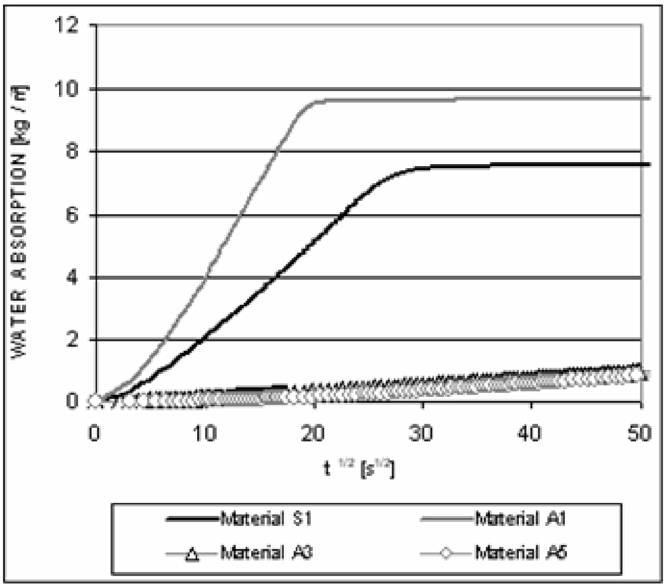

Figure 2 Results of the 1-dimensional water absorption experiment

Table 3 Water transport properties of measured materials

Material	Water absorption coefficient [kg/m2s 1/2]	Apparent moisture diffusivity [m2/s]
S1	**0.31**	**6.11 E-7**
A1	**0.56**	**1.11 E-6**
A3	**0.02**	**1.54 E-9**
A5	**0.02**	**1.75 E-9**

The values of water vapor diffusion resistance factor presented in Table 4 are highest for the material A3, lowest for S1 and A5. However, the differences are not very high to affect the capability of water vapor transport remarkably. So, the effect of hydrophobization was not very important in this case. This is a positive feature for a gypsum element; the capability of fast water vapor removal is substantial factor increasing its durability.

Table 4 Water vapor transport properties of measured materials

Material	**Water vapor diffusion resistance factor [-]** **Relative humidity**	
	5/50 %	**90/50 %**
S1	**14**	**13**
A1	**17**	**16**
A3	**19**	**18**
A5	**14**	**14**

Table 5 shows basic thermal properties of analyzed materials which were determined for the moisture content corresponding to the relative humidity of 50% and temperature about 20°C. The differences in thermal conductivity are in a good agreement with the differences in open porosity (Table 1). So, the lowest thermal conductivity exhibits the material A5 with highest open porosity. The value of water/gypsum ratio is for the material A5 higher than for the material A3, which contains the same admixtures, but effect of expanded pealite EP 150 evokes reduction of bulk density and increase of open porosity.

Differences in volumetric heat capacity of all materials were low, up to 10 %, which was within the error range of the measuring method. Therefore, the differences in thermal diffusivity reflect mainly the differences in thermal conductivity.

Table 5 Thermal properties of measured materials

Material	**Thermal conductivity [W/mK]**	**Volumetric heat capacity [J/m3 K]**	**Thermal diffusivity [m2 /s]**
S1	**0.47**	**1.60 E+6**	**0.29 E-6**
A1	**0.26**	**1.47 E+6**	**0.18 E-6**
A3	**0.28**	**1.52 E+6**	**0.18 E-6**
A5	**0.24**	**1.47 E+6**	**0.16 E-6**

Conclusions

The experimental results presented in this paper have shown that the combination of the plasticizer Polyfor, hydrophobizer Oil MH 15 and expanded pearlite EP 150 has good potential for further applications in gypsum based materials. The 2-3 orders of magnitude decrease of moisture diffusivity which was caused by this combination of admixtures compared to the basic material without modifications was quite remarkable. Taking into account that both compressive and bending strengths and water vapour diffusion parameters were not affected negatively at the same time, which is often the case with using hydrophobization admixtures, the proposed technology can be considered very prospective.

The far best mechanical properties among the studied gypsum based materials were observed for the hardened gypsum S1 produced using flue gas desulphurization gypsum as raw material. The most important reason for this result was probably the very high purity of the raw material. The worse workability of Koberice “grey gypsum plaster” leading to higher necessary water/gypsum ratios was the second important parameter in this respect. However, both these factors cannot explain the remarkable strength improvement completely. Therefore, complementary investigations are necessary to be done, microstructural studies including exact phase analyses in particular. This will be done in the near future.

Acknowledgement

This research has been supported by the Ministry of Industry and Trade of Czech Republic, under grant No FT-TA3/005.

References

[1] BIJEN, J., van der PLAS, C. 1992: Polymer-Modified Glass Fibre Reinforced Gypsum. Materials and Structures 25: 107-114.

[2] COLAK, A. 2001: Characteristics of Acrylic Latex Modified and Partially Epoxy-Impregnated Gypsum. Cement and Concrete Research, 31, 1539-1547.

[3] ČSN 72 2301. 1979. Gypsum binding materials, Czech standard (in Czech), Bureau for Normalization and Measurement, Prague 1979.

[4] DAHL, S.D., KUEHN, T.H., RAMSEY, J.W., YANG, C.H. 1996. Moisture Storage and Non-Isothermal Transport Properties of Common Building Materials. HVAC&R Research, Vol. 2: 42-58.

[5] DANTEN, A., HOSTACHE, G., MURAT, M., DICARD, L. 1984. Influence of Water Content on the Thermal Diffusivity of Gypsum Plaster. Materials and Structures, Vol. 17: 303-306.

[6] HANUSCH, H. 1974. Übersicht über Eigenschaften und Anwendung von Gipskartonplatten. Zement-Kalk-Gips, No. 5: 245-251.

[7] KLEIN, D., von RUFFER, C. 1997. Grundlagen zur Herstellung von Formengips. Keramische Zeitschrift, Vol. 49: 275-281.

[8] KUMARAN M.K. 1994. Moisture Diffusivity of Building Materials from Water Absorption Measurements. IEA Annex 24 Report T3-CA-94/01, Ottawa,: 230-235.

[9] LUCAS, G. 1997. Capillary Conductivity and Body Formation in Moulds of Special Plaster - Results from Laboratory and Practice. Interceram Vol. 46 : 419-424.

[10] MEHAFFEY, J.R., CUERRIER, P., CARISSE, G. 1994. A Model for Predicting Heat Transfer through Gypsum Board/Wood-Stud Walls Exposed to Fire. Fire and Materials, Vol. 18: 297-305.

[11] ROELS S., CARMELIET J., HENS H., ADAN O., BROCKEN H., ČERNÝ R., PAVLÍK Z., HALL C., KUMARAN K., PEL L., PLAGGE R. 2004. Interlaboratory Comparison of Hygric Properties of Porous Building Materials. Journal of Thermal Envelope and Building Science, Vol. 27: 307-325.

[12] SCHULZE W., TISCHER W., Lach V. 1990: Non-cement mortars and concrete, Prague: SNTL: 20-31.

[13] SINGH, M., GARG, M. 1997. Retarding Action of Various Chemicals on Setting and Hardening Characteristics of Gypsum Plaster at Different pH. Cement and Concrete Research, Vol. 27: 947-950.

[14] ŠATAVA, V. 1996: Strength and microstructure of cast gypsum. Ceramics - Silikáty, 40, No. 2: 72-76.

[15] TAZAWA, E. 1998. Effect of Self-Stress on Flexural Strength of Gypsum-Polymer Composites. Advanced Cement Based Materials, Vol. 7: 1-7.

[16] WIRSCHING, F. 1984: Drying and Agglomeration of Flue Gas Gypsum. In The Chemistry and Technology of Gypsum, Philadelphia: American Society for Testing and Materials: 161-174.

Thermal conductivity in dependence on temperature

Jan Toman, Tomáš Korecký

Faculty of Civil Engineering, Czech Technical University in Prague,

Thákurova 7/2077, 166 29 Prague 6 – Dejvice, Czech Republic

email: toman@fsv.cvut.cz

Abstract:

A gradient method for the measurement of thermal conductivity at steady-state heat flow is presented in the paper. At the steady-state heat conduction across a multi-layer wall the heat flux is directly proportional to the temperature differences and thermal conductivity of every material. If the thermal conductivity depends on temperature, for a specified temperature interval a material can be characterized by a constant thermal conductivity value. Knowing the temperature field in a material in steady-state conditions and single value of thermal conductivity at certain temperatures, other thermal conductivity values can be calculated for other temperatures.

***Keywords**: thermal, conductivity, coefficient, temperature*

1. introduction

From theory consequents and practical measuring was proved that thermal conductivity coefficient is relative strong depend on material temperature and moisture [1]. Measuring under non-standard conditions it´s very difficult to find and analytically qualify these consequences. To define dependence of thermal conductivity coefficient on moisture is necessary to use non-stationary measuring methods because during stationary methods is generated temperature gradient on scale material sample for quit long time and it cases the change of moisture by evaporation. For the measuring thermal conductivity coefficient during non-stationary methods it´s necessary only to have quit a short time to start temperature gradient and therefore we can omit evaporation – moisture is possible consider as constant for all time of measuring. There are lots of non-stationary methods which is possible to document this dependence enough by [2]. To define dependence thermal conductivity coefficient on temperature for dry material in normal temperature interval there are quit big deal of methods either stationary or non-stationary. Difficult is implement measuring moisture material in dependence on temperature and also in normal temperature interval. But there is always possibility to realize distribution of dependence on temperature of dry material and dependence on moisture and calculate based on superposition principle.

More complicated is to scale wanted dependence in wide temperature interval [3]. The biggest problem here is in that measuring must by solve during extreme temperatures. For this measuring we developed non-standing method which is based on inverse solution of thermal conduction equation. By know boundary conditions during one way temperature stress is measured distribution of thermal field in different times a by using inverse function it is possible calculate temperature conductivity for different temperatures from thermal conduction equation [4]. If we know thermal dependence of specific thermal capacity and density of given material we can calculate thermal conductivity coefficient for different temperatures from relation:

$$\lambda = a\,.\,\rho\,.\,c \tag{1}$$

where λ is thermal conductivity coefficient $[W.m^{-1}.K^{-1}]$, a coefficient of thermal diffusivity $[m^2.s^{-1}]$, ρ density $[kg.m^{-3}]$, c specific thermal capacity $[J.kg^{-1}K^{-1}]$ and also receive thermal dependence thermal conductivity coefficient.

This method is rather complicated both experimental also mathematical. Therefore we suggested new method for measuring thermal conductivity coefficient in wide thermal interval which is easy to implement – there will on by longer time of measuring thermal field to steady flux it means instead approx. 40 min. it´s necessary to measure about 3 hours – but it is necessary to essential thermal conductivity coefficient scaled material at least at on particular temperature.

2. Theoretical principle of new suggested method

Basic data to settle thermal conductivity coefficient in dependence on temperature is measuring temperature gradient during one way leading thermal at steady-state heat flux and knowledge of thermal conductivity coefficient at one particular temperature.

Is valid

$$P = \frac{(t_2 - t_1)}{R} \tag{2}$$

where *P* is density of heat flux rate $[W.m^{-2}]$, t_1 temperature of one the wall surface $[K]$, t_2 temperature of second the wall surface $[K]$, R thermal resistance of all the wall $[W^{-1}.m^2.K]$.

If we take all the thickness of the wall as if it is composed from several thin layers from which every has thickness d_i and thermal conductivity coefficient λ_i and we will know the difference of temperatures on division lines these thicknesses t_i for constant density of heat flux will be valid

$$P = \frac{t_i\,.\,\lambda_i}{d_i}\,, \tag{3}$$

because generally is valid

$$R = \frac{d}{\lambda}\,. \tag{4}$$

During stable leading of heat trough the wall in direction its thickness is valid this relation

$$\lambda = \frac{Q\,.\,d}{(t_2 - t_1)\,.\,\tau\,.\,S}, \tag{5}$$

where λ is thermal conductivity coefficient $[W.m^{-1}.K^{-1}]$, Q amount of thermal energy [J] which gone trough [J], d wall thickness [m], t_1 temperature of one the wall surface [K], t_2 temperature of second the wall surface [K], τ temperature passing time [s], S wall area [m^2].

During stable thermal conduction trough the wall it is possible to replace vales Q, τ, S by constant K. If we measure temperature t_x inside the board in distance x from its surface there must be valid for average temperature t_1 from interval temperatures, which had been measured in distances x_0 and x_1, must be valid that

$$\lambda_1 = \frac{x_2 - x_0}{t_2 - t_1}.K \;\Rightarrow\; K = \lambda_1.\frac{t_2 - t_1}{x_2 - x_0}. \tag{6}$$

For any temperature $t_n = \frac{(t_{n-1} + t_{n+1})}{2}$ will be valid

$$\lambda_n = \lambda_1.\frac{t_2 - t_1}{x_2 - x_0}.\frac{x_{n+1} - x_{n-1}}{t_{n+1} - t_{n-1}}. \tag{7}$$

If we measure thermal conductivity coefficient given material λ_1 by another method by particular temperature t_1 an if we scale thermal field during steady state we can calculate value of thermal conductivity coefficient of given material by different temperatures and this way we can define its temperature dependence.

Formulation temperature gradient during one way thermal leading through the wall characterized in the best way by scaling temperature t in dependence on distance x from its surface.

Then we can limit increments of distances and temperatures values and use derivation of found function. This way it is possible to calculate value of thermal conductivity coefficient not as average but straight by given temperature.

3. Description of method of thermal field measuring

In order to measure temperature gradient inside the given material during one way thermal leading this apparatus was used:

[1] Sample made of scaled material in cube shape with edge length 7 cm, in which axis are located thermo-couple "tree" [5] – see picture 1 – which is inserted to form during producing samples from cost material.

Distances of particular measuring places from thermal stress front were in our case 0, 1, 2, 3, 5 and 7 cm.

[2] Modified electric kiln – see picture 2 – which is after closing full door heated in the first measuring up to 200 °C and in the second case 1000 °C (800 °C). After reaching

required temperature the first door will be replaced for another one in which scale sample is located.

[3] Measuring recording central control panel (exchange) – see picture 2 – is connected with cable departures from all measuring places (thermo-couples). This control panel records data from each thermo-couples in dependence on time during all measuring time until we reach steady state. After that we subtract needed temperatures to define temperature gradient and through measured out points we interlay curve.

Notice: Temperature record during heating can be used for calculation of thermal conductivity coefficient in dependence on temperature by our develop non-stationary method.

[4] Ventilator which is fan exterior surface of scale sample so that the constant temperature in room was guaranteed.

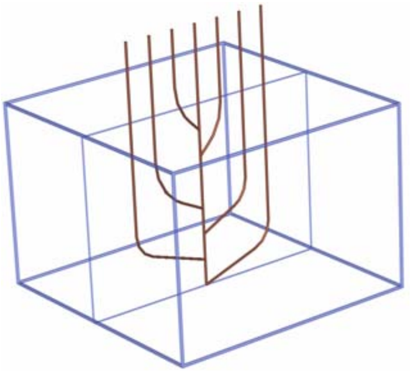

Figure 1: Thermo-couple "tree"

Figure 2: Recording central control panel

4.Measured values and calculation

In order to check measuring we used samples made of cement mortar which had been used for finding temperature dependence on thermal conductivity coefficient by non-stationary method. Measured values of temperature gradient were downloaded in electrical protocol from measuring panel to computer.
To particular calculation was created computer programme. Input data are measured values of temperature gradient and one value of thermal conductivity coefficient by one specific temperature which was define by another method.
In the picture 3 there is output from computer program. In right top part there is figure of temperature gradient after stabilization and in right down part there is temperature dependence on thermal conductivity coefficient calculated according measured values inserted on left side.
In order to compare picture 4 there is plot dependence of thermal conductivity coefficient realized by non-stationary method.

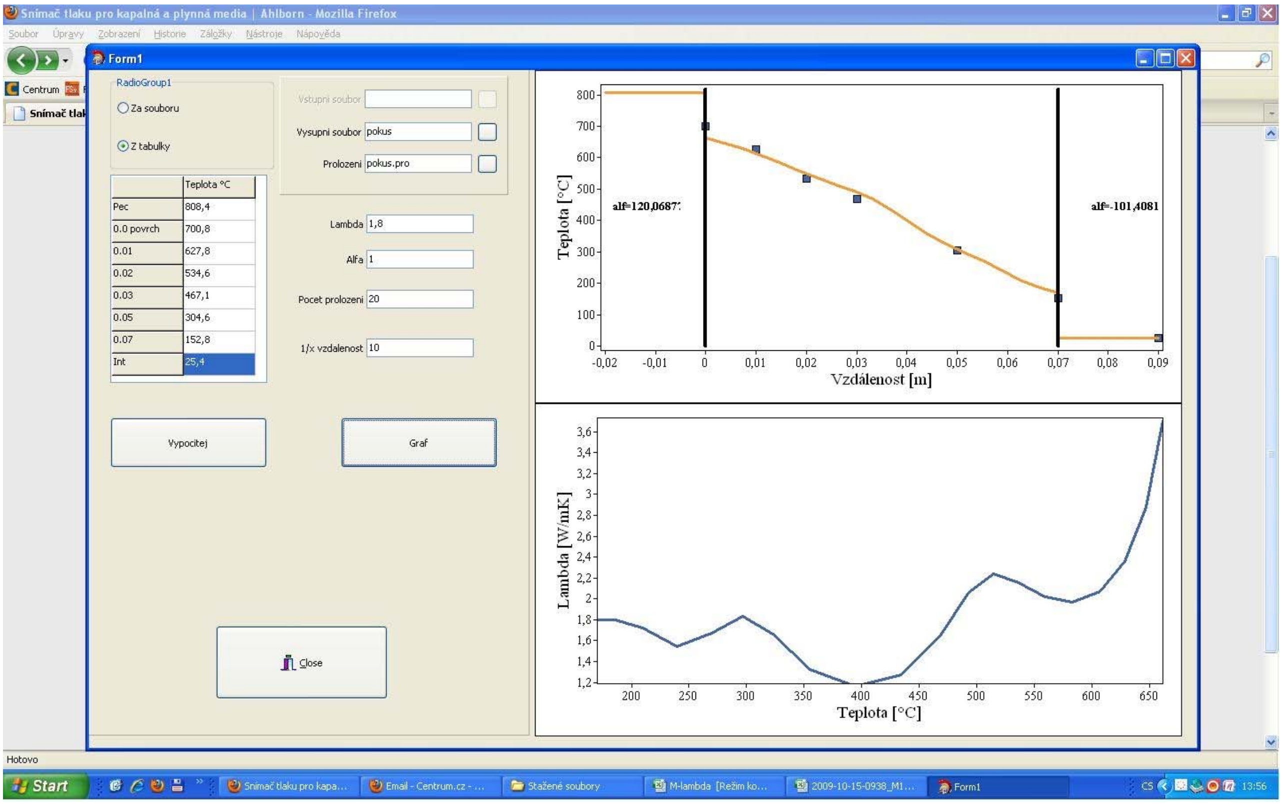

RadioGroup1: ○ Za souboru ● Z tabulky

Vstupni soubor:
Vysupni soubor: pokus
Prolozeni: pokus.pro

	Teplota °C
Pec	808,4
0.0 povrch	700,8
0.01	627,8
0.02	534,6
0.03	467,1
0.05	304,6
0.07	152,8
Int	25,4

Lambda: 1,8
Alfa: 1
Pocet prolozeni: 20
1/x vzdalenost: 10

Figure 3: Output from computer program

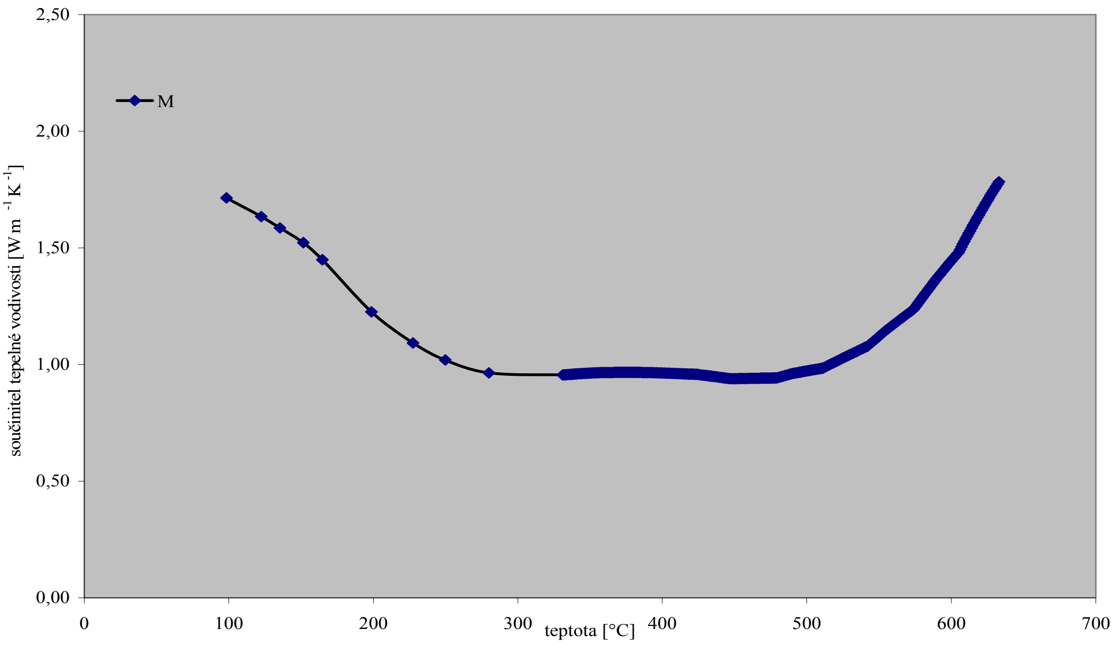

Figure 4: Dependence of thermal conductivity coefficient realized by non-stationary method

5. Discussion and conclusion

As you can see in pictures 3 and 4, the results of dependence thermal conductivity effects on temperature received by different methods aren´t absolutely identical even when there is fundamental agreement in behaviour of measure dependence. The fact that by using both methods first is proved decreasing trend has absolutely logical explanation - initiative increase of temperature lads to total drying of material and therefore capacity of pores gets bigger. Those are then filled with dry air which has lower conductivity then solid framework material or water. Between temperatures 200 to 400 °C is thermal conductivity coefficient on the lowest values. If we increase of temperature the speed of gas molecules motion will play more important role which result from molecular kinetic gas theory and therefore increasing of total conductivity of material will display because will be involve also factor of transfer of heat energy by fluxing.

If we would take as more exactly result given by already verified non-stationary method it´s need implement corrections to calculation on new suggested method from stationary state. They will get by setting more exactly regress scaled temperature dependence on distance and more exactly selection of thermal conductivity coefficient for basic temperature. By conclusion is possible to claim that for simplicity is possible use new suggested method for determination temperature dependence on thermal conductivity coefficient in case observation of stable thermal leading conditions and in case right curve regression selection which define temperature gradient during stable leading and exactly knowledge thermal conductive coefficient on one basic temperature.

Acknowledgements

This research has been supported by Ministry of Education, Youth and Sports: MSM 6840770031 and grant Ministry of industry and trade of the Czech Republic: FR-TI 1/216.

References

[1] TOMAN J.: Vliv teploty a vlhkosti na fyzikální parametry stavebních materiálů. Disertační práce DrSc. ČVUT Praha 1992

[2] CARSLAW, Jaeger : Conduction of heat in solids.Oxford.1959.

[3] KREMPASKÝ J.: Meranie termofyzikálných veličin. SAV Bratislava. 1969.

[4] ČERNÝ R., TOMAN J.: Metody určení součinitele tepelné vodivosti z teplotního pole ve stavebních materiálech. Stavební výzkum 1/91str.1-4. Praha 1991.

[5] TOMAN J.: Přípravek pro určení teplotního spádu uvnitř materiálu. Užitný vzor č.18299. ČVUT FSv Praha 2008.

The thermodilatometric analysis of kaolin-quartz samples

Anton Trník, Igor Štubňa, Ján Ondruška

Department of Physics, Constantine the Philosopher University, Tr. A Hlinku 1, 94974
Nitra, Slovakia
email: atrnik@ukf.sk

Abstract: *The thermodilatometric analysis (TDA) of kaolin-quartz samples from 20 °C to 1200 °C is presented. The samples were prepared from the Sedlec kaolin and 0 wt.%, 9 wt.%, 20 wt.%, 30 wt.%, 40 wt.%, 50 wt.%, 60 wt.%, 70 wt.%, 80 wt.%, and 100 wt.% of quartz. The processes occurring in the samples during heating up to 1200 °C (dehydroxylation of kaolin at 450 °C – 650 °C, the collapse of the metakaolinite structure at 950 °C, the α-β transformation of quartz at 573 °C as well as a solid-state sintering at the temperatures higher than 600 °C) are reflected in thermodilatometric curves in different proportions dependent on the quartz content.*

Keywords: *thermodilatometric analysis, kaolin, quartz*

1 Introduction

Understanding of the behavior of ceramics can provide insights into firing processes, the influence of additives and raw materials, e.g., the densification and sintering process, reaction kinetics, and phase transitions. Thermodilatometric analysis (TDA) is a very suitable method for investigation of such processes in ceramics and is commonly used for that purpose.

Thermodilatometric behavior of a kaolin-quartz sample during heating is determined primarily by the dehydroxylation process in the kaolinite crystals at temperature interval 450 °C – 650 °C [1, 2] and by the α-β transformation of quartz at 573 °C [3]. The elastic behavior is determined mainly by improving the contacts between crystals as a consequence of the solid state sintering [4, 5]. The thermal expansion after completing of dehydroxylation terminates at the temperature 950 °C, when the collapse of the metakaolinite lattice accompanied by a rapid shrinkage appears. At the same time there is a steep increase of some mechanical properties (modulus of elasticity, mechanical strength) as the response to a faster solid state sintering and on the new structure rather than the defect and microporous metakaolinite [6].

The aim of this contribution is to observe the influence of quartz content in kaolin samples with the help of the TDA during heating up to 1200 °C.

2 Samples and measurement method

The samples were molded from the mixture of the Sedlec kaolin and 0 wt.%, 9 wt.%, 20 wt.%, 30 wt.%, 40 wt.%, 50 wt.%, 60 wt.%, 70 wt.%, 80 wt.%, and 100 wt.% of quartz sand by casting in a gypsum form. After free drying in open air, the samples contained ~1 wt.% of the physically bonded water. The samples had the dimension 9.5 mm × 9.5 mm × 40 mm.

In this research, a push rod alumina dilatometer was used [7] for investigation of the quartz influence in kaolin. The green samples were heated in the dilatometer in the air. The temperature was increased linearly at the rate of 5 $°C \cdot min^{-1}$ from the room temperature to 1200 °C. After the first heating, the samples underwent TDA again with the same heating rate.

3 Results

During heating, the structure and composition of kaolin-quartz samples is changed. These changes determine the mechanical and dilatometric behavior of the samples. The results of thermodilatomery of green kaolin-quartz samples at the linear heating up to 1200 °C are shown in Fig. 1.

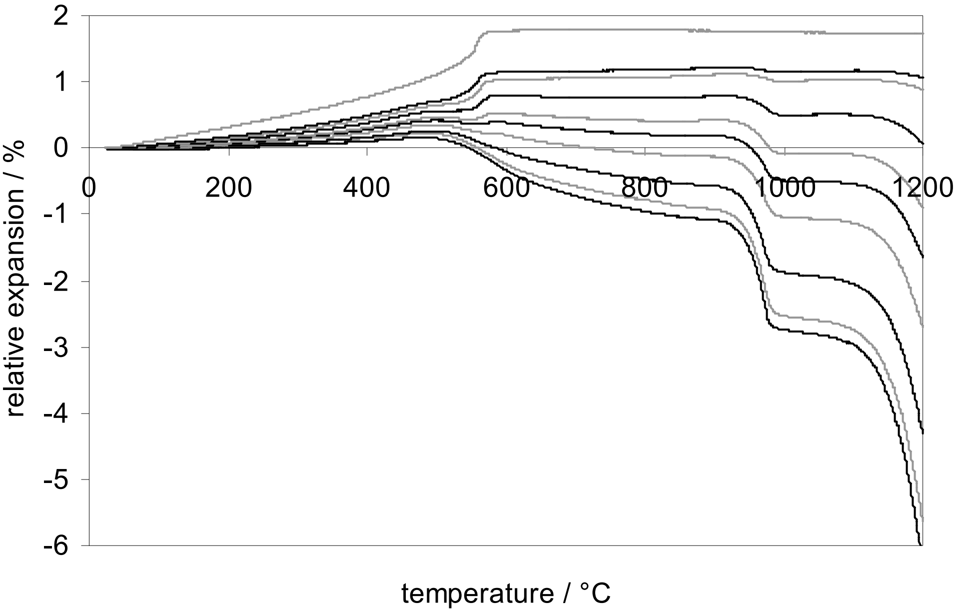

Figure 1: Thermodilatomeric curves of green kaolin-quartz samples. The content of quartz (from the bottom): 0 wt.%, 9 wt.%, 20 wt.%, 30 wt.%, 40 wt.%, 50 wt.%, 60 wt.%, 70 wt.%, 80 wt.%, 100 wt.%

The thermodilatometric curve of green samples can be divided into typical parts corresponding to processes in kaolin and quartz. The liberation of physically bound water at temperatures from 20 °C to 250 °C leads to more tight contacts between kaolinite crystals and, subsequently, to the shrinkage of the sample. On the other side, thermal expansion takes place at the same time which increases the size of the sample. The curve between 20 °C and 250 °C follows from these two competitive mechanisms. After liberation of the physically bound water, only the thermal expansion takes place. Dehydroxylation at temperatures from 450 °C to 650 °C is accompanied by the creation of metakaolinite. Its crystals are of the same type as kaolinite crystals, but have a smaller *c*-parameter, so the shrinkage of the sample can be observed. The $\alpha \rightarrow \beta$ transformation of quartz takes place at 573 °C. If the quartz grains are free and can change their dimensions without any obstruction, then their relative volume change is +0.68 %. However, the quartz grains are not free but surrounded by the kaolin structure. So, the quartz grains increase their volume less than 0.68 %. The beginning of the solid-phase sintering also gives rise to more shrinkage which continues untill the end of heating. The collapse of metakaolinite and the creation of alumina spinell (metastable phase) and primary mullite takes place above 950 °C. This new structure significantly increases the shrinkage.

Initially, it is noted that there are significant differences between thermodilatometric curves of the samples with different content of quartz (see Fig. 1). If the sample contains a larger amount of quartz, its thermal expansion from the room temperature to 570 °C is higher, then the length of sample increases rapidly at 573 °C, and after the α → β transformation of quartz, the shrinkage of the sample and effects of the high-temperature processes are smaller.

The results of thermodilatometry of the fired kaolin-quartz samples at the linear heating up to 1200 °C are shown in Fig. 2.

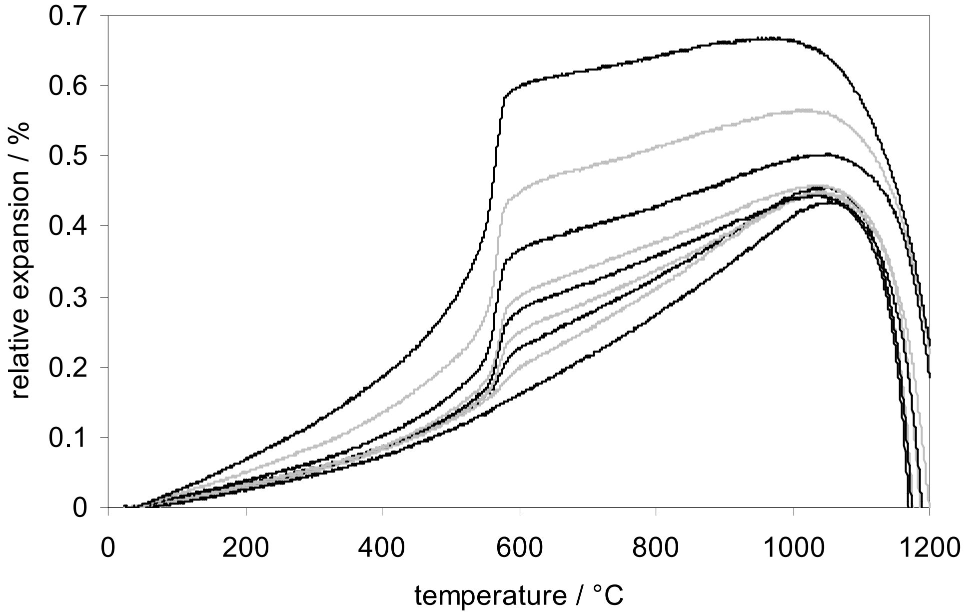

Figure 2: Thermodilatometric curves of fired kaolin-quartz samples. The content of quartz (from the bottom): 0 wt.%, 9 wt.%, 20 wt.%, 30 wt.%, 40 wt.%, 50 wt.%, 60 wt.%, 70 wt.%, 80 wt.%.

The thermodilatometric curves of the fired samples are nearly linear in the most important temperature region from an exploitation point of view, i.e., between 20 °C – 500 °C. Similar results were obtained for porous clay ceramics [8]. Thermal expansion of the quartz grains caused the typical step at 573 °C on the thermodilatometric curves. Above ~950 °C, a contraction of the samples was noted and recorded. That was caused by the pressure of the dilatometer push-rod on the sample, if the sample contains some part of glassy phase, which decreases its viscosity at higher temperatures. This contraction is not a real property of the measured material [9].

4 Conclusion

The thermodilatometric analysis (TDA) of kaolin-quartz samples from 20 °C to 1200 °C was presented. The samples were prepared from the Sedlec kaolin and 0 wt.%, 9 wt.%, 20 wt.%, 30 wt.%, 40 wt.%, 50 wt.%, 60 wt.%, 70 wt.%, 80 wt.%, and 100 wt.% of quartz. The processes occurring in the samples during heating up to 1200 °C (dehydroxylation of kaolin at 450 °C – 650 °C, the collapse of the metakaolinite structure at 950 °C, the α-β transformation of quartz at 573 °C as well as a solid-state sintering at the temperatures higher than 1000 °C) were reflected in the thermodilatometric curves in different proportions dependent on the quartz content.

Acknowledgment

This work was supported by the grants VEGA 1/0302/09, VEGA 1/0216/09 and FCVV initiative of the Constantine the Philosopher University under grant I-06-399-01. The authors appreciate the cooperation with the ceramic plant PPC Čab, Slovakia, a member of the international PPC Insulators group.

References

[1] VARGA, G.; TRNÍK, A.: Štruktúra kaolinitu a metakaolinitu. Silika. 2006, 16, s. 184-187

[2] ŠTUBŇA, I.; VARGA, G.; TRNÍK, A.: Investigation of kaolinite dehydroxylation is still interesting. Építőanyag – Building Materials. 2006, 58, s. 6-9

[3] ŠTUBŇA, I.; TRNÍK, A.; VOZÁR, L.: Thermomechanical analysis of quartz porcelain in temperature cycles. Ceramics International. 2007, 33, s. 1287-1291.

[4] TRAORE, K.; KABRE, T. S.; BLANCHART, P.: Sintering of a clay from Burkina Faso by dilatometry Influene of the applied load and the pre-sintering heating rate. Ceramics International, 27, 2001, p. 875- 882

[5] WINKELMANN, K.; GOBEL, O.; NIKKILA, A. P.; VUORINEN, P.; MANTYLA, T.; ZSCHECH, E.: Influence of sintering aids on sintering, microstructure and mechanical-properties of Al2O3 ceramics. Metall, 48, 1994, p. 382- 387

[6] ŠTUBŇA, I.; TRNÍK, A.; VOZÁR, L.: Thermomechanical and thermodilatometric analysis of green alumina porcelain. Ceramics International, 35, 2009, p. 1181–1185

[7] ŠTUBŇA, I.; VÁŽANOVÁ, A.: Simple push-rod dilatometer for dilatometry of ceramics. In: Proc. Conf. Research and Teaching of Physics on the Context of University Education, SPU Nitra, Nitra 2007, p. 69-74

[8] PLEŠINGEROVÁ, B.; SÚČIK, G.: Thermal and moisture expansion of porous biscuit bodies. Acta Metallurgica Slovaca, 8, 2002, p. 173-179 (in Slovakian)

[9] VENTURELI, C.; PAGENELLI, M.: Sintering behavior of clays for the production of ceramics. cfi/Ber. DKG, 84, 2007, N5, p. E1-E3

Effect of porosity on moisture transport properties of composite materials

Eva Vejmelková[1], Martin Keppert[1], Petr Konvalinka[2] and Robert Černý[1]

[1] Department of Materials Engineering and Chemistry, Faculty of Civil Engineering, Czech Technical University in Prague, Thákurova 7, 166 29 Prague 6, Czech Republic

[2] Experimental Center, Faculty of Civil Engineering, Czech Technical University in Prague, Thákurova 7, 166 29 Prague 6, Czech Republic

Abstract: *Effect of porosity on moisture transport properties of cementitious composites is analyzed in the paper. Empirical relationships between moisture transport parameters and porosity are formulated, based on modifications of the Arrhenius equation. Effects of cement matrix and randomly distributed fibers on moisture transport properties are studied as well.*

Keywords: *cement-based composites, water transport, water vapour transport, pore distribution*

Introduction

High temperatures cause physical and chemical changes in cement based composites and the accompanying variations in the properties of these materials may be quite significant. Therefore, more and more attention is being paid to the mechanical properties of cement composites exposed to high temperatures and to their residual strength after exposure to elevated temperatures. However, only a few recent studies have been devoted to the effect of high temperatures on basic physical and hydric properties of this type of materials.

This paper is aimed to fill at least partially this gap in the overall knowledge and presents simple semi-empirical relations between experimentally determined basic physical properties and moisture transport properties of autoclaved aramid fiber reinforced cement composite exposed to high temperatures and its texture. The main motivation for using the combination of autoclaving preparation procedure and aramid fibers is their supposed complementary effects on the high-temperature resistance of the composite. The autoclaving procedure can help to increase the resistance of the matrix to the temperature range of 600-700°C. The aramid fibers – besides their contribution to good mechanical performance of the composite in the lower temperature range – can reduce damage of the already partially decomposed matrix at temperatures higher than 700°C, as a consequence of their thermal decomposition above approximately 550°C.

Materials

The measurements were done on aramid fibre reinforced cement composite produced in the laboratories of VUSTAH Brno. The composition of the material in mass-% of dry substances and the water/cement ratio are shown in Table 1.

Samples for measurements were prepared using vacuum technology of the OMNI MIXER 10 EV mixing device. First, cement, siliceous aggregates, microsilica and wollastonite were homogenized in the mixing device, then water, plasticizer and shorter aramid fibres were added and the wet mixture mixed again. Finally, the longer aramid fibres were worked into the mixture by short mixing, the mixture put into the forms, evacuated for one hour and autoclaved.

Before the measurements, all specimens were dried in an oven at 110°C. In the experiments, four various sample pre-treatment conditions were tested: reference specimen not exposed to any load (denoted as T-ref in what follows), specimen exposed to a gradual temperature increase up to 600, 800 and 1000°C during two hours, then left for another 2 hours at the final temperature and slowly cooled (denoted as T-600, T-800 and T-1000 according to the loading temperature).

Table 1: Composition of the studied composite material

Components	Amount [%kg/kg]
Cement CEM I 52.5	36
Siliceous aggregates	17
Microsilica 940 US	4
Wollastonite	39
Aramid fiber 1.5 mm	2
Aramid fiber 6 mm	2
w/c	0.9

Experimental Methods

1.1. Determination of pore size distribution

The texture changes of the studied composite were described by means of porosity and pore size distribution. Total porosity was calculated by help of bulk density and matrix density. Matrix density was determined by helium pycnometry (Pycnomatic ATC, Porotec, Germany), bulk density by weighing and measuring dimensions of rectangular specimens. Pore size distribution was determined by Mercury Intrusion Porosimetry (MIP) by equipment Pascal 140 + 440 (Thermo Electron Corp., Italy). The contact angle was assumed to be 130°. The material's samples for MIP were crushed to pieces of about 2 mm in order to avoid presence of any large free spaces in the sample. Since only the pores of diameter from 0.003 to 100 μm are visible for MIP, the volume of pores over 100 μm was estimated by help of total pore volume Vp and pore volume measured by MIP - VHg which corresponds to pores having d < 100 μm.

Water vapor transport properties

The wet cup method and dry cup method [1] were employed in the measurements of water vapor transport parameters. The specimens were water and vapor proof insulated by epoxy resin on all lateral sides, put into the cup and sealed by technical plasticine. The impermeability of the plasticine sealing was achieved by heating it first for better workability and subsequent cooling that resulted in its hardening. In the wet cup method the sealed cup containing saturated K2SO4 solution (the equilibrium relative humidity above the solution was 97.8%) was placed into an air-conditioned room with 30% relative humidity and weighed periodically. The measurements were done at 25±1°C in a period of four weeks. The steady state values of mass loss determined by linear regression for the last five readings were used for the determination of water vapor diffusion coefficient. In the dry cup method the sealed cup containing dried CaCl2 (the equilibrium relative humidity above the desiccant was 5%) was placed in an air-conditioned room with 30% relative humidity. Otherwise, the measurement was done in the same way as in the wet cup method.

The water vapor diffusion coefficient D [m2s-1] was calculated from the measured data according to the equation

$$D = \frac{\Delta m \cdot d \cdot R \cdot T}{S \cdot \tau \cdot M \cdot \Delta p_p} \tag{1}$$

where Δm [kg] is the amount of water vapor diffused through the sample, d [m] the sample thickness, S [m^2] the specimen surface, τ [s] the period of time corresponding to the transport of mass of water vapor Δm, Δp_P [Pa] the difference between partial water vapor pressure in the air under and above specific specimen surface, R the universal gas constant, M the molar mass of water, T [K] the absolute temperature.

Water transport properties

The water sorptivity A [kg m^{-2} s$^{-1/2}$] and apparent moisture diffusivity κ_{app} [m^2 s^{-1}] were measured using a water suction experiment [2].

Experimental Results and Discussion

Thermal degradation of aramid fiber composites

Thermal degradation of cement based composites may be followed by help of determination of the total porosity of thermally loaded samples (Table 2). The total porosity increases almost linearly with the annealing temperature.

Table 2: Fundamental materials characteristics of thermally loaded composites

Material	Density	Bulk density	Porosity	Pore volume	Average pore diameter
	g cm^{-3}	g cm^{-3}	%	cm^3 g^{-1}	μm
T - ref	2.421	1.30	46.3	0.356	0.02
T 600	2.607	1.30	50.1	0.386	0.03
T 800	2.944	1.36	53.8	0.396	0.33
T 1000	2.944	1.31	55.5	0.424	1.34

The mechanism of thermal degradation of the studied composites was clarified by MIP. The intrusion curves of T samples are shown in Figure 1. One observes that the average pore diameter increases with temperature of annealing. Volume of intruded mercury does not relate with the increasing porosity of the samples. It is caused by the fact that the largest pores are not detected by MIP and thus the intrusion curves do not describe the whole pore system of a material. Hence it is more useful to redraw the porosity data to a form of column plot (Figure 2) covering the whole size range of pores.

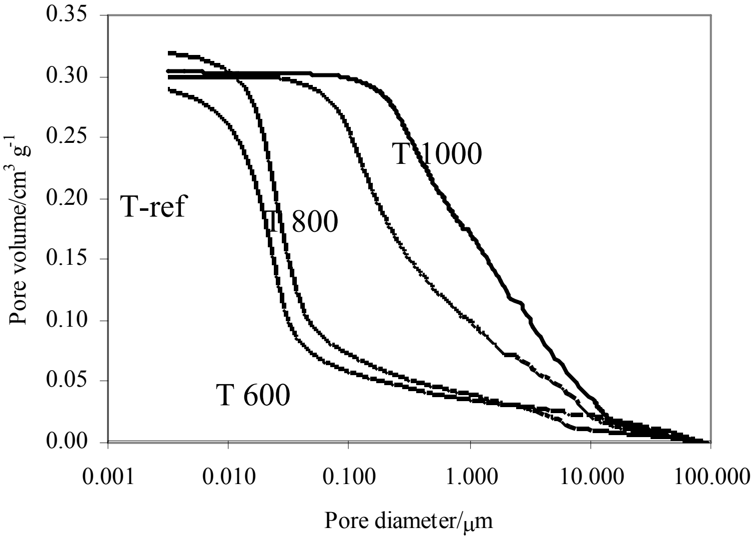

Figure 1: MIP intrusion curves of thermally loaded composites

The material T in its initial – not annealed – state (sample T-ref) features the pore size distribution being typical for cementitious materials. The most frequent are the gel pores (d = 10 to 100 nm), the sample contains also certain amount of large technological pores. The pore distribution of sample T 600 (annealed at 600°C) is similar to the unloaded one; there is observed certain increase of gel pores, the capillary and technological pores remain mostly unaffected by this temperature. The dramatic changes of pore size distribution take place when the sample is annealed at 800°C and continue at 1000°C as well. The volume of gel pores is reduced. It is caused by thermal decomposition of cement binder. The binding components (CSH gels and portlandite) dehydrate back to clinker minerals and CaO (it converts to calcite spontaneously). These decomposition processes are accompanied by sintering of binder which results to the gel pores diminishing.

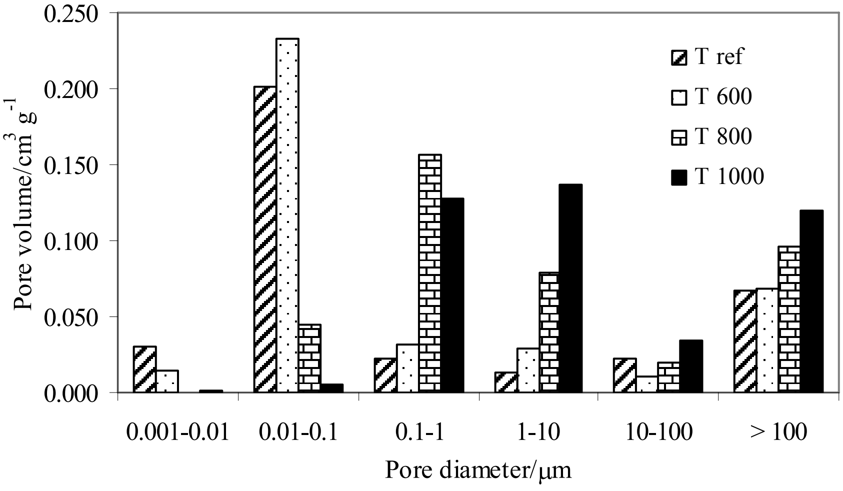

Figure 2: Histogram of pore size distribution of thermally loaded composites T

On the other hand, the volume of capillary pores increases significantly with the thermal load. It is caused by the specific volume changes of the present aggregates – wollastonite and quartz. Quartz undergoes reversible recrystallizations at 573 and 867°C. Wollastonite changes its specific volume continuously from cca 850°C [3]. These volume changes result into irreversible loss of contact between binder and aggregates. New, highly interconnected capillaries are formed in this way. The third process contributing to the thermal degradation of the studied composite is thermal decomposition of aramid fiber. The aramid is thermally stable to 500°C, it decomposes at higher temperatures. The used fibers are of two lengths (1.5 and 6 mm); the fibers consist of filaments having diameter of 12 μm. After the fiber decomposition, channels remain in the composite structure. These channels may have wide range of diameter (at least 12 μm) depending on the degree of defibering of aramide fiber to filaments during the composite mixing. The pore size distribution of T composites (Figure 2) indicates that the fiber channels contribute especially to volume of the largest pore fraction ($d > 100$ μm).

Relationship of moisture transport parameters and materials porosity

The apparent coefficients of moisture diffusivity κ_{app} in T samples are increasing with the porosity. The spontaneous liquid water movement in a porous matrix is caused by capillary forces which are dependent on pore diameter, density and surface tension of the liquid. Thinner capillary leads to higher capillary elevation of the liquid. On the other hand, the rate of capillary movement depends directly on the capillary diameter. Thus the increasing pore volume leads to faster movement of liquid water in the sample. Even though the results of MIP porosimetry might be different from the real pore structure, at least when one compares similar materials (as in this case) the MIP data can be used as input to a simple numerical quantification of apparent moisture diffusivity coefficient and material's pore structure.

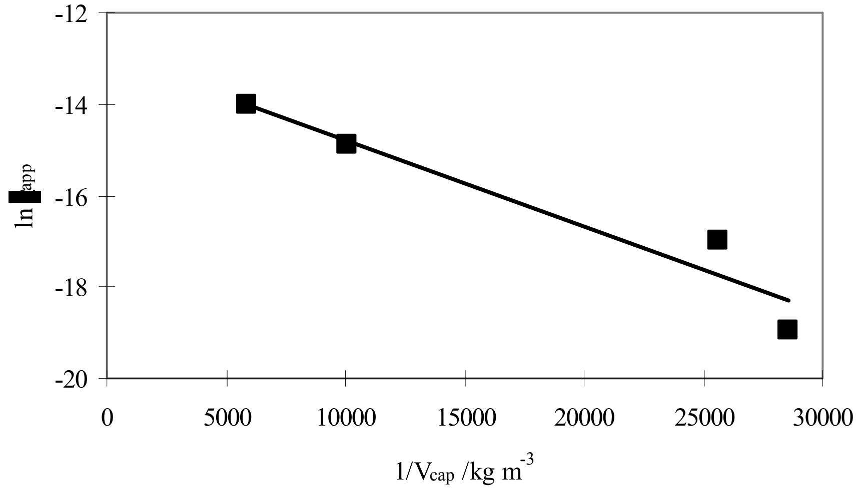

Figure 3: Apparent moisture diffusion coefficient as function of capillary pore volume

In order to find a quantitative relation between material's texture and its apparent moisture diffusivity, the form of well known Arrhenius equation was used. Experimentally determined values of κ_{app} (in form of natural logarithm) were plotted as function of reciprocal volume of capillary pores (1 μm < d < 100 μm) (Figure 3). The data fall into a straight line; it proves the assumption that capillary pore volume is the rate determining factor of the liquid moisture diffusion. The general Arrhenius equation was modified to the studied problem (Eq. 2); linear form is Eq. 3. The constant A (2.50×10^{-6} m^2 s^{-1}) is dependent on type of diffusing liquid (density and surface tension) and B (1.89×10^{-4} m^3 kg^{-1}) is function of the porous material (especially of its surface energy and pore system morphology).

$$\kappa_{app} = A \cdot \exp\left\{-\frac{B}{V_{1-100}}\right\} \tag{2}$$

$$\ln \kappa_{app} = \ln A - \frac{B}{V_{1-100}} \tag{3}$$

The values of water vapor diffusion coefficient D were determined by dry cup and wet cup methods. These values differ each other because the wet cup measurement is influenced by liquid transport of the capillary condensed water in the pore system. The rate of vapor transport increases with porosity of thermally loaded samples. The vapor diffuses through the whole pore system hence the vapor diffusion coefficients were correlated with total pore volume Vp in the same way as in the case of κ_{app} (Figure 4).

$$D = A' \cdot \exp\left\{-\frac{B'}{V_p}\right\} \tag{4}$$

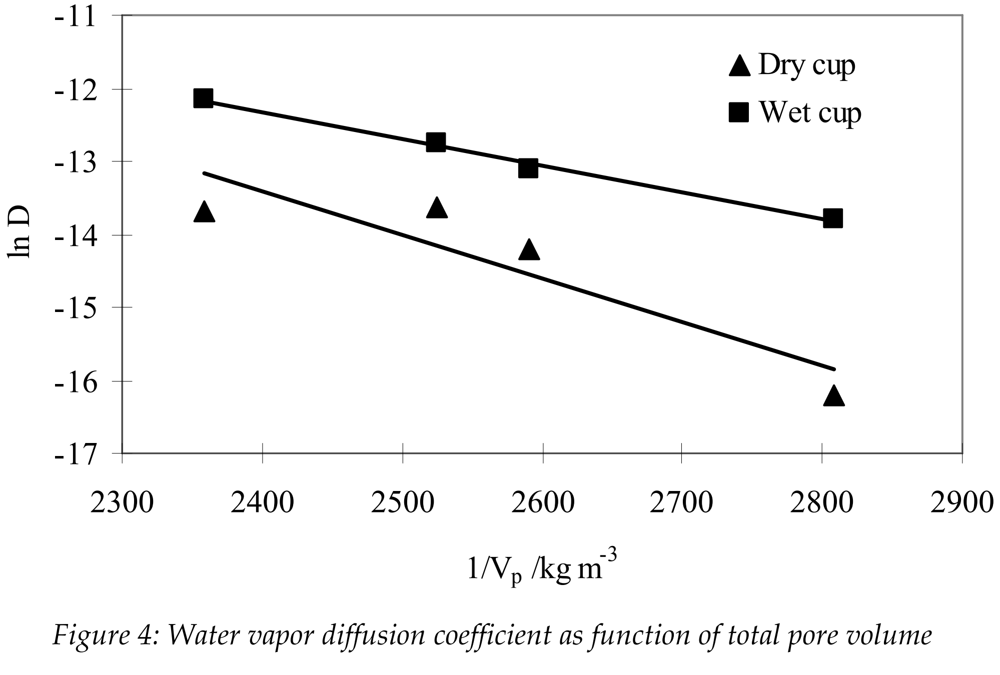

Figure 4: Water vapor diffusion coefficient as function of total pore volume

1.2. Effects of matrix and aramid fibers on moisture transport properties

A comparison of moisture transport properties of aramid fiber reinforced cement composite (AFC) studied in this paper with the properties of cement mortar in the same conditions [4] shows that the moisture diffusivity of AFC was already in reference conditions by several tens of per cent lower than of cement mortar. This is a consequence of using a more convenient preparation technology resulting in more homogeneous pore structure.

The comparison of values of moisture diffusivity after high temperature exposure is for AFC more favorable. While the moisture diffusivity of cement mortar in [4] increased for the pre-heating to 800°C by more than three orders of magnitude, for AFC it was only by less than two orders of magnitude. This is due to the combined positive effects of both matrix and aramid fibers. The autoclaving procedure increased the thermal resistance of the matrix by about 100-200°C as compared to common casting technology, due to the reduction of the negative effect of portlandite which decomposes at 460-480°C. The aramid fibers acted differently for different temperature ranges. For temperatures below 600°C they prevented the material from opening wide cracks due to their good mechanical properties. For higher temperatures than 600°C, after their thermal degradation, they opened channels for removal of gaseous compounds and mitigated the high-pressure induced mechanical damage of the pore structure.

Conclusions

The cementitious composites reinforced by aramid fibers produced by autoclaving procedure thermally decompose from approximately 600˚C. Their thermal decomposition consists from three individual processes: cement binder decomposition and sintering, loss of contact between binder and aggregates and thermal degradation of aramid fibers resulting in formation of channels in the structure of composite. All of these processes together lead to increase of material's porosity and also change the pore size distribution; the small gel pores diminish while the volume of capillary pores increases upon the thermal load. It results in faster transport of liquid water by sorption as well as diffusion of water vapor through the material.

Acknowledgement

This research has been supported by Czech Ministry of Education, Youth and Sports, under project No MEB 050805.

References

[1] ROELS, S., CARMELIET, J., HENS, H., ADAN, O., BROCKEN, H., ČERNÝ, R., PAVLÍK, Z., HALL, C., KUMARAN, K., PEL, L,, PLAGGE, R., Interlaboratory Comparison of Hygric Properties of Porous Building Materials. Journal of Thermal Envelope and Building Science 27 (2004) 307-325.

[2] KUMARAN, M.K., Moisture Diffusivity of Building Materials from Water Absorption Measurements. Journal of Thermal Envelope and Building Science 22 (1999) 349-355.

[3] DEMIDENKO N. I., TELNOVA G. B., Microstructure and properties of a material based on natural wollastonite, Glass and Ceramics 61 (2004) 183 – 186.

[4] ČERNÝ, R., TOTOVÁ, M., PODĚBRADSKÁ, J., TOMAN, J., DRCHALOVÁ, J., ROVNANÍKOVÁ, P., Thermal and Hygric Properties of Portland Cement Mortar after High-Temperature Exposure Combined with Compressive Stress. Cement and Concrete Research 33(2003) 1347-1355.

Thermal conductivity measurement of dynamo sheets

Viliam Vretenár[1], Ľudovít Kubičár[1], Vlastimil Boháč[1] and Miloš Predmerský[2]

[1] Institute of Physics, Slovak Academy of Sciences, Dúbravská cesta 9, 845 11 Bratislava, Slovakia, email: vretenar@savba.sk

[2] U.S. Steel, Košice, Slovakia

Abstract: *Measurements of the thermal conductivity of non-oriented silicon steel (dynamo) sheets in the temperature range from 25 °C to 170 °C are presented. Samples in the form of thin metallic plates were measured by steady-state method based on Guarded Hot Plate standard. Two different shields, guarded and thermal (radiation) shield, were successfully introduced in order to eliminate heat losses along the thin samples even for higher temperatures. Experimental arrangement together with measuring procedure and uncertainty assessment are provided in details. Reliability of the method was verified by stainless steel A310S measurement as a standard.*

Keywords: *thermal conductivity, metallic sheets, steady-state, guarded*

Introduction

Modern technology processes demand for material characterization of every piece and structural member occurring in process. The knowledge of thermophysical properties of individual elements, compounds and alloys might be unsatisfying considering that even different shape of products made of the same materials could induce change of properties due to different technology processes have used. Therefore, the thermophysical properties of some products must be measured as prepared.

For measuring thin metallic samples as dynamo sheets are, we propose the modified version of the steady-state method, where the apparatus, methodology, result and the uncertainty budget are described in details.

Principle of the steady-state method

The principle of the steady-state method is based on Fourier law [1]

$$q = -\lambda \nabla T \tag{1}$$

where q is heat flow per unit area through the specimen that generates a temperature gradient along the specimen and λ is thermal conductivity. For determination of the thermal conductivity, the equation (1) can be rewritten in a form

$$\lambda = \frac{Qh}{S(T_2 - T_1)} \tag{2}$$

where Q is overall heat flow, S is cross-section of the specimen, h is a distance between the thermometers and T_1 and T_2 are the corresponding temperatures (Fig.1). The one end of the specimen is fixed to the heat exchanger while a metering heater is fixed to the second one.

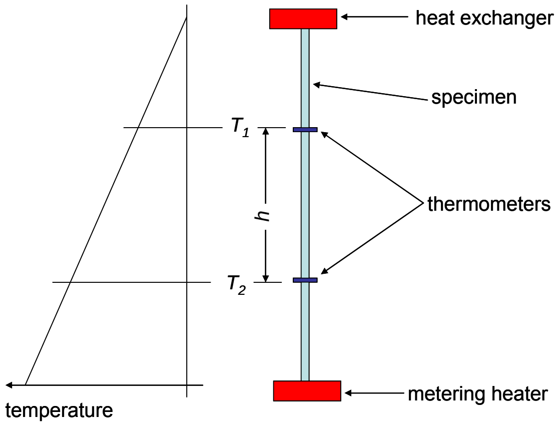

Figure 1: Principle of the steady-state method for measuring thermal conductivity

Fourier law (1) defines the thermal conductivity. A linear course of the temperature along the specimen is required. Any deviation from this linearity is caused by physical processes that influence the measured thermal conductivity value. Thus the linearity of the temperature course is a principal assumption to calculate the correct value of the thermal conductivity according equation (1).

Analysis of sample geometry

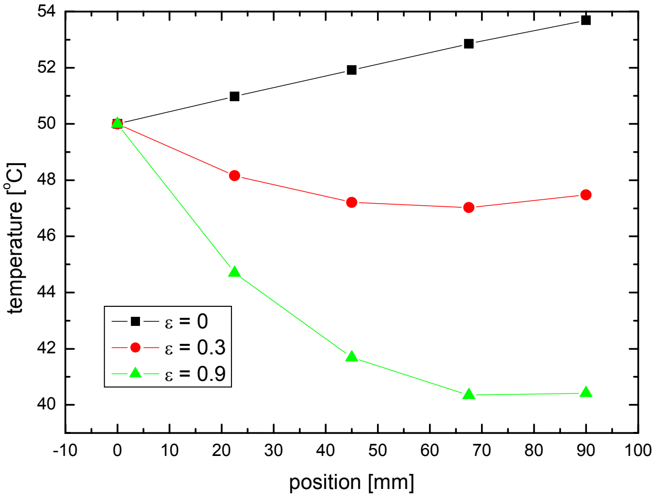

Figure 2: Temperature distribution along the specimen. Emissivity ε = 0 corresponds to ideal case when equations (1) and (2) can be used

The measured data by steady-state technique are influenced primarily by radiation from the specimen to the surrounding. Stefan-Boltzmann law [2] estimates the heat losses from the surface to the surrounding according

$$q = \varepsilon\sigma(T_S^4 - T_0^4) \tag{3}$$

where q is heat flow from the surface unit at temperature T_S to the surrounding at temperature T_0, ε is emissivity (for metals ε ~ 0.3, for surfaces covered by polymer ε ~ 0.9), σ is Stefan-Boltzmann constant $\sigma = 5.69\text{x}10^{-8}$ W m^{-2} K^{-4}. A numerical calculation of derived heat equation for specimen model

$$S\lambda\nabla^2 T = w\varepsilon\sigma(T_s^4 - T_o^4) - q \tag{4}$$

has been performed to analyze the heat losses influence. The following parameters were used: $T_0 = 25°C$, $T_S = 50°C$, $\lambda = 30$ W m^{-1} K^{-1}, $q = 50$ mW m^{-2}, and sheet dimension as width $w = 20$ mm, thickness of 1 mm (2x0.5 mm) and active length of 90 mm.

The temperature distribution along the shield is shown in Fig. 2 for $\varepsilon = 0.3$, and 0.9. The temperature distribution for $\varepsilon = 0$ represents the ideal case, i.e. when equation (1) can be used. Differences for $\varepsilon > 0$ are significant. High nonlinearities can be found. The analysis yields the following conclusions: A specimen holder has to be constructed that heat losses through radiation should be suppressed to minimum. The temperature measurement along the specimen should be performed on several points to use the equation (1), i.e. to check the linear temperature distribution.

Specimen preparation

The specimen is composed of two sheets to place thermometers and the connecting wires among them. Such arrangement suppresses heat radiation from the temperature sensors. Metering heater is made of nickel foil that is isolated by Kapton foil. A schematic picture on thermistor fixing together with a photo of the specimen and the metering heater is shown in Fig. 3. The metering heater having 8 Ω is fixed at one end of the specimen by thin copper plates to homogenize the heat flow. Miniature thermistors having 47 Ω, type NTC 0402 SMD were used for temperature measurement. The accuracy of thermistors after calibration was ± 0.001°C. A varnish has been used for electrical isolation as well as for fixing the thermistors.

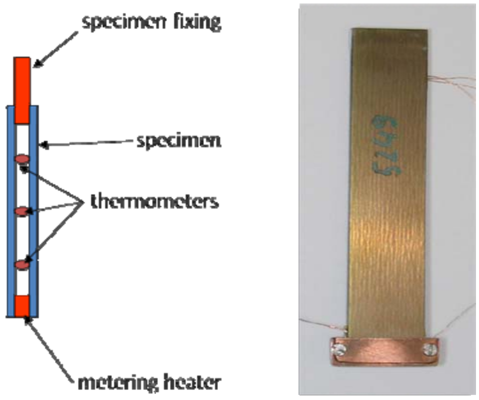

Figure 3: Schematic picture of thermometers position together with the metering heater on the sheets of the specimen (left) and photo of assembled specimen (right)

Specimen holder

The linearity of the temperature distribution along the specimen is a key requirement of a successful experiment. A radiation shields has to be used along the specimen that copies the temperature distribution of the specimen. Then no heat exchange among the radiation shield and the specimen can be found. The heat losses are suppressed and the equation (1) can be used for calculation of the thermal conductivity.

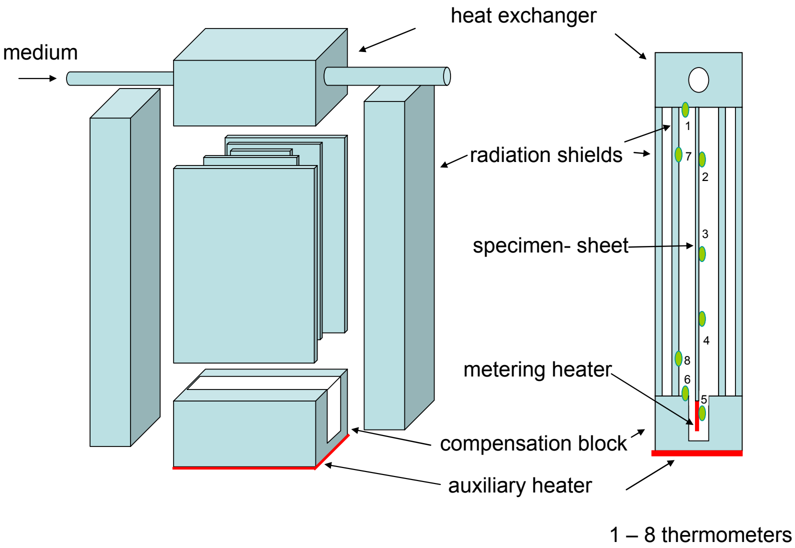

Figure 4: Scheme of the specimen holder

The construction of the specimen holder is shown in Fig. 4. This construction is a result of a range of specimen holder reconstructions to obtain a linear temperature distribution along the specimen. At least 3 thermometers have to be used to check linearity of the temperature distribution. The specimen holder consists of two blocks a block of the heat exchanger and a compensation block. These two blocks determines the temperature distribution along the specimen – the metallic sheet. While temperature of the heat exchanger is given by temperature of the medium, an auxiliary heater establishes the temperature of the compensation block. Both blocks are constructed of copper blocks in a size around 20x20x50 mm.

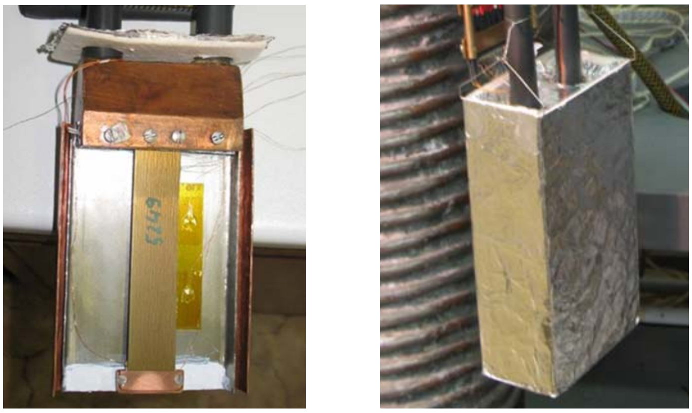

Figure 5: Specimen fixed in holder (left) and specimen holder capsulated in Sibral radiation box (right).

Outer radiation shields are made of copper plates 1 mm thick. A predominant part of the radiation is caught by these shields. It is supposed that negligible temperature gradients exist in both blocks due to large cross-section and high thermal conductivity. As heat flow through the radiation shields can be substantial, temperature drops may be found at contacts of the shields with blocks considering thermal contact resistances. The drops increase when temperature gradient along the specimen is generated. Then linearity of the temperature distribution is distorted. Therefore an additional inner radiation shield has to be used that is constructed of steel 1 mm thick. Difference in thermal conductivity between the copper (400 W m^{-1} K^{-1}) and the steel (20 W m^{-1} K^{-1}) is around one order. Then heat flows in the copper and the steel shields differentiates nearly in one order of the magnitude. This difference can still be adjusted by a proper choice of the shield thickness. Then the thermal resistance of the steel radiation shield is significant high to neglect its contact thermal resistance with both copper blocks. An additional radiation shield in a form of box made of 4 mm thick Sibral (compressed glass wool) is used to intensify the thermal isolation of the specimen holder. All measurements were performed in vacuum of 0.005 Pa. A specimen fixed in the holder and its assembly is shown in Fig. 5.

Experimental apparatus

Scheme of the apparatus is shown in Fig. 6. The temperature of the chamber jacket is stabilized at 25°C by thermostat LAUDA RKS 20. In addition the chamber is wrapped by polyurethane to isolate it from the surroundings influence. The temperature of the chamber jacket is monitored during the experiment by Platinum thermometer Pt 100. The chamber is evacuated by turbomolecular pump TMH 065, Pfeifer, in connection with a rotary pump to vacuum 0.005 Pa. Vacuum is monitored by Compact Full Range Gauge, Balzers. Temperature of the heat exchanger is controlled by thermostat LAUDA RP 845. Both the metering heater and the auxiliary heater were driven by current sources KEPCO ABC 15-7 DM. Two multimeters, Keithly 2010, in connection with the switch unit Model 2001 Scan, Keithly, were used for measurement of the temperatures T1 – T8 by corresponding thermometers. The measuring process has been controlled by PC computer.

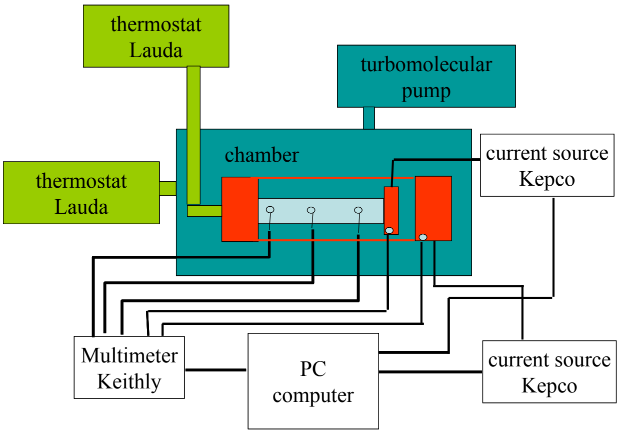

Figure 6: Scheme of the experimental apparatus for measuring of thermal conductivity

Measuring regime and data acquisition

A test of the temperature distribution along the radiation shield is shown in Fig. 7 (left). Deviations from the linearity (red line) can be found at both ends of the shield contacted with the copper blocks. Deviations are caused by the contact thermal resistance. The temperature distribution along the specimen made of stainless steel A 310 is shown in Fig. 7 (right). This distribution corresponds to the output power of the metering heater of q = 50 mW m^{-2}. The deviation from the linearity of the temperature distribution is insignificant, i.e. the contribution to the measurement uncertainty is negligible.

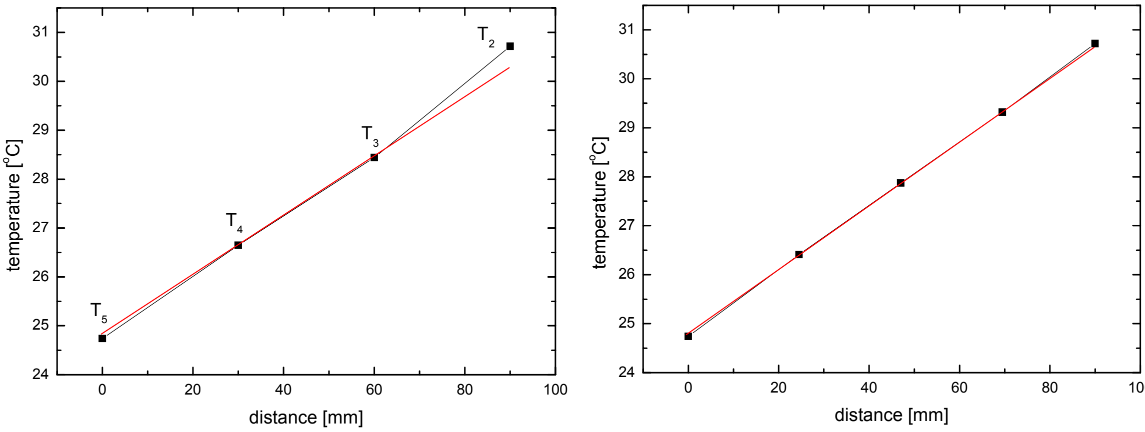

Figure 7: Temperature distribution on the radiation shield (left) and on the specimen (right). Red lines indicate correct linear temperature distribution

Optimization of the experimental parameters (working interval of the parameters) has to be performed like specimen size, distance between the thermometers and the output power of the auxiliary heater before experiment starts. The measurement procedure is simple: The heat exchanger temperature is set in and a temperature gradient along the radiation shields is established due to auxiliary heater. The output of the metering heater is chosen in such a way to reach a negligible temperature difference between the metering and auxiliary heat source (thermometer T4 and T5 in Fig. 8 (left) and in detail in Fig. 8 (right)). The linearity of the temperature distribution along the specimen is monitored by thermometers T1 to T4. The temperature stabilization is shown in Fig. 8 (left), while corresponding temperatures of the radiation shield and the specimen's end, where the metering heater is fixed, is shown in Fig. 8 (right). The temperature difference between the thermometers T4 and T5 has to be negligible.

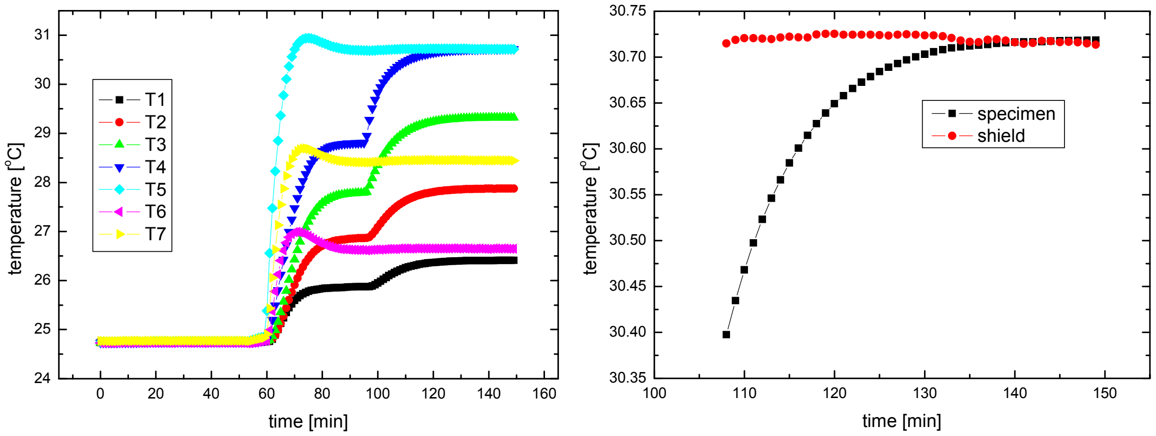

Figure 8: Temperature stabilization on the specimen and shields (left) and the detail at the place of metering heater, T4 and T5, (right)

The thermal conductivity is calculated using equation (2) and the output of the metering heater providing the linearity of the temperature distribution is satisfactorily. Guarded Hot Plate method according standards ISO 8302, ASTM C 177 and EN 1946 part 2 is working in similar way. The standards require a measuring regime when all false heat flows are compensated. Then we can use the equation (1) or (2). The standards consider a specimen size having a significant larger cross-section. Thus the standards cannot be applied for samples in the form of thin sheets. The measurement reliability has been tested by reassembling of the system specimen – radiation shields. The reassembling reproducibility was better than 1%.

Measurement of the dynamo sheets

A search of the construction parameters of the specimen holder, inter-calibration of the thermometers and multiple reconstruction of the specimen holder represent the principal part of the experimentation. Measured data of thermal conductivity of dynamo sheets together with published [3] and measured data of stainless steel A310 are shown in Fig. 9. A deviation at higher temperature between our data and published data on stainless steel could be noticeable. We have used sheets of stainless steel A 310 produced by ITALINOX. Therefore this deviation can be caused by various producers and by different specimen shape. Published data correspond to bulk specimen while our data to sheet shape. Thermal conductivity of dynamo sheets was measured at the following temperatures (25, 50, 75, 100, 125, 159 and 170°C). A detailed experimental analysis requires small temperature intervals to early recognize irregularities caused by fixing of the specimen in the holder. Each irregularity causes data shift. Small temperature intervals allow unequivocally specifying the imperfections in specimen fixing, i.e. data may be shifted for several temperatures.

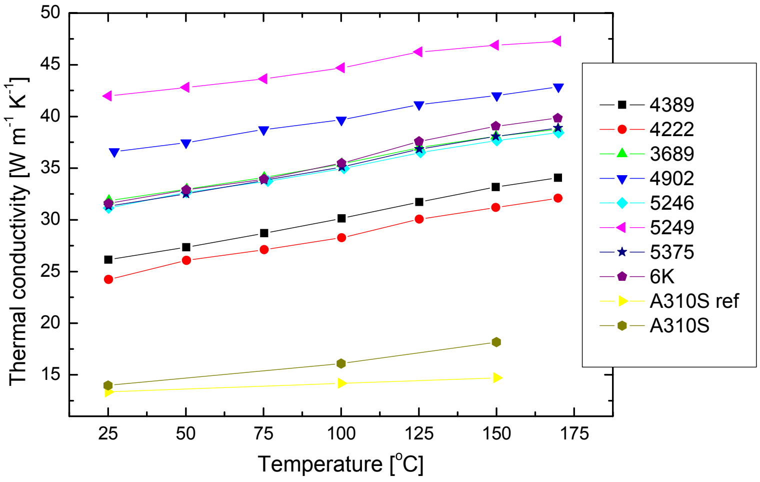

Figure 9: Measured data of dynamo sheets and published (A310S ref) and measured (A310S) data of stainless steel A310 (reference) as a function of temperature

Uncertainty analysis

The uncertainty budget according to GUM [4] and providing that our experiment is working within optimal parameters, is given by

$$\frac{\delta\lambda}{\lambda} = \sqrt{\left(\frac{\delta q}{q}\right)^2 + \left(\frac{\delta h}{h}\right)^2 + \left(\frac{\delta w}{w}\right)^2 + \left(\frac{\delta s}{s}\right)^2 + \left(\frac{\delta \Delta T_h}{\Delta T}\right)^2 + \left(\frac{\delta \Delta T_T}{\Delta T}\right)^2} \tag{5}$$

where w represents the width of the specimen, h is active length of the specimen (fixing of the thermometers), s is specimen thickness, ΔT_h is uncertainty in temperature due to imprecise thermometer fixing and ΔT_T is uncertainty given by thermometer.

Table 1: *The uncertainty contributions corresponding to mean value of the experimental parameters*

Parameter	**Value**	**Uncertainty**	**Contribution [%]**
q [mW]	50	0.05	0.1
w [mm]	45	0.5	1.1
h [mm]	10	0.05	0.5
s [mm]	1	0.005	0.5
ΔT_h [°C]	2.5	0.2	0.8
ΔT_T [°C]	2.5	0.028	1.1

Individual contributions to the overall one are given in Table 1. Data are valid for mean values of the experimental parameters. Overall uncertainty according equation (5) counts 1.9%. This uncertainty includes imperfections of instruments and imprecision of experimental parameters and assumes a linear temperature distribution along the specimen. The distribution is always tested during the measurements. The resulted error is rather optimistic one considering the prototype of the apparatus. Instead an error estimation of 5% should be taken into consideration.

Conclusions

A new experimental instrument for measuring the thermal conductivity of thin metallic sheets has been designed and constructed. In order to suppress radiative exchange between thin specimen and surroundings, the guarding shields have been successfully introduced. It should be stressed that the used specimen holder is marked by multiple reconstructions. Therefore the presented apparatus should be considered as a prototype that needs the final apparatus construction. Nevertheless, the measurements on sample set of dynamo sheets proved its functionality and reliability.

Acknowledgements

The paper was supported by the project APVV – 0497 – 07, the project MVTS - MAFINCO and by the VEGA project 2/5100/25

References

[1] Maglić, K. D.; Cezairliyan, A.; Peletsky, V. E. *Compendium of Thermophysical Property Measurement Methods in Recommended Measurement Techniques and Practices*, Vol.2, Plenum Press, New York and London, 1992

[2] Siegel, R.; Howel, J. R. *Thermal radiation heat transfer*, fourth ed., Taylor & Francis, New York, 2002, pp. 868

[3] *Metals Handbook*, Desk Edition 1999, Eds. H E Boyer, T L Gall, American Society for Metals, Metals Park, Ohio

[4] *Guide to the expression of uncertainty in measurement*, International Organization for Standardization, ISO Geneva, 1995. ISBN 92-67-10188-9

Water and heat transport properties of slag concrete

Eva Vejmelková[1], Petr Konvalinka[2], Stefania Grzeszczyk[3], Robert Černý[1]

[1]Department of Materials Engineering and Chemistry, Faculty of Civil Engineering, Czech Technical University in Prague, Thákurova 7, 166 29 Prague 6, Czech Republic

[2]Experimental Center, Faculty of Civil Engineering, Czech Technical University in Prague, Thákurova 7, 166 29 Prague 6, Czech Republic

[3]Department of Engineering Building Materials, Faculty of Civil Engineering, Technical University of Opole, Katowicka 48, 45061 Opole, Poland

Abstract: *Water and heat transport properties of concrete produced with cement containing blast furnace slag are investigated in the paper. The obtained data can be considered as a step towards establishment of a material database for different types of concrete which is currently not available and which should serve for hydro-thermo-chemo-mechanical modeling, making it possible to perform complex durability and reliability based studies of building structures.*

Keywords: *concrete, water transport properties, thermal properties, slag*

Introduction

Self-compacting concrete (SCC) was first developed in Japan in late 1980s as a concrete that can be placed and compacted without any inner or outer vibration effort. SCC is compacting itself due to its self-weight and is deaerated almost completely while flowing in the formwork ([1]-[4]).

The basic components for the production of SCC mixtures are the same as those of the conventionally vibrated traditional concrete, i.e., cement, aggregates, water, additives and admixtures. Similarly as with the high performance concrete mixtures developed in Europe and North America to increase the strength and durability of concrete, also SCC mixtures contain a superplasticizer for reduction of the liquid limit and better workability. However, there are substantial differences in some other aspects of the mix design. The amount of coarse aggregates is in SCC mixtures much lower than in traditional vibrated concrete. On the other hand, they contain a high amount of fine fillers and/or additives to increase the viscosity in order to maintain stability of the mix, hence to reduce bleeding and avoid separation of coarser aggregates [5]. The most often used fillers increasing viscosity of SCC mixtures are fly ash, glass filler, limestone powder, silica fume and quartzite filler [6]. Some SCC mixtures contain also water retention agents such as polysaccharides to match the possible higher amount of water in the aggregates or to provide the concrete mix with thixotropic properties [7].

SCC is mostly produced with Portland cement as a binder. In this paper, we analyze durability properties of SCC based on an environmental more friendly binder where a substantial part of Portland cement is replaced by blast furnace slag.

Materials

To elaborate the self compacting concrete mixture composition, the design principles established by Okamura and Ozawa [4] have been applied. Metallurgical cement CEM III/A

32.5, containing 56% of blast furnace slag of a specific surface area 400 m^2/kg (Blaine) was used. Chemical composition of the cement is presented in Table 1.

Table 1: Chemical composition of cement

Component	**% by mass**
SiO_2	28.4
Fe_2O_3	1.7
Al_2O_3	6.8
CaO	52.5
MgO	5.0
SO_3	2.7
NaO	0.4
K_2O	0.8

Table 2: Composition of the studied SCC

Component	Unit	Amount
cement	kg/m3	500
water	kg/m3	153
superplasticizer	% by mass	2.6
aggregates 0/2 mm	kg/m3	832
aggregates 2/8 mm	kg/m3	416
aggregates 8/16 mm	kg/m3	416

Natural siliceous aggregates were applied, characterized by regular continuous grading. The ratio of coarse aggregates to sand was chosen 1:1. The maximum grain size was 16 mm. A polycarboxylether–based superplasticizer was used for the liquefaction of the mix. The paste composition was optimized by using the experimentally determined factor β_P [4]. The determined value of β_P was 0.95. The composition of concrete mix is given in Table 2.

The durability properties of the hardened SCC mix were analyzed in dependence on time, in order to assess the effect of the pozzolanic properties of the slag. The first half of the produced specimens was tested 28 days after mixing (we denote them as SCC-3 in what follows), the second half after 1 year (specimens denoted as SCC-4).

Experimental methods

Basic physical parameters

Among the basic properties, the bulk density, matrix density and open porosity were measured by the water vacuum saturation method [8]. Each sample was dried in a drier to remove majority of the physically bound water. After that the samples were placed into a desiccator with deaired water. During three hours air was evacuated with vacuum pump from the desiccator. The specimen was then kept under water not less than 24 hours.

From the mass of water saturated sample m_w [kg] and mass of the immersed water saturated sample m_a [kg], the volume V of the sample was determined from the equation

$$V = \frac{m_w - m_a}{\rho_l} \tag{1}$$

where ρ_l is the density of water.

The open porosity ψ_0 [%], bulk density ρ [kgm^{-3}] and matrix density ρ_{mat} [kgm^{-3}] were calculated according to the equations

$$\psi_0 = \frac{m_w - m_d}{V\rho_l} \tag{2}$$

$$\rho = \frac{m_d}{V} \tag{3}$$

$$\rho_{mat} = \frac{m_w}{V(1-\Psi_0)} \tag{4}$$

where m_d is the mass of the dry sample [kg].

The samples for determination of basic properties were cut from the standard prisms; their size was 40 x 40 x 20 mm.

Water vapor transport properties

The wet cup method and dry cup method were employed in the measurements of the water vapor diffusion parameters [9]. The specimens were water and vapor proof insulated by epoxy resin on all lateral sides, put into the cup and sealed by technical plasticine. In the wet cup method the sealed cup containing water (the equilibrium relative humidity above the solution was 97.8%) was placed into an air-conditioned room with 50% relative humidity and weighed periodically. The measurements were done at 25±1°C in a period of two weeks. The steady state values of mass loss determined by linear regression for the last five readings were used for the determination of water vapor diffusion coefficient. In the dry cup method the sealed cup containing dried $CaCl_2$ (the equilibrium relative humidity above the desiccant was 5%) was placed in an air-conditioned room with 50% relative humidity. Otherwise the measurement was done in the same way as in the wet cup method.

The water vapor diffusion coefficient D was calculated from the measured data according to the equation

$$D = \frac{\Delta m \cdot d \cdot R \cdot T}{S \cdot \tau \cdot M \cdot \Delta p_p} \tag{5}$$

where Δm is the amount of water vapor diffused through the sample [kg], d the sample thickness [m], S the specimen surface [m^2], τ the period of time corresponding to the transport of mass of water vapor Δm [s], Δp_p the difference between partial water vapor pressure in the air under and above specific specimen surface [Pa], R the universal gas constant, M the molar mass of water, T the absolute temperature [K].

On the basis of the diffusion coefficient D, the water vapor diffusion resistance factor μ was determined

$$\mu = \frac{D_a}{D} \tag{6}$$

where D_a is the diffusion coefficient of water vapor in the air.

The samples for determination of water vapor transport properties were as follows: the specimen size was 50 x 50 x 20 mm and samples were on four lateral sides water and water vapor insulated with epoxy resin to ensure the one-dimensional transport.

Water transport properties

The water sorptivity was measured using a standard experimental setup [9]. The specimen was water and vapor-proof insulated on four lateral sides and the face side was immersed 1-2 mm in the water, constant water level in tank was achieved by a Marriott bottle with two capillary tubes. One of them, inside diameter 2 mm, was ducked under the water level, second one, inside diameter 5 mm, was above water level. The automatic balance allowed recording the increase of mass. The water absorption coefficient A [$kgm^{-2}s^{-1/2}$] was then calculated using the formula

$$i = A \cdot \sqrt{t} \tag{7}$$

where i is the cumulative water absorption [kgm^{-2}], t is the time from the beginning of the suction experiment. The water absorption coefficient was then employed for the calculation of the apparent moisture diffusivity in the form

$$\kappa_{app} \approx \left(\frac{A}{w_c - w_0} \right)^2 \tag{8}$$

where w_c is the saturated moisture content [kgm^{-3}] and w_0 the initial moisture content [kgm^{-3}].

The samples for determination of water transport properties had a size of 50 x 50 x 20 mm.

Thermal properties

The thermal conductivity as the main parameter of heat transport and the specific heat capacity as the main parameter of heat storage were determined using the commercial device ISOMET 2104 (Applied Precision, Ltd.). ISOMET 2104 is equipped with various types of optional probes, needle probes are for porous, fibrous or soft materials, and surface probes are suitable for hard materials. The measurement is based on the analysis of the temperature response of the analyzed material to heat flow impulses. The heat flow is induced by electrical heating using a resistor heater having a direct thermal contact with the surface of the sample. The measurements in this paper were done in dependence on moisture content. The samples for determination of thermal properties had a size of 70 x 70 x 70 mm.

Experimental results and discussion

Basic physical parameters

The basic properties of hardened SCC are shown in Table 3. SCC-4 achieved lower porosity, bulk density and matrix density, as compared to SCC-3. The structure compaction of the studied hardened concrete mix after 1-year (compared to the 28-days data) manifested in the lower porosity was apparently due to the secondary pozzolanic reaction which accompanied the use of slag as partial Portland cement replacement and resulted in the consumption of $Ca(OH)_2$ and C-S-H structures formation [10].

Table 3: Basic material parameters of SCC after 28 days

Material	**ϱ [kgm^{-3}]**	**ρ_{mat} [kgm^{-3}]**	**Ψ [%]**
SCC-3	2410	2720	11
SCC-4	2320	2560	9.6

Water vapor transport properties

The water vapor transport parameters of the studied SCC are shown in Table 4. The measured data revealed basic information that the values of water vapor diffusion coefficient corresponding to the lower values of relative humidity (5-50%) were always lower than those for higher relative humidity values (97-50%). This is in accordance with the previous measurements on many other materials including concrete. The main reason for this finding is coupling of water vapor transport with water transport in a material with higher relative humidity where the capillary condensation takes place in a much higher extent than in the range of lower relative humidity [10].

The values of water vapor diffusion coefficient of SCC-3 were about 35% (wet cup) and about 60% (dry cup) higher than for SCC-4. This is in a qualitative agreement with the open porosity data in Table 3 as it is quite obvious that a material with higher porosity should transport water vapor faster than a material with lower porosity.

Table 4: Water vapor transport properties of SCC after 28 days

Material	**D [10^{-6} m^{2}s^{-1}]**		**μ [-]**	
	97-50% RH	**50-5% RH**	**97-50% RH**	**50-5% RH**
SCC-3	1.53	0.97	15.1	24.5
SCC-4	1.13	0.58	20.3	39.6

Water transport properties

The results of liquid water transport parameters measurement in Table 5 show that the material SCC-3 with higher porosity transported liquid water in a much faster way than the material SCC-4. Its water absorption coefficient was by about 35% higher and the moisture diffusivity about 50% higher compared to SCC- 4. Once again, it was a consequence of the secondary pozzolanic reaction in the analyzed SCC resulting in structure compaction.

Table 5: Water transport properties of SCC after 28 days

Material	**A [kg m^{-2}s$^{-1/2}$]**	**κ_{app} [m^{2}s^{-1}]**
SCC-3	0.0074	4.4E-09
SCC-4	0.0055	2.9E-09

Thermal properties

The thermal parameters data in Table 6 show that both materials achieved similar values of thermal conductivity in the whole range of moisture content. This was not in a good agreement with the open porosity data in Table 3 as in general a material with higher porosity should have lower thermal conductivity. However, the differences between both materials were relatively low, within the error range of the measuring method. Also, the lowering of matrix density after 1-year as compared to the 28-days results indicated a possible change in the composition of the porous matrix, the lowering of the open porosity then a change in the topology of the pore space which could be manifested in somewhat different way of mixing the basic phases into the resulting thermal conductivity values.

The differences in specific heat capacity of both materials were in the whole moisture range relatively low, up to 10%, which was well within the error range of the measurement method.

Table 6: Thermal properties of SCC after 28 days

Type of mixture	**u**	**λ**	**c**
	[% kg-water/kg-dry material]	**[$Wm^{-1}K^{-1}$]**	**[$Jkg^{-1}K^{-1}$]**
SCC-3	0.0	2.84	716
SCC-3	2.1	3.27	728
SCC-3	3.8	3.42	725
SCC-3	4.4	4.17	733
SCC-4	0.0	2.79	639
SCC-4	1.8	3.45	764
SCC-4	3.4	3.70	766
SCC-4	3.7	3.78	738

Conclusions

The results of measurement of basic physical parameters and the hygric and thermal properties of SCC produced with cement containing blast furnace slag in this paper showed that the effect of slag was positive in a long term view. Comparing the results obtained 28 days and 1 year after mixing, the values of open porosity, water vapor diffusion coefficient and water absorption coefficient were after 1-year significantly lower than the corresponding 28-days data. This indicates an improvement of durability. The thermal conductivity and specific heat capacity of the studied SCC were for both time periods almost the same, within the error range of the experimental methods.

The obtained data can be considered as a step towards establishment of a material database for SCC which is currently not available and which should serve for hydro-thermo-chemo-mechanical models, making it possible to perform complex durability and reliability based studies of building constructions involving SCC in various applications.

Acknowledgements

This research has been supported by the Czech Ministry of Education, Youth and Sports, under project No MSM 6840770031.

References

[1] OZAWA K., KUNISHIMA M., MAEKAWA K., Development of high performance concrete based on the durability design of concrete structures. Proceedings of the second East-Asia and Pacific Conference on Structural Engineering and Construction (EASEC-2), Vol. 1, pp. 445-450, January 1989.

[2] OZAWA K., MAEKAWA K., OKAMURA H., Development of high performance concrete. J. Faculty Eng. Univ. Tokyo (B), 1992, XLI(3), 381-439.

[3] OKAMURA H., MAEKAWA K., OZAWA K., High Performance Concrete, Gihoudou Pub., Tokyo 1993.

[4] OKAMURA H., OZAWA K., Mix design for self-compacting concrete. Concrete Library, JSCE, No. 25, pp. 107-120, June 1995.

[5] ZHU W., BARTOS P.J.M., Permeation properties of self-compacting concrete. Cement and Concrete Research 33(2003), 921-926.

[6] PERSSON B., A comparison between mechanical properties of self-compacting concrete and the corresponding properties of normal concrete. Cement and Concrete Research 31(2001), 193-198.

[7] SARI M., PRAT E., LABASTIRE J.F., High strength self-compacting concrete. Original solutions associating organic and inorganic admixtures. Cement and Concrete Research 29(1999), 813-818.

[8] ROELS, S., CARMELIET, J., HENS, H., ADAN, O., BROCKEN, H., ČERNÝ, R., PAVLÍK, Z., HALL, C., KUMARAN, K., PEL, L,, PLAGGE, R., Interlaboratory Comparison of Hygric Properties of Porous Building Materials. Journal of Thermal Envelope and Building Science 27 (2004) 307-325.

[9] KUMARAN, M.K., Moisture Diffusivity of Building Materials from Water Absorption Measurements.IEA Annex 24 Report T3-CA-94/01, Ottawa 1994.

[10] ČERNÝ R, ROVNANÍKOVÁ P., Transport Processes in Concrete. Spon Press, London 2002.

Use of step wise and pulse transient methods for the photovoltaic cells laminating films thermal properties study

Oldřich Zmeškal, Lenka Hřebenová, Pavla Štefková

Faculty of Chemistry, Brno University of Technology,

Purkyňova 118, CZ-612 00 Brno, Czech Republic

email: zmeskal@fch.vutbr.cz

Abstract: *The paper reports a study on thermal properties of laminating films used for the production of photovoltaic cells modules. Step wise and pulse transient method were used for the study. The results of measurements (diffusivity, specific heat and thermal conductivity) were compared with results of thermal vision analysis. New fractal model of heat transport through the material and heat losses for thermal parameters determination was used. This model was compared with classical models which have been used so far.*

Keywords: *photovoltaic cells, thermal properties of materials, pulse transient method, step wise method thermovision*

1. Introduction

The use of photovoltaic cells for conversion of light (electromagnetic) energy to electric energy plays important role nowadays. These sources can play a more important role for ensuring the supply of electrical energy for homes and industry in the near future. At present, not only problems associated with the technological aspects related to fabrication of photovoltaic cells need to be addressed, but the ones related to their optimal working temperature, too. The efficiency and their operating life are decreasing with increasing working temperature caused by IR radiation.

Therefore, an attention must be paid to the study of thermal properties of materials used for their encapsulation, too. These materials must be capable of blocking the transition of heat energy into photovoltaic cells and dissipate it into surrounding. Various types of laminating foils can be used for cell encapsulation. Their optimal selection can be done by comparing of their thermal parameters: thermal diffusivity, thermal conductivity and specific heat. The pulse transient and step wise method can be used for effective determination of these parameters.

Many models have been derived for heat transfer though the material and for determining of thermal parameters [1], [2] and [3]. It is evident now, that these models do not describe the experimental dependences accurately enough. The non-homogeneity of heat source, limited sample thickness, heat losses into surrounding and many other influences are some of thre reasons. So, new models, which include some of these influences, have been developed [4], [5], [6], [8]. Better agreements between model and experimental data have been obtained with their application.

One of these models based on the theory of fractal heat propagation ([7], [8]) was applied to a model material (PMMA). As the heat sources, surface resistive heat source encapsulated in capton and encapsulated photovoltaic cells of the same diameter (3 cm) were used. From the comparison of results we can determine the suitability of studied laminating foil for the photovoltaic panel application.

2. Models

Classical and fractal approach

Ideal planar Dirac pulse model [1], [3]

The dependence of the temperature change on time for a simple model after a Dirac pulse of heat supply prom surface heat source can be derived with using of the term [1]

$$\Delta T(t) = \frac{Q}{c_{\mathrm{p}}\rho\sqrt{4\pi a t}} \exp\left(-\frac{h^2}{4at}\right), \tag{1}$$

where $Q = P\Delta t$ means total pulse heat energy (P is a power of heat source, Δt width of the pulse), c_p is specific heat, a is thermal diffusivity and t is time.

Ideal planar Step wise model [1], [3]

The thermal response for this model can be derived by integration of Eq. (1), assuming that the heat power P is constant. The dependence of temperature change on the time can be for planar heat source in this case described by

$$\Delta T(t) = \int_0^t \frac{P}{c_{\mathrm{p}}\rho\sqrt{4\pi at}} \exp\left(-\frac{h^2}{4at}\right) \mathrm{d}t\ . \tag{2}$$

By a simple deriving (integrating per partes) we can get

$$\Delta T(t) = \frac{2P}{c_{\mathrm{p}}\rho\sqrt{4\pi a}} \left[\sqrt{t}\exp\left(-\frac{h^2}{4at}\right) + \frac{h^2}{4a}\int_0^t t^{-3/2}\exp\left(-\frac{h^2}{4at}\right)\mathrm{d}\,t\right], \tag{3}$$

or

$$\Delta T(t) = \frac{P\sqrt{4at}}{2\lambda\sqrt{\pi}} \left[\exp\left(-\frac{h^2}{4at}\right) - \frac{h}{\sqrt{4at}}\mathit{\Gamma}\left(\frac{1}{2},\frac{h^2}{4at}\right)\right] = \frac{P\sqrt{4at}}{2\lambda} i\mathit{\Phi}^*\,, \tag{4}$$

or

$$\Delta T(t) = \frac{P\sqrt{4at}}{2\lambda} \left[\frac{1}{\sqrt{\pi}}\exp\left(-\frac{h^2}{4at}\right) - \frac{h}{\sqrt{4at}}\operatorname{erfc}\left(\frac{h}{\sqrt{4at}}\right)\right] = \frac{P\sqrt{4at}}{2\lambda} i\mathit{\Phi}^*\,, \tag{5}$$

respectivelly. At this equation, the $\lambda = c_{\mathrm{p}}\rho a$ is the thermal conductivity, erfc(x) is complementary error function (also called the Gauss error function, see Appendix). It is defined as

$$\operatorname{erfc}(x) = \frac{\mathit{\Gamma}(1/2, x^2)}{\sqrt{\pi}} = \frac{2}{\sqrt{\pi}}\int_x^\infty \mathrm{e}^{-x^2}\mathrm{d}\,x \ \text{ and } \ i\mathit{\Phi}^* = \frac{\mathrm{e}^{-x^2}}{\sqrt{\pi}} - x\operatorname{erfc}(x), \tag{6}$$

where $x = h/\sqrt{4at}$ and $\mathit{\Gamma}(1/2, A/t) = A^{1/2}\int_0^t t^{-3/2}\mathrm{e}^{-A/t}\mathrm{d}\,t$ is the upper incomplete gamma function.

Ideal fractal Dirac pulse model [8]

The model which was defined by Eq. (1) can be generalized for heat propagation from any source type: point ($D = 0$), linear ($D = 1$), planar ($D = 2$) – generally "fractal" with dimension $D \in \langle 0, E \rangle$) in one, two, three, generally in E-dimensional space [8]

$$\Delta T(t) = \frac{Q}{c_{\mathrm{p}} \rho (4\pi a t)^{(E-D)/2}} \exp\left(-\frac{h^2}{4at}\right). \tag{7}$$

Ideal fractal step wise model

The thermal response can then be derived by integration of Eq. (7) for this model on assumption that the heat power P is constant. The dependence of temperature change on the time can be for fractal heat source in this case described by

$$\Delta T(t) = \int_0^t \frac{P}{c_{\mathrm{p}} \rho (4\pi a t)^{(E-D)/2}} \exp\left(-\frac{h^2}{4at}\right) \, \mathrm{d}t. \tag{8}$$

By simple deriving (integrating per partes) we can get for $s = (E - D)/2$

$$\Delta T(t) = \frac{P}{c_{\mathrm{p}} \rho (1-s)(4\pi a)^s} \left[t^{1-s} \exp\left(-\frac{h^2}{4at}\right) + \frac{h^2}{4a} \int_0^t t^{-(s+1)} \exp\left(-\frac{h^2}{4at}\right) \mathrm{d}\, t \right], \tag{9}$$

which special case is for $s = 1/2$ response for planar arrangement (3).

And finally

$$\Delta T(t) = \frac{P}{4\lambda(1-s)} \frac{(4at)^{1-s}}{\pi^s} \left[\exp\left(-\frac{h^2}{4at}\right) + \left(\frac{h^2}{4at}\right)^{1-s} \Gamma\left(s, \frac{h^2}{4at}\right) \right] = \frac{P(4at)^{1-s}}{4\lambda(1-s)\pi^s} i\Phi^*, \tag{10}$$

where the $\lambda = c_{\mathrm{p}} \rho a$ is thermal conductivity and

$$i\Phi^* = \frac{\mathrm{e}^{-x^2}}{\pi^s} - x^{2(1-s)} \frac{\Gamma(s, x^2)}{\pi^s}, \tag{11}$$

where $x = h/\sqrt{4at}$ and $\Gamma(s, A/t) = A^s \int_0^t t^{-(s+1)} \mathrm{e}^{-A/t} \mathrm{d}t$ is the upper incomplete gamma function.

This equation is for $s = (E - D)/2$ and neglecting upper incomplete gamma function equal to

$$\Delta T(t) = \frac{P}{2\lambda} \frac{(4at)^{(D-E+2)/2}}{\pi^{(E-D)/2}} \exp\left(-\frac{h^2}{4at}\right) \tag{12}$$

and for $E = 3$ (3D space) and $D = 2$ (surface heat source) when $s = 1/2$ equal to

$$\Delta T(t) = \frac{P}{2\lambda} \sqrt{\frac{4at}{\pi}} \exp\left(-\frac{h^2}{4at}\right). \tag{13}$$

Real fractal step wise model

The heat loss effect was solved in a new model by defining the initial and boundary conditions for basic heat transport equation. The heat losses were taken into account at real radius of the specimen and heat source *R* at infinite length *l*. The model parameters are of the same meaning like in an ideal model.

This model will be derived in a more detailed way. The dependence of temperature on radius for the thermal field can be written as ([7], [8])

$$\Delta T(r) = -\frac{\hbar c}{k_\mathrm{B}} \frac{K\, r^{D-E+2}}{D(D-E+2)}, \tag{14}$$

where k_B is Boltzmann constant, $\hbar = h/2\pi$ is modified Planck constant, c is speed of heat propagation and K, D are fractal measure and fractal dimension, respectively. If the vector r in the Eq. (14) is expressed like $r^2 = r_T^2 - c^2(t-t_0)^2 = r_T^2 - c^2t^2 + 4a_0t - c^2t_0^2$, where t_0 is the time response delay, $a_0 = c^2t_0/2$ is maximum value of thermal diffusivity (for $E = D$) and r_T is a radius of fractal space, it is possible (alike by decomposition of the density) to rewrite it to the relation

$$\Delta T(t) = -\frac{K\hbar c}{k_\mathrm{B}} \frac{(4a_0t)^{(D-E+2)/2}}{D(D-E-2)} \left(-\frac{c^2t_0^2 - r_T^2}{4a_0t} - \frac{c^2t}{4a_0} + 1 \right)^{(D-E+2)/2}. \tag{15}$$

If $h^2 = c^2t_0^2 - r_\mathrm{T}^2$ is corrected thickness of specimen and the terms in parenthesis can be viewed as significant in the expansion of exponential function ($1 - x \approx \mathrm{e}^{-x}$), we can write

$$\Delta T(t) = -\frac{K\hbar c}{k_\mathrm{B}} \frac{(4a_0t)^{(D-E+2)/2}}{D(E-D-2)} \exp\left[-\frac{D-E+2}{2} \left(\frac{h^2}{4a_0t} + \frac{c^2t}{4a_0} \right) \right] \tag{16}$$

If we substitute $a = 2a_0/(D-E+2)$ for the thermal diffusivity and $R = 4a/c$ for the effective radius of sample (heat source), where a is the coefficient of thermal diffusivity of the body with fractal dimension D, we obtain

$$\Delta T(t) = \frac{K\hbar c}{k_\mathrm{B}} \frac{\left[(D-E+2)/2\right]^{(D-E)/2}}{2D} (4at)^{(D-E+2)/2} \exp\left[-\left(\frac{h^2}{4at} + \frac{4at}{R^2} \right) \right]. \tag{17}$$

The power of heat source hold out to thermal conductivity of real material (characterised by fractal dimension D) can be written as

$$\frac{P}{\lambda} = \frac{K\hbar c}{k_\mathrm{B} D} \left(\frac{D-E+2}{2\pi} \right)^{(D-E)/2}. \tag{18}$$

Than we can rewrite Eq. (17) to form

$$\Delta T(t) = \frac{P}{2\lambda} \frac{(4at)^{(D-E+2)/2}}{\pi^{(E-D)/2}} \exp\left[-\left(\frac{h^2}{4at} + \frac{4at}{R^2} \right) \right]. \tag{19}$$

This equation is for $R \to \infty$ (real radius of the specimen and heat source *R* at infinite length *l*) is identical with model at Eq. (12). For *E* = 3 (3D space) and *D* = 2 (surface heat source at Eq. (13)

$$\Delta T(t) = \frac{P}{2\lambda} \sqrt{\frac{4at}{\pi}} \exp\left[-\left(\frac{h^2}{4at} + \frac{4at}{R^2} \right) \right]. \tag{20}$$

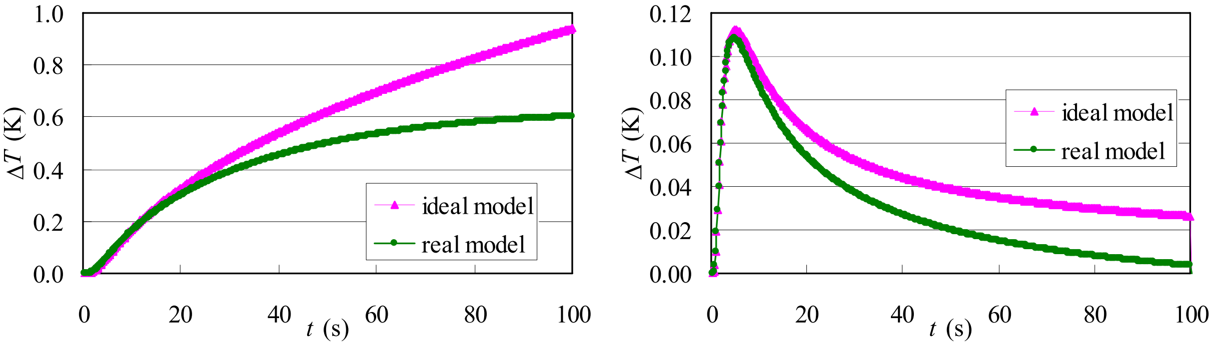

Figure 1: Step wise and pulse transient responses of ideal (up curves) and real (down curves) fractal model (E = 3, D = 2), calculated with using Eq. (19)

The model time dependences of temperature changes on the step unit (left) and Dirac impuls (right) of heat from the planar source ($D = 2$) are presented in Figure 1. The calculations were done for ideal (Eq. (13)) and real models (Eq. (20)). The changes of temperature are less for real model then for ideal model due to heat losses to surrounding.

3. Experimental

The interpretation of experimental results of the pulse transient method (Figure 2) without heat losses (1), (7) was described in the last contributions [8], [9]. The new interpretation of both pulse transient and step wise method without neglecting of the losses is described in this contribution

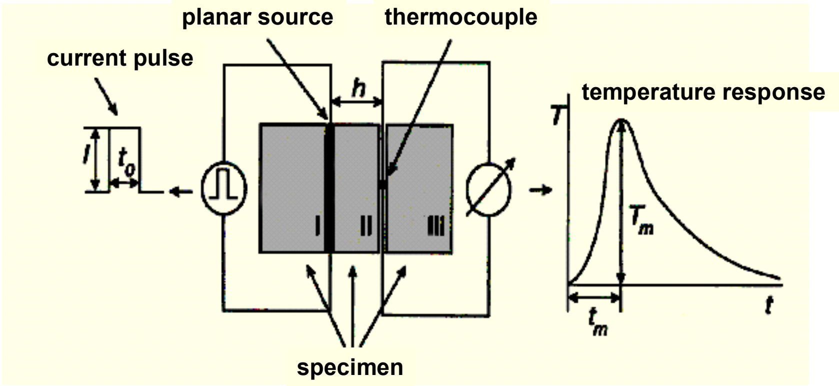

Figure 2: Caption of the figure

Using the pulse transient method, the delivered heat will be constant, and by the step wise method, the delivered heat will change linearly with time. Generally speaking, the actuating quantities (e.g. heat) can take different fractal dimensions in the equation.

The typical time responses of thermocouple voltage for both the rectangle (Dirac) pulse and step wise (up, down) are presented at Figure 3, left. The time responses in semi-logarithmic scale (the step wise dependences after derivation) are presented at Figure 3, right. The linear dependence for the high times give information about heat losses is evident (the term $4a/R^2$ in Eq. (20)).

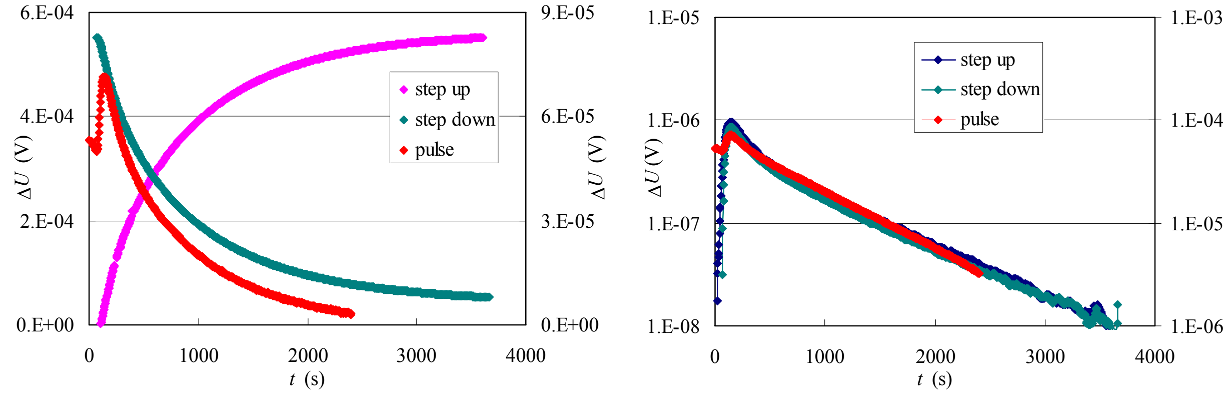

Figure 3: Dependence of thermocouple voltage on the time for stepwise (up, down) and pulse transient method in linear (left) and semi-logarithmic scale (after stepwise responses derivation). As the heat source was used photovoltaic cell.

The linearity of this dependence is more evident from the thermal response derivation (Figure 4). The diffusivity a = 2.25 · 10^{-7} m².s^{-1} was calculated for parameter R = 0.03 m (heat source diameter) and for derivation value of $4a/R^2 \approx 1 \cdot 10^{-3}\,\mathrm{s}^{-1}$. This value correlates with the diffusivity values that were calculated from the thermal response maxima determined by a standard calculation (see Table I)

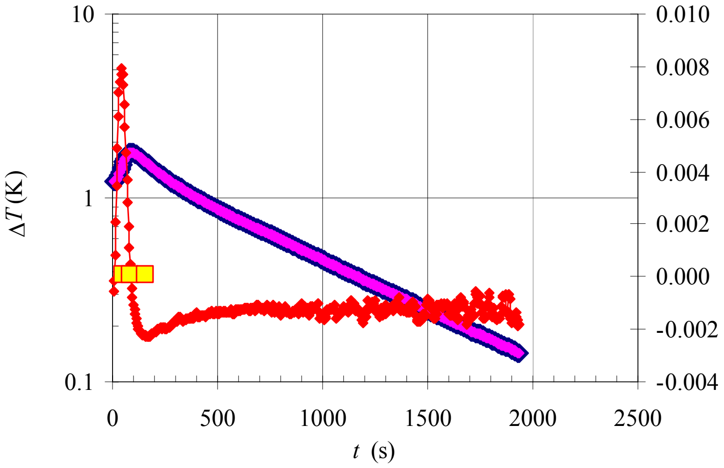

Figure 4: Dependence of thermal response on the time for pulse transient method in semi-logarithmic scale and their derivation (right axis). Infinite limited value is proportional to $4a/R^2$.

Table 1: Thermal parameters PMMA measured with different heat sources and different pulse types

	a (m².s^{-1})	**c_p (J.kg^{-1}.K^{-1})**	**λ (W.m^{-1}.K^{-1})**	**ρ (kg.m^{-3})**
heat source: rectangle pulse	1.12 · 10^{-7}	1.45 · 10^{3}	1.93 · 10^{-1}	1.18 · 10^{3}
photovoltaic cell: rectangle pulse	1.66 · 10^{-7}	0.81 · 10^{3}	1.58 · 10^{-1}	1.18 · 10^{3}
photovoltaic cell: step up	1.39 · 10^{-7}	2.23 · 10^{3}	3.68 · 10^{-1}	1.18 · 10^{3}
photovoltaic cell: step down	2.90 · 10^{-7}	8.69 · 10^{2}	2.98 · 10^{-1}	1.18 · 10^{3}

4. Appendix

In mathematics, the error function (also called the Gauss error function) is a special function (non-elementary) of sigmoid shape which occurs in probability, statistics, materials science, and partial differential equations. It is defined as:

$$\operatorname{erf}(x)=\frac{2}{\sqrt{\pi}}\int_0^x \mathrm{e}^{-t^2}\,\mathrm{d}t \tag{21}$$

The complementary error function, denoted erfc, is defined in terms of the error function:

$$\operatorname{erfc}(x)=1-\operatorname{erf}(x)=\frac{2}{\sqrt{\pi}}\int_x^\infty \mathrm{e}^{-t^2}\,\mathrm{d}t \tag{22}$$

The derivative of the error function follows immediately from its definition:

$$\frac{\mathrm{d}}{\mathrm{d}x}\operatorname{erf}(x)=\frac{2}{\sqrt{\pi}}\mathrm{e}^{-x^2} \tag{23}$$

An antiderivative (primitive function) of the error function is

$$x\operatorname{erf}(x)+\frac{\mathrm{e}^{-x^2}}{\sqrt{\pi}} \tag{24}$$

$$i\mathit{\Phi}^*+x=\frac{e^{-x^2}}{\sqrt{\pi}}+x\operatorname{erf}(x) \tag{25}$$

Therefore, we can define the error function in terms of the incomplete Gamma function:

$$\operatorname{erfc}(x)=\frac{2}{\sqrt{\pi}}\int_x^\infty \mathrm{e}^{-t^2}\,\mathrm{d}t=\frac{1}{\sqrt{\pi}}\int_{x^2}^\infty u^{-1/2}\mathrm{e}^{-u}\,\mathrm{d}u=\frac{\Gamma\left(1/2,x^2\right)}{\sqrt{\pi}} \tag{26}$$

The upper incomplete gamma function is defined as ($u = t^2$, $v = x^2$):

$$\Gamma(s,v)=\int_v^\infty u^{s-1}\mathrm{e}^{-u}\,\mathrm{d}u\,,\ \Gamma\left(s,x^2\right)=2\int_v^\infty x^{2s-1}\mathrm{e}^{-x^2}\,\mathrm{d}x\,,\ \Gamma(s,A/t)=A^s\int_0^t t^{-(s+1)}\mathrm{e}^{-A/t}\,\mathrm{d}t\,. \tag{27}$$

and for $s=1/2$

$$\Gamma(1/2,v)=\int_v^\infty u^{-1/2}\mathrm{e}^{-u}\,\mathrm{d}u\,,\ \Gamma\left(1/2,x^2\right)=2\int_v^\infty \mathrm{e}^{-x^2}\,\mathrm{d}x\,,\ \Gamma(1/2,A/t)=A^s\int_0^t t^{-3/2}\mathrm{e}^{-A/t}\,\mathrm{d}t\,. \tag{28}$$

5. Acknowledgements

This work was supported by grant KAN401770651 from the Academy of Sciences of the CR and by grants FT-TA3/048 and FR-TI1/144 from the Ministry of Industry and Trade of the CR

6. References

[1] CARSLAW H. S.; JAEGER J. C. *Conduction of Heat in Solids*. Clarendon Press London. 1959

[2] KREMPASKÝ J, *Measurement of Thermophysical Quantities*. VEDA Bratislava. 1969

[3] KUBIČÁR Ľ. *Pulse method of measuring basic thermophysical parameters*. Elsevier, Amsterdam, Tokyo, Oxford, New York, 1990

[4] DIEŠKOVÁ M.; DIEŠKA P.; BOHÁČ V.;, KUBIČÁR Ľ. Determination of temperature field and an analysis of influence of certain factors on a temperature fields. In collection of manuscripts of the *17th ECTP*, 2005, Bratislava, Slovakia. Vozár L., Medveď I. and Kubičár Ľ. editors. (CD-ROM).

[5] ŠTOFANIK V., MARKOVIČ M., BOHÁČ V., DIEŠKA P., KUBIČÁR Ľ.: RT-Lab - the Equipment for Measuring Thermophysical Properties by Transient Methods, *Measurement Science Review*, 7: 15-18 (2007)

[6] BOHÁČ V., DIEŠKA P., KUBIČÁR Ľ.: The Heat Loss Effect at the Measurements by Transient Pulse Method. In *Measurement Science Review*. 7: 24-27 (2007)

[7] ZMEŠKAL, O.; BUCHNÍČEK, M.; VALA, M. Thermal properties of bodies in fractal and cantorian physics. *Chaos, Solitons & Fractals*. 2005. 25(5). p. 941 - 954. ISSN 0960-0779.

[8] ŠTEFKOVÁ, P.; ZMEŠKAL, O.; CAPOUŠEK, R. Study of Thermal Field in Composite Materials. In *Complexus Mundi*. WS. London, World Scientific. 2006. p. 217 - 224. ISBN 981-256-666-X.

[9] ZMEŠKAL, O., ŠTEFKOVÁ, P., HŘEBENOVÁ, L., BAŘINKA R. Pulse Transient Method as a Tool for the Study of Thermal Properties of Solar Cell Laminating Films. *International Journal of Thermophysics*. 2009. DOI 10.1007/s10765-009-0687-y

High-performance materials containing alternative silicate binders: analysis of properties and recommendations for application in building practice

Eva Vejmelková[1], Michal Ondráček[2], Martin Sedlmajer[2], Zbyšek Pavlík[1], Robert Černý[1]

[1]Czech Technical University in Prague, Faculty of Civil Engineering, Department of Materials Engineering and Chemistry, Prague, Czech Republic

[2] Brno University of Technology, Faculty of Civil Engineering, Institute of Technology of Building Materials and Components, Brno, Czech Republic

Abstract: *An analysis of properties of high-performance materials containing alternative silicate binders is presented in the paper, and recommendations for their application in building practice are formulated. It is concluded that the utilization of alternative silicate binders as a partial replacement of Portland cement can be considered a prospective way to the production of high performance materials beneficial to the environment. However, from the point of view of their practical application it is necessary to comply with certain limitations, in particular concerning the recommended amount of an alternative silicate binder in a concrete mixture.*

Keywords: *metakaolin, fly ash, ground granulated blast furnace, high-performance concrete*

Introduction

Alternative silicate binders such as fly ash, ground granulated blast furnace slag, silica fume and metakaolin/calcined clay have found the application in concrete production couple of decades ago because of their potential to replace a part of Portland cement in concrete. Fly ash, ground granulated blast furnace slag and silica fume are waste materials. Metakaolin is produced by thermal decomposition of kaolin without production of CO_2. Therefore, these materials or their combinations can be considered as environmental friendly cement substitutes.

The measurements of properties of materials containing alternative silicate binders are – similarly as with many other cement-based composites – mostly concentrated on mechanical properties. This may not always be sufficient because superior mechanical properties are often not accompanied by comparably good resistance against water or salt penetration. In this paper, properties of three different cement based composites containing alternative silicate binders as partial replacement of Portland cement, the first with ground granulated blast furnace slag, the second with metakaolin, and the third with fly ash are investigated in much wider extent than it is usual in concrete research. The results are also compared with those obtained for reference material containing only Portland cement as binder.

Materials

Four different types of cement-based composites were studied. Three of them contained alternative silicate binders, namely metakaolin MEFISTO K 05 (BM, BM2), ground granulated blast furnace slag (BS, BS2) and fly ash (BP, BP2). The fourth was reference mixture with only Portland cement as binder (BR). The studied materials BM, BP, BS contained 9.1% of alternative silicate binders as partial replacement of Portland cement. Materials BS2 and BP2 contained 40%, material BM2 20% of alternative silicate binders. Table 1 presents the composition of the studied concrete mixtures.

The amount of water added into the each prescription was chosen in order to assure the same S3 consistence and workability of fresh concrete mixture according to the Czech Standard [1].

Table 1. The composition of concrete mixtures [kgm^{-3}]

Component	**BR**	**BM**	**BM2**	**BP**	**BP2**	**BS**	**BS2**
cement CEM I 42,5 Mokrá	484	440	387	440	290	440	290
aggregates 0-4 mm,	812	812	812	812	812	812	812
aggregates 8-16 mm	910	910	910	910	910	910	910
Plasticizer Mapei Dynamon SX	5,30	5,30	5,30	5,30	5,30	5,30	5,30
metakaolin MEFISTO	-	44(9,1%)	97(20%)	-	-	-	-
fly ash Dětmarovice	-	-	-	44(9,1%)	194(40%)	-	-
ground granulated blast furnace slag Štramberk	-	-	-	-	-	44(9,1%)	194(40%)
water	148	142	188	137	182	146	160

Experimental methods

Mechanical properties

The measurement of compressive strength and bending strength was done using the hydraulic testing device VEB WPM Leipzig 3000 kN. The apparatus consists of a stiff loading frame having the capacity of 3000 kN. A constant strain rate of 0.1 – 0.2 MPa/s was imposed on the specimens. The measurement of bending strength was done on 100 x 100 x 400 mm prisms. The measurement of compressive strength was done on the samples 150 x 150 x150 mm. After the time period of 28 days after mixing, the samples were dried and prepared for testing.

Basic material properties

As fundamental physical material characteristics, bulk density ρ_b [kgm^{-3}], open porosity ψ [Vol.-%] and matrix density ρ_m [kg m^{-3}] were determined. They were obtained using the gravimetric method and the water vacuum saturation method [2]. The measurement was done on the samples with dimension 50 x 50 x 20 mm.

Water vapor transport properties

The wet cup method and dry cup method were employed in the measurements of water vapor transport parameters [2]. The water vapor diffusion coefficient D [m^2 s^{-1}] and water vapor diffusion resistance factor μ [-] were measured. The measurement was done on the samples with dimension 50 x 50 x 20 mm.

Water transport properties

The water sorptivity A [kg m^{-2} s$^{-1/2}$] and apparent moisture diffusivity κ [m^{2} s^{-1}] were measured using a water suction experiment [3]. The measurement was done on the samples with dimension 50 x 50 x 20 mm.

Frost resistance

Frost resistance tests were carried out according to ČSN 73 1322/Z1:1968. The samples were tested after 28 days of concrete maturing and standard curing. The total test required 100 freezing and thawing cycles. One cycle consisted of 4 hours freezing at -20°C and 2 hours thawing in 20°C warm water. Frost resistance coefficient K was determined as the ratio of bending or compressive strength of specimens subjected to 100 freezing and thawing cycles to the strength of reference specimens which did not undergo the frost resistance test. 100 x 100 x 400 mm samples were used in the experiments.

Resistance against de-icing salts

The resistance of studied composites against de-icing salts was measured according to ČSN 731326/Z1:1984. The tested specimens are saturated by water and put into a bath with 3% NaCl solution. Then, freeze-thaw cycles are applied. In one cycle the tested specimen is cooled at first in an automatic conditioning device from 20°C to -15°C during 45 minutes, then it is left at -15°C for 15 minutes, subsequently heated to 20°C during 45 minutes and left 15 minutes at that temperature. After every 25 cycles the specimens are removed from the bath, their mass loss due to spalling of particles on the surface determined, the NaCl solution is replaced and specimens put into the bath again. The test is finished either after the prescribed number of cycles or after the mass loss exceeds 1000 g/m^{2}.

Experimental results and discussion

Mechanical properties

Table 2 shows the compressive and bending strength of the studied composites after 28 days. All materials safely met the basic criterion of the compressive strength of 60 MPa to be considered high-performance materials. The results were very similar for all materials, only the material BP with fly ash achieved lower values. The highest value of compressive strength achieved material BR and concrete with lower content of slag BS. The highest value of bending strength achieved material with lower content of metakaolin BM and higher content of slag BS2. The lowest value achieved material with higher content of fly ash BP2 and higher content of metakaolin BM2.

Taking into account that the course of pozzolanic reaction is slower than of Portland cement hydration, it can be anticipated that the strengths of composites containing alternative silicate binders did not achieve yet their maximum effective values, and will grow substantially during the subsequent time period.

Table 2. Mechanical properties

HPC	Compressive strength [MPa]	Bending strength [MPa]
BR	77.4	10.36
BM	69.6	11.94
BM2	61.5	8.5
BS	78	9.86
BS2	71.5	11.7
BP	69	9.79
BP2	54	8.6

Basic material properties

The basic physical properties of studied composites measured by the water vacuum saturation method are shown in Table 3. The bulk densities of all materials differed (except for BP2) only up to about 7%. The highest value of matrix density achieved material BM2 with higher content of metakaolin, the lowest material BS2 with higher content of fly ash. The lowest value of porosity achieved the material BS with lower content of slag, it was in average about 25% lower than the other materials, the highest value achieved material BP2 with higher content of fly ash, it was on the other hand in average about 25% higher then the other studied materials.

Table 3. Basic material parameters

HPC	Bulk density [kg m^{-3}]	Matrix density [kg m^{-3}]	Open porosity [%]
BR	2380	2720	12.3
BM	2370	2690	13.0
BM	2370	2690	13.1
BM2	2372	2729	13.3
BS	2330	2600	9.7
BS2	2351	2711	12.8
BP	2360	2720	12.5
BP2	2211	2634	16.0

1.1 Water vapor transport properties

The results of measurements of water vapor diffusion resistance factor μ of the analyzed composites are presented in Table 4. Comparing the data measured for all studied materials, we can see that the highest μ value achieved material BP with lower content of fly ash and the reference material BR, the lowest value the material with higher fly ash amount BP2. Values of water vapor diffusion resistance factor μ of other materials differed only slightly.

The measured data revealed basic information that the values of water vapor diffusion coefficient corresponding to the lower values of relative humidity (5-50%) were always lower than those for higher relative humidity values (97-50%). This is in accordance with the previous measurements on many other materials including concrete. The main reason for this finding is coupling of water vapor transport with water transport in a material with higher relative humidity where the capillary condensation takes place in a much higher extent than in the range of lower relative humidity [6].

Table 4. Water vapor transport properties

HPC	**5/25-30 %**			**97/25-30 %**		
	δ	**D**	**μ**	**δ**	**D**	**μ**
	[s]	**[m^2s^{-1}]**	**[-]**	**[s]**	**[m^2s^{-1}]**	**[-]**
BR	5.16E-12	7.09E-07	32.44	8.01E-12	1.10E-06	20.99
BM	9.52E-12	1.31E-06	17.70	1.90E-11	2.61E-06	8.99
BM2	8.89E-12	1.22E-06	19.65	1.20E-11	1.65E-06	14.09
BS	1.09E-11	1.50E-06	15.80	2.64E-11	3.63E-06	6.60
BS2	1.10E-11	1.51E-06	16.39	1.33E-11	1.83E-06	15.02
BP	3.81E-12	5.23E-07	44.63	9.76E-12	1.34E-06	17.18
BP2	1.72E-11	2.37E-06	10.16	3.11E-11	4.28E-06	7.06

Water transport properties

The effect of alternative silicate binders on the liquid moisture transport parameters was for their lower amount pronounced for materials with ground granulated blast furnace slag and metakaolin. The apparent moisture diffusivity of BM and BS (Table 5) was about 30 – 40% lower than for BR.

The highest ability of liquid water transport had the materials with higher content of fly ash BP2 and higher content of slag BS2. The results showed that the higher content of alternative silicate binders caused faster transport of liquid water.

Frost resistance

Table 6 shows that all studied composite materials could be characterized as frost resistant. The frost resistance coefficient *K* calculated as ratio of both compressive strength and bending strength was always higher than 0.75.

The results showed that the sufficient frost resistance of HPC can be obtained even without adding of air entraining agent.

Table 5. Water transport properties

HPC	A $[kg\ m^{-2}s^{-1/2}]$	κ $[m^2\ s^{-1}]$
BR	0.0099	7.15E-09
BM	0.0070	4.09E-09
BM2	0.0103	6.00E-09
BS	0.0057	3.77E-09
BS2	0.0128	1.00E-08
BP	0.0105	6.49E-09
BP2	0.0226	2.00E-08

Table 6. Frost resistance

HPC	**Frost resistance coefficient K**	
	as the ratio of compressive strengths [-]	**as the ratio of bending strengths [-]**
BR	1.00	0.80
BM	1.00	1.00
BM2	1.10	0.80
BS	1.00	0.80
BS2	1.07	0.78
BP	0.95	0.85
BP2	0.94	0.93

Resistance against de-icing salts

Experimental results presented in Figure 1 show that all analyzed materials (except for the material BP2 with higher content of fly ash) met the basic condition of satisfactory resistance against de-icing salts which is 1000 gm^{-2} after 100 cycles. The best performance exhibited the material with higher content of slag BS2. Very good resistance against de-icing salts had also the material BM with metakaolin and the reference material BR.

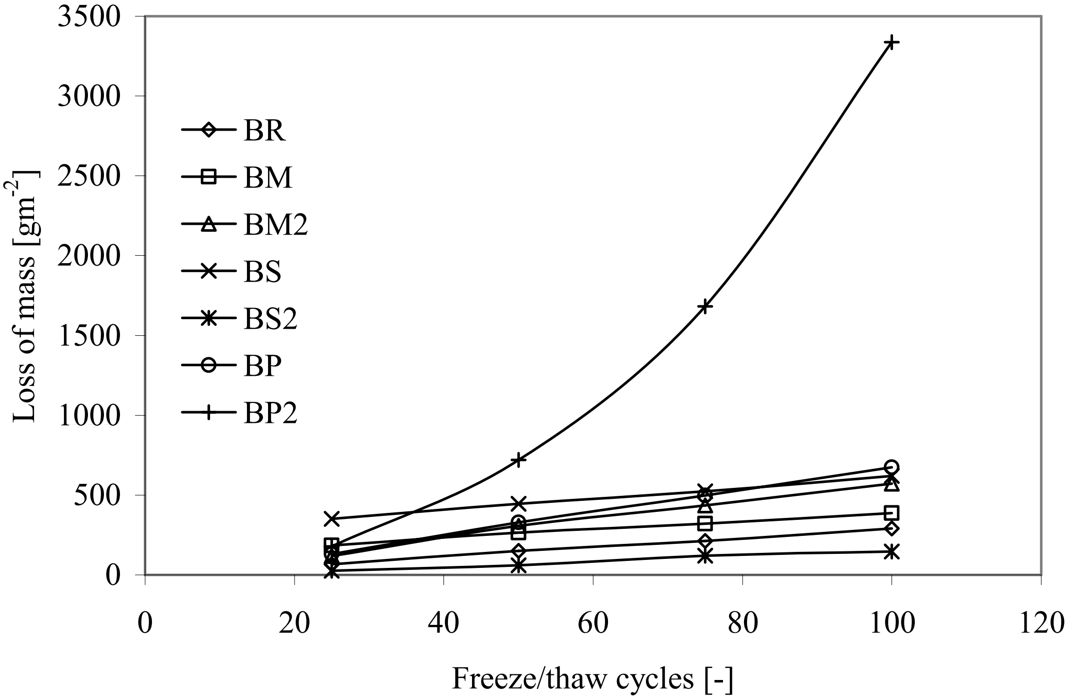

Figure 1: Loss of mass of studied composites due to the de-icing salts action

Conclusions and recommendations for practical application

Experimental results presented in this paper showed that the application of alternative silicate binders as a partial replacement of Portland cement can be considered a prospective way to the production of high performance materials beneficial to the environment. However, from the point of view of their practical application it is necessary to comply with certain limitations, in particular concerning the recommended amount of an alternative silicate binder in a concrete mixture.

If metakaolin, ground granulated blast furnace slag or fly ash are used as a replacement of Portland cement up to 10% of the mass of cement, the resulting properties of high performance concrete are satisfactory and the practical application can be recommended without limitation. The experimental analyses have shown that all high performance concretes achieved sufficient compressive and bending strengths. A limit of 80 MPa in compression was safely met. The differences in mechanical properties due to the application of alternative silicate binders were low, similarly as the bulk density of hardened mixtures. The materials containing slag and metakaolin transported liquid water significantly slower than the reference material and the material containing fly ash. All tested specimens safely met the requirements for frost resistance without air-entraining agents. The resistance against chemical de-icing substances was also very good. Metakaolin was found the most convenient replacement alternative silicate binder. The use of slag was also quite satisfactory. The application of fly ash as partial replacement of Portland cement led to a slight decrease of strength and higher mass loss in testing the resistance against chemical de-icing substances.

The results obtained for using higher amounts of metakaolin, ground granulated blast furnace slag and fly ash were not so unambiguous as in the case of 10% Portland cement replacement. A principal problem was a significant loss of compressive strength after 28 days which appeared for metakaolin already for the replacement of 20% of Portland cement and for fly ash for 40% replacement. Satisfactory results were achieved for slag only where for the replacement of 40% of Portland cement the mechanical properties were on an acceptable level. From the point of view of durability properties, in a comparison with reference high performance concrete the best results were obtained for 40% of slag and 20% of metakaolin. These materials had very high frost resistance coefficients and very high resistance against de-icing salts. The high performance concrete with 40% of fly ash had the highest porosity and significantly higher water transport coefficients than the other hardened mixtures. Its frost resistance was significantly lower and resistance against de-icing salts very bad, 3300 $g \cdot m^{-2}$ after 100 frost cycles. For the replacement of Portland cement by alternative silicate binders higher than 10% of mass of cement, only the use of ground granulated blast furnace slag up to 40% can be recommended without limitation. If the strength values are not of primary importance for a given concrete and durability is the decisive factor, the use of up to 20% of metakaolin as Portland cement replacement can be an acceptable solution.

Acknowledgments

This research has been supported by the Czech Science Foundation, under project No 103/07/0034.

References

[1] EN 206-1: 2001. Concrete - Part 1: Specification, performance, production and conformity.

[2] ČSN 72 7031. Measurement of water vapor diffusion coefficient of building materials using a method without temperature gradient.

[3] KUMARAN M. K.. Moisture Diffusivity of Building Materials from Water Absorption Measurements. IEA Annex 24 Report T3-CA-94/01. Ottawa 1994.

[4] ČSN 73 1322/Z1:1968 Concrete testing – Hardened concrete – Frost resistance. Czech Standardization Institute, Prague 2003.

[5] ČSN 731326/Z1:1984. Determination of the resistance of the surface of concrete against water and de-icing salts. Czech Standardization Institute, Prague 2003.

[6] ČERNÝ R. ROVNANÍKOVÁ P. Transport Processes in Concrete. Spon Press. London 2002., ISBN 0-415-24264-9

Investigation of the thermal diffusivity of $Fe_{52}Ni_{48}$ and $Fe_{40}Ni_{60}$ iron-nickel alloys by means of modified flash method

Janusz Terpiłowski[1] , **Grzegorz Woroniak**[2]

[1] Faculty of Mechatronics, Military University of Technology, Kaliskiego 2,

00-908 Warsaw, Poland, e-mail: Janusz.Terpilowski@wat.edu.pl

[2] Department of Heat Engineering, *Bialystok Technical University, Wiejska 45E,*

15-333 Bialystok, Poland, e-mail: woroniak@pb.edu.pl

Abstract: *The paper presents the results of the thermal diffusivity investigation of the two two-component Fe52Ni48 and Fe40Ni60 alloys. Investigations have been performed using the modified flash method, which consists in measuring the temperature difference between opposite surfaces of a disc-like sample, just after the laser shot on the front sample surface. The investigated samples were 12 mm in diameter and had thicknesses - 1.60 mm (Fe52Ni48) and 1.51 mm (Fe40Ni60). Temperature range of the investigations was from 300 K to 900 K. It has been found that the thermal diffusivity values for both investigated alloys and for the above temperature range were within the range* $(4.5 \div 8.5)\times10^{-6}$ m^2/s. *In the both cases the hysteresis loops of the Curie Points T were observed* [$T_C (T \uparrow) = 774.4$ K *and* $T_C (T \downarrow) = 773.9$ K *for Fe52Ni48 as well as* $T_C (T \uparrow) = 861.1$ K *and* $T_C (T \downarrow) = 855.1$ K *for Fe40Ni60 alloy].*

Keywords: *flash method, thermal diffusivity, Iron-Nickel alloy.*

1. Introduction

Fe-Ni binary alloys have special physical properties which can be implemented in technics. A characteristic feature of these alloys is the occurrence of phase transitions of the first and second kind are shown in Fe-Ni Phase Diagram (Figure 1). The nature and location of the phase transitions depend on the temperature and on the percent of Ni in the alloy. During the phase transitions of the first kind there is a jump density ρ change of the substance as well as a jump change of its entropy. It is connected with the occurrence of the latent heat of phase transition. During the phase transitions of the second kind there is a jump change of the coefficient of thermal expansion α , the specific heat c_p, the coefficient of compressibility γ, the thermal diffusivity a and magnetic constant μ . The second kind phase transition temperature, also called The Curie Point temperature T_C, is characteristic for Fe – Ni binary alloys (Fig.1). Some of the above mentioned properties have been well researched and described but the measurements of thermal diffusivity of Fe – Ni alloys are scarce. In most cases they are limited to the temperature ranges not covering Curie Point.

The results of thermal diffusivity investigations of three alloys - FeNi29, FeNi35 and FeNi39 at the temperature range 300 ÷ 900 K have been presented in [7]. The first one is alloy FeNi29 commonly used in aircraft industry and as powder catalyst for composing high-grade synthetic diamonds. The second one is alloy FeNi35 used in telecommunications, aeronautical and aerospace engineering, cryogenic engineering (liquefied natural gas tankers) etc. The third one is alloy FeNi39 commonly used in thermostatic bimetals production (up to 400 ^{0}C).

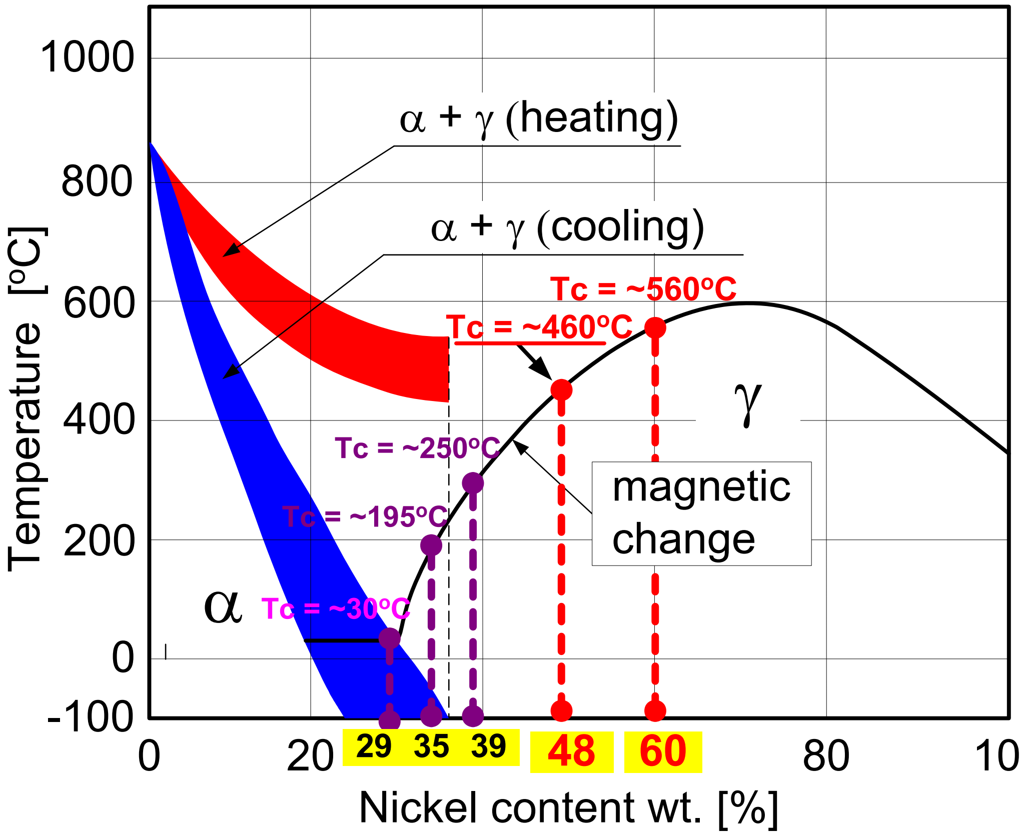

Figure 1:. Fe-Ni Binary Alloy Phase Diagram with a prediction change of the Curie Point [2] as well as with marked : ● compositions of FeNi48, and FeNi60 studied alloys; ● compositions of FeNi29, FeNi35 and FeNi39 invar alloys which have been investigated and described in [7]

This paper presents the results of the thermal diffusivity investigation of the two two-component FeNi48 and FeNi60 alloys at the identical temperature range (300 ÷ 900 K). The first alloy is used in metal to glass seals, especially with soft glasses and for metal to ceramic sealing applications (UV bulbs). The second alloy is applied in coated electrode with a core wire of FeNi60, especially suited for welding of spheroidal cast iron. The weld deposit is free from porosity and has the highest resistance to cracking.

2. Method of the measurement

The theoretical temperature distribution $\theta(x,t) = T(x,t) - T_0$ in the sample, where at time $t = 0$ the surface layer ($0 < x \le g$) absorbs radiation energy of the surface density Q, is obtained by solving the Fourier equation, under the boundary conditions as it is shown in Figure 2. In this case the general solution [5] is written as :

$$\theta(x,t) = \frac{1}{l}\int_0^l \theta(x',0)dx' + \frac{2}{l}\sum_{n=1}^{\infty} e^{\frac{-n^2}{\tau}t} \cos\frac{n\pi x}{l} \int_0^l \theta(x',0)\cos\frac{n\pi x'}{l}dx' \tag{1}$$

where $\tau = l^2 / \pi^2 a$ - is the characteristic time.

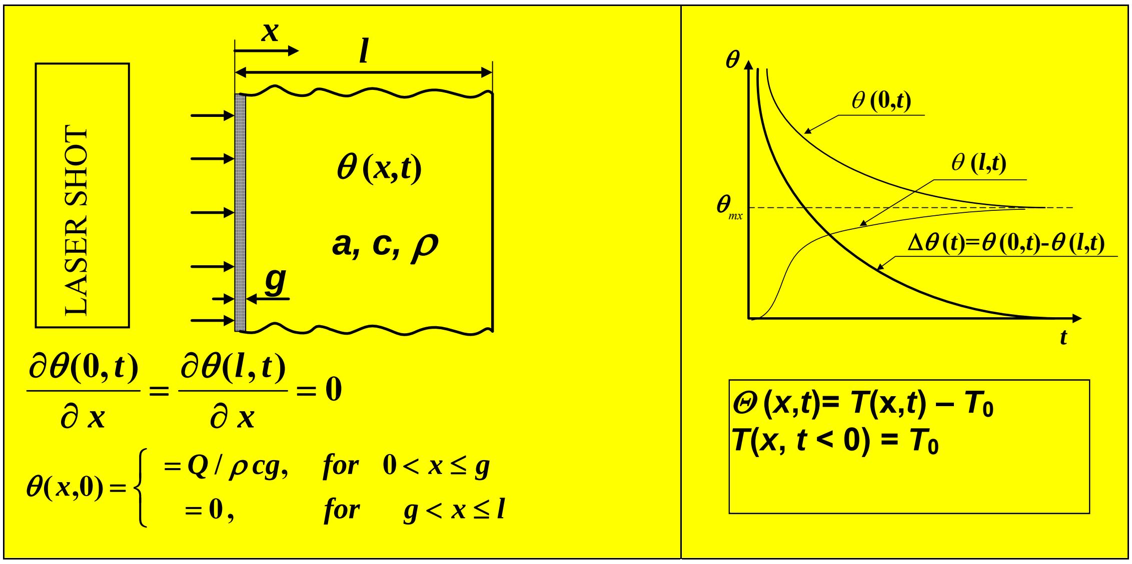

Figure 2: Model of heat exchange and the temperature and their difference changes on the side surfaces of the sample during thermal diffusivity investigation.

Determination of the thermal diffusivity by means of modified flash method is based on:

- theoretical determination of the temperature distribution inside the opaque sample as well as the temperature difference between its two side surfaces. In this case a one dimensional model approximating a real heat exchange in the „sample-surroundings" system is assumed;
- recording of the transient temperature difference between the front and the rear surface of the sample, as a result of a one dimensional process of the temperature equalisation in the sample;
- identification of the best fitting of the experimental results by a curve, obtained as one from the several theoretical curves which will be solutions of the problem. The optimisation parameter is the thermal diffusivity. A value of the thermal diffusivity corresponding to the best fitting is taken as the right one.

The thermal diffusivity *a* is determined by measuring the temperature difference $\Delta\theta^{'}(t)$ between the two opposite parallel surfaces ($x = 0, x = l$) of the sample. According to the theory (1)) :

$$\Delta\theta(t)=\theta(0,t)-\theta(l,t)=$$

$$=\frac{2}{l}\sum_{n=1}^{\infty} e^{\frac{-n^2 t}{\tau}}[1-(-1)^n]\int_0^l \theta(x',0)\cos\frac{n\pi x'}{l}dx' = \frac{4}{l}\sum_{n=1}^{\infty} e^{-(2n-1)^2\frac{t}{\tau}}\int_0^l \theta(x',0)\cos\frac{(2n-1)\pi x'}{l}dx' =$$

$$\frac{4}{l}\sum_{n=1}^{\infty} e^{-(2n-1)^2\frac{t}{\tau}}\int_0^l \theta(x',0)\cos\frac{(2n-1)\pi x'}{l}dx' \tag{2}$$

After truncation of the infinite series in (2) for n > 1, with respect to initial condition as it is indicated in Figure 2 and assuming that $g << l$, the formula (2) gives:

$$\Delta\theta(t) = \frac{4}{l}\left[\int_0^l \theta(x',0)\cos\frac{\pi x'}{l}dx'\right]e^{\frac{-t}{\tau}} = 4\,\theta_\infty\, e^{\frac{-t}{\tau}} \tag{3}$$

The error of truncation is not greater then 1 % if $t/\tau > 0.58$.

In order to determine the thermal diffusivity a from recordings of the appropriate part of the temperature difference $\Delta\theta'(t)$ the characteristic time τ should be obtained first. From Eq. (3) we get :

$$y = \ln\Delta\theta(t) = \ln(4\theta_\infty) - t/\tau \tag{4}$$

Next, the data after logarithmic transformation are approximated within a certain interval [t_1, t_2]. Least square approximation is used. From a linear approximate parameters Θ_∞ and τ are derived. On the basis of the characteristic time τ the thermal diffusivity is calculated from:

$$a = l^2/\left(\pi^2\tau\right) \tag{5}$$

The thermal diffusivity defines a theoretical dependence of $\Delta\theta(t)$ (see Eq. (2)). On the basis of this curve a square root of sums of squares of differences between the recorded and theoretical value of the temperature difference between the two opposite sides of the specimen $\Delta\theta(t)$ is calculated. This parameter is minimised with reference to t_1, t_2 and the signal $\Delta\theta'(t)$ shift in such a way that the whole procedure is repeated with changed values of those parameters. The process is stopped when a satisfactory agreement between the theoretical curve $\Delta\theta(t)$ and the recorded experimental one $\Delta\theta'(t)$ is achieved.

3. Measurement and results

A block diagram of the laboratory stand for the thermal diffusivity investigation by the modified pulse method is shown in Figure 3. Experiments are performed on condition that the following requirements are satisfied: ● the density distribution of the radiation flux Q in a cross section of the radiation beam is homogeneous; ● the diameter of the radiation beam exceeds slightly that of the sample; ● the process of heat exchange in the sample is one-dimensional; ● the transition process of the temperature stabilisation after the laser flash heat absorption ($t > 0$) must be adiabatic. The above method has been used in the experimental investigation of the thermal diffusivity of the Fe52Ni48 (≡ FeNi48) and Fe40Ni60 (≡ FeNi60) alloys, as well as three other invar alloys (FeNi29, FeNi35 and FeNi39) described in [7].

The components weight of the investigated alloys are shown in Table 1. The investigations were carried out in the temperature range from room temperature to about 900 K. The thermal diffusivity investigations were carried out on disk-shaped samples of diameter 12 mm and thicknesses about 1.50 mm for all alloys (Table 2).

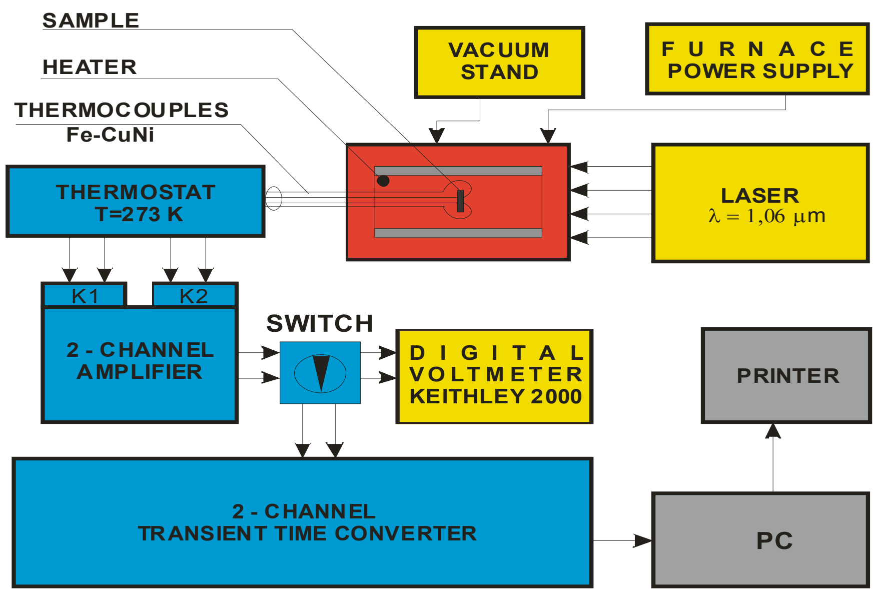

Figure 3:

Laboratory stand for the thermal diffusivity investigation by the modified

pulse method

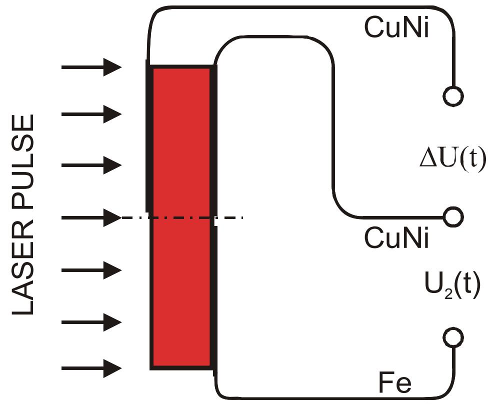

Figure 4: Measurement of the temperature difference $\Delta\Theta(t)$ between the extreme surfaces and the temperature $\Theta 2(t)$ on the rear surface of the sample:

$$\Delta U(t) = \Delta E(t) = k \cdot \Delta\Theta(t) =$$

$$= k \cdot [\Theta(0,t) - \Theta(l,t)] = k \cdot [\Theta_1(t) - \Theta_2(t)]\,;$$

$$U_2(t) = k \cdot \Theta_2(t)$$

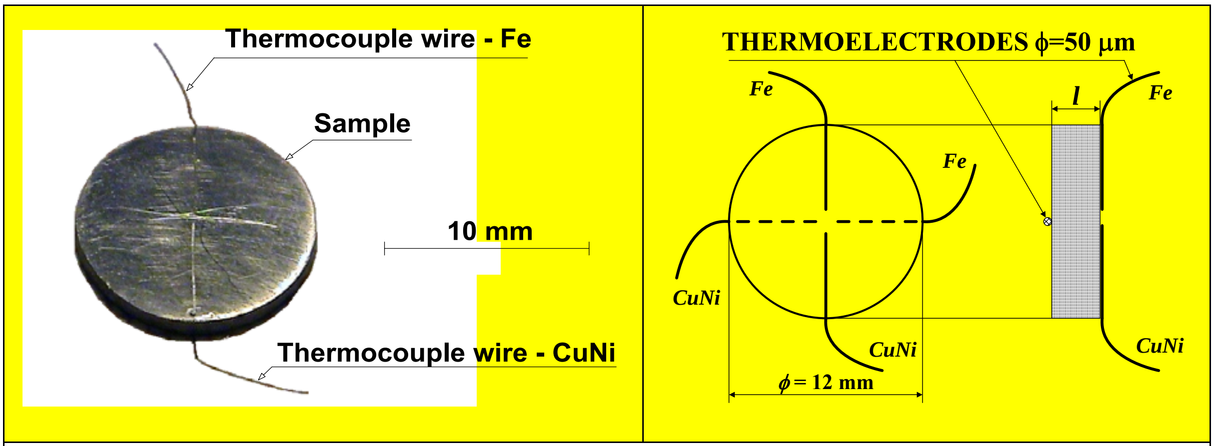

Figure 5: View and overall dimensions of the sample with two thermoelectrodes (diameter 50 μm) electrically welded to its front surface

Table 1: Components Weight of investigated Fe-Ni alloys

Alloy	*Components Weight Percent, [%]*										
	Ni	**Co**	**Cu**	**Mn**	**Mg**	**Cr**	**Al**	**Si**	**Mo**	**Ca**	**Zn**
FeNi29	29.21	0.005	0.005	-	-	0.005	0.005	-	-	-	-
FeNi35	35.45	0.05	0.1	0.005	0.001	0.01	0.005	0.005	0.001	0.005	0.005
FeNi39	39.12	0.05	0.1	0.005	0.001	0.01	0.005	0.005	0.001	0.005	0.005
FeNi48	48.34	-	-	-	-	-	-	-	-	-	-
FeNi60	60.0	-	0.001	0.005	-	0.05	0.001	-	0.005	-	-
Remark : Results of the thermal diffusivity and Curie Points investigations of FeNi29, FeNi35 and FeNi39 invar alloys were described in [7] and are presented in this paper as comparable results.											

A typical record of the final handling of experimental data $\Delta\Theta'(t)$ during the thermal diffusivity evaluation, according to procedure described above, for FeNi48 and FeNi60 alloys are shown in Figure. 6 and 7. Results of the thermal diffusivity investigations for the measured alloys are shown in Figure 8.

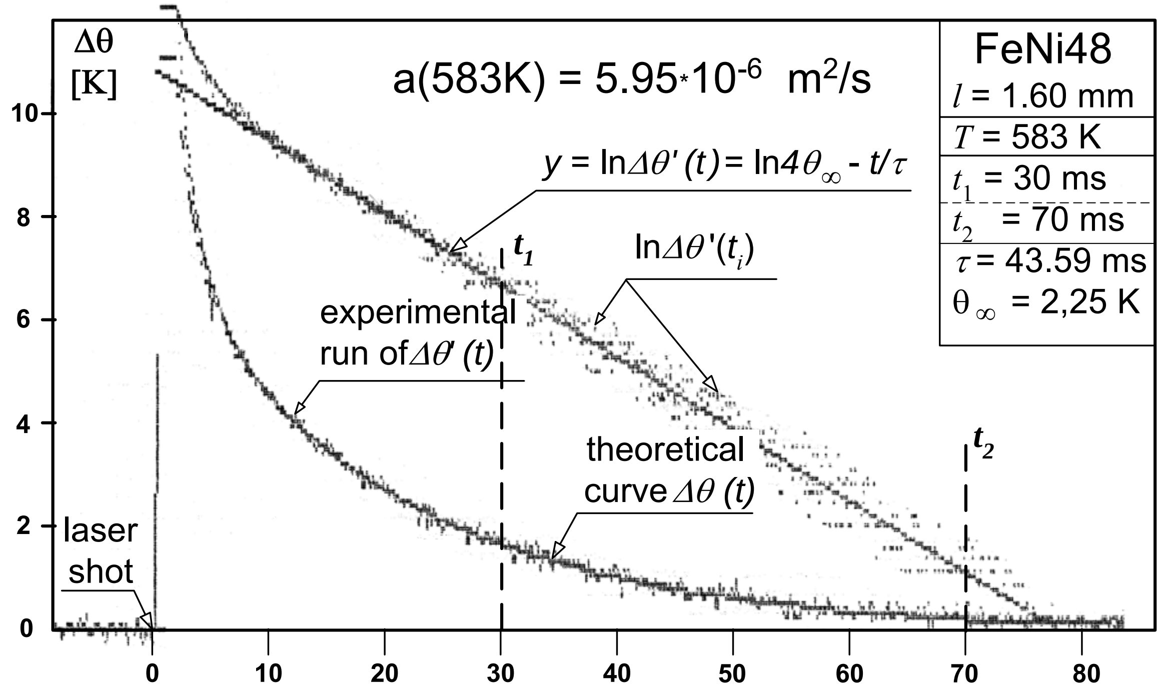

Figure 6: Final handling of experimental data ΔΘ '(t) during thermal diffusivity evaluation for FeNi48 alloy at T = 583 K

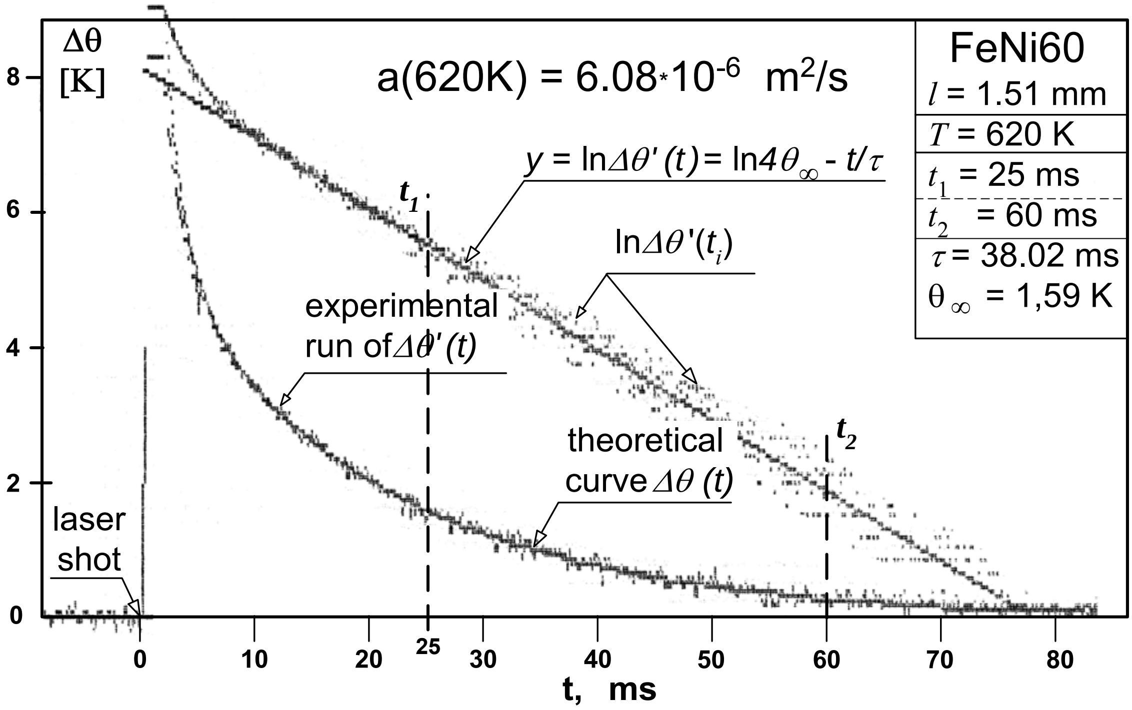

Figure 7: Final handling of experimental data ΔΘ’(t) during thermal diffusivity evaluation for FeNi60 alloy at T = 620 K.

The measurement of the thermal diffusivity error was determined using expression (5), then:

$$\left|\frac{\Delta a}{a}\right| = 2\left|\frac{\Delta l}{l}\right| + \left|\frac{\Delta \tau}{\tau}\right| \qquad (6)$$

where : Δl - absolute error of the sample thickness measurement (usually $\Delta l = 10^{-2}$ mm);
$\Delta\tau$ - absolute error connected with the determination of the characteristic time:

$$\left|\frac{\Delta \tau}{\tau}\right| = \left|\frac{\Delta \tau'}{\tau}\right| + \left|\frac{\Delta \tau_l}{\tau}\right|,$$

where: $\Delta\tau'$ - absolute error connected with the characteristic time τ' determination. In this method it is average square error of the τ' determination in the time range $t_1 \div t_2$ (see Fig. 6 and 7), $\Delta\tau_l$ - characteristic time τ error determination connected with the radiation heat losses from both surfaces of the investigated sample.

In the case of modified flash method $|\Delta\tau'/\tau|$ is determined by means of numerical processing of signal ΔΘ′(t) recorded in the transient process memory in the time range $t_1 \div t_2$. During evaluation of thermal diffusivity measurement error $|\Delta\tau_l/\tau|$ with respect to radiation heat losses of the sample it was assumed that the real temperature change values on the rear sample surface and the temperature differences on the extreme surfaces are from the experiment (τ and Θ_∞) , as it results from (1) for $x = l$ and (3). The procedure of the error $|\Delta a/a|$ determination is described in [8] in detail. In the case of the investigated alloys the total error of the thermal diffusivity measurement does not exceed 5 %

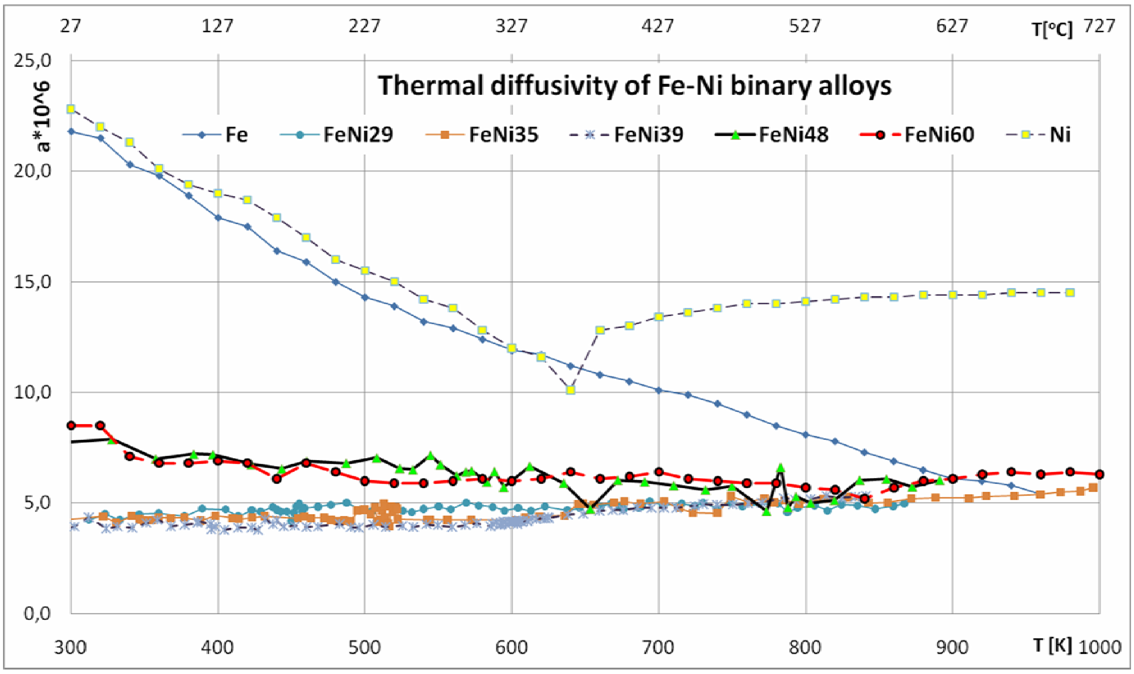

Figure 8: Final results of the thermal diffusivity own investigation of the Fe-Ni alloys with regard to pure iron and nickel [6].

Fe-Ni phase diagrams show that phase transition from the ferromagnetic into paramagnetic state takes place in each of these alloys at the Curie point. Based upon Figure 1 for alloys of compositions given in Table 1 the Curie temperature (magnetic change) should be of change and reaches values within the range 300 ÷ 900 K. The determination of the Curie Point based on the temperature characteristic of the thermal diffusivity is very difficult, because besides in the iron-nickel alloys appears also another phase transition. It was the reason why another method of the localization of the Curie Points was applied. For this purpose the special laboratory stand was built. The investigation of the position of Curie point in function of temperature T_C (T) was carried out using the measuring stand shown in Figure 9.

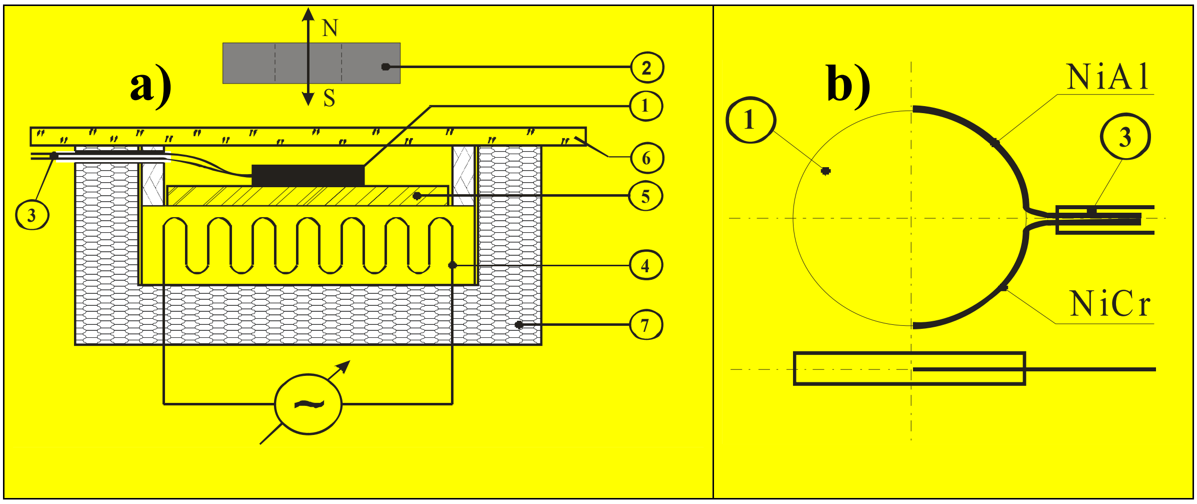

Figure 9: Laboratory stand for the Curie Point of Fe-Ni alloys investigation: 1 - investigated sample, 2 - magnet, 3 - thermocouple, 4 - heater, 5 - Cu plate (1.3 mm thick), 6 - glass (1 mm thick),
7 – insulation.

The same samples were used in the case which had been earlier applied in the thermal diffusivity measurements (diameter – 12 mm, thickness ≅ 1.5 mm). The NiCr–NiAl thermocouples were used to measure a sample temperature. The thermocouple wires were 50 µm in diameter and they were electrically welded to the side surfaces of the sample on its whole contact length (Figure 9b). The estimated temperature decrease on the extreme sample surfaces did not exceed 0.5 K under T_C determining.

When the material of the sample has the temperature lower then the temperature of its Curie Point then it is ferromagnetic material. In this case when the magnet approached the glass plate, the sample moved toward it. When the material of the sample has the temperature higher than the temperature of its Curie Point then it is paramagnetic material. In this case when the magnet approached the glass plate, the sample did not move toward it.

The results of the investigations of the localization of the Curie Points during the heating and cooling of the sample using the laboratory stand as it shown in Figure 9 are shown in Table 2.. The results of the T_C (↑) and T_C (↓) measurements, for the FeNi48 and FeNi60 alloys are also shown in Figure 10, 11 and 12 with respect to results of earlier performed similar investigation [7] for the FeNi29, FeNi35 and FeNi39 alloys. Additionally, in the Figures 11 and 12 are shown the Curie Points T_C (↑) and T_C (↓) for the FeNi20 alloy. In this case the hysteresis loop width was equal about ΔT_C= 354 K.

Table 2: Results of the Curie point investigation of the FeNi48 and FeNi60 alloys as well as of the FeNi29, FeNi35 and FeNi39 invar alloys [7] (the stand shown in Figure 9).

	d/*l* [mm/mm]	**$T_{C,1}$ dla T↑ [^{0}C]**	**$T_{C,2}$ dla T↓ [^{0}C]**	**ΔT_C [K]**
FeNi29	12,0 /1,50	162,0	146,0	16,0
FeNi35	12,0 /1,52	240,0	242,0	2,0
FeNi39	12,0 /1,50	328,5	330,0	1,5
FeNi48	12,0/1,60	501,3	500,8	0,5
FeNi60	12,0/1,51	588,0	582,0	6,0

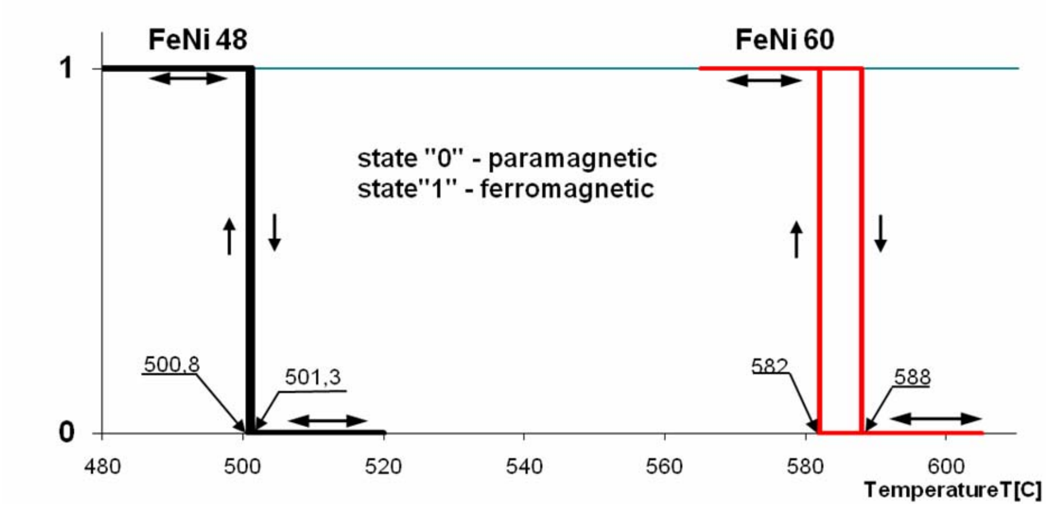

Figure 10: Results of the Curie Points investigation of the FeNi48 and FeNi60 alloys during heating and cooling of the sample.

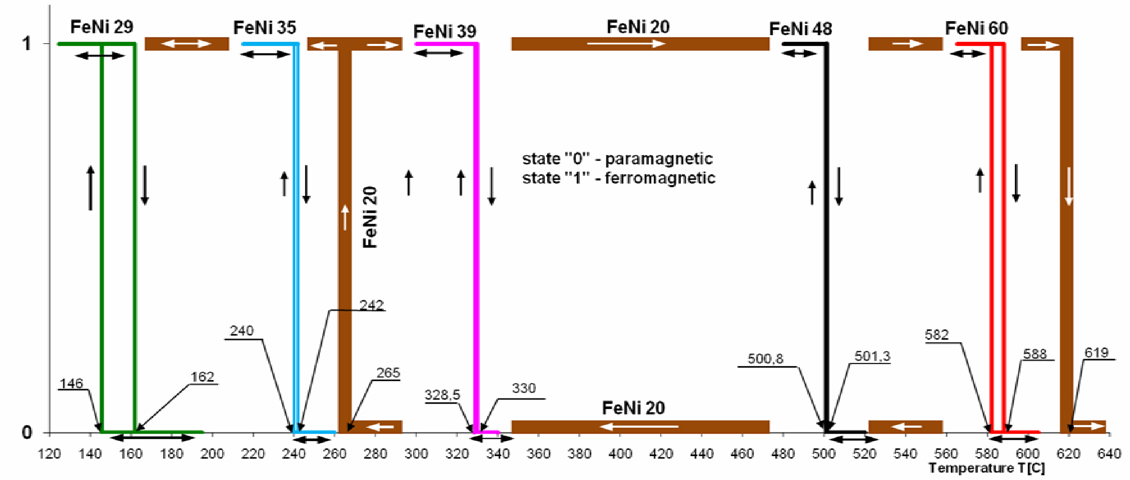

Figure 11: Preliminary results of the Curie points investigation of the FeNi48 and FeNi60 alloys as well as of the FeNi29, FeNi35 and FeNi39 invar alloys [7] during heating and cooling of the sample.

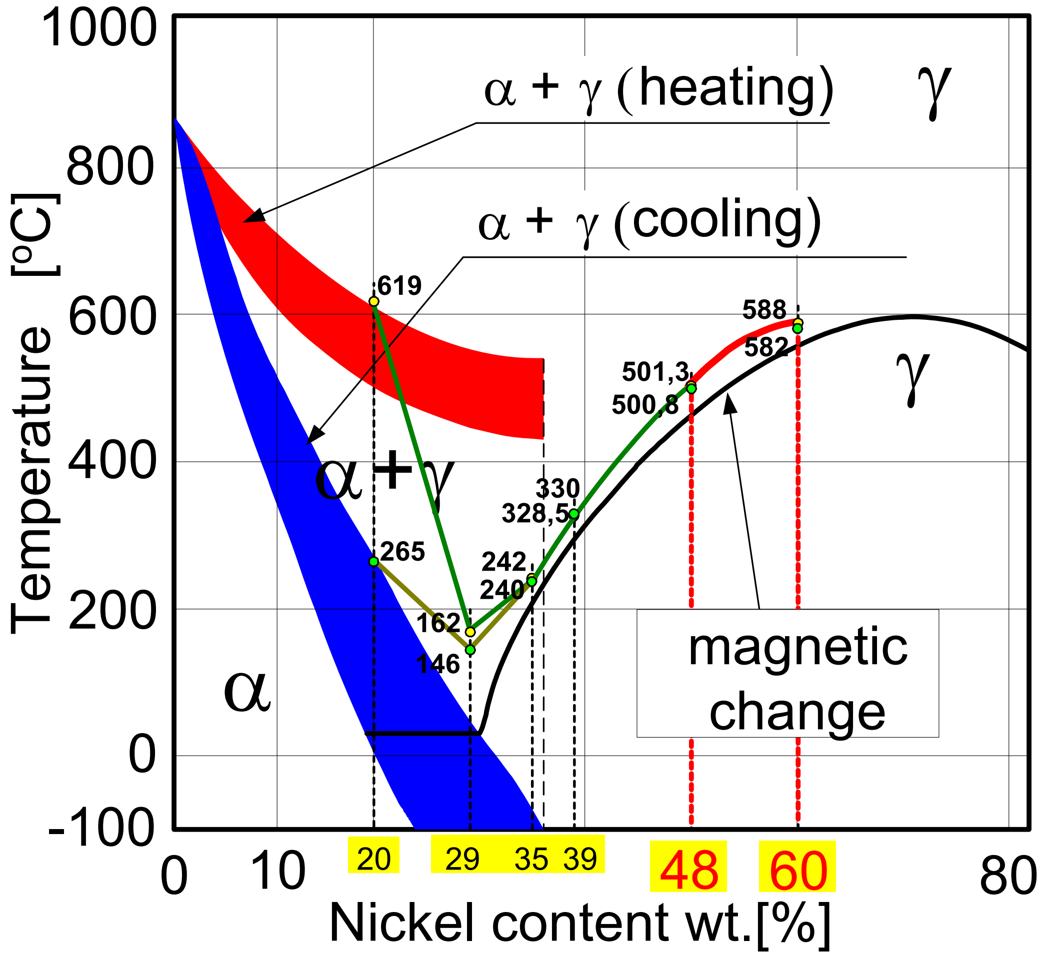

Figure 12: Results of the own investigations of the Curie Points of the FeNi20, FeNi29, FeNi35, FeNi39, FeNi48 and FeNi60 alloys in the context of investigations publicated by THYSSEN-KRUPP [2] (yellow points – during heating, green points – during cooling of the sample)

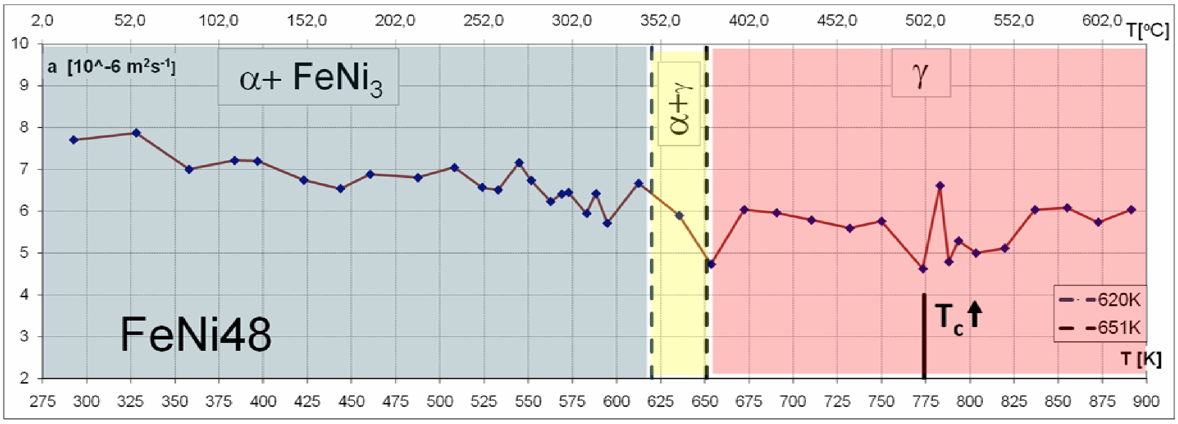

Figure 13: Thermal diffusivity of the FeNi48 alloy in the context of investigations of the Curie Point by means of laboratory stand shown in Fig.9 (during heating)

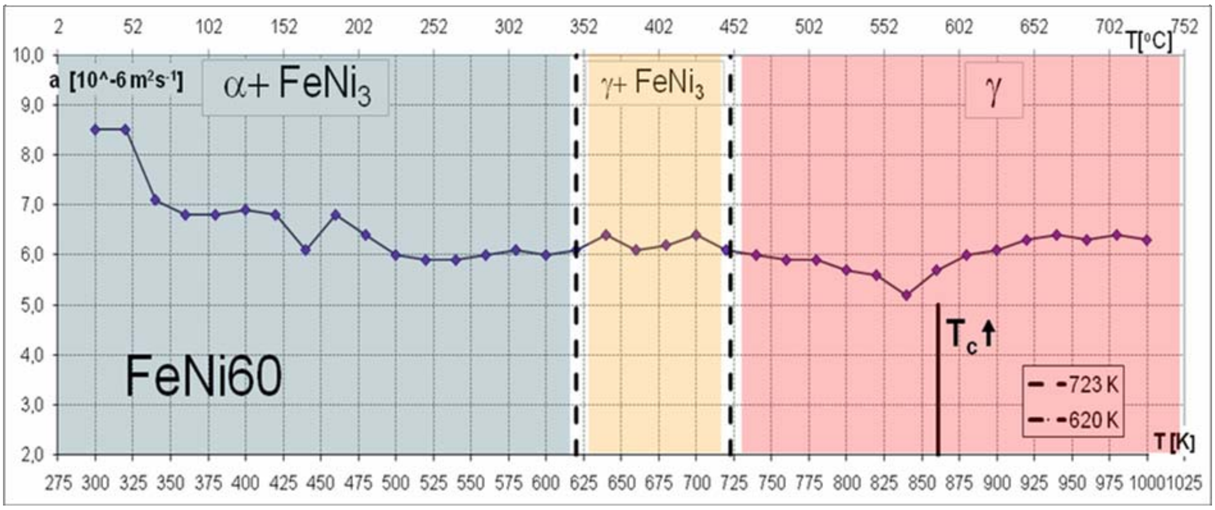

Figure 13: Thermal diffusivity of the FeNi60 alloy in the context of investigations of the Curie Point by means of laboratory stand show in Fig.9 (during heating)

4. Summary and conclusions

- The work presents results the preliminary investigation of the thermal diffusivity of the FeNi48 and FeNi60 alloys in the temperature range from room temperature to about 900 K. The results of this investigations are presented in context of the earlier investigations of the thermal diffusivity of the FeNi29, FeNi35 and FeNi39 alloys described in [7]. In every case the thermal diffusivity characteristics were determined during the heating of the sample.
- In the temperature range 290 ÷ 750 K the thermal diffusivity characteristics $a=f(T)$ of the FeNi48 and FeNi60 alloys are located above identical characteristics of the three earlier investigated invar FeNi29, FeNi35 and FeNi39 alloys, but below the pure iron and nickel thermal diffusivity characteristics.
- It seems that if the preliminary determination of the Curie Point for investigated alloys is not done, it would be very difficult to establish it only on the basis of the temperature characteristic $a = f(T)$.

- In case of the FeNi35, FeNi39 and FeNi48 alloys the position of their loop of hysteresis of the Curie Points did not, practically, change after the cycles of heating and cooling on laboratory stand shown in Fig. 9. However an anomaly was found for the FeNi29 and FeNi60 alloys consisting in moving of the loop of hysteresis of the Curie Point towards, respectively, lower and higher values of its temperature and its width.

Acknowledgement

This research work was supported by the Military University of Technology. Internal grant GW-PT 715/2009.

References

[1] SWARTZENDRUBER L.,J., ITKIN V., P., ALCOCK C., B.:*ASM Handbook vol.3: Binary Alloy Phase Diagrams*, 1992, p.2199, ASM International®, The Materials Information Society

[2] Katalog „*Pernifer and Pernima Alloys. Alloys with special thermal expansion characteristics. THYSSEN-KRUPP VDM*. www.thyssenkruppvdm.com

[3] VOZÁR L., HOHENAUER W.: *Flash method of measuring the thermal diffusivity, A review*, Proceedings – 16th European Conference on Thermophysical Properties. Imperial College, London, 2002 *(CD)*, pp. 1-25.

[4] TERPIŁOWSKI J.: *A modified flash method for determination of thermal diffusivity in solids*. Archives of Thermodynamics. Vol.24, No. 1, pp.59-80, 2003

[5] CARSLAW H.S., JAEGER I.C.: *Conduction of Heat in Solids*. Oxford University Press, Oxford, 1959, pp. 18-20, 28, 32-33, 97-108.

[6] *Properties of Selected Ferrous Alloying Elements*,. McGraw-Hill/Cindas Data Series on Material Properties. Volume III-1. pp.110-113.

[7] TERPIŁOWSKI J., WORONIAK G.: *Zastosowanie zmodyfikowanej metody impulsowej do badań dyfuzyjności cieplnej inwarowych stopów Fe-Ni*. Termodynamika w nauce i gospodarce. T.2, str.455-460. Oficyna Wydawnicza Politechniki Wrocławskiej, ISBN 978-83-7493-407-7

[8] TERPIŁOWSKI J., PIOTROWSKA-WORONIAK J., WORONIAK G.: *Porównanie klasycznej i zmodyfikowanej metody impulsowej do wyznaczania dyfuzyjności cieplnej metali na przykładzie żelaza elektrolitycznego*. Część II, Ciepłownictwo Ogrzewnictwo Wentylacja, 2007, nr 2, s. 15-19.

Mechanical, thermal and hygric properties of cracked self compacting concrete

Eva Vejmelková[1], Jan Toman[1],Petr Konvalinka[2] and Robert Černý[1]

[1] Department of Materials Engineering and Chemistry, Faculty of Civil Engineering, Czech Technical University in Prague, Thákurova 7, 166 29 Prague 6, Czech Republic

[2] Experimental Center, Faculty of Civil Engineering, Czech Technical University in Prague, Thákurova 7, 166 29 Prague 6, Czech Republic

Abstract**:** *Paper Mechanical, thermal and hygric properties of self compacting concrete with randomly distributed cracks induced by high-temperature exposure are measured and compared with reference self compacting concrete. The most significant differences in the properties of reference and thermally treated specimens are observed for liquid water transport parameters and compressive strength. These parameters are the best indicators of damage induced by thermal decomposition processes in the cement matrix*

Keywords: *self compacting concrete, high temperatures, water transport properties, water vapour transport properties, mechanical properties, cracks*

Introduction

Concrete subjected to high temperatures undergoes chemical reactions which result in decomposition of some of the original compounds of the cement gel. The reliable knowledge of these reactions and their consequences for both the cement matrix and the pore space is of crucial importance for understanding the behavior of concrete at high temperatures. The decomposition processes may lead to major changes in the pore structure; thus they can have significant influence on all the principal material properties. Besides the mechanical parameters, the hydric and thermal properties belong to those which are most remarkably affected.

In this paper, effect of high temperatures on two types of self compacting concrete is studied. The specimens are heated to 600 °C with the heating rate of 10 °C/min, then left at the final temperature for two hours and finally slowly cooled. After completing the loading procedure, their mechanical, hydric and thermal properties are measured and compared with the data obtained for reference specimens, which did not undergo any thermal load.

Materials

In the production of SCC mixtures, laboratory prepared Portland cement obtained by grinding Portland industrial clinker and gypsum dihydrate (in the amount of 5 % by mass) to the specific surface area of 318.8 m^2/kg was used. Limestone (SCC-1) and fly ash (SCC-2) were applied as microfillers in the preparation of the two studied mixtures.

Concrete mixtures were prepared according to Okamura and Ozawa's [1]recommendations. On the basis of data included in the literature and our own experience the voluminous ratio of coarse aggregate and sand was chosen. The composition of concrete mixtures is given in Table 1.

Table 1 Composition of the studied SCC

Component	Unit	SCC-1	SCC-2
cement	kg/m^3	379	394
water	kg/m^3	177	155
limestone	kg/m^3	253	-
fly ash	kg/m^3	-	263
superplasticizer	% by mass	2.4	2.0
sand 0/2	kg/m^3	746	746
aggregate 2/16	kg/m^3	746	746
w/c	-	0.46	0.39

Experimental Methods

Compressive strength

The measurement of compressive strength was done using the electromechanical testing device MTS Alliance RT 30.

Basic physical parameters

As fundamental physical material characteristics, bulk density ρ_b [kgm^{-3}], open porosity ψ [Vol.-%] and matrix density ρ_m [kg m^{-3}] were determined. They were obtained using the gravimetric method and the water vacuum saturation method [2].

Water vapor transport properties

The wet cup method and dry cup method were employed in the measurements of water vapor transport parameters [2]. The water vapor diffusion coefficient D [m^2 s^{-1}] and water vapor diffusion resistance factor μ [-] were measured.

Water transport properties

The water sorptivity A [kg m^{-2} s$^{-1/2}$] and apparent moisture diffusivity κ [m^2 s^{-1}] were measured using a water suction experiment [3].

Sorption isotherms

The water adsorption and desorption isotherms were determined using the desiccator method [2].

Thermal properties

Thermal conductivity λ [W m^{-1} K^{-1}], and specific heat capacity c [J kg^{-1} K^{-1}], were measured using the commercial device ISOMET 2104 (Applied Precision, Ltd.). ISOMET 2104 is a multifunctional instrument for measuring thermal conductivity, thermal diffusivity, and volumetric specific heat capacity.

Experimental results and discussion

Compressive strength

Table 2 presents compressive strength of the materials SCC-1 and SCC-2 with and without cracks. In unloaded case achieved SCC-1 higher value of compressive strength by about 25%. After thermal loading the compressive strength decreased by about 50% for both studied materials. Although the differences between the unloaded and thermally loaded specimens were rather distinctive, it was a very good result for a concrete without fiber reinforcement. As both concrete mixtures were produced using Portland cement, the main reason for the observed differences was apparently the decomposition of portlandite which occurs at 460-480°C.

Table 2: Compressive strength of SCC after 28 days [MPa]

Type of mixture	Without cracks	With cracks
SCC-1	54.2	24.8
SCC-2	43.2	21.2

1.2. Basic physical parameters

The results of basic parameter measurements are presented in Table 3. The SCC-1 mixture exhibited higher bulk density than SCC-2 by approximately 100 kg/m^3.The bulk density and matrix density of cement mixtures with cracks were similar to those without cracks, the differences being within a 5% margin. The open porosity of SCC-2 increased after heating by only 4%. For SCC-1 the increase was 32%. This could mean that SCC-2 had better thermal stability.

Table 3: Basic material parameters of SCC after 28 days

Type of mixture	Without cracks			With cracks		
	ϱ_b	ρ_m	ψ	ϱ_b	ρ_m	ψ
	[kgm^{-3}]	[kgm^{-3}]	[%]	[kgm^{-3}]	[kgm^{-3}]	[%]
SCC-1	2260	2540	11.0	2240	2622	14.6
SCC-2	2160	2490	13.3	2140	2488	13.9

Water vapor transport properties

The results of measurement of water vapor transport parameters of the studied SCC are presented in Table 4. Apparently, the effect of thermal treatment was not very distinctive for both materials. The differences were caused by measurement errors rather than by the thermal decomposition processes in the materials.

Table 4: Water vapor transport properties of SCC after 28 days

Type of mixture	Without cracks			
	D [10^{-6} m^{2}s^{-1}]		μ [-]	
	97-50% RH	50-5% RH	97-50% RH	50-5% RH
SCC-1	2.13	1.18	10.8	19.6
SCC-2	3.58	1.18	6.5	19.6
	With cracks			
	D [10^{-6} m^{2}s^{-1}]		μ [-]	
	97-50% RH	50-5% RH	97-50% RH	50-5% RH
SCC-1	2.58	0.94	9.0	24.4
SCC-2	1.99	0.86	11.6	26.9

Water transport properties

The results of measurement of water transport parameters of the studied materials are presented in Table 5. In the reference state, the water sorptivity *A* of SCC-1 was about 30% higher than for SCC-2. These results did not agree well with the measurements of total open porosity (Table 3). The most probable reason was the different pore distribution of both materials, with SCC-1 having more pores in the μm range. After heating the difference in *A* between both materials almost vanished as for SCC-1 it increased 3 times but for SCC-2 more than 5 times. The effect of cracks acting as preferential paths for water transport was the main reason for these findings. The differences in apparent moisture diffusivity practically copied those in water sorptivity.

Table 5: Water transport properties of SCC after 28 days

Type of mixture	Without cracks		With cracks	
	A [kg m^{-2}s$^{-1/2}$]	κ_{app} [m^{2}s^{-1}]	A [kg m^{-2}s$^{-1/2}$]	κ_{app} [m^{2}s^{-1}]
SCC-1	0.0086	6.0E-09	0.0243	2.8E-08
SCC-2	0.0052	1.5E-09	0.0298	4.6E-08

1.3. Sorption isotherms

Figures 1, 2 show the measured adsorption (lower curves) and desorption (upper curves) isotherms. In the range of lower relative humidity, the differences in adsorption isotherms were for the reference and thermally treated specimens relatively low; the pre-heated specimens had slightly lower water vapor adsorption capacity. This was an expected behavior as the specific surface of thermally affected cementitious materials decreased due to the increase of the amount of pores with higher radii.

However, for higher relative humidity than 70-80% the water vapor adsorption capacity of thermally treated specimens dramatically increased. This finding can be explained by the reaction of capillary condensed water in the pores with the quicklime remaining in the pre-heated specimens after decomposition of portlandite. Thus, the increase in measured water adsorption capacity was rather due to the irreversible than reversible water vapor adsorption as it was also confirmed by the shape of desorption isotherms where substantial amount of water irreversibly bound in the cement matrix was perceptible.

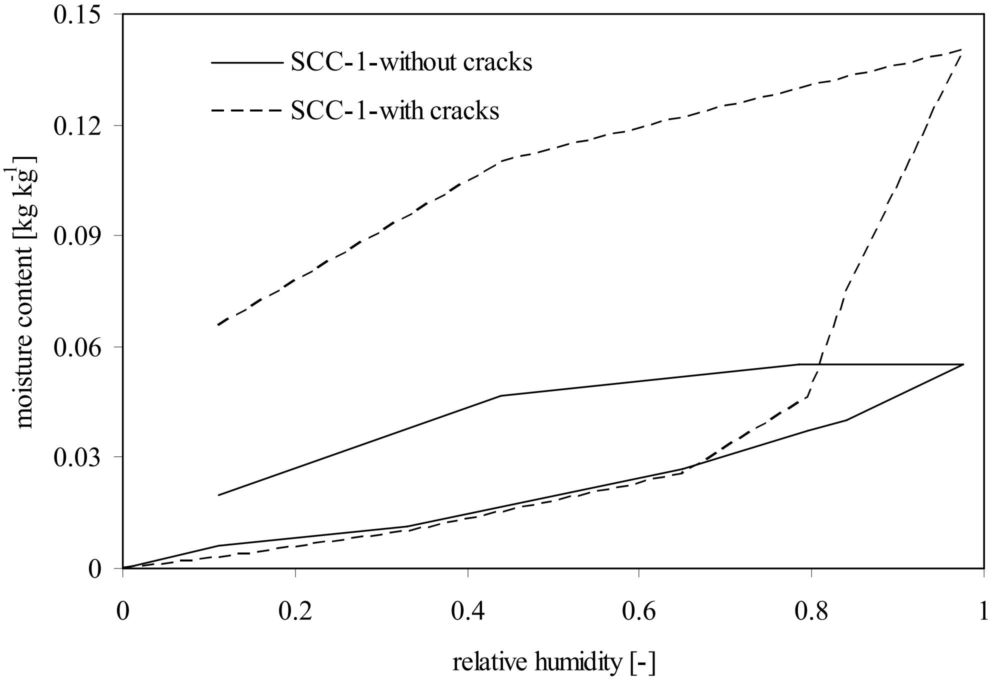

Figure 1: Sorption isotherms of SCC-1 after 28 days

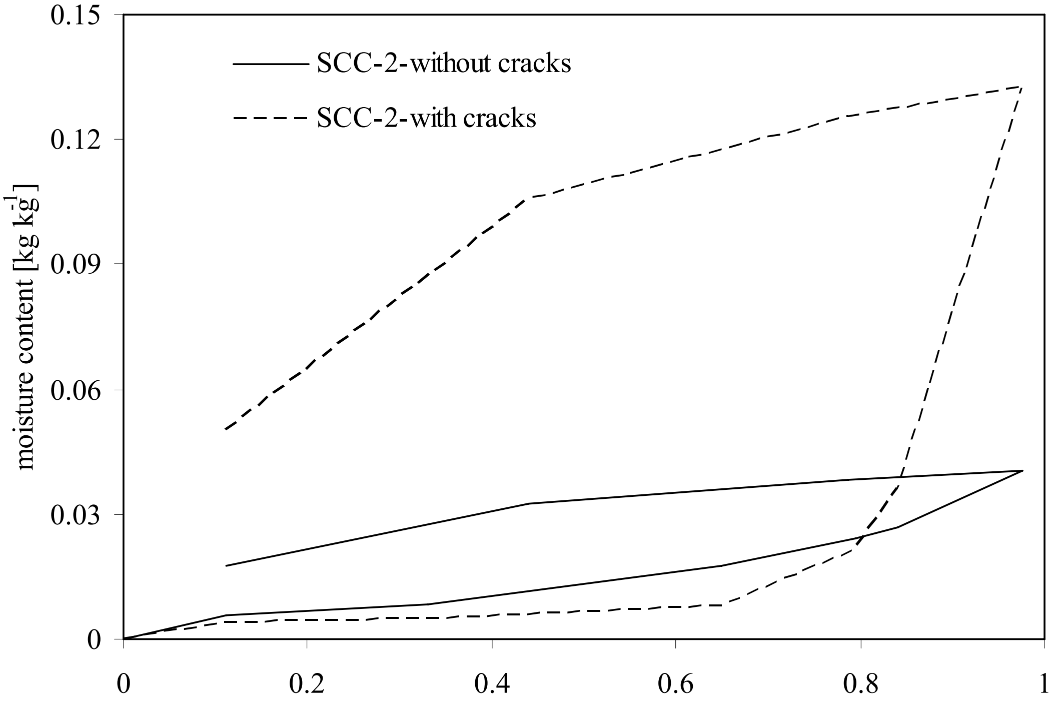

Figure 2: Sorption isotherms of SCC-2 after 28 days

Thermal properties

The thermal parameters data in Table 6 show that the material SCC-1 had systematically higher values of thermal conductivity than SCC-2 in the whole range of moisture content. This was a consequence of its lower porosity (Table 3), i.e. the difference in the significance of the low thermal conductivity of air in the cement matrix-air system.. After heating, the thermal conductivity of both materials in dry state decreased by about 20-25%; clearly due to the increase of porosity (Table 3). The thermal conductivity in fully water saturated state was affected by the presence of water in the most significant way so that - as compared to the dry state - it increased by 20-30% in the reference state and almost two times for the thermally treated specimens.

The specific heat capacity was affected by the measurement uncertainty rather than by any other factors. However, the main trend was apparent for both materials, the increase of specific heat capacity with increasing water content as a consequence of the high specific heat capacity of water.

Table 6: Thermal properties of SCC after 28 days

Type of mixture	**Without cracks**			**With cracks**		
	u	λ	c	u	λ	c
	[kgkg^{-1}]	[Wm^{-1}K^{-1}]	[Jkg^{-1}K^{-1}]	[kgkg^{-1}]	[Wm^{-1}K^{-1}]	[Jkg^{-1}K^{-1}]
SCC-1	0.000	3.50	814	0.000	2.62	744
SCC-1	0.034	3.72	863	0.052	3.23	756
SCC-1	0.044	3.84	800	0.063	4.63	977
SCC-2	0.000	2.60	819	0.000	2.08	810
SCC-2	0.028	2.79	864	0.048	2.99	817
SCC-2	0.037	3.17	933	0.058	4.29	1028

Conclusions

The experimental work performed in this paper has shown that the effect of heating to 600°C was distinctive for both analyzed SCC. However, the extent of changes was different for different material parameters. The most significant differences in the properties of reference and thermally treated specimens were observed for liquid water transport parameters and compressive strength. These parameters were the best indicators of damage induced by thermal decomposition processes in the cement matrix. The thermal conductivity in dry state was changed by high-temperature exposure in a distinct way but the results obtained for partially and fully water saturated specimens were not so indicative. The differences in water vapor diffusion properties and specific heat capacity were not unambiguous. The results obtained for water vapor adsorption capacity were affected by the combination of reversible and irreversible bonding of water vapor in thermally exposed specimens.

Acknowledgement

This research has been supported by the Ministry of Education, Youth and Sports of Czech Republic, under grant No MEB 050811.

References

[1] OKAMURA H., OZAWA K. Mix Design for Self-Compacting Concrete. Concrete Library of JSCE, No. 25, June 1995.

[2] ROELS, S., CARMELIET, J., HENS, H., ADAN, O., BROCKEN, H., ČERNÝ, R., PAVLÍK, Z., HALL, C., KUMARAN, K., PEL, L,, PLAGGE, R., Interlaboratory Comparison of Hygric Properties of Porous Building Materials. Journal of Thermal Envelope and Building Science 27 (2004) 307-325.

[3] KUMARAN, M.K., Moisture Diffusivity of Building Materials from Water Absorption Measurements.IEA Annex 24 Report T3-CA-94/01, Ottawa 1994.

Identification of Some Thermophysical and Boundry Parameters of Black Foamglas by an Inverse Method

Janusz Zmywaczyk, Monika Wielgosz, Piotr Koniorczyk, Marcin Gapski

Military University of Technology, Faculty of Mechatronics, Kaliskiego 2, 00-908
Warsaw, Poland

E-mail: Janusz.Zmywaczyk@wat.edu.pl

Abstract: *In this paper the temperature-dependent thermal conductivity* λ *and the volumetric heat capacity (*ρcp*) as well as the heat transfer coefficients hi of the cylindrical sample made of black foamglas with a medium density* $\rho = 132$ *kg m-3 were estimated simultaneously using an inverse method. The experimental setup consisted of a thin-layer Kapton heater put symmetrically into the sample which was divided into four parts. Temperature histories were recorded in the sample using the K-type thermocouples. The temperature histories located in the sample on both sides of the thin-layer heater were used to determine the heat partition generated by the heater and the temperature responses at some locations of the outer faces of the sample were input data for an inverse procedure of the parameter estimation. The results of parameter estimation obtained by an inverse method and the measured ones by using of commercial apparatus ISOMET 2104 with surface probe revealed that the values of the thermal conductivity of the sample were consistent with one another but there were some discrepancies with respect to values of the volumetric heat capacity.*

Keywords: *inverse method, thermophysical parameters, Foamglas.*

1. Introduction

Knowledge of temperature characteristics of thermophysical parameters such as the thermal conductivity $\lambda(T)$, the specific heat $c_p(T)$ and the thermal diffusivity $a(T)$ of solids is essential to perfom calculations of temperature fields in a variety of engineering applications. The thermal conductivity decides about material's fitness for use under stady-state conditions and the thermal diffusivity of a material decides about its usage under non-stationary conditions, especially where big thermal loads impact on the working material. An increasing of accuracy in determining or identifying with high reliability the temperaturature characteristics of the thermophysical parameters of materials is still an open problem. On the one hand each of the thermophysical parameters can be measured experimentally with high accuacy using a specialized commercial apparatus which is usually very expensive, but on the other hand such thermophysical parameters can be identified simultaneously but less accurately (more uncertainty of results) by transient methods or by inverse methods using considerably much more simpler and cheaper setups. Transient methods used to estimate of thermophysical parameters of solids can be divided with respect to the shape of a thermal input function into two main groups, namely the pulse transient method [1] and the transient step-heating method [2]. For practical applications of the transient methods a heat transfer in a medium is limited to heat conduction with constant thermophysical coefficients and the medium is regarded as a semi-infinite one (ideal model). If the finite geometric dimensions of the specimen are taken into considerations in the model then a more complicated form of analytical solution of the boundary-value problem is obtained and more sophisticated fitting procedure with respect to the transient temperature response of the system should be applied. A brief review of progress in development of new models for pulse transient method was given by Boháč et al in [1]. The Authors' demonstrated in [1] that one point evaluation procedure that uses an ideal heat conduction model to estimate the thermophysical properties of an investigated material gives reliable results only when optimized specimen geometry is used. The problem of optimized geometry of the specimen can be neglected when the transient hot-ball method, being intensively developed by Kubičár et al. [3] for typical sizes of specimens, is used. In this method the sensor (thermistor) with a small geometric dimensions is submerged in the medium (specimen) and acts as a pulse heat generator and the temperature sensor, simultaneously. The thermal conductivity of the specimen is determined just after reaching the steady-state regime of heat transfer in it. Due to the steady-state conditions are to be met for realization of the hot-ball method hence this method is limited to determining the thermal conductivity of a medium. The above mentioned restrictions are excluded to some extent the inverse methods. Zmywaczyk in [4] showed that by optimizing the experimental conditions with respect to the number of temperature sensors, their displacement in the specimen, selection of the heating and the total measuring times, it was possible to estimate simultaneously using the inverse method the temperature-dependent thermal conductivity in axial and radial directions, the volumetric heat capacity and Biot numbers. In this paper the Authors' paid particular attention to the development of research methodics using the inverse method with respect to identification of the thermal conductivity and the specific heat of an insulating material made of black foamglas with its medium density of 132 kg/m^3.

2. Problem formulation and its solution

2.1 The Direct Problem

It is considered a problem of a transient heat conduction in an orthotropic medium. The following simplifying assumptions were accepted

1. Geometry of the medium is 2D axially-symmetric;
2. Medium is homogenous and orthotropic (there are thermal conductivities λr and λz in the radial and axial directions, respectively);
3. Thermophysical and boundary parameters (λ, ρcp, hi) are locally constant;
4. Heat is generated for time tg which is shorter than the final time tf of measurement;
5. The radius Rg of the heater is smaller than the radius R of the sample;
6. Initially at time t = 0 there is a homogenous temperature distribution T0 in the sample;
7. The ambient temperature T∞ is constant and is equal to the initial temperature T0;
8. The boundary conditions are of the second and the third kinds with different heat transfer coefficients h and hR

Physical model of the direct problem is illustrated in Figure 1. This 2D axially-symmetric boundary-value problem was adopted from [2] for the heating regime but for the cooling regime of the sample ($t_g < t \le t_f$) the solution of the problem was proposed.

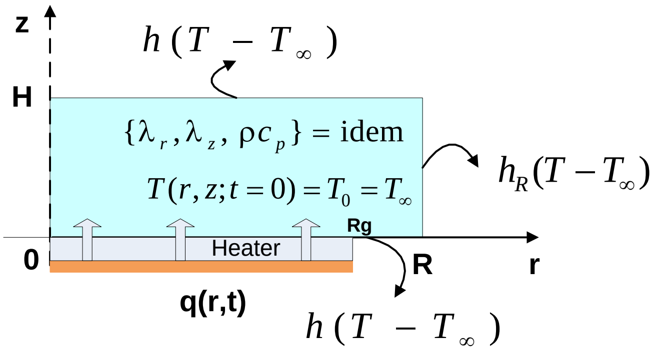

***Figure 1**: Physical model*

In the direct problem the seeking parameters which can be presented as a vector u of the components $[\lambda_r, \lambda_z, \rho c_p, h_R, h]^T$ are assumed to be know. After introducing the temperature excess ϑ defined as

$$\vartheta(r,z;t) = T(r,z;t) - T_0 \tag{1}$$

mathematical formulation of the problem can be expressed as follows:

The energy conservation equation:

$$r\rho c_p \frac{\partial \vartheta}{\partial t} = \frac{\partial}{\partial r}\left(r \cdot \lambda_r \frac{\partial \vartheta}{\partial r} \right) + \frac{\partial}{\partial z}\left(r \cdot \lambda_z \frac{\partial \vartheta}{\partial z} \right), (r,z,t) \in (0,R) \times (0,H) \times (0,t_f] \tag{2a}$$

with initial condition at time t = 0

$$\vartheta(r,z,0) = 0, \ \ (r,z) \in [0,R] \times [0,H] \tag{2b}$$

and with boundary conditions

$$\lambda_z \frac{\partial \vartheta}{\partial z}\Big|_{z=0} = q(r,t) + h \cdot \vartheta, \ \ (r,t) \in [0,R] \times (0,t_f] \quad \text{at} \ \ z = 0 \tag{2c}$$

$$-\lambda_z \frac{\partial \vartheta}{\partial z}\Big|_{z=H} = h \cdot \vartheta, \quad \text{at} \ \ z = H \tag{2d}$$

$$-\lambda_r \frac{\partial \vartheta}{\partial z}\Big|_{r=R} = h_R \cdot \vartheta \quad \text{at} \ \ r = R \tag{2e}$$

$$\lim_{r \to 0}\left(\lambda_r \frac{\partial \vartheta}{\partial r} \right) = 0 \tag{2f}$$

The heat flux q(r, t) in Eq. (2c) is expressed by Eq. (2g) as

$$q(r,t)=\begin{cases} q_0 \ \text{dla} \ (r,t)\in[0,R_g]\times(0,t_g] \\ 0 \ \text{dla} \ (r,t)\in(R_g,R]\times(0,t_g] \\ 0 \ \text{dla} \ (r,t)\in[0,R]\times(t_g,t_f] \end{cases} \tag{2g}$$

where t_g – is the time of heating and $(t_f - t_g)$ – is the time of cooling.

After introducing the Biot numbers in radial direction

$$\mathrm{Bi_R} = \frac{h_R \cdot R}{\lambda_r} \tag{3a}$$

and in axial direction

$$\mathrm{Bi} = \frac{h \cdot H}{\lambda_z} \tag{3b}$$

as well as after introducing the orthotropic thermal diffusivities

$$a_r = \frac{\lambda_r}{\rho c_p}, \quad a_z = \frac{\lambda_z}{\rho c_p} \tag{3c}$$

then the analytical solution of the direct problem (2) has a form [2, 4]

$$\vartheta(r,z;t)=\begin{cases} \dfrac{4q_0}{\rho c_p H}\displaystyle\sum_{m=1}^{\infty}\sum_{n=1}^{\infty} A_m(r/R)B_n(z/H)\left(\frac{1-\exp(-\gamma_{m,n}t)}{\gamma_{m,n}}\right), & \text{for} \ t\le t_g \\ \\ \dfrac{4q_0}{\rho c_p H}\displaystyle\sum_{m=1}^{\infty}\sum_{n=1}^{\infty} A_m(r/R)B_n(z/H)\left(\frac{\exp(-\gamma_{m,n}(t-t_g))-\exp(-\gamma_{m,n}t)}{\gamma_{m,n}}\right) \\ & \text{for} \ t_g \le t \le t_f \end{cases} \tag{4a}$$

where

$$A_m(r/R)=\frac{\omega_m \dfrac{R_g}{R} J_1\left(\omega_m \dfrac{R_g}{R}\right) J_0\left(\omega_m \dfrac{r}{R}\right)}{J_0^2(\omega_m)\left(\omega_m^2+\mathrm{Bi}_R^2\right)} \tag{4b}$$

$$B_n(z/H)=b_n\left[\cos\left(\lambda_n \frac{z}{H}\right)+\frac{\mathrm{Bi}}{\lambda_n}\sin\left(\lambda_n \frac{z}{H}\right)\right] \tag{4c}$$

$$b_n=\frac{\lambda_n^2}{\lambda_n^2+\mathrm{Bi}^2+2\mathrm{Bi}}, \quad \gamma_{m,n}=\left(\frac{\omega_m^2 \cdot a_r}{R^2}+\frac{\lambda_n^2 \cdot a_z}{H^2}\right) \tag{4d}$$

Here a set of eigenvalues $\{\omega_m\}$ and $\{\lambda_n\}$ is a solution of the following characteristic equation

$$\omega_m: \ \omega J_1(\omega)-\mathrm{Bi}_R J_0(\omega)=0 \tag{5a}$$

$$\lambda_n : \ \left(\lambda^2 - \mathrm{Bi}\right)\sin(\lambda) - 2\lambda\,\mathrm{Bi}\cos(\lambda) = 0 \tag{5b}$$

An exemplary solution of the direct problem (2) for typical data used in experiment at some locations P^i marked on supplementary chart as P^1, P^2 and P^3 is shown in Figure 2.

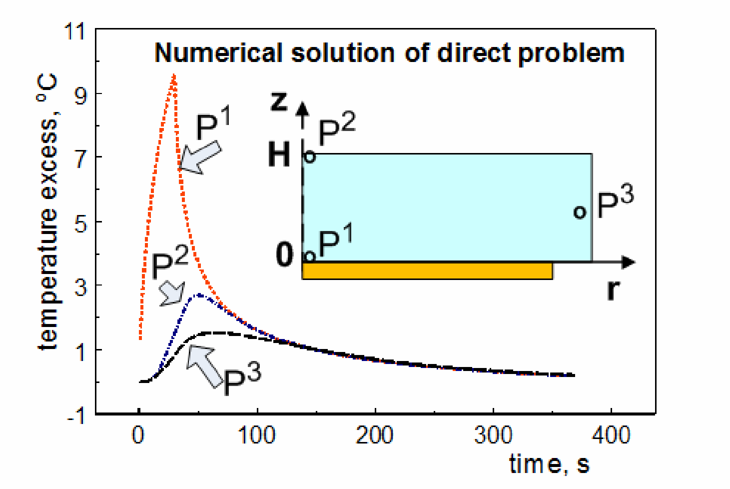

Figure 2: Modelling solution of the direct problem at some locations Pi

2.2 The Inverse Problem

There are known from experiment the temperature histories $Y_i(t_n)$ at locations P^i, where $\{i=1,2,..,\mathrm{NMP}\}$, $\{n = 1,2,...,Nt\}$, NMP - stands for the number of measurement points, Nt – is the total number of time readings taken at discrete moments $t_n = n{\cdot}\Delta t$. The measured experimentally temperature histories $Y_i(t_n)$ resulting from the thermal response of the system on a given by the user thermal input function. In the inverse problem a set of the unknown parameters $\{a_r, a_z, \rho c_p, \mathrm{Bi}_R, \mathrm{Bi}\}$ is to be determined by minimizing the mean square functional J

$$J(\mathbf{u}^{\mathrm{T}}) = \sum_{i=1}^{\mathrm{NMP}}\sum_{n=1}^{Nt}\left[T(P^i, t_n, \mathbf{u}^{\mathrm{T}}) - Y_i(t_n)\right]^2 = \mathbf{e}^{\mathrm{T}}\mathbf{e} \to \min \tag{6}$$

where

$T(P^i, t_n\,;\,\mathbf{u}^{\mathrm{T}})$ is the model temperature being a solution of the direct problem (4), mapping the experimental conditions, at the same locations P^i, and moments t_n for the currently estimated components of the vector $\mathbf{u}$, where $\mathbf{u}^{\mathrm{T}} = [\, a_r, a_z, \rho c_P, \mathrm{Bi}_R, \mathrm{Bi}]$ and vector $\mathbf{e}$ stands for the residual vector with components $\mathbf{e}_i = T(P^i, t_n; \mathbf{u}^{\mathrm{T}}) - Y_i(t_n)$.

The solution of the inverse problems is equivalent to find the minimum of the mean square functional (6). The simplest method is the ordinary least squares (OLS) but when the optimal point is too far away from the exact one then OLS procedure of minimization is unstable and one can not get a solution. In such a case the Levenberg-Marquardt method of minimization the mean square functional J – (6) is recommended. The solution of the inverse method using the Levenberg-Marquardt algorithm is sought iteratively. In the matrix form the vector **u** of the unknown parameters at the iteration (s+1) is given by

$$\mathbf{u}^{(s+1)} = \mathbf{u}^{(s)} + \mathbf{P}_{\mathrm{L-M}}^{(s)} \{\mathbf{X}^{\mathrm{T}}(\mathbf{u}^{(s)})[\mathbf{Y} - \mathbf{T}(\mathbf{u}^{(s)})]\} \tag{7a}$$

where

$$\mathbf{P}_{\mathrm{L-M}}^{(s)} = [\mathbf{X}^{\mathrm{T}}(\mathbf{u}^{(s)})\mathbf{X}(\mathbf{u}^{(s)}) + \mu_s \mathbf{\Omega}^{(s)}]^{-1} \tag{7b}$$

$$\mathbf{\Omega}^{(s)} = \mathrm{diag}[\mathbf{X}^{\mathrm{T}}(\mathbf{u}^{(s)})\mathbf{X}(\mathbf{u}^{(s)})] \quad \text{lub} \quad \mathbf{\Omega}^{(s)} = \mathbf{I} \tag{7c}$$

X – is the matrix of sensitive coefficients with elements

$$\mathbf{X}_i(\mathbf{u}) = [\nabla_{\mathbf{u}} \mathbf{T}_i^{\mathrm{T}}]^{\mathrm{T}} = \begin{bmatrix} \frac{\partial T_i(t_1)}{\partial u_1} & \frac{\partial T_i(t_1)}{\partial u_2} & \cdots & \frac{\partial T_i(t_1)}{\partial u_{\mathrm{NUP}}} \\ \frac{\partial T_i(t_2)}{\partial u_1} & \frac{\partial T_i(t_2)}{\partial u_2} & \cdots & \frac{\partial T_i(t_2)}{\partial u_{\mathrm{NUP}}} \\ \cdots\cdots & \cdots\cdots & \cdots & \cdots\cdots \\ \frac{\partial T_i(t_{Nt})}{\partial u_1} & \frac{\partial T_i(t_{Nt})}{\partial u_2} & \cdots & \frac{\partial T_i(t_{Nt})}{\partial u_{\mathrm{NUP}}} \end{bmatrix}_{\mathrm{P}=\mathrm{P}^i}$$

$$\{i = 1,2,\ldots,\mathrm{NMP}\}, \{j = 1,2,\ldots,\mathrm{NUP}\}, \ \{n = 1,2,\ldots,Nt\} \tag{7d}$$

Here NUP stand for the number of unknown parameters

The sensitivity coefficients with respect to the volumetric heat capacity and the thermal diffusivity are given by

$$X_{(\rho c_p)} = \frac{\partial T}{\partial(\rho c_p)} = -\frac{\vartheta(r,z,t)}{\rho c_p} \tag{8}$$

$$X_{a_r} = \frac{\partial T}{\partial a_r} = \\ = \frac{4q_0}{\rho c_p H} \begin{cases} \sum_{m=1}^{\infty}\sum_{n=1}^{\infty} A_m B_n \frac{\omega_m^2}{R^2 \gamma_{m,n}^2} \left[e^{-\gamma_{m,n} t}(t\gamma_{m,n} + 1) - 1 \right], \ t \le t_g \\ \sum_{m=1}^{\infty}\sum_{n=1}^{\infty} A_m B_n \frac{\omega_m^2}{R^2 \gamma_{m,n}^2} \left[e^{-\gamma_{m,n} t}(t\gamma_{m,n} + 1) - e^{-\gamma_{m,n}(t-t_g)}((t - t_g)\gamma_{m,n} + 1) \right] \\ \qquad t_g \le t \le t_f \end{cases} \tag{9}$$

$$X_{a_z} = \frac{\partial T}{\partial a_z} = \\ = \frac{4q_0}{\rho c_p H} \begin{cases} \sum_{m=1}^{\infty}\sum_{n=1}^{\infty} A_m B_n \frac{\lambda_n^2}{H^2 \gamma_{m,n}^2} \left[e^{-\gamma_{m,n} t}(t\gamma_{m,n} + 1) - 1 \right], \ t \le t_g \\ \sum_{m=1}^{\infty}\sum_{n=1}^{\infty} A_m B_n \frac{\lambda_n^2}{R^2 \gamma_{m,n}^2} \left[e^{-\gamma_{m,n} t}(t\gamma_{m,n} + 1) - e^{-\gamma_{m,n}(t-t_g)}((t - t_g)\gamma_{m,n} + 1) \right] \\ \qquad t_g \le t \le t_f \end{cases} \tag{10}$$

To calculate the sensitivity coefficients with respect to the Biot number the following general formula should be used:

For the spatial part of the solution

$$\frac{\partial A_m}{\partial \mathrm{Bi}_R}=\frac{\partial F}{\partial \mathrm{Bi}_R}+\frac{\partial F}{\partial \omega_m}\frac{\partial \omega_m}{\partial \mathrm{Bi}_R} \tag{11a}$$

$$\frac{\partial B_n}{\partial \mathrm{Bi}}=\frac{\partial F}{\partial \mathrm{Bi}}+\frac{\partial F}{\partial \lambda_n}\frac{\partial \lambda_n}{\partial \mathrm{Bi}} \tag{11b}$$

where

$$\frac{\partial F}{\partial \mathrm{Bi}_R}=-2\frac{\mathrm{Bi}_R\omega_m\frac{R_g}{R}J_1\left(\omega_m\frac{R_g}{R}\right)J_0\left(\omega_m\frac{r}{R}\right)}{J_0^2(\omega_m)\left(\omega_m^2+\mathrm{Bi}_R^2\right)^2} \tag{11c}$$

$$\frac{\partial \omega_m}{\partial \mathrm{Bi}_R}=\left\{\omega J_1(\omega)-\mathrm{Bi}_R J_0(\omega)=0\right\}=\frac{J_0(\omega_m)}{\omega_m J_0(\omega_m)+\mathrm{Bi}_R J_1(\omega_m)} \tag{11d}$$

$$\begin{aligned}\frac{\partial F}{\partial \omega_m}=\frac{\omega_m\frac{R_g}{R}}{J_0^3(\omega_m)\left(\omega_m^2+Bi_R^2\right)^2}&\Bigg\{2\left(\omega_m^2+Bi_R^2\right)J_0\left(\omega_m\frac{r}{R}\right)J_0\left(\omega_m\frac{R_g}{R}\right)J_1(\omega_m)+\\ &J_0(\omega_m)\Bigg[\left(\omega_m^2+Bi_R^2\right)\frac{R_g}{R}J_0\left(\omega_m\frac{R_g}{R}\right)J_0\left(\omega_m\frac{r}{R}\right)-J_1\left(\omega_m\frac{R_g}{R}\right)\Bigg(\omega_m J_0\left(\omega_m\frac{R_g}{R}\right)+\\ &\left(\omega_m^2+Bi_R^2\right)J_1\left(\omega_m\frac{r}{R}\right)\cdot\frac{r}{R}\Bigg)\ \Bigg]\Bigg\}\end{aligned} \tag{11e}$$

$$\frac{\partial B_n}{\partial \mathrm{Bi}}=\frac{\lambda_n\left[\left(\lambda_n^2-\mathrm{Bi}^2\right)\sin\left(\lambda_n\frac{z}{H}\right)-2\lambda_n(1+\mathrm{Bi})\cos\left(\lambda_n\frac{z}{H}\right)\right]}{\left(\lambda_n^2+\mathrm{Bi}^2+2\mathrm{Bi}\right)} \tag{11f}$$

$$\frac{\partial \lambda_n}{\partial \mathrm{Bi}}=\frac{2(\mathrm{Bi}\sin\lambda_n+\lambda_n\cos\lambda_n)}{\left(\lambda_n^2-\mathrm{Bi}^2-2\mathrm{Bi}\right)\cos\lambda_n+2\lambda_n(1+\mathrm{Bi})\sin\lambda_n} \tag{11g}$$

$$\begin{aligned}\frac{\partial B_n}{\partial \lambda_\mathrm{n}}=\frac{\mathrm{Bi}\cdot\lambda_n}{\left(\lambda_n^2+\mathrm{Bi}^2+2\mathrm{Bi}\right)^2}&\Bigg\{\left[(2+\mathrm{Bi})(2H+\mathrm{Bi}\cdot z)\right]\cos\left(\lambda_n\frac{z}{H}\right)+\\ &\left[H\cdot\mathrm{Bi}^2(2+\mathrm{Bi})-\mathrm{Bi}\cdot(H+(2+\mathrm{Bi})\cdot z)\cdot\lambda_n^2-\lambda_n^4\cdot z\right]\sin\left(\lambda_n\frac{z}{H}\right)\Bigg\}\end{aligned} \tag{11h}$$

For the temporal part of the solution

$$
\begin{aligned}
\frac{\partial}{\partial \omega_m}\left(\frac{1-\exp(-\gamma_{m,n}t)}{\gamma_{m,n}}\right) &= \frac{2\,\omega_m a_r \exp(-\gamma_{m,n}t)}{H^2R^4\gamma_{m,n}^2}\bigl\{\omega_m^2\, H^2 a_r\, t + \\
&\quad R^2\Bigl[\bigl(1-\exp(\gamma_{m,n}\, t)\bigr)H^2 + \lambda_n^2\, a_z\, t\ \Bigr]\bigr\}, \quad 0 < t \le t_g
\end{aligned}
\tag{12a}
$$

$$
\begin{aligned}
\frac{\partial}{\partial \lambda_n}\left(\frac{1-\exp(-\gamma_{m,n}t)}{\gamma_{m,n}}\right) &= \frac{2\,\lambda_n a_z \exp(-\gamma_{m,n}t)}{R^2H^4\gamma_{m,n}^2}\bigl\{\omega_m^2\, H^2 a_r\, t + \\
&\quad R^2\Bigl[\bigl(1-\exp(\gamma_{m,n}\, t)\bigr)H^2 + \lambda_n^2\, a_z\, t\ \Bigr]\bigr\}, \quad 0 < t \le t_g
\end{aligned}
\tag{12b}
$$

$$
\begin{aligned}
\frac{\partial}{\partial \omega_m}\left(\frac{\exp(-\gamma_{m,n}(t-t_g))-\exp(-\gamma_{m,n}t)}{\gamma_{m,n}}\right) &= \frac{2\omega_m\, a_r \exp(-\gamma_{m,n}t)}{H^2R^4\gamma_{m,n}^2}\bigl\{H^2\bigl(R^2+\omega_m^2 a_r\, t\bigr) + \\
&\lambda_n^2 R^2 a_z\, t - \exp(\gamma_{m,n}\, t_g)\bigl[H^2R^2 + \bigl(\omega_m^2 H^2 a_r + \lambda_n^2 R^2 a_z\bigr)\bigl(t-t_g\bigr)\ \bigr]\bigr\} \\
&t_g \le t \le t_f
\end{aligned}
\tag{12c}
$$

$$
\begin{aligned}
\frac{\partial}{\partial \lambda_n}\left(\frac{\exp(-\gamma_{m,n}(t-t_g))-\exp(-\gamma_{m,n}t)}{\gamma_{m,n}}\right) &= \frac{2\lambda_n\, a_z \exp(-\gamma_{m,n}t)}{H^4R^2\gamma_{m,n}^2}\bigl\{H^2\bigl(R^2+\omega_m^2 a_r\, t\bigr) + \\
&\lambda_n^2 R^2 a_z\, t - \exp(\gamma_{m,n}\, t_g)\bigl[H^2R^2 + \bigl(\omega_m^2 H^2 a_r + \lambda_n^2 R^2 a_z\bigr)\bigl(t-t_g\bigr)\ \bigr]\bigr\} \\
&t_g \le t \le t_f
\end{aligned}
\tag{12d}
$$

So the sensitivity coefficients with respect to the Biot numbers can be expressed as

$$
X_{\mathrm{Bi}_R} = \frac{\partial T}{\partial \mathrm{Bi}_R} = \frac{4q_0}{\rho c_p H}
\begin{cases}
\displaystyle\sum_{m=1}^{\infty}\sum_{n=1}^{\infty} B_n \left\{\left[\frac{\partial A_m}{\partial \mathrm{Bi}_R} + \frac{\partial A_m}{\partial \omega_\mathrm{m}}\frac{\partial \omega_\mathrm{m}}{\partial \mathrm{Bi}_R}\right]\left[\frac{1-\exp(-\gamma_{m,n}t}{\gamma_{m,n}}\right] + \right. \\
\displaystyle\left. A_m \frac{\partial}{\partial \omega_\mathrm{m}}\left[\frac{1-\exp(-\gamma_{m,n}t}{\gamma_{m,n}}\right]\frac{\partial \omega_\mathrm{m}}{\partial \mathrm{Bi}_R}\right\}, & t \le t_g \\
\displaystyle\sum_{m=1}^{\infty}\sum_{n=1}^{\infty} B_n \left\{\left[\frac{\partial A_m}{\partial \mathrm{Bi}_R} + \frac{\partial A_m}{\partial \omega_\mathrm{m}}\frac{\partial \omega_\mathrm{m}}{\partial \mathrm{Bi}_R}\right][\ldots] + A_m \frac{\partial}{\partial \omega_\mathrm{m}}[\ldots]\frac{\partial \omega_\mathrm{m}}{\partial \mathrm{Bi}_R}\right\}
\end{cases}
$$

$$
t_g \le t \le t_f \tag{13a}
$$

Where the expression in brackets [...] is given by

$$
[\ldots] = \left(\frac{\exp(-\gamma_{m,n}(t-t_g))-\exp(-\gamma_{m,n}t)}{\gamma_{m,n}}\right) \tag{13b}
$$

By analogy to Eq. 13 one is able to obtain the sensitivity coefficients with respect to the Biot number Bi using the above relationships (11-12).

Where to locate the measurement points ?

Analyzing the spatial dependence of the sensitivity coefficients in Figure 3 one can observe that optimal location of the measurement points should be taken in an axial-symmetry of the specimen when the thermal diffusivity and the volumetric heat capacity are to be identified because the sensitivity coefficients are of the greatest magnitude in these areas. Similarly, the measurement points should be located on the specimen's border when the Biot numbers are estimated.

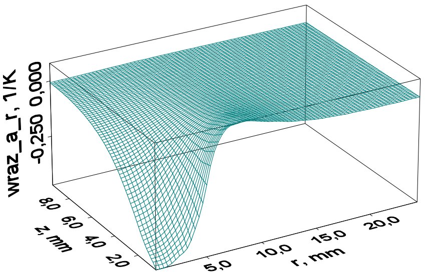

Figure 3a: Normalized sensitivity (X_ar)

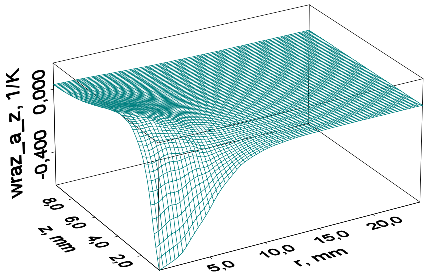

Figure 3b: Normalized sensitivity (X_az)

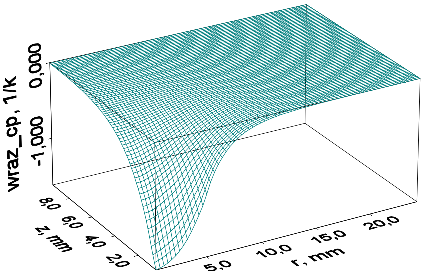

Figure 3c: Normalized sensitivity (X_ρcp)

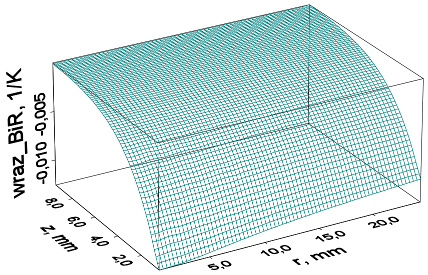

Figure 3d: Normalized sensitivity (X_BiR)

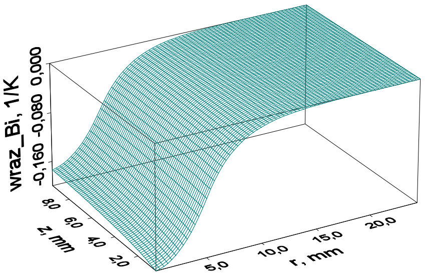

Figure 3e: Normalized sensitivity (X_Bi)

3. Experiment and results

The sketch of experimental setup is shown in Figure 4. The experimental setup consisted of a thin-layer Kapton heater put symmetrically into the sample which was divided into four parts. Temperature histories were recorded in the sample using the K-type thermocouples made by OMEGA. The temperature histories at points located in the sample on both sides of the thin-layer heater were used to determine the heat partition generated by the heater and the temperature responses at some locations of the outer faces of the sample were input data for an inverse procedure of the parameter estimation.

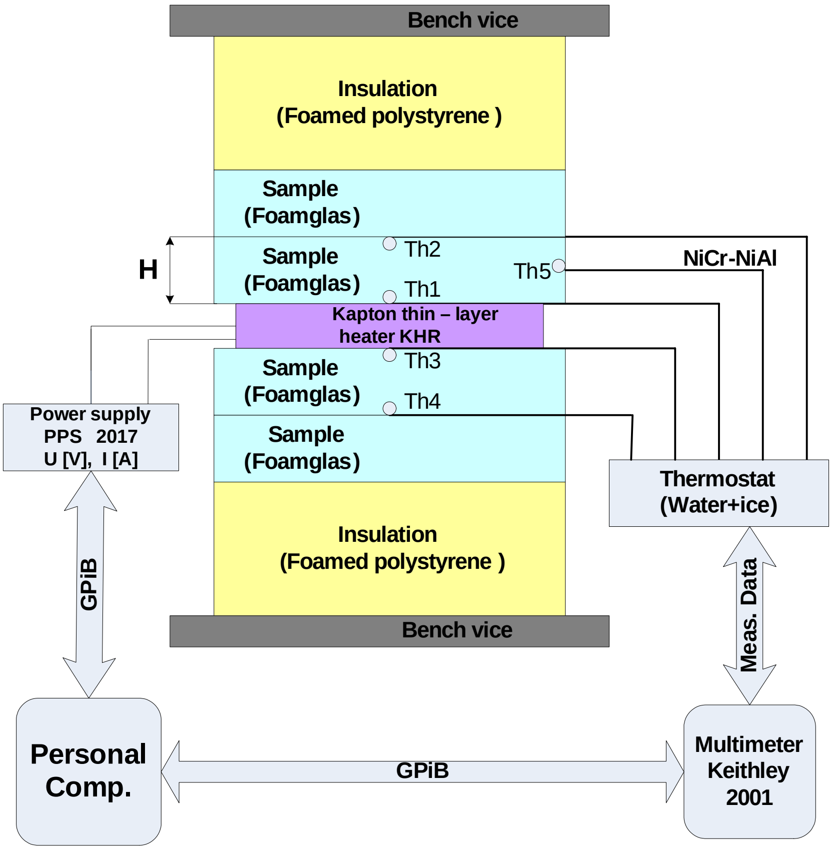

Figure 4: Sketch of measurement setup (scale not preserved)

The thin-layer Kapton heater of thickness 0.15 mm and of effective diameter ($2R_g = 29.09$ mm) was program driven due to stabilized power supply PPS 2017 made by AMREL firm (USA). To obtain temperature characteristics of the estimated thermal conductivity $\lambda_z(T)$, and the specific heat $c_p(T)$ of the investigated material the specimen was kept in the oven with a set and controlled temperature. The view of some parts of the experimental setup is shown in Figure 5.

Figure 5: View of experimental setup

The accepted data for inverse calculations are given in Table 1.

Table 1: Accepted data for inverse calculation

Sample (Black foamglas with density ρ = 132.0 kg/m3)	
Diameter	- 2R = 40.0 mm
Hight	- H =10.0 mm
Thin-layer Kapton heater	
Effective diameter	- 2Rg = 29.09 mm
Thickness	- d = 0.15 mm
Input function of the power supply (Amrel - PPS 2017 series)	
Voltage	U = 5.0 V
Current	I = 0.065 A
Time of heating	tg = 30 s
Initial time (without heating)	t0 = 30 s
Final time	tf = 400 s

$$q(r,t)=\begin{cases}\dfrac{1}{2}\dfrac{U\cdot I}{\pi R_g^2}=244.67\ \text{W/m}^2, & \text{for}\ \ 0<t\le t_g\\ 0, & \text{for}\ \ t_g<t\le t_f\end{cases}$$

Starting values: $c_p^{(0)}=1000,\ \ \lambda_r^{(0)}=\lambda_z^{(0)}=0.1,\ h_R^{(0)}=4,\ h^{(0)}=1$ Locations of the K-type thermocouple hot junctions (r, z in [mm])

P1(0.5, 0.5), P1(0.5, 9.5), P3(19.5, 5.0)

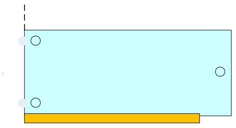

The results of inverse calculations are shown in Figures 6-8. Performing the inverse calculations the following procedure was carried out:

STEP 1: Assumption of the initial data for performing calculations (Table 1 – starting values) and calculation of the initial components of the unknown vector **u** for the zero-iteration as

$$\mathbf{u}^{(0)}=[a_r^{(0)}=\frac{\lambda_r^{(0)}}{\rho c_p^{(0)}},\quad a_z^{(0)}=\frac{\lambda_z^{(0)}}{\rho c_p^{(0)}},\ \rho c_p^{(0)},\quad Bi_R^{(0)}=\frac{h_R^{(0)}R}{\lambda_r^{(0)}},\ \ Bi=\frac{h^{(0)}H}{\lambda_z^{(0)}}]^{\mathrm{T}}$$

STEP 2: Applying the solution (6) of the direct problem together with the iterative Levenberg-Marquardt procedure (7) so as to minimize the functional *J* – (6) (*s*-iteration)

STEP 3: Analysis of the obtained results.

During the inverse calculations the obtained results were acceptable only for the thermal conductivity in the axial direction λ_z, the specific heat c_p and heat transfer coefficients h_i. The estimated thermal conductivity in the radial direction λ_r fulfilled the role of a degree of freedom in the simulated temperature respond and allowed better tuning of the measured and the simulated temperatures during a minimization process of the mean square functional.

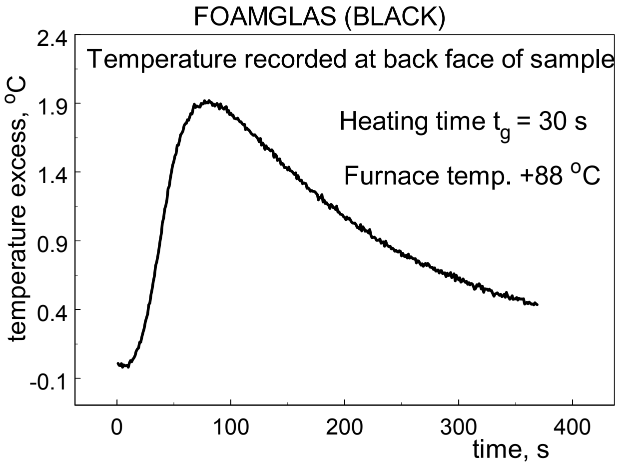

Figure 6a: Experimentally obtained temperature history at the back face of the investigated sample

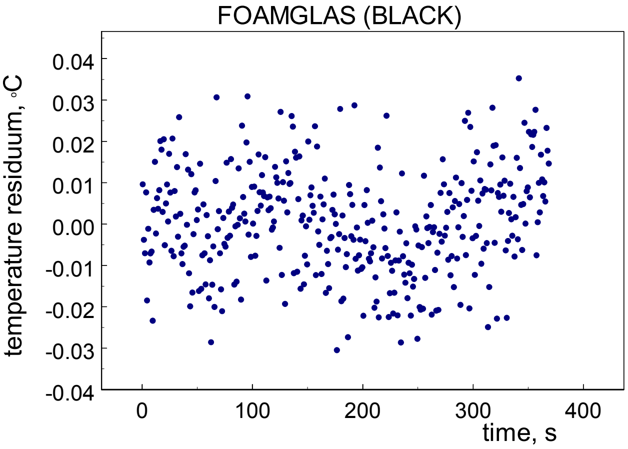

Figure 6b: History of temperature residuals at the back face of the investigated sample

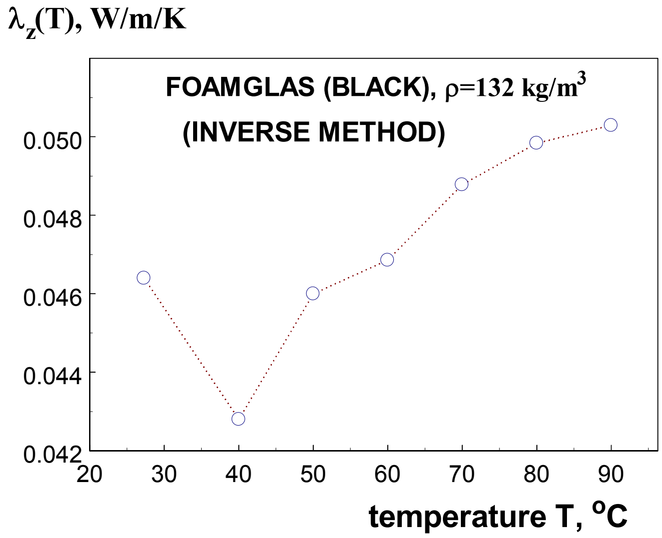

Figure 7: Thermal conductivity vs. temperature for black foamglas obtained using inverse method

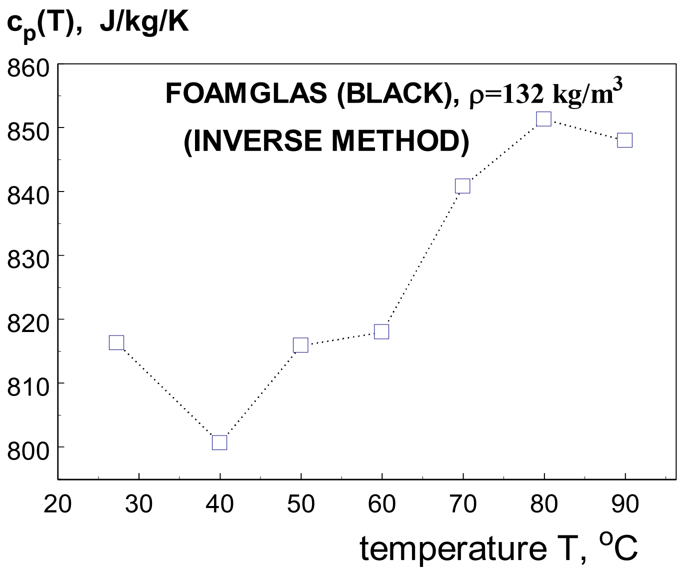

Figure 8: Specific heat vs. temperature for black foamglas obtained using inverse method

$h_R = 0.3\,\mathrm{W/m^2/K}$, $h = 5.1\ \mathrm{W/m^2/K}$ - estimated values of the heat transfer coefficients

Complementary investigations

To verify the results the thermal conductivity and the specific heat of identification of the black foamglas the following complementary investigations were carried out:

Specific heat c_p – DSC (Perkin-Elmer Pyris 1)

Thermal conductivity λ – Plate Apparatus (FOX 314)

(c_p+λ) - ISOMET 2104 with surface probe

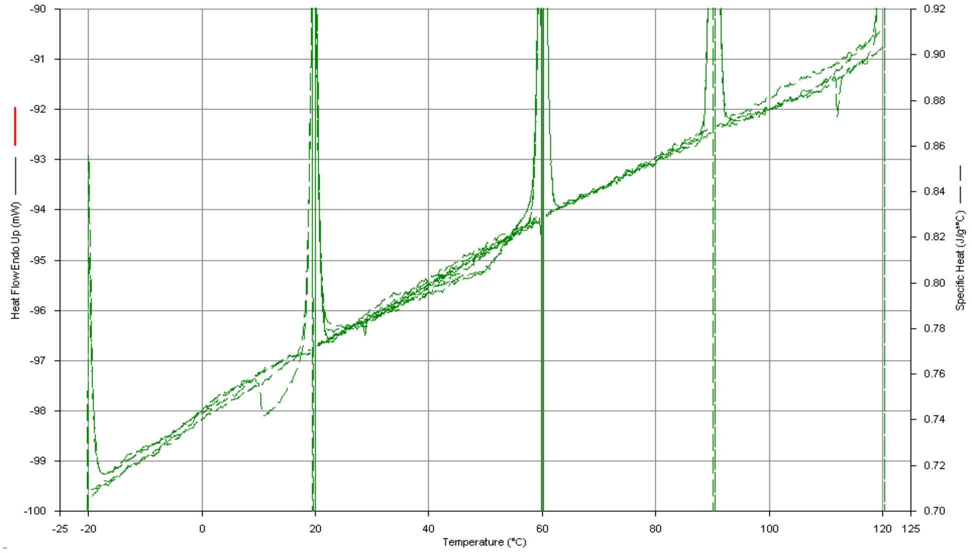

Figure 9: Results of DSC measurement of specific heat for black Foamglas from -20 oC to +120 oC

The results of experimental investigations of the specific heat for the black foamglas using DSC (Perkin-Elmer Pyris 1) micro-calorimeter are presented in Figure 9 [5]. The investigated temperature range was involved from -20 °C to +120 °C and was divided into 4 temperature subintervals where the results were obtained in each of them, separately. The specific heat temperature dependence for the black foamglas is almost of linear shape. The values of the specific heat belong to the interval from 720 J/kg/K at *T* = -20 °C up to 920 J/kg/K at *T* = +120 °C.

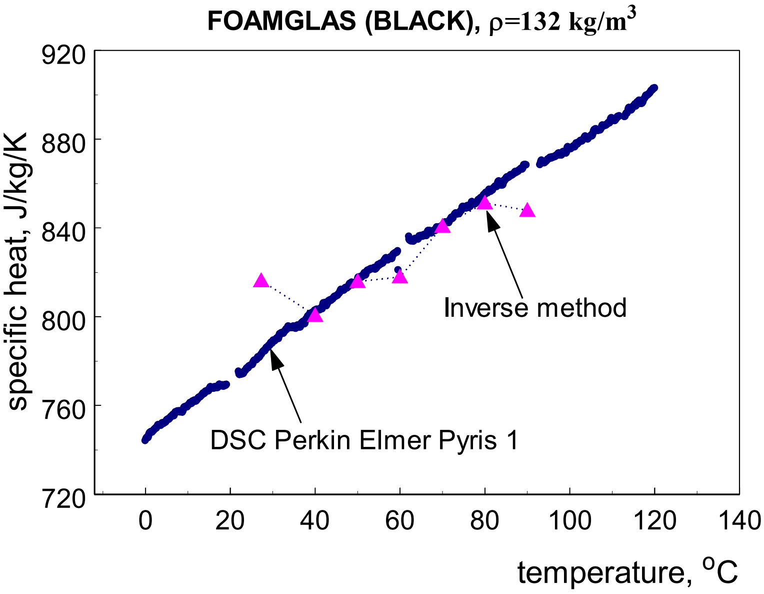

Figure 10: Specific heat of black foamglas - DSC vs. inverse method

The results of the specific heat investigations obtained using the inverse method and using the DSC technique are shown in Figure 10 and are quite consistent with each other.

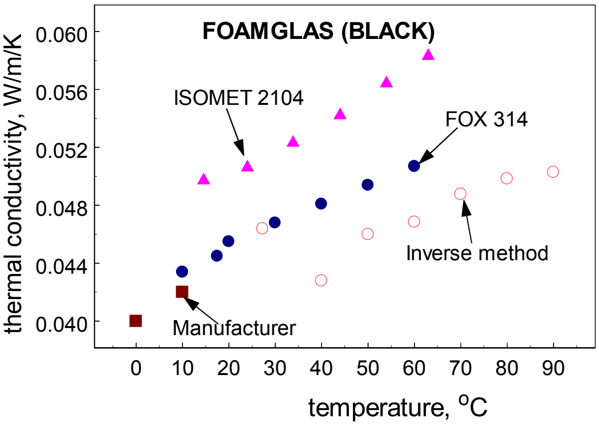

Figure 11: Thermal conductivity of black foamglas – FOX 314, ISOMET 2104, Manufacturer vs. inverse method

The results of the thermal conductivity investigations obtained using the inverse method and using commercial Plate apparatus FOX 314 and ISOMET 2104 with the surface probe API 210411 (thermal conductivity range from 0.030 to 0.30 W/m/K) are shown in Figure 11. One can observe that the results of the thermal conductivity obtained using inverse method are a little underestimated and obtained using ISOMET 2104 are a little overestimated with respect to the ones obtained using the Plate apparatus FOX 314. Generally speaking the results obtained by various techniques can be regarded as consistent to each other.

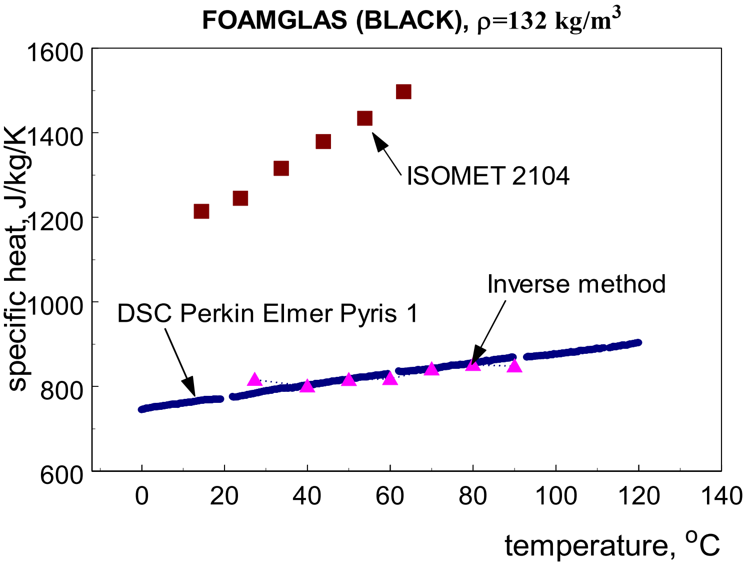

Figure 12: Specific heat of black foamglas – DSC Perkin Elmer Pyris 1, ISOMET 2104 vs. inverse method

However, the situation is changing when the results of the specific heat obtained by various techniques are compared to each other (see Figure 12). This time the values of the specific heat obtained using the ISOMET 2104 with surface probe API 210411 were too distant from the exact ones (DSC-technique).

Because the results of the specific heat investigations obtained using ISOMET 2104 were too distant from the DSC results we have decided to repeat them. This time the sample made of black foamglas was put into the oven (see Figure 5) and the surface probe and the sample were covered by a cotton wool in order to ensure the same experimental conditions as they were when the inverse method was used. At each temperature set in the oven the sample was kept so long in the oven to reach the temperature equilibrium of the system consisted of the sample - surface probe - oven. It lasted from 9 to 11 hours for each temperature set in the oven. The re-measurement results obtained by using the ISOMET 2104 are given in Table 2.

Table 2: The re-measurement results of the black foamglas obtained by using the ISOMET 2104

Temperature	**Thermal conductivity**	**Specific heat**	**Thermal diffusivity**
[°C]	**[W/m/K]**	**[J/kg/K]**	**[m2/s]**
30	**0.0470**	**1015.2**	**0.352·10-6**
40	**0.0493**	**1068.2**	**0.350·10-6**
50	**0.0558**	**1386.4**	**0.305·10-6**

The re-measurement results given in Table 2 revealed that the values of the thermal conductivity of the black foamglas were similar to those presented in Figure 11 but the values of the specific heat results exceeded the manufacturer's acceptable range of accuracy (more than 15%)

4. Conclusions

The results of the thermal conductivity and the specific heat identification by the inverse method within temperature range (30 – 90) ^{0}C are consistent with results obtained by using DSC and Plate Apparatus.

Average absolute discrepancy with respect to **c_p** (DSC) equals was equal to **10.9**% and with respect to λ (Plate Apparatus) **6.6**%.

The discrepancy results of the specific heat measurements by using ISOMET 2104 vs. DSC method were bigger than **15**% what was inconsistent with the manufacturer declaration of the accepted accuracy.

Acknowledgements

This research work was supported by the Military University of Technology internal grants GW-HB No. 703 and 701.

The Authors would like to express their gratitude to Professor A. Panas for delivering the research results of the specific heat of black foamglas using DSC Perkin-Elmer Pyris 1 micro-calorimeter.

References

[1] V. BOHÁČ, P. DIEŠKA, Ľ. KUBIČÁR, The progress in development of new models for pulse transient method, Proc. THERMOPHYSICS 2007, 24-33, October 11 – 12, 2007, Kočovce chateau, Slovakia.

[2] L. VOZÁR, T. ŠRÁMKOVÁ, Simultaneous measurement of axial and radial thermal diffusivities of anisotropic media by the radial-heat flow step-heating method, High Temp – High Press, 29 (1997), 183-190.

[3] Ľ. KUBIČÁR, V. VRETENÁR, V. ŠTOFANIK, V. Boháč, Hot-ball method for measuring thermal conductivity, Int. J. Thermophysics, DOI 10.1007/s10765-008-0544-4.

[4] J. ZMYWACZYK, Estimation of thermophysical parameters of solids by using of selected methods of optimization, DSc Thesis, Warszawa WAT 2006 (in Polish).

[5] A. PANAS, J. ZMYWACZYK, DSC Specific heat measurements of a Black Foamglas thermal insula tor, Private Communication 2009.

Numerical Validation of the Scanning Mode Procedure of Thermal Diffusivity Investigation Applying Temperature Oscillation

Andrzej J. Panas[1], **Mirosław Nowakowski**[2]

[1] Military University of Technology, Kaliskiego 2 Street, 00-908 Warsaw, Poland,
email: Andrzej.Panas@wat,edu,pl

[2] Air Force Institute of Technology, Księcia Bolesława 6 Street, 01-494 Warsaw, Poland,
email: Miroslaw.Nowakowski@itwl.pl

Abstract: *Problem of the thermal diffusivity investigation applying a modified Ångström thermal wave technique has been analysed. The analysis has been focussed on effect of the linear changes of the oscillation offset temperature on the results in view of the temperature dependent thermal properties of the investigated material. In the course of the numerical analysis effects of violation of model boundary conditions has also been investigated. Convective heat loses and the temperature sensor positioning have been considered at the most. A numerical model for calculations has been developed applying Comsol software that is a finite element method modelling package. Effectiveness of the proposed procedure for the thermal property investigation even in case of strongly temperature dependent properties has been finally proved. The outcomes of the numerical experiments contributed to optimisation of real experiments.*

Keywords: *thermal diffusivity, temperature oscillation / periodic heating / temperature wave techniques, thermal properties*

1. Introduction

Periodic heating or so-called temperature (thermal) wave technique is probably the oldest one transient technique for investigation of thermophysical properties. Initially described by Ångström in 1861 in application for investigation of metal bars and extended within limits of certain heat conduction problem models [5, 13] it for many years was treated as a standard thermophysical property measurement method. However, in view of a growing application of mostly laser flash and pulse techniques (comp. e.g [8], [10]) in the last decades it has been limited in its general application. Nowadays we can observe renaissance of the temperature oscillation technique [3] especially in specific domains like microscopic measurements, studies of thermal processes [6], [7] and investigation of special materials [2]. It is due to some advantages of the thermal wave method like possibility of application for different materials [12], the unique potential for a cross-validation by comparing results obtained from the amplitude and phase analyses [1, 14], possibility of multiproperty investigation, spectral Fourier studies and thermal cycling measurements [14], possibility of application with different instrumentation [5, 7].

One of the Ångström's method modifications was developed for investigation of bad thermal conductors studied as plates [1, 2]. The thermal diffusivity of such specimens is obtained in cross-planar direction applying solutions of a certain heat conduction problem with a temperature oscillation applied over a certain steady mean temperature [4]. In the present paper an extension of the above-described modification is analysed. This extension is based of introducing a scanning mode measurement procedure that means that measurements are performed with oscillations applied to a linearly changed mean temperature. In addition selected effects of temperature dependent thermal property are examined. The analysis is conducted by numerical modelling (comp. e.g. [7]). In addition effects of simplification of the basic formulae for the thermal diffusivity calculation are investigated. The results complement a digest information provided in [1] and [2] and create a background for numerical study.

2. Theory

Assuming that the temperature oscillation – temperature wave amplitude – is relatively small

$$\theta_{\max} \ll T_m \tag{1}$$

where T_m is a certain mean temperature and that the oscillation frequency is high enough to confine several oscillations within a single ramp of a steady or a linearly changed temperature

$$f = \frac{1}{\tau_\Omega} \gg \frac{1}{\tau_{i+1} - \tau_i} \ , \quad i = 0, 1, \ldots, k \tag{2}$$

where T_m is the mean temperature, τ - time and τ_Ω - oscillation period, the problem can be treated as superposition of two linear problems of heat conduction. The first one refers to the temperature oscillations, the second to linear temperature changes in time. Both of them are referred as regular heating regime of the third and second type respectively.

If we focus our attention on the temperature differences with respect to the initial temperature T_0

$$\theta(x,\tau) = T(x,\tau) - T_0 \tag{3}$$

which is uniform over the object i.e. a plate of thickness l at $\tau = 0$ than mathematical formulation of component problems is given by the governing equation

$$\frac{\partial \theta}{\partial \tau} = a \frac{\partial^2 \theta}{\partial x^2} \ , \quad a = \frac{\lambda}{\rho\, c_p} \tag{4}$$

where a is the thermal diffusivity (TD), λ - thermal conductivity, ρ - density and c_p – specific heat, with initial condition

$$\theta(x,0) = 0 \qquad \text{at} \quad 0 \le x \le l \qquad \text{for} \quad \tau = 0 \tag{5}$$

and two sets of boundary conditions (BC), one for harmonic temperature changes problem

$$\frac{\partial \theta(0,\tau)}{\partial x} = 0 \, , \qquad \theta(l,\tau) = A_0 \sin(2\pi f \tau - \varepsilon) \tag{6}$$

and one for the linear temperature changes problem

$$\frac{\partial \theta(0,\tau)}{\partial x} = 0 \, , \qquad -\lambda \frac{\partial \theta(l,\tau)}{\partial \tau} = T_0 + b\tau \tag{7}$$

The solution of the BC (6) problem is [4]

$$\theta(x,\tau) = A_0 \;\; \psi \sin(2\pi f\tau - \varphi - \varepsilon) +$$
$$+ 4\pi\, k \sum_{n=0}^{\infty} \frac{(-1)^n (2n+1)\left[4l^2 \omega \cos\varepsilon + a(2n+1)^2 n^2 \sin\varepsilon\right]}{16 l^4 \omega^2 + a^2 \pi^4 (2n+1)^4} \exp\left[-\frac{a(2n+1)\pi^2}{4l^2}\tau\right] \cos\frac{(2n+1)\pi\, x}{2l} \tag{8}$$

where (compare Fig. 1)

$$\psi(x) \;=\; \sqrt{\frac{\cosh\, 2kx + \cos 2kx}{\cosh 2kl + \cos 2kl}} \tag{9}$$

$$\varphi(x) \;=\; \arg\left[\frac{\cosh\, kx(1+i)}{\cosh\, kl(1+i)}\right] \tag{10}$$

$$k \;=\; \sqrt{\frac{\pi\; f}{a}} = \sqrt{\frac{\pi}{a\;\tau_\Omega}} \tag{11}$$

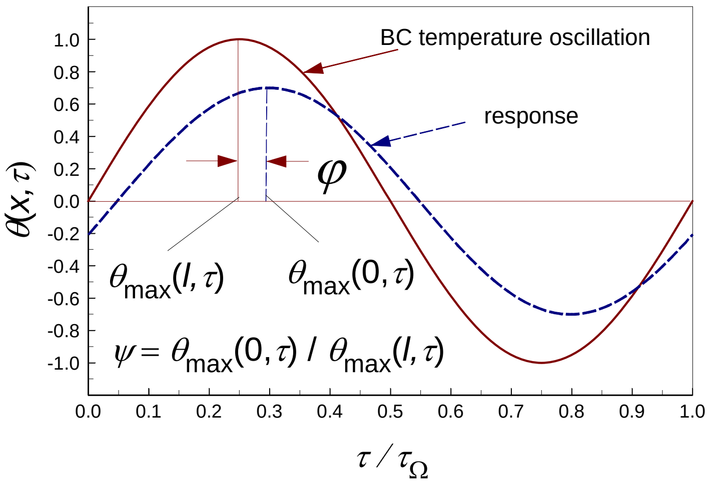

Figure 1: Illustration of components and parameters of a solution given by Eqs. (8)-(12)

while for the BC given by Eq. (7) we get [4]

$$\theta(x,\tau) = b\tau + \frac{b(x^2 - l^2)}{2a} +$$
$$+16\frac{bl^2}{a\pi^3}\sum_{n=0}^{\infty}\frac{(-1)^n}{(2n+1)^3}\exp\left[-a\frac{(2n+1)^2\pi^2}{4l^2}\tau\right]\cos\frac{(2n+1)\pi x}{2l} \tag{12}$$

The series terms with exponential components in (8) and (12) represents transients that die away as $\tau \to \infty$. The representative solution of the steady oscillations over a linearly changed temperature expressed by superposition of the two appropriate components is:

$$\theta(x,\tau) \cong A_0 \;\; \psi \sin(2\pi f\tau - \varphi - \varepsilon) + b\tau + \frac{b(x^2 - l^2)}{2a} \tag{13}$$

3. Thermal diffusivity identification procedure

Knowing the parameter *l* and having obtained the amplitude of temperature response attenuation ψ and the response phase lag φ one can evaluate the parameter *k* (or directly the thermal diffusivity *a*) by solving nonlinear equations (9) and (10). These two solutions should be the same that creates opportunity for the procedure validation. However, because the solutions can not be expressed in direct form, and because numerical routine in the case of Eq. (10) is badly conditioned, the approximations of (9) and (10) are usually applied [1], [2]. These approximations lead to the following formulae

$$a \cong \frac{\pi f l^2}{\ln^2 \frac{2}{\psi}} = \frac{\pi l^2}{\tau_\Omega \ln^2 \frac{2}{\psi}} \tag{14}$$

$$a \cong \frac{\pi f l^2}{\varphi^2} = \frac{\pi l^2}{\tau_\Omega \varphi^2} \tag{15}$$

the first of which is the "amplitude" one and the second is the "phase" second respectively. It is interesting that Eq. (15) has the same form as that obtained for the semi-infinite solid problem solution (comp. e.g. [4], [13] and [15]). However these solutions are valid only under the assumption that the frequency *f* is high enough i.e.:

$$k\, l > K_{\min} \qquad \Leftrightarrow \qquad f > \frac{K_{\min}^2}{\pi} \frac{a}{l^2} \tag{16}$$

According to [2] the recommended value for $K_{\min}$ is 1.5. However, for $K_{\min}$ strictly equal to 1.5 the "amplitude" thermal diffusivity identified when applying Eq. (14) is overestimated by about 6.5 %. From our own analyses it follows that for

$$K_{\min,\,2\%} = 1.87 \;\; ; \qquad K_{\min,\,1\,\%} = 2.25 \tag{17}$$

the approximation accuracy regarding the identified *a* value for both procedures is equal to 2 % and 1 % respectively.

The thermal diffusivity may be determined from amplitude and phase measurements. In both cases the two temperature signals are analysed: one corresponding to the thermally treated surface $\theta(\tau, x=l)$ and the response signal $\theta(\tau, x=0)$. The two signals are approximated by function

$$f(\tau) = A \sin(2\pi f \tau + B) + C + D\tau \;\; ; \qquad n\,\tau_\Omega \le \tau < (n+1)\tau_\Omega \;, \quad n = 0,1,\ldots,N \tag{18}$$

and parameters ψ and φ are calculated from

$$\psi = \frac{A_{x=0,\,calc.}}{A_{x=l,calc.}} \;\; , \quad \varphi = B_{x=l,calc.} - B_{x=o,calc.} \tag{19}$$

where the subscript *calc* stands for the approximation results. As it follows from (18) the procedure is applied within time intervals corresponding to every consecutive oscillation period. Next, the thermal diffusivity can be derived:

- directly from simplified relations (14) and (15);
- after correction of the Eqs (14) and (15) results applying differential formulae;

- from numeric solution of Eqs (9) and (10) expressed as [12]

$$\frac{\sqrt{2}}{\psi} = \sqrt{\cosh\left(2\sqrt{\frac{\pi\, f}{a}}\cdot l\right) + \cos\left(2\sqrt{\frac{\pi\, f}{a}}\cdot l\right)} \tag{20}$$

$$\mathrm{tg}\,\varphi = \ \mathrm{tg}\left(\sqrt{\frac{\pi\, f}{a}}\cdot l\right)\tanh\left(\sqrt{\frac{\pi\, f}{a}}\cdot l\right) \tag{21}$$

4. Numerical modelling

Because of a complex character of the thermal diffusivity identification problem direct analyses of any negative effects on the measurement procedure are difficult. For this reason a procedure of numerical validation of the measurement procedure has been started. The numerical analysis discussed here is of a preliminary character. It refers to real experiments performed while the temperature oscillation procedure has been validated [12]. This is why certain thermophysical parameters have been assumed for the modelled media (Table 1). Despite the fact that the analysis has been focussed mostly on the effect of a scanning mode procedure it was started from consideration of the heat loses and finite specimen lateral dimension on the identification result (Fig. 2). The analysis has been performed applying finite element modelling (FEM) software Comsol. Prior to main calculations all the numerical modelling procedures have been tested and optimal parameter values for the time step, finite element type and dimension etc. have been established. The numerical details have not been discussed here as we will rather focus on the obtained results.

At first effects of convective heat transfer loses and a thermocouple (TC) location on the thermal diffusivity identification have been studied. The calculations have been performed applying thermal properties of the ice-type solid with the temperature oscillation applied to the bottom specimen surface (Fig. 3; z=0 mm) while the upper and the side surfaces have been exposed to convection into the ambient of a certain temperature. Direct effects of the heat loses on the temperature recordings are shown in Fig. 4. Results of the thermal diffusivity identification listed in Table 2 prove that these effects are of a minor importance regarding thermal insulation applied in real experiment [12]. It should be underlined that the expected real value of the heat transfer coefficient is close to 4 $W\cdot m^{-2}\cdot K^{-1}$. The observed effects of TC location are non significant.

Table 1: Thermal properties of the modelled media

Material	**Density**	**Heat capacity**	**Thermal conductivity**
	$kg\cdot m^3$	$J\cdot kg^{-1}\cdot K$	$W\cdot m^{-1}\cdot K^{-1}$
model ice-like solid	925	2200	2
model H_2O (Comsol Script notation)	925+75*flc2hs(T-273,4)+(273-T)	2200+83250*(flc2hs(T-271,2)-flc2hs(T-275,2))+2000*flc2hs(T-273,4)	2.2-1.7*flc1hs(273,10)

Table 2: Effect of the convective heat loses on the thermal dffusivity identification when the average oscillation temperature is equal to 273 K and τ_Ω is equal to 180s (see Fig. 4)

Assumed heat transfer coefficient in W·m^{-2}·K^{-1}	4	16	40
Ambient temperature in K	273		
Amplitude identification relative difference / %	-1.4	-4.5	-12.7
Phase identification relative difference / %	1.2	4.9	12.2
Ambient temperature in K	293		
Amplitude identification relative difference / %	-1.3	-3.2	___
Phase identification relative difference / %	1.3	5.2	___

Figure 2: Specimens on the measuring plate with side and upper thermal insulation removed (photo at the left) and a scheme of some disturbing effects analysed numerically (at the right)

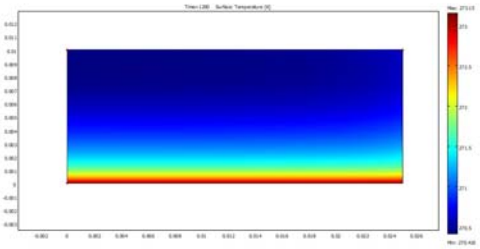

Figure 3: Illustration of a geometry of the analysed model: a 10 mm high 50 mm in diameter disk shape specimen has been modelled in 2-D axial symmetry

Main calculations have been devoted to problems of the linearly changed temperature superimposed to the temperature oscillation (Fig. 5) and to the temperature dependent thermal properties. The results obtained for a medium with a phase change occurring within the range of simulated measurements (comp. Table 1) are shown in Fig. 5. The identified TD values are in agreement with the expected ones. Moreover, the overestimation of the amplitude TD results in the low temperature "solid" region fully agrees with the result of solution of a non-linear problem defined by Eq. (9). The TD relative difference of 6.4 % is just as has been expected for the *kl*=1.55. The results from the linear temperature scan outside the phase change region are more than satisfactory.

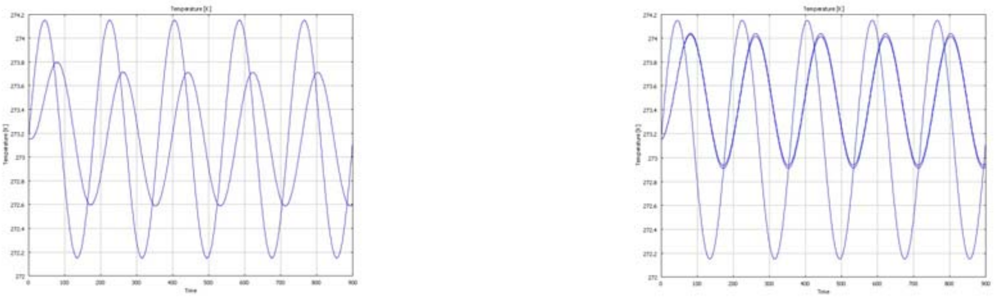

Figure 4: Comparison between numerical simulation results with no upper and side surface heat loses (left hand diagram) and with convective heat loses taken into consideration (right hand diagram)

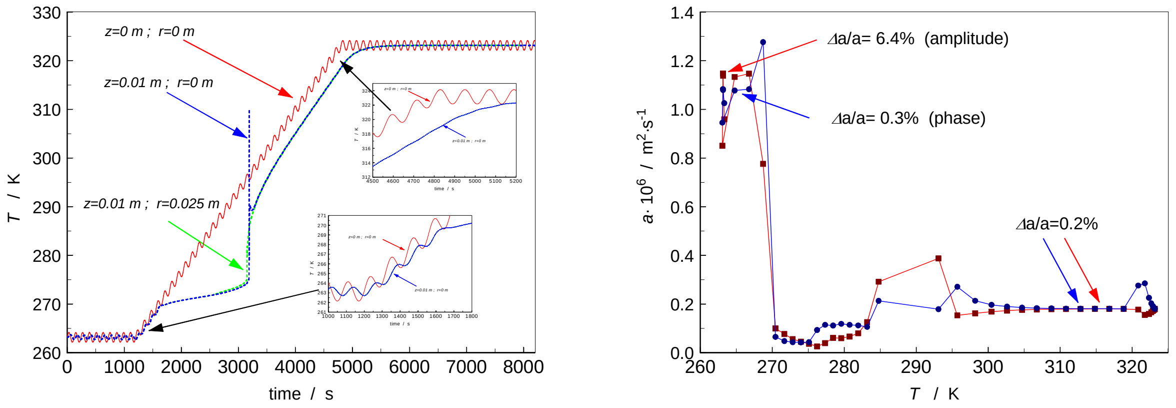

Figure 5: The simulated temperature recordings (left hand diagram) and results of the thermal diffusivity identification (right hand diagram; red line – amplitude calculations according (14), blue – phase calculations according (15))

5. Conclusion

Despite a preliminary character of the presented numerical analysis the results obtained are very promising. The agreement between the assumed model parameters and the identified data for the case when a scanning mode procedure is analysed is better than satisfactory. Moreover, effectiveness of the proposed procedure for the thermal property investigation even in case of strongly temperature dependent properties has been proved. The effects of the heat loses seem to be of a minor significance when the proper thermal insulation for the investigated specimen is applied. The outcomes of the numerical experiments contributed to optimisation of real experiments.

References

[1] BELLING, J.M.; UNSWORTH, J. Modified Ångström's method for measurement of thermal diffusivity of materials with low conductivity. Rev. Sci. Instrum. 1987. 58 (6), p. 997-1002. ISSN 0034-6748

[2] BODZENTA, J.; BURAKA, B.; NOWAK, M.; PYKA, M.; SZAŁAJKO, M.; TANASIEWICZ, M. Measurement of the thermal diffusivity of dental filling materials using modified Angstrom's method. Dental Materials. 2006. Vol. 22, pp. 617–621. ISSN 0 109-5641

[3] BODZENTA J. Thermal wave methods in investigation of thermal properties of solids. Eur. Phys. J. Special Topics. 2008. 154. p. 305-311. ISSN 1951-6355

[4] CARSLAW, H. S.; JAEGER, J. C. Conduction of Heat in Solids, 2nd Edition, Oxford - Clarendon Press, London, 2003, pp. 64-70, 102-105, 105-112, ISBN 0-19-853368-3

[5] de CONINCK, R.; PELETSKY, V.E. Electron Bombardment Modulated Heat Input. In Maglić K. D., Cezairliyan A. and Peletsky V. E., eds.: Compendium of Thermophysical Property Measurement Methods. Plenum Press, New York 1984, pp. 367-428, ISBN 0-306-41424-4

[6] FRIIS-PEDERSEN, H.H.; PEDERSEN, J.H.; HAUSSLER, L.; STORM, B.K. Online measurement of thermal diffusivity during cure of an epoxy composite. Polymer testing. (2006). 25, p. 1059-1068. ISSN 0142-9418

[7] KAPISCHKE, J.; HAPKE, J. Measurement of the effective thermal conductivity of a Mg-MgH2 packed bed with oscillating heating. Experimental Thermal and Fluid Science. 1998. 17, p. 347-355. ISSN 0894-1777

[8] KUBIČAR, L. Pulse Method of measuring Basic Thermophysical Parameters, 1990, Elsevier Sc. Publ. Co., Inc. and Veda Publ. House of the Slovak Academy of Sciences (Thermal Analysis, V. XII, Part E, A Sub-Series of Monographs Ed. by W.W. Wendlandt). ISBN 0-444-98851-3

[9] LYKOV A.V., Tieoria tirploprovodnosti. Vyshaia Schola, Moskva 1967, pp. 274-321, UDK-536.2

[10] MAGLIĆ K. D., Cezairliyan A. and Peletsky V. E., eds. Compendium of Thermophysical Property Measurement Methods. Plenum Press, New York 1984, ISBN 0-306-41424-4

[11] ÖZIŞIK, M.N., Heat Conduction, 2-nd Ed., 1993, John Willey & Sons, Inc. p. 204-208. ISBN 0-471-53256-8

[12] PANAS, A.J.; Tkaczyk, P. Development of a test stand for dynamic investigation of composite shell structure thermal property. (2009), Military University of Technology Report No 992/WAT/2008, Warsaw (in Polish)

[13] PATLE S.D. Analysis and measurement of thermophysical properties by temperature oscillation. PhD Thesis, National Institute of Technology Rourkela, India, 2006

[14] PHYLIPPOV, L.P. Temperature Wave Techniques. In Maglić K. D., Cezairliyan A. and Peletsky V. E., eds.: Compendium of Thermophysical Property Measurement Methods. Plenum Press, New York 1984, pp. 337-365, ISBN 0-306-41424-4

[15] TIKHONOV, A.N.; Samarski, A.A., Equations of mathematical physics. 5th ed. Moskow, Nauka, 1977, pp. 241-250, UDK 517.946 (in Russian)

List of participants

Mgr. Matúš Holúbek
Slovak University of Technology
Faculty of Civil Engineering
Radlinského 11
81368 Bratislava
SLOVAKIA

prom. fyz. Ol'ga Koronthályová, CSc.
Slovak Academy of Sciences
Institute of Construction and Architecture
Dubravska cesta 9
845 03 Bratislava
SLOVAKIA

Ing. Peter Mihálka
Slovak Academy of Sciences
Institute of Construction and Architecture
Dubravska cesta 9
81368 Bratislava
SLOVAKIA

doc. RNDr. Igor Medveď, Ph.D.
Constantine the Philosopher University
Faculty of Natural Sciences
Tr. A. Hlinku 1
94974 Nitra
SLOVAKIA

Ing. Peter Matiašovský, CSc.
Slovak Academy of Sciences
Institute of Construction and Architecture
Dubravska cesta 9
81368 Brastislava
SLOVAKIA

Ing. Jan Kočí
Czech Technical University
Faculty of Civil Engineering
Thákurova 7
166 29 Praha 6
CZECH REPUBLIC

prof. RNDr. Ivan Baník, Ph.D.
Slovak University of Technology
Faculty of Civil Engineering
Radlinského 11
81368 Bratislava
SLOVAKIA

MSc Laura Casares
Slovak Academy of Sciences
Institute of Physics
Dubravska cesta 9
84511 Bratislava
SLOVAKIA

Ing. Danica Fidríková
Slovak Academy of Sciences
Institute of Physics
Dúbravská cesta 9
84511 Bratislava
SLOVAKIA

MSc. Carlos Calvo Anibarro
Slovak Academy of Sciences
Institute of Physics
Radlinskeho, 11
81368 Bratislava
SLOVAKIA

prof. Mgr. Jan Toman, DrSc.
Czech Technical University
Faculty of Civil Engineering
Thákurova 7
166 29 Praha
CZECH REPUBLIC

doc. RNDr. Jozefa Lukovičová, Ph.D.
Slovak University of Technology
Faculty of Civil Engineering
Radlinskeho 11
81368 Bratislava
SLOVAKIA

prof. Ing. Robert Černý, Dr.Sc.
Czech Technical University
Faculty of Civil Engineering
Thákurova 7
166 29 Praha
CZECH REPUBLIC

doc. Ing. Juraj Veselský, Ph.D.
Slovak University of Technology
Faculty of Civil Engineering
Radlinského 11
81368 Bratislava
SLOVAKIA

doc. Ing. Jiří Vala, CSc.
Brno University of Technology
Faculty of Civil Engineering
Žižkova 17
602 00 Brno
CZECH REPUBLIC

Ing. Zbyšek Pavlík, Ph.D.
Czech Technical University
Faculty of Civil Engineering
Thákurova 7
166 29 Praha 6
CZECH REPUBLIC

Mgr. Ján Ondruška
Constantine the Philosopher University
Faculty of Natural Sciences
Tr. A. Hlinku 1
94974 Nitra
SLOVAKIA

Assoc. Prof. Piotr Koniorczyk, Ph.D., DSc. Eng.
Military University of Technology
Institute of Aviation Technology
Kaliskiego 2
00-908 Warsaw
POLAND

Mgr. Jana Moravčíková
Constantine the Philosopher University
Faculty of Natural Science
Tr. A. Hlinku 1
949 74 Nitra
SLOVAKIA

RNDr. Anton Trník, Ph.D.
Constantine the Philosopher University
Faculty of Natural Sciences
Tr. A Hlinku 1
949 74 Nitra
SLOVAKIA

Ing. Ludovit Kubicar, DrSc
Slovak Academy of Sciences
Institute of Physics SAS
Dubravska cesta 9
845 11 Bratislava
SLOVAKIA

doc. RNDr. Ing. Stanislav Šťastník, CSc.
Brno University of Technology
Faculty of Civil Engineering
Žižkova 17
602 00 Brno
CZECH REPUBLIC

Assoc. Prof. Janusz Zmywaczyk, Ph.D., DSC. Eng.
Military University of Technology
Institute of Aviation Technology
Kaliskiego 2
00-908 Warsaw
POLAND

Ing. Vlastimil Boháč, CSc.
Slovak Academy of Sciences
Institute of Physics, SAS
Dúbravská cesta 9
845 11 Bratislava 45
SLOVAKIA

Ing. Danica Fidríková
Slovak Academy of Sciences
Institute of Physics
Dúbravská cesta 9
84511 Bratislava
SLOVAKIA

Bc. Lenka Hřebenová
Brno University of Technology
Faculty of Chemistry
Purkyňova 118
612 00 Brno
CZECH REPUBLIC

prof. Henryk Sobczuk, Ph.D.
Lublin University of Technology
Faculty of Environmental Enginering
ul. Nadbystrzycka 40B
20-618 Lublin
POLAND

Eng. Zbigniev Suchorab, Ph.D.
Lublin University of Technologyr...
Faculty of Enviromental Engineering
Nadbystrzycka 40B Str.,
20-618 Lublin
POLAND

Ing. Viliam Vretenár, PhD.
Slovak Academy of Sciences
Institute of Physics
Dúbravská cesta 9
84511 Bratislava
SLOVAKIA

Prof. Ing. Oldřich Zmeškal, CSc.
Brno University of Technology
Faculty of Chemistry
Purkyňova 118
612 00 Brno
CZECH REPUBLIC

Prof. Andrzej Panas, Ph.D., DSc. Eng.
Military University of Technology
Faculty of Mechatronics
gen. S. Kaliskiego 2
00-908 Warsaw
POLAND

Jaroslav Nováček
Brno University of Technology
Faculty of Civil Engineering
Technology institute of building materials and components
Veveří 95
60200 Brno
CZECH REPUBLIC

Title	Thermophysics 2009 - Proceedings
Editor	Oldřich Zmeškal
Publisher	Brno University of Technology, Faculty of Chemistry, Purkyňova 464/118, CZ-612 00 Brno
Print	Brno University of Technology, Faculty of Chemistry, Purkyňova 464/118, CZ-612 00 Brno
Edition	first
Year of first edition	2009
Number of pages	264
Number of copies	50
ISBN	**ISBN 978-80-214-3986-3**